OUTLINE

OF

THE OPERATIONAL NUMERICAL WEATHER PREDICTION

AT

THE JAPAN METEOROLOGICAL AGENCY

Appendix to WMO Technical Progress Report on the Global Data-processing and

Forecasting System (GDPFS) and Numerical Weather Prediction (NWP) Research

March 2013

JAPAN METEOROLOGICAL AGENCY

Contents

Preface

The Japan Meteorological Agency (JMA) started the operation of numerical weather prediction (NWP) in June 1959 after several years of extensive research activities of the Numerical Weather Prediction Group of Japan. That was the third NWP operation in the world, following the Swedish Meteorological and Hydrological Institute (SMHI) in September 1954 and the US Weather Bureau in May 1955. The development of NWP since then has been tremendous. Operational NWP centers, including JMA, have benefited from ever better understanding of meteorological phenomena, improved modeling techniques, increasing computing power, efficient telecommunication systems, and improved observing systems, especially meteorological and earth-observing satellite systems.

This report is published to present technical details of the operational NWP systems of JMA as of February 2013, as an appendix to "WMO Technical Progress Report on the Global Data-processing and Forecasting System (GDPFS) and Numerical Weather Prediction (NWP) Research".

The first chapter provides an overview of the configurations and specifications of the current computer system at JMA. Thereafter follows a description of the operational suite and the operational job management system on the current computer system. The second chapter deals with three major data assimilation systems for atmospheric fields, namely, Global Analysis, Meso-scale Analysis and Local Analysis including the observation data used in these analyses. A description on the JMA Climate Data Assimilation System as well as more aspects on data assimilation is given in this chapter.

The third chapter describes a suite of NWP models for very short-range prediction of meso-scale disturbances, and for short- and medium-range prediction of synoptic-scale disturbances. The global model is used in ensemble prediction systems for the typhoon forecast, one-week and one-month prediction, and the coupled ocean-atmosphere model is employed for the seasonal forecast and El Niño forecast. An atmospheric transport models are applied to the prediction of transport of trace elements such as radioactive materials and Kosa (Aeolian Dust) for environmental information. The fourth chapter describes various kinds of application products of NWP such as weather charts, grid point values (GPV) products, very-short-range forecasting of precipitation, hourly analysis in wind and temperature, guidance for short-range forecasting, products for aviation services, products of ensemble prediction systems and atmospheric angular momentum functions. The last chapter is on sea state models, specifically ocean wave models, storm surge models, a sea ice model and an oil spill prediction model as well as sea surface temperature analysis systems and ocean data assimilation systems.

JMA is working forward a further strengthening of models (e.g., expanding the operation frequency of the Local Forecast Model (LFM) to hourly and its area to Japan and the surrounding area and raising the top level of the Global Spectral Model to include the whole stratosphere). The reader will find updated information on the NWP systems of JMA on the website of JMA <http://www.jma.go.jp/jma/en/Activities/nwp.html> and in the WMO Technical Progress Report on GDPFS and NWP Research that is issued every year.

TAKEUCHI Yoshiaki
Director
Numerical Prediction Division
Japan Meteorological Agency

Chapter 1

Computer System

1.1 Introduction

The Japan Meteorological Agency (JMA) installed its first-generation computer (IBM 704) to run an operational numerical weather prediction model in March 1959. Since then, the computer system at JMA has been repeatedly upgraded, and the current system (HITACHI SR16000) was completed in June 2012 as the ninth-generation computer. Figure 1.1.1 shows the history of computers at JMA, their peak performance, and a change in peak performance calculated using Moore's law[1] from the first computer (IBM 704). The peak performance of the second (HITAC 5020), the third (HITAC 8800), and the eighth (HITACHI SR11000) computers at the beginning of their implementation was almost the same as that projected using Moore's law, while it was lower during the 1980s, 1990s, and the first half of the 2000s. Recent growth is faster and the peak performance of the current computer is higher than the projection.

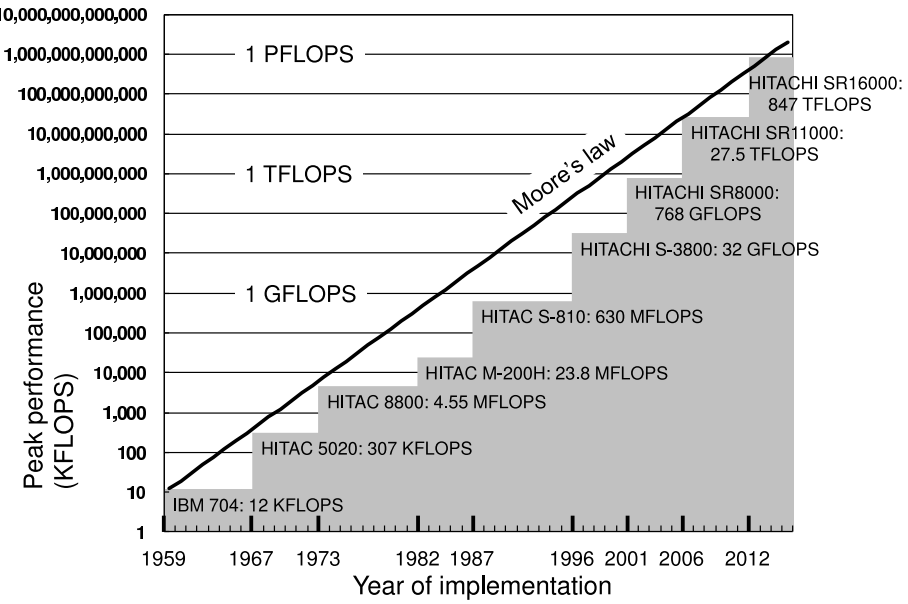

Figure 1.1.1: History of computers used at JMA and their peak performance. The line "Moore's law" represents the projection of peak performance using Moore's law from the first computer (IBM 704).

[1]The term "Moore's law" has many formulations. Here we refer to exponential growth of peak performance which doubles every 18 months.

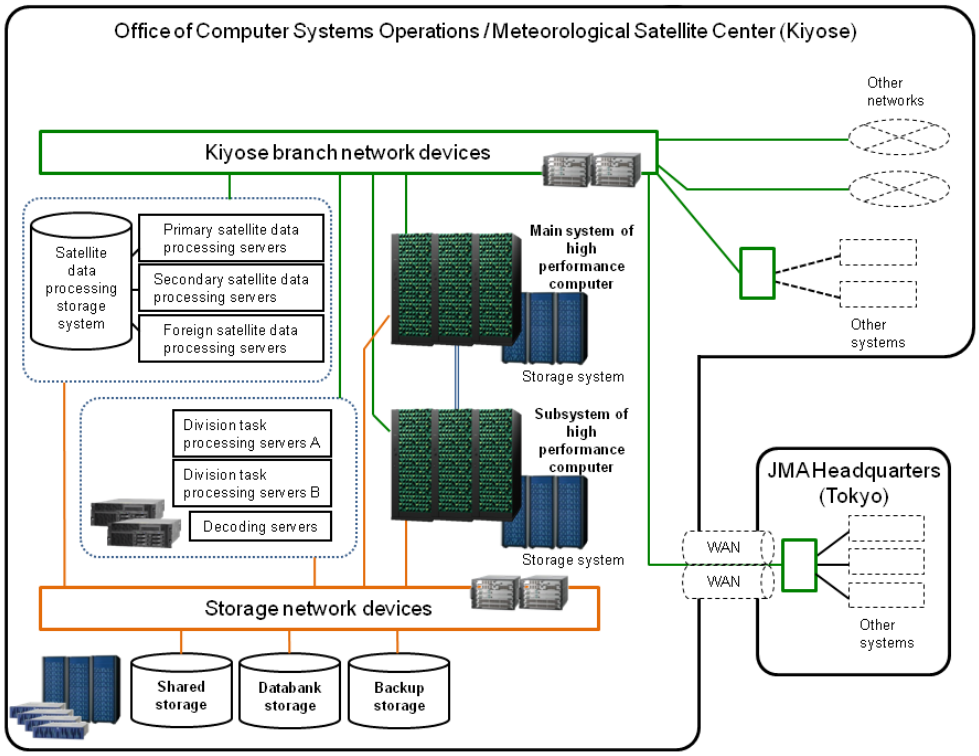

Figure 1.2.1: Schematic illustration of computer system

In this chapter, Section 1.2 briefly describes the configurations and specifications of the current computer system at JMA. Section 1.3 outlines the operational suite and the operational job management system on the current computer system.

1.2 System Configurations and Specifications

1.2.1 Overview

Figure 1.2.1 illustrates major components of the computer system at JMA including HITACHI SR16000 model M1 high performance computers, server computers, storages, terminals, and networks. This system has been in operation since 5 June 2012. Most of the computing facilities are installed at the site of the Office of Computer Systems Operations and the Meteorological Satellite Center in Kiyose City located 24 km west of the JMA headquarters (HQ) in central Tokyo. A wide area network (WAN) connects the Kiyose site and the HQ site. The specifications of the high performance computers and server computers are summarized in Table 1.2.1 and Table 1.2.2, respectively.

1.2.2 High Performance Computer

Two independent systems called a main system and a subsystem of an SR16000 model M1 high performance computer with the same specifications are installed at the Kiyose site. The main system usually runs operational numerical weather prediction jobs, while the subsystem usually runs development jobs. However, in case the main system is under maintenance or out of order, the subsystem runs operational jobs to make the system stable for operational use.

Table 1.2.1: Specifications of high performance computers

Computer	SR16000 model M1
Processor, clock frequency	IBM POWER7, 3.83 GHz
Cores per processor	8
Cores per logical node	32
Logical nodes per system	412 (computation), 10 (I/O), 4 (system), 6 (spare)
Number of systems	2
Peak performance per logical node	0.98 TFLOPS
Peak performance per system	423.5 TFLOPS (total), 403.9 TFLOPS (computation)
Memory per logical node	128 GiB
Memory per system	54.0 TiB (total), 51.5 TiB (computation)
Operating system	AIX 7.1

Table 1.2.2: Specifications of server computers

	Primary satellite data processing servers	Secondary satellite data processing servers	Foreign satellite data processing servers
Computer	EP8000/750	EP8000/750	HA8000/RS220AK1
Processor, clock frequency	IBM POWER7, 3.0 GHz	IBM POWER7, 3.0 GHz	Intel Xeon X5670, 2.93 GHz
Cores per processor	8	8	6
Cores per server	16	16	12
Number of servers	3	6	2
Memory per server	128 GiB	128 GiB	32 GiB
Operating system	AIX 6.1	AIX 6.1	Linux

	Division processing servers A	Division processing servers B	Decoding servers
Computer	BS2000	EP8000/520	EP8000/750
Processor, clock frequency	Intel Xeon E5640, 2.66 GHz	IBM POWER6+, 4.7 GHz	IBM POWER7, 3.0 GHz
Cores per processor	4	2	8
Cores per server	8	2	16
Number of servers	16	2	2
Memory per server	48 GiB	32 GiB	64 GiB
Operating system	Linux	AIX 6.1	AIX 6.1

The computational basis of SR16000 model M1 is an IBM POWER7 processor with a clock frequency of 3.83 GHz. One socket of a POWER7 processor is a multi-core chip which has eight separate cores.

One logical node comprises one multi-chip module with four sockets of POWER7 processors and dual inline memory modules. Therefore, the number of cores in one logical node is $4 \times 8 = 32$. The theoretical performance per logical node is 980.48 GFLOPS and the total memory capacity is 128 GiB per logical node[2]. The inter-node communication rate between each POWER7 processor and a hub processor is 96 GiB/s for one-way communication.

One physical node consists of eight logical nodes. Therefore, the number of cores in one physical node is $8 \times 4 \times 8 = 256$. The theoretical performance per physical node is 7,843.84 GFLOPS. Each logical node within a physical node is connected to another one with an inter-node communication rate of 24 GiB/s for one-way communication.

One super node consists of four physical nodes. Each physical node within a super node is connected to another one with a communication rate of 5 GiB/s for a one-way path. Eight paths are available for each communication between physical nodes, and therefore the total rate of communication becomes 40 GiB/s for one-way communication.

One system is composed of fourteen super nodes. Since one of fourteen super nodes in a system has only two physical nodes, the total numbers of logical nodes and physical nodes within a system are 432 and 54,

[2]The International Electrotechnical Commission approved names and symbols for the power of $2^{10} = 1,024$ instead that of 1,000 for prefixes of units. Symbols such as GiB or TiB refer to the former sense. In contrast, symbols such as GB or TB mean the latter.

respectively. In a system, 432 logical nodes are assigned to 412 computational nodes only for computation, 10 I/O nodes for data transfer between the system and external storages, 4 service nodes for system management, and 6 spare nodes as reserve stocks. Each logical node runs the AIX 7.1 operating system independently. Therefore, one system can be regarded as an aggregation of 432 separate computers. The theoretical performance per system is 423.5 TFLOPS for total 432 logical nodes and 403.9 TFLOPS for only 412 computational nodes. The total memory capacity per system is 54.0 TiB for total 432 logical nodes and 51.5 TiB for only 412 computational nodes.

The main system and subsystem have high-speed magnetic disks with capacities of 135 TB and 210 TB, respectively. Every time an operational job running on the main system is completed, the output files from the job are copied to the disk on the subsystem to keep the subsystem ready to run succeeding operational jobs if the operation is switched to it.

1.2.3 Server and Terminal Computers

A number of server computers are installed for various kinds of tasks such as processing and decoding of observational data, analyses of weather charts, management of the operational suite, and other small jobs.

The primary, secondary, and foreign satellite data processing servers are used for automatic data processing of various kinds of satellite observations. The primary satellite data processing servers consist of three servers of EP8000/750 with two IBM POWER7 (3.0 GHz) processors. The secondary satellite data processing servers consist of six servers of EP8000/750 with two IBM POWER7 (3.0 GHz) processors. The foreign satellite data processing servers consist of two servers of HA8000/RS220AK1 with two Intel Xeon X5670 (2.93 GHz) processors.

The division task processing servers A and B are used for weather chart analyses and small operational jobs that are transaction-intensive rather than compute-intensive. The division task processing servers A consist of sixteen servers of BS2000 with two Intel Xeon E5640 (2.66 GHz) processors. The division task processing servers B consist of two servers of EP8000/520 with one IBM POWER6+ (4.7 GHz) processor.

The decoding servers are used for decoding jobs of observational data and consist of two servers of EP8000/750 with two IBM POWER7 (3.0 GHz) processors.

There are other server computers that manage the operational suite of numerical weather predictions, satellite data processing, and other jobs. In addition, there are server and terminal computers to monitor and manage the computer system.

1.2.4 Mass Storage System

Three kinds of storage systems are available to share data between the high performance computers and server computers. They are shared storage, data bank storage, and backup storage systems.

The shared storage system is used from jobs running on the high performance computers or server computers. This system comprises four network-attached storage (NAS) units which consist of RAID 6 magnetic disks[3] with a total capacity of 754 TB.

The data bank storage system is used for long-time archiving. This system comprises six NAS units which consist of RAID 6 magnetic disks with a total capacity of 2,932 TB.

The backup storage system automatically makes backup copies under specified directories of the data bank storage system. This system consists of a tape library, two management servers, and a shared storage between the servers. The total capacity of the backup storage system is 1,520 TB.

1.2.5 Networks

The Kiyose branch network connects the high performance computers, server computers, and other networks and servers out of the computer system mentioned above.

The storage network connects the high performance computers, server computers, shared storage system, databank storage system, and backup storage system.

[3]The term RAID is short for redundant array of independent disks or redundant array of inexpensive disks. In particular, RAID 6 utilizes block-level striping with double distributed parity and provides fault tolerance of two drive failures.

Users at the HQ site remotely log in to computers at the Kiyose site through a WAN (Figure 1.2.1). This WAN consists of two independent links with a transfer speed of 100 Mbps each. One link is used for operational jobs, while the other is used for development jobs. All the network equipment is configured redundantly to avoid a single equipment failure causing a total interruption.

1.3 Operational Aspects

1.3.1 Operational Suite

The operational suite of JMA that will be described in later chapters consists of about 70 job groups including the global analysis, global forecast, and so on. The number of total jobs composing all the job groups is about 10,600 per day. All the jobs are submitted using a parallel job scheduling system, LoadLeveler. The numbers of kinds of constant and variable datasets are about 3,000 and 8,800, respectively.

Figure 1.3.1 illustrates the daily schedule of the operational suite job groups[4] running on the main system of the high performance computer as of February 2013.

1.3.2 Management System of Operational Jobs

There are complicated dependencies between jobs in a job group and between input and output datasets. To manage a vast number of operational jobs and datasets systematically and to assure the jobs run correctly by eliminating man-made errors, JMA developed a comprehensive system using database management systems (DBMSs). All the information about jobs, input and output datasets, and executables is registered in the DBMSs. The dependencies between these elements can be checked using utility programs.

The management system of operational jobs is comprised of four kinds of files, two DBMSs, and several utility programs to register information, check the consistency and so on:

- Files

  Registration form: Information about job groups, jobs, datasets, executables, and so on. A registration form is submitted when jobs are added or deleted, datasets or executables are updated, or the configurations of job groups or jobs are modified.

  Job definition file: Information about a job group and jobs within the job group such as the job group name, the job name, the schedule (time to run), the order of job groups and jobs (preceding job groups and jobs), and computational resources required (the LoadLeveler job class, the number of nodes, the computational time).

  Job control language: Information about executables such as a shell script, a ruby script, an awk script and a load module, and input and output datasets used in each job. A job control language file is converted into a shell script using a utility program to be submitted to LoadLeveler.

  Program build file-format: Information about source files, object modules, libraries, options for compilation, and so on. A program build file-format is converted into a makefile using a utility program to compile load modules.

- DBMSs

  DBMS for registration: Information from the above four files is registered using utility programs.

  DBMS for job management: Information from the DMBS for registration is stored and this information is used by job schedulers.

When a job control language is converted into a shell script, the following procedures are made:

[4] Semi-operational job groups running on the main system of the high performance computer and operational job groups running on the decoding servers are not included here.

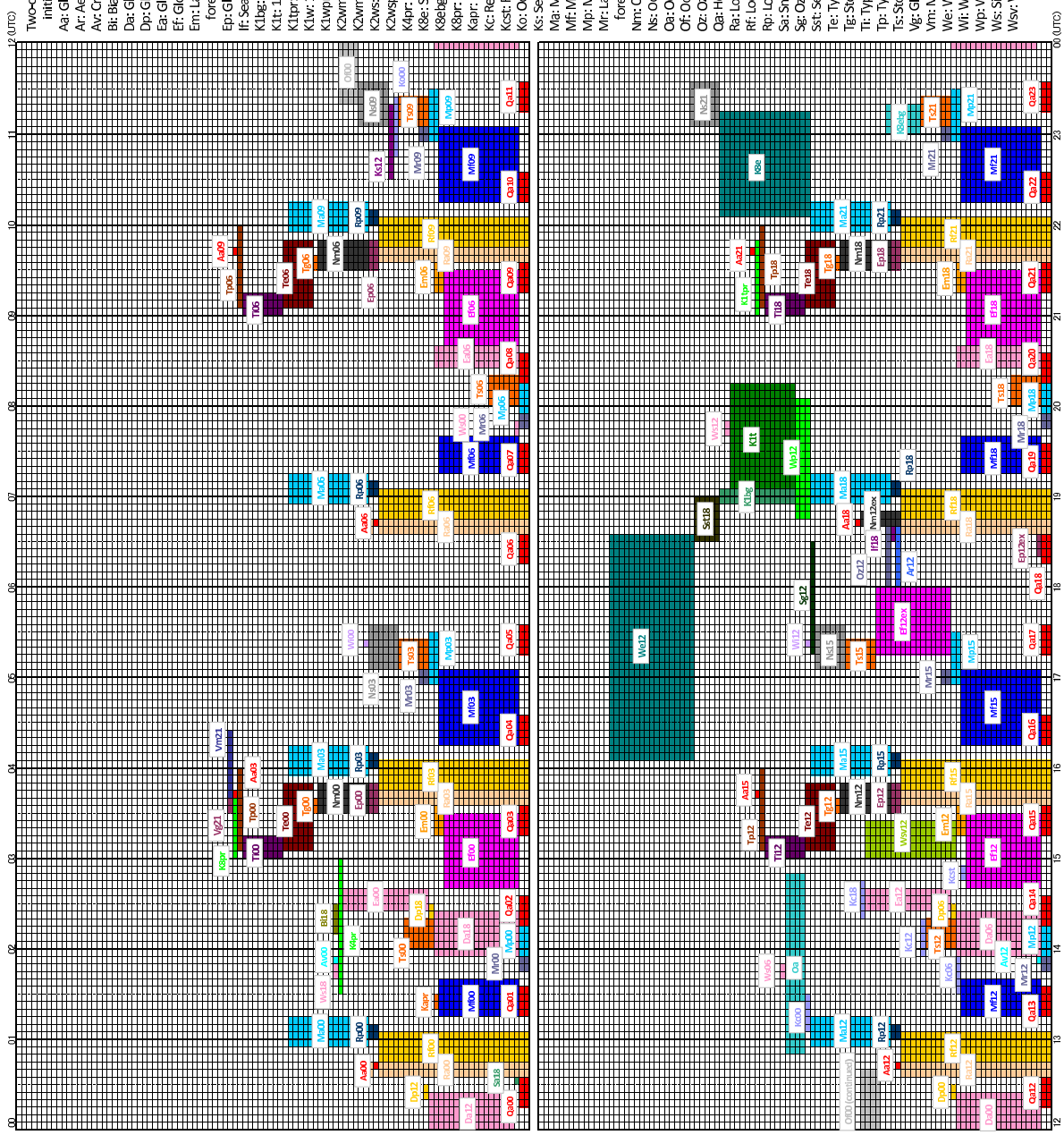

Figure 1.3.1: Daily schedule of operational suite running on main system of high performance computer as of February 2013. Height and width of each box indicate the approximate number of nodes and time range, respectively.

- Existence test: A shell script tests the existence of all non-optional input datasets at the beginning in order to avoid wasting time if the preceding job failed.
- Quasi-atomic output: Every step of a job calling an executable creates output files with temporary names at first and renames them to final names when the step successfully terminates.

The development of the management system of operational jobs was started in 2004 on the seventh computer system and installed in the operational system in 2006 when the eighth computer system was implemented. The number of man-made errors after the inclusion of this management system was reduced to about one sixth of that before the adoption.

Chapter 2

Data Assimilation Systems

2.1 Summary

Three kinds of major data assimilation systems for the analysis for atmospheric fields are operated at JMA: Global Analysis (GA), Meso-scale Analysis (MA) and Local Analysis (LA). Specifications of the JMA data assimilation systems are summarized in Table 2.1.1. All the analyses are performed by using the procedures shown in Figure 2.1.1.

The following is a brief description of the major components of the analysis systems.

1. Observational data are received from the GTS, Internet and dedicated network. They are decoded according to their code forms. If typhoons exist in the western North Pacific, typhoon bogus profiles are created.

2. Various pre-analysis procedures, such as quality control, data selection and bias correction, are applied to the decoded observational data. In the pre-analysis process, first guess fields retrieved from forecast models are used as a reference of the present atmospheric conditions.

3. The four-dimensional variational method is adopted in the global analysis and the meso-scale analysis. And the three-dimensional variational method is adopted in the local analysis. All the analyses are carried out on the grid of the corresponding forecast models except for the local analysis.

The atmospheric fields analyzed from the data assimilation systems are used as initial conditions of forecast models. First guess field and boundary conditions of data assimilation systems are provided from forecast models as shown in Figure 2.1.2.

Sea surface temperature field (see Section 5.2) and snow depth field are also analyzed every day. For climate monitoring, JMA Climate Data Assimilation System (JCDAS) is operated taking over the data assimilation cycle of the Japanese 25-year Reanalysis (JRA-25) (see Section 2.10).

2.2 Observation Data

2.2.1 Summary of Observation Data Used in the Analysis

A variety of observations has been utilized in the present NWP systems in JMA. Table 2.2.1 summarizes the utilized observation types and the parameters which are inputted into the objective analysis systems, as of 1 January 2013. The additional information for each observation type is described in the following subsection.

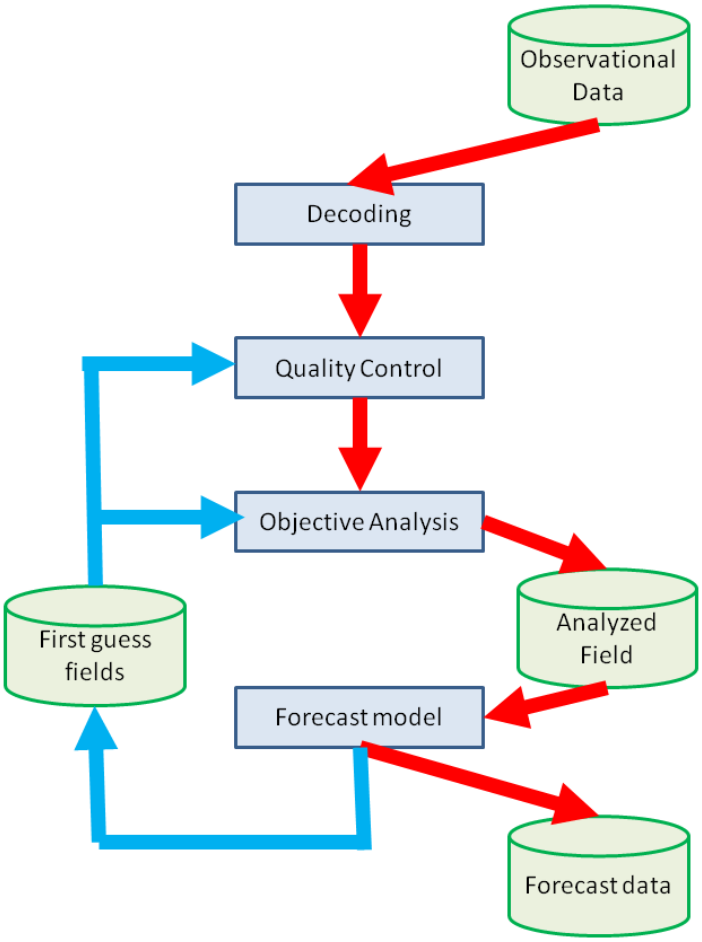

Figure 2.1.1: Major functional components and data flow in the JMA data assimilation system

Table 2.1.1: Specifications of the JMA data assimilation systems

Analysis Model	Global Analysis (GA)	Meso-scale Analysis (MA)	Local Analysis (LA)
Analysis time	00, 06, 12, 18 UTC	00, 03, 06, 09, 12, 15, 18, 21 UTC	00, 03, 06, 09, 12, 15, 18, 21 UTC
Data cut-off time	Early analysis: 2h20m (00,06,12,18UTC) Cycle analysis: 11h50m (00,12UTC) 7h50m (06,18UTC)	50m (00,03,06,09,12,15,18,21 UTC)	30m (00,03,06,09,12,15,18,21 UTC)
Horizontal Grid system	Reduced Gaussian grid	Lambert projection	Lambert projection
Horizontal resolution	TL959 (20km)	5km at 60°N and 30°N	5km at 60°N and 30°N
Number of grid points	$(1920-60)\times 960$	721×577	441×501
Horizontal resolution of inner model	TL319 (55km)	15km at 60°N and 30°N	-
Number of grid points of inner model	$(640-60)\times 320$	241×193	-
Vertical coordinate	σ-p hybrid	z-$z^\star$ hybrid	
Vertical levels	Surface +60 levels up to 0.1hPa	Surface +50 levels up to 21.8km	50 levels up to 21.8km
Analysis scheme	4-dimensional variational method		3-dimensional variational method

Global snow depth analysis is carried out everyday on $1^\circ\times 1^\circ$ longitude-latitude grids.
JMA Climate Data Assimilation System (JCDAS) is performed taking over the data assimilation cycle of the Japanese 25-year Reanalysis (JRA-25)(see Section 2.10).

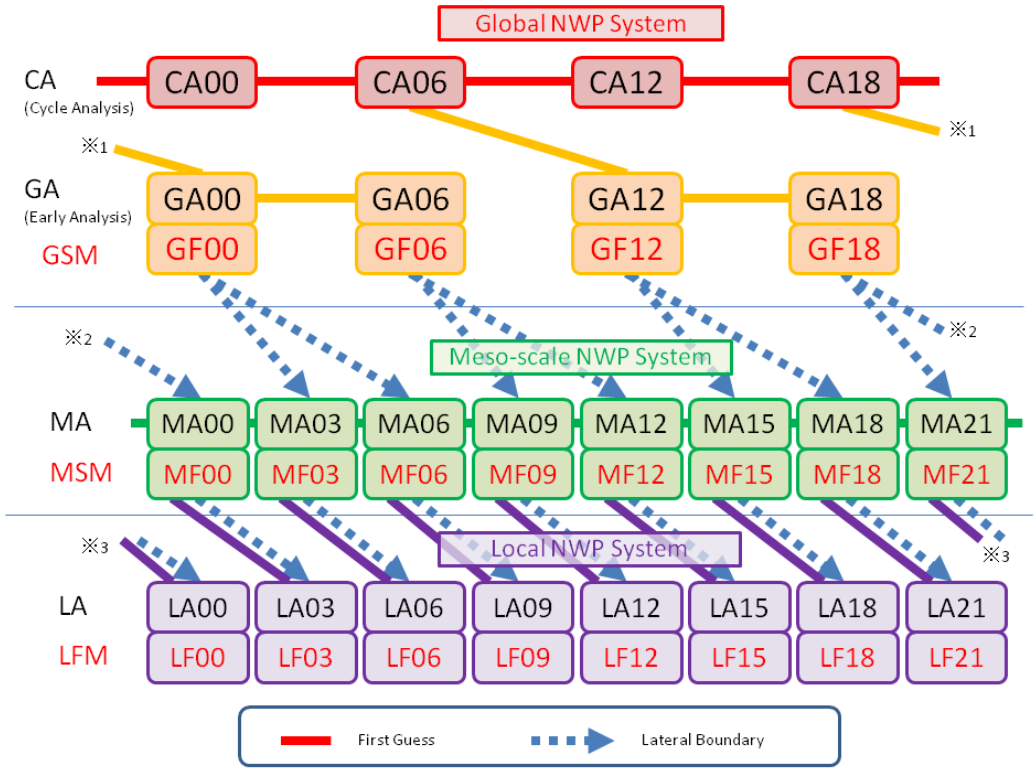

Figure 2.1.2: Major flow of the JMA data assimilation systems

Table 2.2.1: Summary of the observation types and the parameters used in the objective analysis. The meanings of the symbols in the third column are as follows. P: Surface pressure; u: zonal wind; v: meridional wind; T: Temperature; Rh: Relative humidity; T_B: Radiance in brightness temperature; R_1: Precipitation amount; Pwv: Precipitable water vapor; Vr: Radial velocity. The meanings of the symbols in the fourth columns are as follows. GA: Global Analysis; MA: Meso-scale Analysis; LA: Local Analysis.

Observation types (or the code name used for reporting the observation)	Short description	Parameters used in the analysis	The analyses which use the observation
SYNOP	Land surface observations at the world's weather stations	P, u, v, T, Rh	GA, MA, LA
AMeDAS	Land surface automated observation network in Japan	u, v, T	LA
SHIP	Sea surface observations by ships, oil rigs and moored buoys	P, u, v, T, Rh	GA, MA
BUOY	Sea surface observations by drifting buoys	P, u, v, T, Rh	GA, MA
TEMP	Upper-air observations by radiosondes	P, u, v, T, Rh	GA, MA
PILOT	Upper-air wind observations by rawins or pilot balloons	u, v	GA, MA
Aircraft	Upper-air observations by (mainly commercial) aircrafts.	u, v, T	GA, MA, LA
Wind Profiler	Upper-air wind profile observations in Japan, Hong Kong, Europe and the U.S.	u, v	GA, MA, LA
AMV	Atmospheric motion vector (AMV) wind data from geostationary (GEO) satellites and polar orbiting satellites	u, v	GA, MA
Scatterometer	Ocean surface wind vector (OSWV) data from scatterometers on low earth orbit (LEO) satellites	u, v	GA
MW Sounder	Radiance data from microwave (MW) sounders on polar orbiting satellites	T_B	GA, MA
MW Imager	Radiance data from MW imagers on LEO satellites and precipitation amount estimated from the MW imager radiance data	T_B, R_1	$GA(T_B$ only$), MA$
CSR	Clear sky radiance (CSR) data of water vapor channels on GEO satellites' infrared imagers	T_B	GA, MA
GNSS-RO	Refractivity profile data retrieved from radio occultation (RO) measurements of the global navigation satellite systems (GNSS) receivers on LEO satellites	refractivity	GA
GNSS-PWV	Precipitable water vapor data estimated from atmospheric signal delay measurements of the ground-based GNSS receivers	Pwv	MA, LA
Radar Reflectivity	Relative humidity data estimated from 3-dimensional reflectivity data of JMA weather (Doppler) radars.	Rh	MA
Radial Velocity	Radial velocity data from JMA weather Doppler radars (WDRs) and Doppler radars for airport weather (DRAWs).	Vr	MA, LA
R/A	Radar estimated precipitation amount calibrated by AMeDAS raingauge network data	R_1	MA
Typhoon Bogus	see Section 2.4	P, u, v	GA, MA

2.2.2 Supplemental Information for Used Observation

2.2.2.1 SYNOP

SYNOP is a numerical code name used for reporting surface observations at land stations. About 16,000 reports are available within every 6 hours.

2.2.2.2 AMeDAS

AMeDAS (Automated Meteorological Data Acquisition System) is a JMA land surface automated observation network. Near surface temperature and wind observations at about 840 stations are available in Japan with 10 minutes interval. For precipitation, about 1,300 raingauges are available in the AMeDAS network.

2.2.2.3 SHIP

SHIP is a numerical code name used for reporting surface observations at sea stations, such as ships, oil rigs and moored buoys anchored at fixed locations. About 4,500 reports are available within every 6 hours.

2.2.2.4 BUOY

BUOY is a numerical code name used for reporting surface observations by drifting buoys. About 7,500 reports are available within every 6 hours.

2.2.2.5 TEMP

TEMP is a numerical code name used for reporting upper-level pressure, temperature, humidity and wind observations by radiosondes. The upper air observations are usually taken at the same time each day (00 and/or 12 UTC). About 650 reports are available at these times.

2.2.2.6 PILOT

PILOT is a numerical code name used for reporting upper-level wind observations by rawins or pilot balloons. About 300, 200 and 100 reports are available at 00 and 12 UTC, 06 UTC and 18UTC, respectively.

2.2.2.7 Aircraft

Aircraft observations are reported by Aircraft Report (AIREP), Aircraft Meteorological Data Relay (AMDAR), and Aircraft Communications Addressing and Reporting System (ACARS). Since numerous reports are received from the U.S., the reports are thinned to one-fiftieth over the continental U.S. in the pre-process of the analysis. Even after the pre-process, 30,000-50,000 reports are available within every 6 hours in the world. While vertical profile data can be obtained in the vicinity of airports, only flight level data are available along the airways apart from airports.

2.2.2.8 Wind Profiler

Upper air wind speeds and directions are observed by wind profilers at the ground. 33 wind profilers are operated by JMA and the data are available every 10 minutes. The detailed specifications are found in Ishihara *et al.* (2006). Wind profiler data from the U.S., Europe, and Hong Kong is also available.

2.2.2.9 AMV

Atmospheric motion vector (AMV) is the wind data derived by tracing the movement of individual cloud or water vapor patterns in successive satellite images. The AMVs from 5 geostationary (GEO) satellites (Meteosat-7, -9, GOES-13, -15 and MTSAT-2) and 2 polar orbiting satellites (Terra and Aqua) are used. AMVs from GEO satellites cover 60°N – 60°S and those from polar orbiting satellites cover the polar regions (higher latitudes than 60°).

2.2.2.10 Scatterometer

Ocean surface wind vectors from scatterometers onboard polar orbiting satellites are used. Only ASCAT (advanced scatterometer) onboard Europe's polar orbiting satellite, Metop-A, is being used.

2.2.2.11 MW Sounder

Clear radiances from microwave (MW) sounders are used. The used sounders are AMSU-A (Advance Microwave Sounding Unit - A) onboard NOAA-15, -16, -18, -19, Metop-A and Aqua, and MHS (Microwave Humidity Sounder) onboard NOAA-18,-19 and Metop-A. The AMSU-A is a temperature sounder and the radiance is sensitive to the temperature profiles. MHS is a humidity sounder.

2.2.2.12 MW Imager

The less cloud/rain-affected radiances from MW imagers are used. The used imagers are SSMIS (Special Sensor Microwave Imager Sounder) onboard DMSP-F16, -F17, -F18 and TMI (TRMM (Tropical Rainfall Measuring Mission) Microwave Imager) onboard TRMM. The radiance is sensitive to the water vapor amount at the lower troposphere. Precipitation amounts estimated from the radiances by MSC method (Takeuchi and Kurino 1997) are also used in the Meso-scale Analysis.

2.2.2.13 CSR

Clear sky radiance (CSR) is the product name of the radiances averaged over cloud-free pixels on water vapor channels in GEO satellites' imagers. The CSRs from 5 GEO satellites (Meteosat-7, -9, GOES-13, -15 and MTSAT-2) are used. The CSR is sensitive to the water vapor amount at the upper troposphere.

2.2.2.14 GNSS-RO

GNSS-RO (Global Navigation Satellite Systems - Radio Occultation) is a technique for measuring atmospheric profiles. In this technique, a set of atmospheric time delay data of GNSS radio signals received by a low earth orbit (LEO) satellite is measured during each radio occultation event. Since the delay is a result of the atmospheric radio refraction along the propagation path of the signal, the vertical profiles of refractivity (or bending angle) of the atmosphere at the tangent point can be estimated with the set of delay data. As the refractivity is a function of temperature, humidity and pressure, it can be used for determining the profiles of these properties. The currently used LEO satellites and their GNSS receivers are IGOR (Integrated GPS Occultation Receiver) onboard COSMIC (Constellation Observing System for Meteorology, Ionosphere and Climate) satellites and TerraSAR-X, GRAS (GNSS Receiver for Atmospheric Sounding) onboard Metop-A, BlackJack onboard GRACE-A (Gravity Recovery and Climate Experiment) and CORISS (C/NOFS Occultation Receiver for Ionospheric Sensing and Specification) onboard C/NOFS (Communications/Navigation Outage Forecasting System).

2.2.2.15 GNSS-PWV

GNSS-PWV (GNSS - Precipitable Water Vapor) is a product name of the observations by ground-based GNSS receivers. Atmospheric time delays of GNSS radio signals are observed by the receivers and zenith total delay (ZTD) is estimated by averaging the delays of multiple GNSS satellite signals measured by one receiver. Since the ZTD depends on the amount of water vapor and temperature over the receiver, PWV amount can be estimated by using ZTD and supplemental temperature data. GEONET GNSS receiver data are used for GNSS-PWV analysis in JMA. The GEONET is the ground based GNSS receiver network operated by Geospatial Information Authority in Japan. About 1,200 receives are operated continuously over Japan.

2.2.2.16 Radar Reflectivity

Twenty C-band weather radars are operated by JMA and eighteen of them are equipped with Doppler function. Three-dimensional reflectivity data are obtained every five minutes. Relative humidity profiles are estimated from the reflectivity data and NWP grid point values by the technique based on Bayes' theorem (Caumont *et al.* 2010). The relative humidity data are produced within 200 km radius from each radar site below freezing level.

2.2.2.17 Radial Velocity

Eighteen C-band weather Doppler Radars (WDRs) and 9 Doppler Radars for Airport Weathers (DRAWs) are operated by JMA. Three-dimensional radial velocity data are available every five minutes within 150 km radius for WDRs and every six minutes within 120 km for DRAWs. The range resolution is 0.5 km and the azimuthal resolution is 0.703°.

2.2.2.18 R/A

Radar/Raingauge Analyzed Precipitation (R/A) data are a product name of composite precipitation data produced by JMA. The precipitation data are the accumulated precipitation estimation by weather radars with Z-R relationship ($Z = 200R^{1.6}$) calibrated by AMeDAS raingauge data in real time. The details are found in Subsection 4.4.1.

2.3 Quality Control and Relating Procedures

Quality control (QC) is a series of procedures by which "bad" observations are screened out. The QC is a vital component of the objective analysis system, because observations sometimes include large error and the erroneous data might degrade the quality of atmospheric analysis extremely. Such degradation leads to the worse forecast skill. The QC procedures in the JMA objective analysis systems are described in the following subsections.

2.3.1 SYNOP, AMeDAS, SHIP, BUOY, TEMP, PILOT, Aircraft and Wind Profiler

Direct observations (i.e. SYNOP, AMeDAS, SHIP, BUOY, TEMP, PILOT and aircraft) and wind profiler are the observations measuring prognostic variables in the NWP such as pressure, temperature, wind and humidity. The total QC system for these observations is composed by "Internal QC" and "External QC".

2.3.1.1 Internal QC

Internal QC is the procedures to check and correct observation values using the collocated data in the report and several external lists or tables. The check items are shown as follows.

1. Blacklist check: Blacklist is a list of problematic stations or data prepared in advance with non-real-time QC (see Section 2.9). The observations enlisted in the blacklist are rejected in this step.

2. Climatological check: Climatological reasonability is checked in this step. The criteria are defined based on WMO (1993) in advance.

3. Trajectory check: Consistency of consecutive locations is checked for the reports from moving stations such as SHIP, BUOY and aircrafts. The moving velocity and direction are checked in this step. It is also checked for SHIP and BUOY whether the location is in the ocean or not.

4. Inter-element consistency check: Temporal continuity of consecutive reports from surface stations are checked. Consistencies among observation elements within the report are also checked.

5. Vertical consistency check: The vertical consistency is checked for TEMP and PILOT data. The check items are (1) icing of instruments, (2) temperature lapse rate, (3) hydrostatic relationship, (4) consistency among data at standard pressure levels and those at significant levels and (5) vertical wind shear.

6. Bias correction: A bias correction is applied to the TEMP data which are reported without radiative heating correction or have apparent systematic biases. The bias correction constants are prepared with the one-month statistics in the previous month. Same bias correction approach is applied to the aircraft temperature data for the Global Analysis but not for the meso-scale and Local Analysis.

2.3.1.2 External QC

External QC is the procedures to check the observation values with comparing to the (external) first guess and neighboring observations. The check items are as follows.

1. Gross error check: The departure ($D \equiv O - B$) of the observed value (O) from the first guess (B) is calculated for all the observations. The absolute value of D is compared with the tolerance limits C_P (the criterion for "pass") and C_R (the criterion for "reject"). The datum with $|D| \leq C_P$ passes the QC and the datum with $|D| > C_R$ is rejected. The datum with $C_P < |D| \leq C_R$ is regarded as "suspected" and sent to the following spatial consistency check.

2. Spatial consistency check: The departure D of the suspected observations are compared with the departures interpolated by the optimum interpolation method (D_{OI}) using the neighboring observations. The absolute difference of the D and D_{OI} is compared with the tolerance limit C_S (the criterion for "suspect") for the final judgment and the datum with $|D - D_{OI}| \leq C_S$ is accepted.

   Where, the tolerance limits C_P, C_R, and C_S are variable according to the local atmospheric conditions in the first guess fields. The limits are made small if the time tendency and horizontal gradient are small in the fields, and *vice versa*. The scheme is called "Dynamic QC" (Onogi 1998).

3. Duplication check: Duplication of observation reports is frequently found for the data obtained through different communication lines. The most appropriate report is picked up from the duplicated reports after the above mentioned checks with considering the status.

2.3.2 AMV

The AMVs enlisted in the blacklist (Table 2.3.1) are rejected in the first step. Then the AMVs with the low quality indicator (QI, Holmlund 1998) are also rejected. The QI thresholds are defined for each satellite, domain, vertical level and type of image, respectively. It is followed by a thinning step. The thinning distance is 200 km. The following steps are the climatological check (see Subsection 2.3.1.1) and the external QC (see Subsection 2.3.1.2). The details of the QC for AMV are described in the NWP SAF AMV monitoring page[1].

2.3.3 Scatterometer

Level 2 ocean surface wind products are used in the Global Analysis. Low quality data over land or sea ice are rejected at the first step. The wind data with the speed larger than 15 m/s are also rejected for ASCAT because of the negative bias in the intense wind against the first guess. Then, the most likely wind directions are selected from the inherent ambiguity wind directions in the scatterometer measurements by both NWP nudging technique and median filter technique. The next step is the gross error check (see Subsection 2.3.1.2). In this step, correct wind data are occasionally rejected in and around severe weather systems such as cyclones and fronts where the wind direction and speed vary sharply. To avoid such undesirable rejection, a specialized quality control named "Group-QC" is applied. In the Group QC, spatial consistency among the wind vectors is checked in terms of smooth transition in wind direction and wind speed. The Group-QC-passed data are excluded from the rejection in the gross error check. The details of the QC for scatterometer are described in the NWP SAF scatterometer monitoring page[2].

[1] `http://research.metoffice.gov.uk/research/interproj/nwpsaf/satwind_report/amvusage/jmamodel.html`
[2] `http://research.metoffice.gov.uk/research/interproj/nwpsaf/scatter_report/scatusage/jmamodel.html`

Table 2.3.1: Summary of the blacklisting areas for AMV. The acronyms in the table are as follows. IR: infrared; WV: water vapor; CSWV: clear sky water vapor; NH: Northern Hemisphere; SH: Southern Hemisphere; Polar AMV: AMV from polar orbiting satellites; GEO AMV: AMV from geostationary satellite

Kind	Blacklisting area
Polar AMV (IR) at NH	above 300 hPa or below 900 hPa
Polar AMV (WV/CSWV) at NH	above 300 hPa or below 550 hPa
Polar AMV (IR/WV) at SH	above 300 hPa or below 550 hPa
Polar AMV (CSWV) at SH	above 350 hPa or below 550 hPa
Polar AMV (All)	poleward of 88°N or 88°S
GEO AMV (All)	above 175 hPa or below 975 hPa
GEO AMV (IR)	above 275 hPa at poleward of 20°N or 20°S
GEO AMV (WV)	above 225 hPa at poleward of 20°N or 20°S

Table 2.3.2: Summary of the used channel sets of microwave sounders under each condition

	AMSU-A	MHS
clear sky ocean	ch. 4–13	ch. 3–5
clear sky land/coast/sea-ice	ch. 6–13	ch. 3–5
cloudy ocean	ch. 7–13	ch. 3–5
rainy ocean	ch. 9–13	n/a

2.3.4 Satellite Radiance

Satellite radiance data are used in the Global and Meso-scale Analysis as a form of brightness temperature. A fast radiative transfer model RTTOV10 (Saunders *et al.* 2012) is employed for the radiance assimilation. The common QC procedures for the radiance data are blacklist check, thinning and external QC. The blacklist is the list for problematic instrument prepared in advance with non-real-time QC (see Section 2.9). The data enlisted in the blacklist are rejected in the first step. In the next step, the data are thinned spatially at each time slot of assimilation window (approximately one hour) to reduce the computational costs. The following external QC includes reduction of instrumental scan biases (except for CSR), cloud/rain contamination check, location check, channel selection and gross error check (see Subsection 2.3.1.2). The QC passed data are thinned again for the reduction of observation error correlation. The thinned data are outputted to be used in the data assimilation systems. In the Global Analysis, variational bias correction (VarBC, Derber and Wu 1998; Dee 2004) is used for the reduction of air-mass dependent biases. VarBC is an adaptive bias correction scheme where a linear regression formula to represent biases is embedded in the observation operator and the regression coefficients are set as analysis variables. The formulations are described in Subsection 2.5.7.4. In the Meso-scale Analysis, the air-mass dependent biases are removed in the pre-process by using the VarBC coefficients obtained in the latest Global Analysis. The used satellite radiance data are the data from MW sounder, MW imager and CSR. The specific procedures for each data are described in the following subsections.

2.3.4.1 MW sounder

The sets of used channels are defined according to each surface and atmospheric condition in advance. The sets are summarized in Table 2.3.2.

2.3.4.2 MW imager

The less cloud/rain-affected radiances of vertically polarized channels are assimilated over the ice-free ocean. In the Meso-scale Analysis, precipitation retrievals are also assimilated over the ocean surrounding Japan. The precipitation amount estimations are resampled onto the grid of inner model with spatial smoothing.

2.3.4.3 CSR

The CSR are thinned to every 2.0 degrees horizontally and every 2 hours temporally. The CSR having a low percentage of clear pixels and a large standard deviation of brightness temperature are excluded because these data have low representativeness of the area. For Meteosat-7, data in nearly local midnight are also excluded to avoid solar stray light contamination (Munro *et al.* 2004).

2.3.5 GNSS-RO

Refractivity data at the altitudes up to 30 km are used in the Global Analysis with the 500 m vertical intervals. The observation errors are defined as a function of height.

2.3.6 GNSS-PWV

The PWV data are used in the meso-scale and Local Analysis. Since there are steep mountains in Japan, large differences are found between the actual ground surface elevation and the model surface elevation especially in mountain area. In the Meso-scale Analysis, the stations with 500 m or higher elevation from the mean sea level are not used. The stations from which the absolute difference of the elevation to the model surface is larger than 200 m are also not used. The GNSS-PWV with the value smaller than 1 mm or larger than 90 mm is rejected in a climatorogical check. Then, the first guess PWV is interpolated or extrapolated to the actual terrain surface and compared to the GNSS-PWV. The data with the absolute difference from the first guess are larger than 8 mm are rejected in a gross error check. Since there are dense GNSS-PWV network for the analysis systems, the data are thinned by 30 km for the Meso-scale Analysis and 15 km for the Local Analysis.

2.3.7 Radar Reflectivity

To assimilate the radar reflectivity data in the Meso-scale Analysis, an indirect assimilation technique which is called 1D+4DVAR (Ikuta and Honda 2011) is employed. The technique is based on Caumont *et al.* (2010). In the 1D+4DVAR, radar reflectivity data are used for retrieving relative humidity (RH), and the RH retrievals are assimilated as conventional observation data by 4D-Var. In this system, only the RH retrievals below the melting layer are used because it is known the reflectivity can be only inappropriately simulated in ice phase with the operational MSM hydrometeors forecast and it causes large biases for the RH retrievals. In addition, the data around the height of 2000 m above sea level are also not used since the data used for making R/A, which are already assimilated in the Meso-scale Analysis in another form (surface rainfall, see Subsection 2.3.9). For the operation, reflectivity data from the JMA C-band radar network are used.

2.3.8 Radial Velocity

The hourly radial velocity data from the WDRs and the DRAWs are used in the Meso-scale Analysis. In the pre-process, the data are resampled into the 5 km range resolution and the 5.625° azimuthal resolution. The resampled data are checked with respect to the sampling data number, radial velocity variance and difference of the maximum and minimum velocity. High elevation angle data ($\geq 5.9°$) and the data close to the radar site (< 10km) are not used. The reason for the former procedure is to avoid the contamination of precipitation fall velocity, and the latter is to avoid the back scattering noise. The data with the wind speed less than 10 m/s is also not used to avoid ground clutter contamination.

2.3.9 R/A

Hourly R/A data are assimilated in the Meso-scale Analysis. Since the R/A data are the quality controlled product, the 1 km grid R/A data are simply resampled into the inner-model grid box (15 km) and inputted into the Meso-scale Analysis.

2.3.10 CDA: Feedback Data Base

All information concerning the quality of observational data obtained during the quality control procedure are archived in the Comprehensive Database for Assimilation (CDA). CDA is extensively used for both real-time and non real-time data monitoring activities. All information contained in CDA is managed by the form of integer 2 byte. The format of CDA is quite simple and is designed for flexible use so that any information concerning observation can be archived easily. CDA is so user-friendly that any information can be extracted easily. The CDA file size tends to become large but it can be remarkably compressed using utilities in UNIX.

2.4 Typhoon Bogussing

For tropical cyclones (TCs) over the western North Pacific, typhoon bogus data as a form of pseudo-observation data are generated and assimilated for a realistic TC structure analysis according to the model resolutions. They are made up of pressures at the mean sea level (P_{msl}) and vertical profiles of the wind (W_{prf}) around TC. The wind profiles are placed at 1000 hPa, 925 hPa, 850 hPa, 800 hPa, 700 hPa, 600 hPa, 500 hPa, 400 hPa and 300 hPa. The generated bogus has axially asymmetric structure in all the analyses.

Firstly, symmetric bogus profiles are generated automatically from the central pressure and the 15m/s wind speed radius of TC (R_{15}) analyzed by forecasters. The surface pressure profile is defined using Fujita's formula (Fujita 1952). The gradient wind balance is assumed to calculate the surface pressure profile meeting the requirement from the wind speed at the particular radius R_{15}. Upper geopotential profiles are defined by the empirical formula based on the TC analysis described in Frank (1977). It is assumed that the temperature anomaly has its maximum at 250 hPa. The wind field on each level is derived from the geopotential height profiles with the gradient wind balance. The surface wind field is also derived from the gradient wind balance but it is modified to include the effect of surface friction.

Secondly, asymmetric components are retrieved from the first guess fields and added to the symmetric bogus profile to generate the final asymmetric bogus structure. When the target area of bogussing is across the lateral boundary in the Meso-scale Analysis, asymmetric components are not added.

Finally, pseudo-observation data are generated from the resulting bogus structure at the analyzed TC center (P_{msl}), TC center on the first guess (P_{msl}), and several points surrounding the analyzed TC center (P_{msl} and W_{prf}). The configuration for the surrounding point distribution is adaptive to the typhoon track error on the first guess.

2.5 Global Analysis

2.5.1 Introduction

The 4-dimensional variational data assimilation (4D-Var) system for the JMA Global Spectral Model (GSM) has been in operation since February 2005 in place of the 3-dimensional variational data assimilation (3D-Var) system. The JMA global 4D-Var system is used for the global cycle analysis (00,06,12,18UTC) and the global early analysis for the GSM forecast (00,06,12,18UTC). The scheme has the following benefits over the 3D-Var scheme.

- The dynamics and physics of the forecast model are considered in assimilating data. As a result, observational data are optimally used in a meteorologically consistent way, so that the analysis increments become flow-dependent (Figure 2.5.1).
- The observations are assimilated at appropriate observation time.
- It can directly assimilate all observations data including precipitation amount that can be derived from model variables, although precipitation amount is not assimilated in the JMA global 4D-Var system.

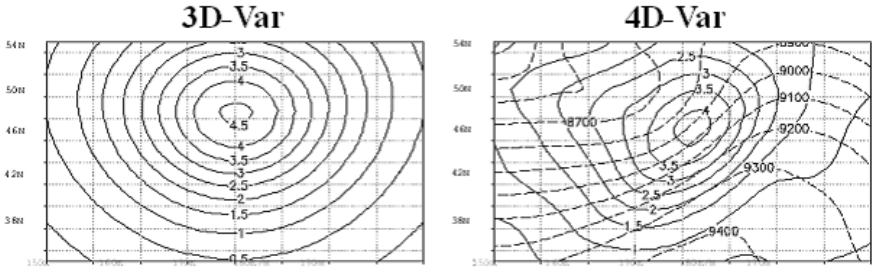

Figure 2.5.1: Analysis increments (solid line) by 3D-Var (left) and 4D-Var (right) when one pseudo observation height data (departure 5m) is assimilated (the 20th model level). The broken line indicates the first guess height field. 4D-Var analysis increments are flow-dependent in accordance with the first guess field.

2.5.2 Description of the Algorithm

The 4D-Var uses 3-9 hour forecast from GSM (TL959L60) as a first guess (background). All data within 3 hours from analysis time are assimilated at appropriate observation time with hourly assimilation slots. The cost-function measures the distance between the model trajectory and the observations over a 6-hour assimilation window.

An incremental method (Courtier *et al.* 1994) is adopted in the 4D-Var to save computer resources. In this method, analysis increment is computed at lower resolution (inner loop:TL319L60) and then is added to the high-resolution first guess (outer loop:TL959L60). The resolution of inner loop was upgraded from T159L60 to TL319L60 in October 2011 (Kadowaki and Yoshimoto 2012).

To obtain the analysis increment Δx_i , the minimization of the cost function J defined by Eq. (2.5.1) is performed in the inner loop.

$$J\left(\Delta x_0\right) = \frac{1}{2}\Delta x_0^{\mathrm{T}}\mathbf{B}^{-1}\Delta x_0 + \frac{1}{2}\sum_{i=0}^{n}\left(\mathbf{H}_i\Delta x_i - d_i\right)^{\mathrm{T}}\mathbf{R}_i^{-1}\left(\mathbf{H}_i\Delta x_i - d_i\right) + J_C \tag{2.5.1}$$

$$\Delta x_{i+1} = \mathbf{M}_i\Delta x_i = \mathbf{M}_i\mathbf{M}_{i-1}\mathbf{M}_{i-2}\ldots\mathbf{M}_0\mathbf{N}\Delta x_0 \tag{2.5.2}$$

where subscript i indicates the time and n denotes the end of the assimilation window. Δx_0 is the low resolution increment at the initial time before the initialization, and Δx_i is the increment evolved according to the tangent linear model from the initial time to time i and $\mathbf{R}_i$ denotes the covariance matrix of observation errors at time i and $\mathbf{B}$ is the covariance matrix of background errors, which are described in detail in Subsection 2.5.6 and Subsection 2.5.7. $\mathbf{M}_i$ is the tangent linear (TL) model of the low resolution nonlinear (NL) forecast model M_i described in detail in Subsection 2.5.4. $\mathbf{N}$ is a nonlinear normal-mode initialization operator (Machenhauer 1977). $\mathbf{H}_i$ is the TL operator of the observation operator H_i. The innovation vector is given at each assimilation slot by $d_i = y_i^0 - H_i x_i^b$, where x_i^b is the background state evolved by the high resolution NL model, and y_i^0 is the observation data at time i. J_C is the penalty term to suppress the gravity wave described in Subsection 2.5.5.

To minimize the cost function J, the limited memory Broyden-Fletcher-Goldfarb-Shanno (L-BFGS) algorithm (Liu and Nocedal 1989) with Veersé's preconditioner (Veersé *et al.* 2000) is applied. Here, the gradient of the cost function ∇J is required. It is obtained from the following adjoint procedures Eq. (2.5.3)-Eq. (2.5.6), which is computed reverse in time.

$$p_{n+1} = 0 \tag{2.5.3}$$

$$p_i = \mathbf{M}_i^{\mathrm{T}}p_{i+1} + \mathbf{H}_i^{\mathrm{T}}\mathbf{R}_i^{-1}\left(\mathbf{H}_i\Delta x_i - d_i\right) \qquad (i = n, \ldots, 1) \tag{2.5.4}$$

$$p_0 = \mathbf{M}_0^{\mathrm{T}}p_1 + \mathbf{B}^{-1}\left(\Delta x_0\right) + \mathbf{H}_0^{\mathrm{T}}\mathbf{R}_0^{-1}\left(\mathbf{H}_i\Delta x_i - d_i\right) \tag{2.5.5}$$

$$\nabla J\left(\Delta x_0\right) = p_0 \tag{2.5.6}$$

where p_i is a dummy variable, $\mathbf{M}_i^{\mathrm{T}}$ is the adjoint (AD) model of the TL model $\mathbf{M}_i$, and $\mathbf{H}_i^{\mathrm{T}}$ is the AD operator of $\mathbf{H}_i$. Note that Eq. (2.5.3)-Eq. (2.5.6) should contain additional terms of the penalty term and the initialization in Eq. (2.5.1), which are neglected here for the simplicity.

The analyzed variables are the relative vorticity, divergence, temperature, surface pressure and the logarithm of specific humidity in the spectral space on the model layers (eta-coordinate). Observational data y_i^0 are wind vector, temperature, relative humidity, satellite radiances, etc.

The low resolution increment Δx_i obtained from the minimization of the cost function in the inner loop is interpolated to the high resolution analysis increment. By adding the increment to the first guess field, high resolution analysis field is derived.

2.5.3 Description of the Procedure

The JMA global 4D-Var system are performed 4 times a day (00,06,12,18UTC). The observations within 3 hours from each analysis time (within assimilation window) are assimilated. The flow of 4D-Var is shown in Figure 2.5.2 for the case of 12UTC analysis time. It is the same for the cycle and early analyses.

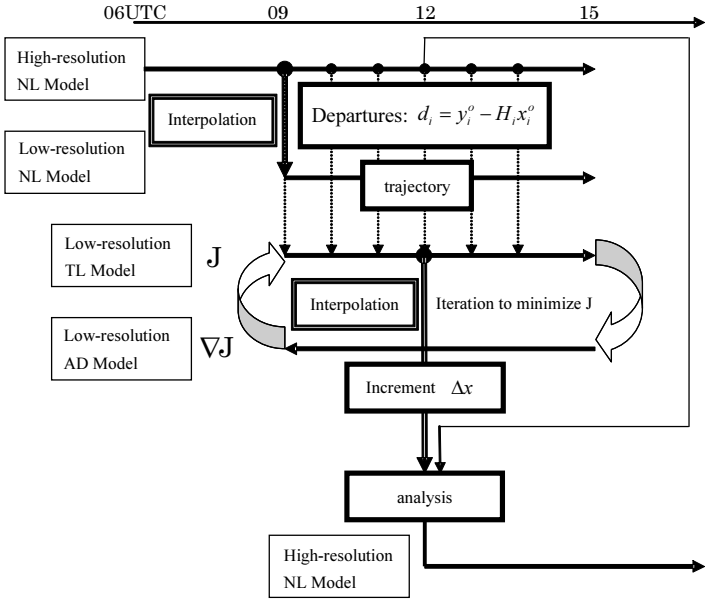

Figure 2.5.2: Flow of 4D-Var procedure for the case of 12UTC analysis time

The procedure is as follows:

1. 9-hour forecast (09UTC-15UTC) of the high resolution outer NL model (same as GSM with the resolution of TL959L60) from previous analysis is used as a first guess (background). The departures between the model trajectory and observations $d_i = y_i^0 - H_i x_i^b$ over a 6-hour assimilation window (09UTC-15UTC) are measured. Observations are organized in six time-slots. The time intervals for the first and last slots are 0.5 hour and 1.5 hour and the others are 1 hour (Figure 2.5.3). All observations in each time slot are regarded as observed in each representative time.

2. The 3 hour forecast field (valid at 09UTC) of the first guess is interpolated into the field with the resolution of the inner model (TL319L60). The interpolation is performed not only horizontally but also vertically to consider the difference of the topography between TL959 and TL319.

3. The inner NL model is performed from the interpolated field to calculate the background state in the low resolution model space.

4. The TL model and AD model are performed to calculate the cost function J and its gradient ∇J with the innovation vector $d_i = y_i^0 - H_i x_i^b$. These processes are iterated to minimize the cost function J. The iteration is performed up to about 70 times. The background trajectory is not updated in our system.

5. After the minimization of J, the field of 3 hour forecast (valid at 12UTC) of the TL model is chosen to be the analysis increment. It is interpolated horizontally and vertically into the field with the resolution of the first guess field (TL959L60). Finally the analysis increment is added to the first guess field (valid at 12UTC) to obtain the final product.

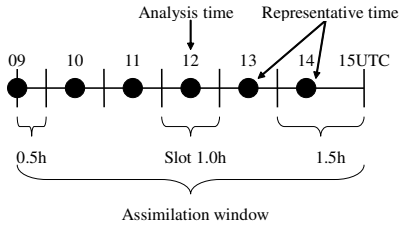

Figure 2.5.3: Schematic diagram of time slots for the analysis time 12UTC. The black circles indicate the representative time of each time slot.

2.5.4 Inner Model

The inner NL model is basically based on the JMA GSM, but moisture processes (convection scheme and cloud scheme) are replaced with those of the older GSM (GSM0103; JMA 2002), mainly for the stability of the inner TL model integration. In addition, the nonlinear normal-mode initialization (Machenhauer 1977) is added.

The inner TL model includes the following simple processes and most of those are based on the inner NL model.

1. **Initialization:** To control the gravity wave, nonlinear normal-mode initialization is adopted.

2. **Horizontal Diffusion:** Horizontal diffusion is enhanced over that of the inner NL model, according to Buizza (1998).

3. **Surface Turbulent Fluxes:** The surface turbulent fluxes are formulated as the Monin-Obukhov bulk formulae based on the inner NL model. The sensible and latent heat flux are perturbed only over the sea.

4. **Vertical Turbulent Diffusion:** The vertical turbulent diffusion of momentum, heat and moisture is formulated as the level 2 turbulence closure scheme of Mellor and Yamada (1974) based on the inner NL model. The diffusion coefficients are not perturbed.

5. **Gravity Wave Drag:** The parameterization for the orographic gravity wave drag consists of two components: one for long waves (wavelength > 100km) and the other for short waves (wavelength ≈ 10km) based on the inner NL model. The Richardson number is not perturbed in some part for the long waves for the stability of the inner TL model integration.

6. **Long-wave Radiation:** Two kinds of the long-wave radiation are included in the TL model. One is based on Mahfouf (1999). The tendency of the perturbed temperature T' is given by

$$\frac{\partial T'}{\partial t} = -\alpha \frac{g}{C_p} \frac{\partial}{\partial p} \Big(4FT'/T \Big) \tag{2.5.7}$$

where $\alpha = 1/\{1 + (P_r/P)^{10}\}$, $p_r = 300$hPa and F is the net radiation fluxes calculated in the inner NL model, g and C_p denote the gravitational constant and the isobaric specific heat respectively. The other is related to the difference between the surface ground temperature T_G and the bottom level temperature T_1. The tendency of the temperature T for the nonlinear model is:

$$\frac{\partial T}{\partial t} = \text{const} + \beta \Big(T_G - T_1 \Big) \tag{2.5.8}$$

where β is a coefficient given by a function of the position. The tendency of the perturbed temperature T' is given by:

$$\frac{\partial T'}{\partial t} = -\beta T_1' \tag{2.5.9}$$

7. **Clouds and Large-scale Precipitation:** Clouds and large-scale precipitation are based on the inner NL model. In the inner NL model, clouds are prognostically determined in a similar fashion to that of Smith (1990). A simple statistical approach proposed by Sommeria and Deardorff (1977) is employed to compute the cloud amount and the cloud water content. The parameterization of the conversion rate from cloud ice to precipitation follows the scheme proposed by Sundqvist (1978). They are much simplified in the TL model. The cloud fraction, the amount of dropping cloud ice, and the dependence on the water vapor of the isobaric specific heat are not perturbed. Only some variables are perturbed in computing the conversion from cloud water to precipitation and in computing the evaporation of the precipitation.

8. **Cumulus Convection:** Cumulus convection is formulated as prognostic Arakawa - Schubert scheme (Arakawa and Schubert 1974) based on the inner NL model, but much simplified. The vertical wind shear and the planetary mixing length are not perturbed. The magnitude of perturbation of mass-flux is set bound for the stability of the inner TL model integration and it causes that the inner "TL" model is not exactly linear.

2.5.5 Penalty Term

The penalty term, which is the third term of Eq. (2.5.1), is given by

$$J_C = \alpha \left(\left| \mathrm{N}_G \Delta x_0 \right|^2 + \sum_{i=2}^{\text{maxslot}} \left| \mathrm{N}_G \Delta x_i \right|^2 \right) \tag{2.5.10}$$

where N_G denotes an operator to calculate the tendency of the gravity wave mode based on Machenhauer (1977). Δx_0 is the increment at the initial time before the initialization, and Δx_i is the increment evolved according to the tangent linear model from the initial time to the representative time of the i-th time slot after the initialization and the summation is from the second time slot ($i = 2$) to the last time slot ($i =$ maxslot). α is a constant $3.0 \times 10^{-2}[\mathrm{s}^4/\mathrm{m}^2]$, determined empirically. Though this penalty term is introduced to suppress the gravity wave in the increment Δx_i, it is also effective to stabilize the calculation.

2.5.6 Background Term

The background term, which is the first term of Eq. (2.5.1), dominates how the 4D-Var analysis procedure converts the difference between the observation data and first guess into corrections to the first guess. The multivariate couplings in the analysis variables are based on the geostrophic linear balance between mass

and wind. To reduce the correlations among the analysis variables, control variables are introduced. In the algorithm some additional statistical relations are also considered such as the less geostrophic balance in the smaller horizontal and vertical scales, virtually no geostrophic balance near the equator, the dependency of the geostrophy on the vertical level, a weak coupling between divergence and vorticity, as well as between divergence and mass.

The control variables in the 4D-Var are the relative vorticity ζ, unbalanced divergence D_U, unbalanced temperature and surface pressure $(T,\ P_s)_U$ and the logarithm of specific humidity $\ln q$ in the spectral space on the model layers. Autocovariances of the control variables are assumed to be homogeneous and isotropic. The correlation structures do not depend on the geographical location, but vertical correlations depend on horizontal scale. The unbalanced variables D_U and $(T,\ P_s)_U$ are defined as

$$\Delta D_U \equiv \Delta D - P\Delta\phi_B \qquad (\phi_B = \phi_B(\zeta)) \tag{2.5.11}$$

$$\begin{pmatrix}\Delta T\\ \Delta p_s\end{pmatrix}_U \equiv \begin{pmatrix}\Delta T\\ \Delta p_s\end{pmatrix} - Q\Delta\phi_B - R\Delta D_U \tag{2.5.12}$$

where $P,\ Q,\ R$ are regression coefficients, ϕ_B is a modified balance mass variable derived from relative vorticity described as follows. Δ denotes the deviation from the first guess. This formulation is similar to that used in ECMWF before (Derber and Bouttier 1999), they call the regression coefficients as the balance operator. The regression coefficients are computed statistically using the NMC method (Parrish and Derber 1992) with 24/48-hour forecast differences to estimate the total covariances for each total spectral coefficient.

In the following subsections, modified balance mass variable is described in Subsection 2.5.6.1, the regression coefficients are described in Subsection 2.5.6.2, the covariance matrix of background errors are described in Subsection 2.5.6.3 and Subsection 2.5.6.4, and conversions from control variables to analysis variables are described in Subsection 2.5.6.5.

2.5.6.1 Modified Balance Mass Variable

The geostrophic balance is well kept at midlevels in the troposphere in extratropics. In other areas the balance is weak. To consider these relationships a modified balance mass variable is introduced. The statistical relationships among relative vorticity, divergence and temperature and surface pressure are calculated. First, the singular value decomposition of the linear balance operator L[3] is conducted.

$$\Delta\tilde{\phi_B} = L\Delta\zeta = UWV^{\mathrm{T}}\Delta\zeta \tag{2.5.13}$$

where $\tilde{\phi_B}$ is the original balance mass variable, W is a positive semi-definite diagonal matrix, U and V are orthogonal matrices. The decomposed modes depend on latitude: a singular mode with a small singular value has large amplitude in low latitude. Second, the regression coefficients between mass variables[4], derived from temperature and surface pressure, and balance mass variables are calculated as follows:

$$D_n = \frac{\left\langle \left(U^{\mathrm{T}}\Delta\Phi\right)_n^m \left(U^{\mathrm{T}}\Delta\tilde{\phi_B}\right)_n^m \right\rangle}{\left\langle \left[\left(U^{\mathrm{T}}\Delta\tilde{\phi_B}\right)_n^m\right]^2 \right\rangle} \tag{2.5.14}$$

where $\langle\ \rangle$, D_n and n denote statistical, zonal-wavenumber and vertical-level mean, a positive definite diagonal matrix and index of singular vectors in latitudinal wave number respectively. The regression coefficients D_n $(0-1)$ indicates how much the geostrophic balance is satisfied. Then the modified balance mass variables are constructed as follows;

[3]Each wave number components of L is denoted as

$\delta\tilde{\phi_B}_n^m = c_n^m\delta\zeta_{n-1}^m + c_{n+1}^m\delta\zeta_{n+1}^m \quad ((n,\ m) \neq (0,\ 0),\ n = m,\ m+1,\ \ldots,\ N)\ , \qquad c_n^m = -\frac{2\Omega a^2}{n^2}\sqrt{\frac{n^2-m^2}{4n^2-1}}\ , \qquad \delta\tilde{\phi_B}_0^0 = 0$

where Ω is angular velocity of the Earth, a Earth radius, n total wavenumber, m zonal wavenumber.

[4]The mass variable Φ_k on the k-th model level is defined by $\Phi_k = \phi_k + R_d\bar{T}_k\ln p_k$.

where Φ_k is the geopotential height, $\bar{T}_k$ is the reference (global mean) temperature, and p_k is the pressure on the k-th level, and R_d is the dry gas constant.

$$\Delta\phi_B = UDU^{\mathrm{T}}\Delta\tilde{\phi}_B = UDWV^{\mathrm{T}}\Delta\zeta = \tilde{L}\Delta\zeta \tag{2.5.15}$$

Note that the modified balance operator $\tilde{L}$ consists of 1) the conversion from the spectral space to the singular vector space, 2) the product of the regression coefficients D, and 3) the conversion from the singular vector space to the spectral space. The correlation between the modified mass variables and unbalanced mass variables (i.e. original mass variables – modified balance mass variables) could be neglected in all regions including the tropics.

2.5.6.2 Regression Coefficients

The regression coefficient matrices P, Q, and R are calculated for each total wavenumber n as follows:

$$P_n = \left\langle \Delta D_n^m \left(\Delta\tilde{\phi}_{Bn}^{\ m}\right)^{\mathrm{T}} \right\rangle \left\langle \Delta\tilde{\phi}_{Bn}^{\ m} \left(\Delta\tilde{\phi}_{Bn}^{\ m}\right)^{\mathrm{T}} \right\rangle^{-1} \tag{2.5.16}$$

$$Q_n = \left\langle \begin{pmatrix} \Delta T_n^m \\ \Delta(p_s)_n^m \end{pmatrix} \left(\Delta\tilde{\phi}_{Bn}^{\ m}\right)^{\mathrm{T}} \right\rangle \left\langle \Delta\tilde{\phi}_{Bn}^{\ m} \left(\Delta\tilde{\phi}_{Bn}^{\ m}\right)^{\mathrm{T}} \right\rangle^{-1} \tag{2.5.17}$$

$$R_n = \left\langle \left[\begin{pmatrix} \Delta T_n^m \\ \Delta(p_s)_n^m \end{pmatrix} - Q_n \Delta\tilde{\phi}_{Bn}^{\ m} \right] \left((\Delta D_U)_n^m\right)^{\mathrm{T}} \right\rangle \left\langle \left((\Delta D_U)_n^m\right) \left((\Delta D_U)_n^m\right)^{\mathrm{T}} \right\rangle^{-1} \tag{2.5.18}$$

where $\langle\ \rangle$ denotes statistical and zonal-wavenumber mean.

2.5.6.3 Background Error Covariance Matrix

The background error covariance matrices of the control variables are calculated for each total wavenumber n and the matrix size is equivalent to the number of vertical levels for ζ, D_U and $\ln q$ or the number of vertical levels +1 for $(T,\ P_s)_U$.

$$B_{\zeta\, n} = \left\langle \Delta\zeta_n^m \overline{\Delta\zeta_n^m}^{\mathrm{T}} \right\rangle, \qquad B_{D_U\, n} = \left\langle (\Delta D_U)_n^m \overline{(\Delta D_U)_n^m}^{\mathrm{T}} \right\rangle \tag{2.5.19}$$

$$B_{\begin{pmatrix} T \\ p_s \end{pmatrix}_U\, n} = \left\langle \Delta \begin{pmatrix} T \\ p_s \end{pmatrix}_{Un}^m \overline{\Delta \begin{pmatrix} T \\ p_s \end{pmatrix}_{Un}^m}^{\mathrm{T}} \right\rangle, \qquad B_{\ln q\, n} = \left\langle \Delta \ln q_n^m \overline{\Delta \ln q_n^m}^{\mathrm{T}} \right\rangle \tag{2.5.20}$$

where $\langle\ \rangle$ denotes statistical and zonal-wavenumber mean. Total variances of the control variables are rescaled by a factor of 0.81.

2.5.6.4 Cholesky Decomposition of Background Error Covariance Matrix

The background error covariance matrix mentioned above is decomposed by the Cholesky decomposition. It gives the independent and normalized (i.e. preconditioned) control variables Δy_n^m as follows:

$$J_n^{(x)} = \sum_{m=-n}^{n} \frac{1}{2} \left(\Delta\bar{x}_n^m\right)^{\mathrm{T}} B_n^{-1} \Delta x_n^m = \sum_{m=-n}^{n} \frac{1}{2} \left(\Delta\bar{x}_n^m\right)^{\mathrm{T}} \left(L_n L_n^{\mathrm{T}}\right)^{-1} \Delta x_n^m = \sum_{m=-n}^{n} \frac{1}{2} \left(\Delta\bar{y}_n^m\right)^{\mathrm{T}} \Delta y_n^m \tag{2.5.21}$$

$$\Delta y_n^m \equiv L_n^{-1} \Delta x_n^m \tag{2.5.22}$$

where $J_n^{(x)}$ is a background error term for a control variable x at total wavenumber n, B_n is a background covariance matrix for x, L_n is a lower triangular matrix.

In summary, normalized control variables $\Delta y_n^m(k)$ are independent completely, and normalized by the background error variance. The background term of the cost function is simplified as a summation of square of the normalized control variables.

2.5.6.5 Conversions from Preconditioned Control Variables to Analysis Variables

The conversions from the preconditioned control variables to the analysis variables are performed by the following procedures:

$$\Delta y \xrightarrow{XCT2QD} \begin{pmatrix} \Delta\zeta \\ \Delta D_U \\ \Delta\left(p_S,\, T\right)_U \\ \Delta \ln q \end{pmatrix} \xrightarrow{RO2BMA} \begin{pmatrix} \Delta\zeta \\ \Delta D_U \\ \Delta\left(p_S,\, T\right)_U \\ \Delta \ln q \\ \Delta\phi_B \end{pmatrix} \xrightarrow[LNQ2Q]{\substack{UPT2PT \\ UDI2DI}} \begin{pmatrix} \Delta\zeta \\ \Delta D \\ \Delta\left(p_S,\, T\right) \\ \Delta q \end{pmatrix} \tag{2.5.23}$$

First, the control variables (relative vorticity, unbalanced divergence, unbalanced temperature and surface pressure, the logarithm of specific humidity) on each model level in the spectral space are reconstructed by using Eq. (2.5.22) (XCT2QD in Eq. (2.5.23)). Then, the modified balance mass variable $\Delta\phi_B$ is calculated from the relative vorticity $\Delta\zeta$ by Eq. (2.5.15). The temperature and the surface pressure and the divergence are calculated by Eq. (2.5.11)-Eq. (2.5.12) from the unbalanced variables (UPT2PT and UDI2DI). The logarithm of specific humidity is converted to specific humidity (LNQ2Q). If the specific humidity of the first guess in the grid space is negative due to the wave-to-grid transform, Δq is set to be zero.

2.5.7 Observation Terms

2.5.7.1 Observation Data

Assimilated observation types are shown in Table 2.2.1. Brief explanation for each data type and the quality control procedures are found in Section 2.2 and Section 2.3.

Observational data and the departures (observation minus first guess) are given with the location and time through pre-analysis procedure. Reported surface pressure data at the station height and sea surface pressure data of surface observation are assimilated after converted onto the model surface height in prior to assimilation. Scatterometer data are assimilated as the wind data at the lowest model level, although the data are considered as wind data at 10 m height above the sea level. Satellite radiance data from MW sounders, MW imagers and CSRs are directly assimilated using the K matrix model of RTTOV10 (Saunders *et al.* 2012). GNSS-RO data are assimilated in the form of refractivity at the tangent point.

2.5.7.2 Observation Error

Observation errors (the diagonal part of the observation error covariance matrix) are estimated based on the innovation statistics (Desroziers *et al.* 2005). The observation errors are summarized in Table 2.5.1. The error at arbitrary reported pressure level is linearly interpolated in the logarithm of pressure ($\log(p)$). The cross correlations of the observation errors (off diagonal part of the observation error covariance matrix) are not considered explicitly in the 4D-Var. To ignore the cross correlation term in the cost function, (horizontally or vertically) dense observations are thinned spatially in the pre-analysis procedure and the observation errors are inflated with the predefined factors.

2.5.7.3 Observation Operator

In the 4D-Var, observations at the given location and time are simulated by using the forecast variables at the surrounding grids in the nearest forecast hour with the spatial inter/extrapolation and the variable conversion. Observation operator consists of these consecutive procedures. Linear vertical interpolation is performed first with respect to logarithm of pressure. Extrapolation under the model ground surface is also performed. Then linear horizontal interpolation and extrapolation to the North and South poles are carried out.Then the variable conversions such as u, v wind components to wind speed are performed.

Table 2.5.1: The observation error tables used in the operational Global Analysis for (a) direct observations, (b) AMV, (c) AMSU-A, (d) MHS, (e) SSMIS, (f) TMI and (g) CSR from five geostationary satellites . P_s, u, v, T, RH and T_B denote surface pressure, (u, v wind components), temperature, relative humidity and brightness temperature, respectively. "x" in (c)-(g) denotes that the channel is not used.

(a) conventional observation				
element level(hPa)	P_s(hPa)	u, v(m/s)	T(K)	RH(%)
1000		2.3	1.7	6.4
850		2.4	1.2	15.9
700		2.5	1.0	19.8
500		2.5	0.8	31.5
300		2.7	0.9	31.7
200		2.8	1.1	24.1
100	0.7	3.1	1.2	3.8
50		3.0	1.4	1.4
30		3.0	1.5	1.3
10		3.9	2.5	1.3
1		4.6	5.4	1.3
0.4		7.7	7.6	1.3
0.1		7.7	7.6	1.3

(b) AMV	
element level(hPa)	u, v(m/s)
1000	4.5
850	4.5
700	4.5
500	4.5
300	5.3
200	5.8
100	6.8
50	7.0
30	7.2
10	7.6
1	9.1
0.4	10.6
0.1	10.6

(c) AMSU-A T_B (K)						
satellite channel	Aqua	Metop-A	NOAA-15	NOAA-16	NOAA-18	NOAA-19
4	x	0.45	0.45	x	0.45	0.45
5	x	0.3	0.3	0.3	0.3	0.3
6	0.45	0.3	0.3	0.3	0.3	0.3
7	x	x	0.3	x	0.3	0.3
8	0.3	0.3	0.3	x	0.3	x
9	0.3	0.3	0.3	0.3	0.3	0.3
10	0.3	0.3	0.3	0.3	0.3	0.3
11	0.3	0.45	x	0.45	0.45	0.45
12	0.64	0.64	0.64	0.64	0.64	0.64
13	1.02	1.02	0.85	0.85	1.02	1.02

(d) MHS T_B (K)			
satellite channel	Metop-A	NOAA-18	NOAA-19
3	18	18	x
4	13.5	13.5	13.5
5	9	9	9

(e) SSMIS T_B (K)			
satellite channel	DMSP-F16	DMSP-F17	DMSP-F18
13	7.6	7.6	7.6
14	10	10	10
16	8	8	8
17	8.8	8.8	8.8

(f) TMI T_B (K)	
satellite channel	TRMM
3	7.2
5	10
6	7.2
8	8.8

(g) CSR T_B (K)					
satellite	GOES-13	GOES-15	Meteosat-7	Meteosat-9	MTSAT-2
	1.5	1.5	1.5	1.5	1.5

2.5.7.4 Variational Bias Correction

As mentioned in the Subsection 2.3.4, biases of satellite radiance data are corrected by variational bias correction (VarBC). In the 4D-Var with VarBC, the observation operators are extended to include bias correction terms and the control (analysis) variables are extended to include bias correction (regression) coefficients. The coefficients are optimized as control variables in each analysis.

The extended form of the cost function Eq. (2.5.1) is defined as follows.

$$J(\Delta z_0) = \frac{1}{2}\Delta x_0^{\mathrm{T}}\mathbf{B}^{-1}\Delta x_0 + \frac{1}{2}\Delta\beta^{\mathrm{T}}\mathbf{B}_\beta{}^{-1}\Delta\beta + \frac{1}{2}\sum_{i=0}^{n}\left(\mathbf{H}_i\Delta x_i + \sum_{j=0}^{m}\Delta\beta_j p_{i,j} - d_i\right)^{\mathrm{T}}\mathbf{R}_i^{-1}\left(\mathbf{H}_i\Delta x_i + \sum_{j=0}^{m}\Delta\beta_j p_{i,j} - d_i\right) + J_C \tag{2.5.24}$$

where,

$$\Delta z_0 \equiv \left[\Delta x_0{}^{\mathrm{T}}, \Delta\beta^{\mathrm{T}}\right]^{\mathrm{T}}, \quad \mathbf{B}_\beta \equiv diag\left(\frac{F_{inf}{}^2}{N_{var}}, \ldots, \frac{F_{inf}{}^2}{N_{var}}\right), \quad N_{var} \equiv \begin{cases} \frac{N}{\log_{10}\frac{N}{N_0}+1} & (N \geq N_0) \\ N_0 & (N < N_0) \end{cases}$$

Δz_0 is the extended increments which consists of the low resolution model variables' increments Δx_0 and the bias correction coefficients' increments $\Delta\beta$, $\mathbf{B}_\beta$ is the background error covariance matrix for the bias correction coefficients β, $p_{i,j}$ is the predictors for the bias correction, m is the number of all the predictors for all the radiance observation types, F_{inf} is the inflation factor defined arbitrarily, N is the number of data and N_0 is the threshold for valid number of data.

The second term of the right hand side of Eq. (2.5.24) is the background term for the bias correction coefficients and the term $\sum_{j=0}^{m}\Delta\beta_j p_{i,j}$ is the bias correction term. This equation is used in the 4D-Var instead of the Eq. (2.5.1).

2.6 Meso-scale Analysis

2.6.1 Introduction

The Meso-scale Analysis (MA) produces initial conditions for the Meso-scale Model (MSM, Section 3.5) every three hours, aimed at incorporating information from observations into the model to assist in better forecasting weather phenomena, with emphasis on high impact events.

In March 2002, a 4-dimensional variational (4D-Var) scheme was introduced as the data assimilation scheme of the MA (Ishikawa and Koizumi 2002) in place of a 3-dimensional optimal interpolation (3D-OI) scheme. This is the first operational limited-area 4D-Var system in the world. After the MSM forecast model was upgraded to a non-hydrostatic model (JMA-NHM; Saito *et al.* 2006) in September 2004, a non-hydrostatic model-based 4D-Var, the "JMA Nonhydrostatic model"-based Variational Analysis Data Assimilation (JNoVA; Honda *et al.* 2005), replaced the former hydrostatic 4D-Var in April 2009, allowing the MA to produce initial conditions more consistent with the revised MSM forecast model.

Various observations are used to contribute to improve accuracy of predictions for meso-scale weather events, including those from weather radars, satellite observations, and ground-based GNSS. Assimilating these observations with an advanced data assimilation scheme of 4D-Var, the MA is designed to produce highly-balanced initial conditions consistent with the model equations.

2.6.2 Operational System

The MA adopts the JNoVA system and produces initial conditions for the MSM forecasts every 3 hours (00, 03, 06, 09, 12, 15, 18 and 21UTC). Figure 2.6.1 shows a schematic depiction of the MA process. This process is carried out as follows (ordinal numbers correspond to those in Figure 2.6.1):

1. Initialized with the previous MA, run the high-resolution (5km) forecast model within the data assimilation window (0 to 3-hours) to obtain the first guess.

2. Perform quality-control of observations (see Section 2.3 for details) and calculate deviations of the observations from the first guess.

3. Execute the JNoVA to assimilate the observations on a low-resolution (15km) space.

4. Add analysis increments (on the low-resolution space) to the (high-resolution) first guess through an interpolation process, and make an initial condition for the next step.

5. With the initial condition made in the previous step, run the high-resolution (5km) forecast model within the data assimilation window to obtain an initial condition for the MSM.

In the MA, the first and the last steps in which the high-resolution forecast model is run are called "outer loop", and the step in which the JNoVA on the low-resolution space is executed is called "inner loop". The forecast model used in the two outer loops is identical to the model used in the MSM, namely, JMA-NHM. The analysis domain is shown in Figure 2.6.2, with a topographic map at a 5-km resolution used in the MA. Lateral boundary conditions are given by the Global Spectral Model (GSM) forecasts, while the initial conditions of the first guess are taken over from the previous MA (3-hour forecast in the last outer loop). In other words, the MA frames a cycle analysis being nested into the GSM.

The data assimilation window is set to 3 hours, and the end of the window corresponds to an analysis time. The cut-off time of the inputted observation data for the MA is 50 minutes after each analysis time. The received observational data by the cut-off time are distributed to 4 time-slots by rounding off the observation time to hours (as described by 4 starry shapes under curly braces in Figure 2.6.1). Therefore, the data observed within the period from 3.5 hours before to 0.5 hours after the analysis time are assimilated in the inner loop.

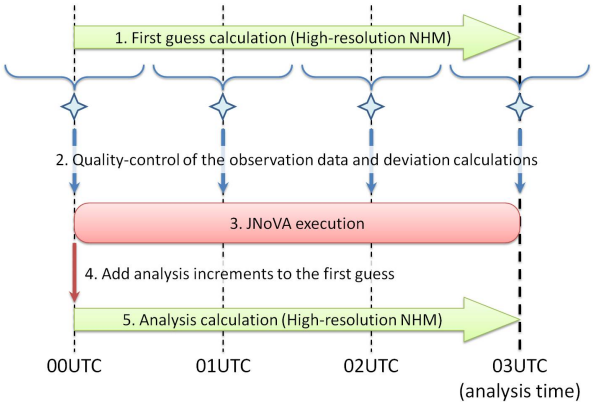

Figure 2.6.1: Schematic procedure of the MA (an example of 03UTC analysis)

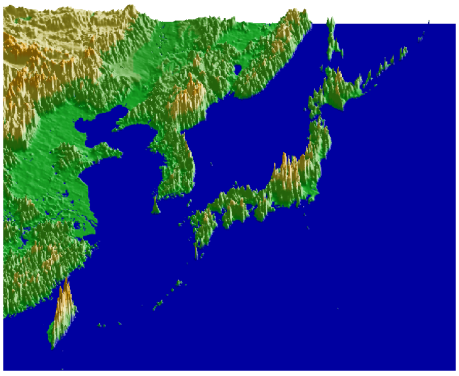

Figure 2.6.2: Analysis domain and topography of the MA

The JNoVA in the inner loop, as mentioned above, is a data assimilation system based on the 4-dimensional variational (4D-Var) method, detailed in the following Subsection 2.6.3. The variational method is based on the maximum likelihood estimation, and the optimal values (i.e. analysis fields) are determined by minimizing the "cost function" (see Subsection 2.6.3.1 for details). In this minimizing procedure, the cost function and its gradient require to be calculated iteratively (about 32 times on average) and it needs considerable computational costs. For the purpose of reducing these costs, the operational JNoVA adopts the incremental approach (Courtier *et al.* 1994). In this approach, a low-resolution model relative to the model used in the outer loop (equivalent to the MSM) is used in the minimization of the cost function. Operational formulation of minimizing the cost function with this incremental approach is explained in Subsection 2.6.3.1. The model used in the minimization process in the JNoVA is called "inner model", and its specifications are described in Subsection 2.6.3.3. As for the model resolution, we use the horizontal grid spacing of 5km (721×577 grid points) with 50 vertical layers in the outer loops. On the other hand, larger horizontal grid spacing of 15km (241×193 grid

points) with 40 vertical layers are used in the inner loop. In daily operation, the calculation time of the inner loop is about 21 minutes, while the outer loops are about 3 minutes each.

2.6.3 Basic Formulation

2.6.3.1 Cost Function

In the MA system, 4D-Var data assimilation is used to seek the model trajectory in a phase space by minimizing its deviation from observations and the first guess. The deviation is measured using a cost function J, defined as

$$J(\boldsymbol{x}_0) = J_b + J_o + J_p = \frac{1}{2}\Big(\boldsymbol{x}_0 - \boldsymbol{x}_0^b\Big)^T \mathbf{B}^{-1}\Big(\boldsymbol{x}_0 - \boldsymbol{x}_0^b\Big) + \sum_{t=0}^{N} \frac{1}{2}\Big(H(\boldsymbol{x}_t) - \boldsymbol{y}_t\Big)^T \mathbf{R}^{-1}\Big(H(\boldsymbol{x}_t) - \boldsymbol{y}_t\Big) + J_p \ , \tag{2.6.1}$$

where subscript T indicates transpose.

The first and the second terms of Eq. (2.6.1) are called the background and the observation terms, which measure the deviation from the first guess and the observations, respectively. $\boldsymbol{x}_0$ is the model state at the beginning of the data assimilation window (time level $t = 0$) to be optimized[5], $\boldsymbol{x}_0^b$ the first guess of the model state at $t = 0$, $\boldsymbol{y}_t$ a column vector consisting of observational data available at t ($t = 0, ..., N$). $\boldsymbol{x}_t$ is a model state at t which is forecasted from the initial condition $\boldsymbol{x}_0$, that is

$$\boldsymbol{x}_t = M_t(\boldsymbol{x}_0) \ , \tag{2.6.2}$$

where M_t denotes the forecast operator. H is an observation operator which converts a model state space to an observation space. The H typically consists of conversions from model variables to observed parameters and interpolations from model grid points to observation points. The error covariance matrixes, $\mathbf{B}$ and $\mathbf{R}$, specify error profiles (uncertainty and error correlation) of $\boldsymbol{x}_0^b$ and $\boldsymbol{y}_t$, respectively(see Subsection 2.6.3.2 and Subsection 2.6.4.2).

The third term of Eq. (2.6.1) J_p is the penalty term based on a digital filter to suppress high frequency noises (mainly gravity wave noises)(Gauthier and Thépaut 2001). The penalty term is given as

$$J_p = \frac{\lambda}{2}\left\|\delta\boldsymbol{x}_{N/2} - \delta\overline{\boldsymbol{x}}_{N/2}\right\|_E^2 \ , \tag{2.6.3}$$

where λ denotes a weighting factor, $\delta\boldsymbol{x}_{N/2}$ the model state analysis increment at the center of the data assimilation window ($t = N/2$), $\delta\overline{\boldsymbol{x}}_{N/2}$ digital-filtered analysis increment at $t = N/2$, $\|\cdots\|_E$ the moist total energy norm suggested by Ehrendorfer *et al.* (1999).

For a time series of the model states over the data assimilation window, $\{\boldsymbol{x}_0, ..., \boldsymbol{x}_N\}$, the digital-filtered state $\overline{\boldsymbol{x}}$ at $t = N/2$ is given as

$$\overline{\boldsymbol{x}}_{N/2} \quad = \quad \sum_{k=0}^{N} h_{N/2-k} W_k \boldsymbol{x}_k \ , \tag{2.6.4}$$

where

$$h_k \quad = \quad \frac{\sin k\theta_c}{k\pi} \ , \tag{2.6.5}$$

denotes the low-pass filter that removes time oscillations exceeding a cutoff frequency θ_c. The Dolph-Chebyshev window function W_k (Lynch 1997) is also used to suppress the noise from the Fourier truncation (Gibss oscillation).

In the MA, the incremental approach is adopted to reduce the computational costs. Some implementations to reduce the computational costs of 4D-Var scheme are proposed by Courtier *et al.* (1994). In the MA, the

[5]The vector to be optimized, $\boldsymbol{x}_0$, can also include lateral boundary conditions over the data assimilation window, but this is not adopted in the operational MA.

Remark5 of Section3 in the Courtier *et al.* (1994) is used[6]. In the incremental approach of MA, the optimization is performed using a inner model (see Subsection 2.6.3.3) to obtain an analysis increment in the low resolution model space (inner loop). A low resolution version of an analysis increment at $t = 0$, $\delta \boldsymbol{w}_0$, and background error covariance $\mathbf{B}_W$ are given as

$$\delta \boldsymbol{w}_0 = \mathbf{S}(\boldsymbol{x}_0 - \boldsymbol{x}_0^b) , \tag{2.6.6}$$

$$\mathbf{B}_W \approx \mathbf{S}\mathbf{B}\mathbf{S}^T , \tag{2.6.7}$$

where $\mathbf{S}$ denotes a conversion operator from the high resolution to the low resolution. As a result, the low resolution cost function can be expressed as

$$J(\delta \boldsymbol{w}_0) = \frac{1}{2}\delta \boldsymbol{w}_0^T \mathbf{B}_W^{-1} \delta \boldsymbol{w}_0 + \frac{1}{2}\sum_t \Big[G(\boldsymbol{w}_t) - \hat{\boldsymbol{y}}_t\Big]^T \mathbf{R}^{-1}\Big[G(\boldsymbol{w}_t) - \hat{\boldsymbol{y}}_t\Big] + J_p , \tag{2.6.8}$$

$$\boldsymbol{w}_t = L_t(\boldsymbol{w}_0) , \tag{2.6.9}$$

where G denotes the low resolution observation operator, L_t the inner model forecast operator. The observation vector $\boldsymbol{y}_t$ is modified as

$$\hat{\boldsymbol{y}}_t = \boldsymbol{y}_t - H(\boldsymbol{x}_t^b) + G(\boldsymbol{w}_t^b) , \tag{2.6.10}$$

to input the high resolution departures $\boldsymbol{y}_t - H(\boldsymbol{x}_t^b)$ to the inner loop. The high resolution analysis at $t = 0$ is given as

$$\boldsymbol{x}_0 = \boldsymbol{x}_0^b + \mathbf{S}^{-I}\delta \boldsymbol{w}_0 , \tag{2.6.11}$$

where $\mathbf{S}^{-I}$ denotes an interpolation operator from the low resolution to the high resolution model space. The final analysis $\boldsymbol{x}_N$ is obtained by running forecast with the high resolution model over the data assimilation window (outer loop).

$$\boldsymbol{x}_N = M_N(\boldsymbol{x}_0) . \tag{2.6.12}$$

2.6.3.2 Background Error Covariance

As mentioned above, the background error covariance $\mathbf{B}$ specifies error profiles of the first guess (Subsection 2.6.3.1). However, calculations using explicit $\mathbf{B}$ are unfeasible, because of an extremely large dimension of the model state space. In practice, drastic simplifications are applied on $\mathbf{B}$ to make the problem tractable.

A group of parameters are defined as control variables, and their background errors are treated to be uncorrelated with each other. The control variables used in the MA are as follows.

- u: x-component of horizontal wind
- v: y-component of horizontal wind
- (θ, p_s): potential temperature and surface pressure
- $\tilde{q}_v = q_v/q_v^{bs}$: pseudo relative humidity (q_v: specific humidity, q_v^{bs}: saturation specific humidity of the first guess)

For each control variable (denoted by ϕ), spatial structure of the background error covariance $\mathbf{B}^\phi$ is modeled as

$$\mathbf{B}^\phi = \mathbf{B}_v^{\phi 1/2}\mathbf{C}_h^{\phi 1/2}\mathbf{C}_h^{\phi 1/2T}\mathbf{B}_v^{\phi 1/2T} . \tag{2.6.13}$$

The $\mathbf{B}_v^{\phi 1/2}$ is a square root of the vertical background error covariance $\mathbf{B}_v^\phi (= \mathbf{B}_v^{\phi 1/2}\mathbf{B}_v^{\phi 1/2T})$, which is diagonal with respect to horizontal locations, and is assumed to be homogeneous over the domain, that is, the matrix element corresponding to a pair of spatial points (i, j, k) and (i', j', k'), $B^\phi_{v(i,j,k)(i'j'k')}$, is expressed as

$$B^\phi_{v(i,j,k)(i'j'k')} = \delta_{ii'}\delta_{jj'}B^{\phi\mathrm{col}}_{vkk'} . \tag{2.6.14}$$

[6]This method approximates a propagation in time of the perturbation ($\delta \boldsymbol{x}_0 = \boldsymbol{x}_0 - \boldsymbol{x}_0^b$) using the non-linear inner model in the lower resolution, by taking a finite difference of inner model forecasts of observables from perturbed and unperturbed states ($\boldsymbol{w}_0 = \boldsymbol{w}_0^b + \delta \boldsymbol{w}_0$ and $\boldsymbol{w}_0^b$), that is, by taking $G(\boldsymbol{w}_t) - G(\boldsymbol{w}_t^b)$ as seen from Eq. (2.6.9) and Eq. (2.6.10).

Therefore, taking a single vertical column, we discuss properties of $\mathbf{B}_v^{\phi\mathrm{col}}$ for simplicity. The $\mathbf{B}_v^{\phi\mathrm{col}}$ can be written as an eigenvalue decomposition

$$\mathbf{B}_v^{\phi\mathrm{col}} = \mathbf{V}\mathbf{D}\mathbf{V}^T \ , \tag{2.6.15}$$

where columns of $\mathbf{V}$ are eigenvectors of $\mathbf{B}_v^{\phi\mathrm{col}}$, and $\mathbf{D}$ is the diagonal matrix of eigenvalues. The form of the $\mathbf{B}_v^{\phi\mathrm{col}1/2}$ used in the MA is given as

$$\mathbf{B}_v^{\phi\mathrm{col}1/2} = \mathbf{V}\mathbf{D}^{1/2} \ . \tag{2.6.16}$$

Thus, the matrix element of $\mathbf{B}_v^{\phi 1/2}$ is given as

$$B^{\phi 1/2}_{v(i,j,k)(i'j'\kappa')} = \delta_{ii'}\delta_{jj'}B^{\phi\mathrm{col}1/2}_{vk\kappa'} \ , \tag{2.6.17}$$

where κ' denotes an vertical eigenmode.

The $\mathbf{C}_h^{\phi 1/2}$ is a square root of the horizontal background error correlation, $\mathbf{C}_h^{\phi}(= \mathbf{C}_h^{\phi 1/2}\mathbf{C}_h^{\phi 1/2T})$, which is diagonal with respect to eigenmodes of $\mathbf{B}_v^{\phi\mathrm{col}}$. The matrix element of $\mathbf{C}_h^{\phi 1/2}$ is expressed as

$$C^{\phi}_{h(i,j,\kappa)(i',j',\kappa')} = \delta_{\kappa,\kappa'}C^{\phi\kappa}_{h(i,j)(i',j')} \ , \tag{2.6.18}$$

where (i, j) and (i', j') denotes horizontal coordinates, and κ and κ' denote vertical eigenmodes. A Gaussian form is assumed for the horizontal correlation between points (i, j) and (i', j') for an eigenmode κ, that is, a matrix element $C^{\phi\kappa}_{h(i,j)(i',j')}$,

$$C^{\phi\kappa}_{h(i,j)(i',j')} = \exp\Big[-\frac{1}{2}\Big\{\Big(\frac{i-i'}{\sigma_x^{\phi\kappa}}\Big)^2+\Big(\frac{j-j'}{\sigma_y^{\phi\kappa}}\Big)^2\Big\}\Big] = C^{\phi\kappa}_{hxii'}C^{\phi\kappa}_{hyjj'} \ . \tag{2.6.19}$$

The horizontal correlation length in x- and y-directions σ_x^{κ} and σ_y^{κ} are also assumed to be homogeneous over the domain. In the MA, $\mathbf{C}_h^{\phi 1/2}$ is given as

$$C^{\phi 1/2}_{h(i,j,\kappa)(i',j',\kappa')} = \delta_{\kappa,\kappa'}C^{\phi\kappa 1/2}_{h(i,j)(i',j')} = \delta_{\kappa,\kappa'}C^{\phi\kappa 1/2}_{hxii'}C^{\phi\kappa 1/2}_{hyjj'} \ , \tag{2.6.20}$$

where $\mathbf{C}_{hx}^{\phi\kappa 1/2}$ ($\mathbf{C}_{hy}^{\phi\kappa 1/2}$) is taken to be the Cholesky decomposition of $\mathbf{C}_{hx}^{\phi\kappa}$ ($\mathbf{C}_{hy}^{\phi\kappa}$), that is, a lower triangular matrix. The final background error covariance $\mathbf{B}$ in the model state space is given as

$$\mathbf{B} = \mathbf{B}^{1/2}\mathbf{B}^{1/2T} \ , \tag{2.6.21}$$

$$\mathbf{B}^{1/2} = \mathbf{K}\ \mathrm{diag}(\mathbf{B}^{u1/2}, \mathbf{B}^{v1/2}, \mathbf{B}^{(\theta,p_s)1/2}, \mathbf{B}^{\tilde{q}_v 1/2}) \ , \tag{2.6.22}$$

where $\mathbf{K}$ is a linearized transform from the space of control variables to the model state space. In the transform $\mathbf{K}$, pressure is determined from the control variable (θ, p_s), assuming hydrostatic balance.

Based on this simplified $\mathbf{B}$, a variable transform is made from the analysis increment in the model state $\delta\boldsymbol{x}_0$ to a new variable $\boldsymbol{\lambda}$, which is related to $\delta\boldsymbol{x}_0$ by $\mathbf{B}^{1/2}$

$$\delta\boldsymbol{x}_0 = \boldsymbol{x}_0 - \boldsymbol{x}_0^b = \mathbf{B}^{1/2}\boldsymbol{\lambda} \ . \tag{2.6.23}$$

and the variational optimization is performed with respect to $\boldsymbol{\lambda}$. This transform, called as a preconditioning, simplifies the background term of the cost function J (see Eq. (2.6.1) and Eq. (2.6.9). For simplicity, the present discussion does not deal with J_p). The cost function and its gradient after the transform are given as [7]

$$J(\boldsymbol{\lambda}) = \frac{1}{2}\boldsymbol{\lambda}^T\boldsymbol{\lambda} + \sum_{t=0}^{N}\frac{1}{2}\Big(H(M_t(\boldsymbol{x}_0^b + \mathbf{B}^{1/2}\boldsymbol{\lambda})) - \boldsymbol{y}_t\Big)^T\mathbf{R}^{-1}\Big(H(M_t(\boldsymbol{x}_0^b + \mathbf{B}^{1/2}\boldsymbol{\lambda})) - \boldsymbol{y}_t\Big) \ , \tag{2.6.24}$$

[7] Here, the resolutions of the inner model is set to be the same with that of the outer model for simplicity. The actual operational implementation uses two different resolutions based on the incremental approach as discussed previously (see Eq. (2.6.9)). The formulation in line with the operational implementation is obtained by making replacements, $(\delta\boldsymbol{x}_0, \boldsymbol{x}_0, \boldsymbol{x}_0^b, \mathbf{B}^{1/2}, \boldsymbol{y}_t, M_t, H) \rightarrow (\delta\boldsymbol{w}_0, \boldsymbol{w}_0, \boldsymbol{w}_0^b, \mathbf{B}_w^{1/2}, \hat{\boldsymbol{y}}_t, L_t, G)$, in Eq. (2.6.23), Eq. (2.6.24), and Eq. (2.6.25).

$$\nabla_\lambda J = \lambda + \sum_{t=0}^{N} \mathbf{B}^{1/2T} \mathbf{M}_t^T \mathbf{H}^T \mathbf{R}^{-1} \Big(H(M_t(\boldsymbol{x}_0^b + \mathbf{B}^{1/2}\lambda)) - \boldsymbol{y}_t \Big), \tag{2.6.25}$$

where $\mathbf{M}_t^T$ and $\mathbf{H}^T$ are the adjoint model and the adjoint of the observation operator.

The parameters that characterize the error profile, $\mathbf{B}_v^\phi$, $\sigma_x^{\phi\kappa}$, and $\sigma_y^{\phi\kappa}$, are estimated using the NMC method (Parrish and Derber 1992). Differences between 6h and 12h MSM forecasts valid at the same time are calculated for different cases, and used as statistical samples of the background error. The samples are generated for the first ten days of each month of 2005, two pairs of the MSM forecasts a day, with each pair using the same boundary condition. The background error statistics, $\mathbf{B}_v^\phi$, $\sigma_x^{\phi\kappa}$, and $\sigma_y^{\phi\kappa}$, are obtained by taking an average over all these samples. The MA uses constant error statistics throughout the year, without taking into account seasonal variation of the error profiles.

2.6.3.3 Inner Model

In the JNoVA, a simplified nonlinear version of the JMA-NHM (NLM, M_t in Subsection 2.6.3.1 and Subsection 2.6.3.2) is used in the inner loop to provide trajectories at every iteration instead of the tangent linear model (TLM) of the NLM due to discontinuity and nonlinearlity of the JMA-NHM. The adjoint model (ADM, $\mathbf{M}_t^T$ in Subsection 2.6.3.2) of the NLM provides gradient information Eq. (2.6.25). The TLM has been developed only for use in the process of the ADM development. In addition to the use of simplified model, the inner loop of the JNoVA is executed using the NLM and ADM with a lower resolution (15 km horizontal grid spacing and 40 vertical layers) to reduce computational cost. In this subsection, the specification of the inner model in the JNoVA is surveyed focusing on schemes different from those of the MSM and also briefly listed in Table 2.6.1.

The version of the JMA-NHM in the NLM and ADM is not same as the MSM. In order to develop the TLM and ADM, the version of the JMA-NHM was fixed at the time when the development started in 2002. After that, some improvements of the MSM were included in the JNoVA. However, only some of the improvements have been adopted because of the development cost of the TLM and ADM. The NLM in the JNoVA gives the basic fields of the ADM, and all the grid point values at each time step are saved within the memory at the operation. The forecast variables are momentum (3 components), potential temperature, pressure and mixing ratio of water vapor. Additionally, temperature and evaporation efficiency at the land surface are predicted (those at the sea surface are assumed to be constant). Prognostic variables of the ADM are the same as those of the NLM except for evaporation efficiency.

In the NLM and ADM, fully compressible elastic equations are only supported as governing equations. The vertical coordinate is z*-coordinate, which is different from hybrid coordinate of the MSM. For this reason, the vertical interpolation from the outer loop to the inner loop is necessary. Regarding to the advection scheme, flux form fourth-order centered difference, same as the MSM, is adopted, but the advection correction scheme is only used for the NLM. In the horizontally explicit, and vertically implicit (HE-VI) scheme of the NLM and ADM, gravity wave and sound wave are split and calculated in a smaller time step. The smaller time step interval divides one larger time step (40 sec.) to seven small steps. In the JNoVA, all prognostic variables of the smaller time step are reserved and used for the ADM integration. As for the nonlinear computational diffusion,

$$D_{NL} \propto \frac{\partial}{\partial x}\left(\left| \frac{\partial \phi}{\partial x} \right| \frac{\partial \phi}{\partial x} \right)$$

is used in MSM and NLM(Nakamura (1978)), however, the perturbation of $\left|\frac{\partial \phi}{\partial x}\right|$ is not considered in ADM. Targeted moisture diffusion is adopted in the NLM, but not available in the ADM. Except for the advection correction, the nonlinear computational diffusion and targeted moisture diffusion, the dynamical processes of NLM are strictly linearized in the ADM.

For the moist processes, the large-scale condensation (LSC) scheme for the grid scale precipitation are used in the NLM and ADM. As a sub-grid scale convective parameterization, the NLM adopts the modified Kain-Fritsch scheme and the ADM does not considered.

As a turbulence scheme, the diagnostic-type Deardorff scheme (Deardorff 1980) is used in the NLM and ADM. Perturbations of turbulent kinetic energy in the ADM is not considered, resulting in no perturbation for the diffusive coefficients.

For a surface process in the NLM and ADM, Louis *et al.* (1982) for the land surface and Kondo (1975) for the sea surface, which were previously used in the MSM, are adopted. In the both schemes of the ADM, the perturbations of the bulk coefficients are not considered.

The NLM and ADM also use the four-layer heat diffusive model for ground temperature same as the MSM, but the perturbation is only considered at the highest layer which is close to the lowest layer of the atmosphere. The evaporation efficiency is given by the climate value in the NLM and ADM for simplicity.

The scheme for the radiation process in the NLM is slightly different from that in the MSM. The cloud is diagnosed by not partial condensation scheme but relative humidity. A method to evaluate the effective radius of a cloud ice particle in the NLM is based on Ou and Liou (1995) without modification by McFarquhar *et al.* (2003) . Additionally, Räisänen (1998) have been adopted for a method to calculate long wave radiation at each cloud layer in the MSM, whereas, it has not been adopted in the NLM. In the ADM, the radiation process is not considered for simplicity.

Table 2.6.1: Specification of MSM and models employed in JNoVA

	MSM	NLM	ADM
Resolution	5km, 50layers	15km, 40layers	15km, 40layers
Horizontal advection	Flux form fourth-order with advection correction	Flux form fourth-order with advection correction	Flux form fourth-order
Solver of pressure equation	HE-VI	HE-VI	HE-VI
Targeted moisture diffusion	Considered	Considered	Not considered
Moist physics	3-ice bulk microphysics	LSC	LSC
Convection	modified Kain-Fritsch	modified Kain-Fritsch	None
Turbulence	Mellor-Yamada-Nakanishi-Niino level-three	Deardorff	Deardorff
Surface flux	Beljaars and Holtslag	Louis(land) and Kondo(sea)	Louis(land) and Kondo(sea)
Ground temperature	4-layer thermal diffusion	4-layer thermal diffusion	4-layer thermal diffusion
Radiation	Considered	Considered	Not considered

2.6.4 Observation Terms

2.6.4.1 Observation Data

Assimilated observation types are shown in Table 2.2.1. Brief explanation for each data type and the quality control procedures are found in Section 2.2 and Section 2.3.

2.6.4.2 Observation Error

Observation error covariance matrix $\mathbf{R}$ in Eq. (2.6.1) is assumed to be a diagonal matrix and the cross correlation between the different observations are not considered. The observation errors (diagonal components of $\mathbf{R}$) are estimated based on the innovation statistics (Desroziers *et al.* 2005). The observation errors for conventional observations and wind profilers, and AMV are summarized in Table 2.6.2. The errors for satellite radiances are the same as the Global Analysis (See Table 2.5.1(c)-(g)). The errors for GNSS-PWV and radial velocity is 3 mm and 3.3 m/s, respectively. The error at an arbitrary reported pressure level is linearly interpolated in the logarithm of pressure ($\log(p)$). The cross correlations of the observation errors between different observations

Table 2.6.2: The observation error tables used in the operational Meso-scale Analysis for (a) direct observations and (b) AMV. P_s, u, v, T and RH denote surface pressure, (u, v wind components in MSM Lambert projection space), temperature and relative humidity respectively.

(a) conventional observation and wind profiler					
element level(hPa)	P_s(hPa)	u(m/s)	v(m/s)	T(K)	RH(%)
1000		2.1	1.9	1.3	9.8
925		2.0	1.9	0.9	10.3
850		2.0	2.0	0.9	12.7
700		2.0	1.9	0.9	12.8
500		1.9	1.9	0.7	12.9
400		2.2	2.2	0.7	13.3
300		2.6	2.6	0.9	13.5
250	0.7	2.7	2.6	1.0	14.4
200		2.7	2.6	1.1	13.7
150		2.6	2.6	1.1	16.6
100		3.2	3.0	1.5	15.1
70		3.7	3.1	1.9	13.6
50		3.2	2.8	1.9	12.1
30		3.2	2.8	1.9	11.8
10		3.2	2.8	1.9	12.2

(b) AMV		
element level(hPa)	u(m/s)	v(m/s)
1000	4.1	3.3
850	2.9	2.3
700	3.2	2.6
500	3.7	3.0
300	4.6	3.7
200	3.8	4.9
100	4.4	6.0
50	3.5	5.1
30	5.1	6.2
10	6.2	7.2

are not considered explicitly in the 4D-Var. To ignore the cross correlation terms in the cost function, dense observations are thinned spatially and the observation errors are inflated in the pre-analysis procedure.

2.6.4.3 Special Treatment for Precipitation Data

The observation terms of the cost function Eq. (2.6.1) assume that the probability density function (PDF) for observation errors is a Gaussian function. However, the PDF for precipitation amount data does not follow the Gaussian function. Therefore, the following observation term is used for one-hour precipitation amount data (Koizumi *et al.* 2005).

$$J_o{}^{PREC}(x) = \sum_{j\ (\text{where } r_j^o \geq 0.5)}^{n} \frac{\left(H_j(x) - r_j^o\right)^2}{2\sigma_o(r_j^o)^2} \tag{2.6.26}$$

where, $H_j(x)$ denotes the observation operator that converts the state variables x to one-hour accumulated precipitation at the j-th grid point, and r_j^o the observed precipitation at the grid point. n is the number of grid points in the inner model. $\sigma_o(r_j^o)$ is the observation error which is defined as follows.

$$\sigma_o(r_j^o) \equiv \begin{cases} C_{sat} \max(r_{min}, r_j^o) & \left(H_j(x) \leq r_j^o\right) \\ C_{sat} C_a \max(r_{min}, r_j^o) & \left(H_j(x) > r_j^o\right) \end{cases}, \quad \begin{cases} C_a = 3,\ C_{sat} = 1 & \text{for R/A} \\ C_a = 5,\ C_{sat} = 2 & \text{for satellite retrievals} \end{cases}, \quad r_{min} \equiv 1\text{mm/h} \tag{2.6.27}$$

where, C_{sat} is an observation error inflation factor for satellite retrievals, C_a is the tuning factor for the asymmetric structure of the departure frequency distribution around 0.

The observations of one-hour precipitation less than 0.5 mm are not assimilated, since the quality of such observations is rather poor in snowfall cases. The observation error of the satellite retrievals is considered to be larger than R/A because the retrieval is not from one-hour accumulated observations but from instantaneous observations.

2.6.4.4 Variational Quality Control

Variational quality control (VarQC, Andersson and Järvinen 1999) is applied in the 4D-Var for the conventional observations. With VarQC, PDF of the observation error is supposed to be not a Gaussian function but a summation of a Gaussian function and a positive constant in the certain range. The constant means the probability of "rough error".

The following observation term and its gradient are used for the conventional observations in the cost function Eq. (2.6.1) in the 4D-Var with VarQC.

$$j_o^{VarQC} = -\log\left(\frac{\gamma + \exp(-j_o)}{\gamma + 1}\right), \quad \gamma \equiv \frac{A\sqrt{2\pi}}{(1-A)\,2d} \tag{2.6.28}$$

$$\nabla j_o^{VarQC} = W^{VarQC} \nabla j_o, \quad W^{VarQC} \equiv 1 - \frac{\gamma}{\gamma + \exp(-j_o)} \tag{2.6.29}$$

where, A is a prior probability of rough error, d is the maximum standard deviations below which rough error is possible, j_o^{VarQC} is the observation term for a single observation component with VarQC and j_o is the term without VarQC

Eq. (2.6.29) means that ∇j_o^{VarQC} is almost the same (effective) as ∇j_o when j_o is small ($W^{VarQC} \approx 1$) and ∇j_o^{VarQC} is almost 0 (not effective) when j_o is large ($W^{VarQC} << 1$). The observations with $W^{VarQC} < 0.25$ are regarded to be rejected by the VarQC.

2.7 Local Analysis

2.7.1 Introduction

The Local Analysis (LA), in operation starting from August 2012, produces initial conditions for the Local Forecast Model (LFM) (see Subsection 3.6.1) at a horizontal resolution of 2km.

Aimed at providing initial conditions to the high-resolution forecast model targeting small-scale severe weather events, the LA is designed to allow rapid production and frequent update of the analysis at a resolution of 5km (Subsection 2.7.2). An analysis cycle with hourly 3-dimensional variational (3D-Var) data assimilations is executed every time for the last 3 hours to incorporate information from newly received observations in each case.

As in the Meso-scale Analysis (MA), high density remote sensing data including those from weather radars and ground-based GNSS are hourly assimilated in the LA as important sources of detailed information that can contribute to a better forecast of high-impact phenomena (Subsection 2.7.4). Capability of high-resolution NWP to capture small-scale variations of topography is expected to help to reduce representativeness errors in assimilation of surface observations. Based on this viewpoint, the LA also assimilates automated surface station (AMeDAS) data ahead of other operational data assimilation systems in lower resolutions, in order to appropriately reflect effects from local-scale environments near the surface.

With these features, the LA is characterized as a data assimilation system for a high-resolution and high-frequency NWP.

2.7.2 Operational System

The LA is performed 8 times(00,03,06,09,12,15,18,21 UTC) a day to produce initial conditions for the LFM. The domain of the LA covers Japan and its surrounding areas at a horizontal resolution of 5 km with 441×551 grid points and 50 vertical layers (shown with the solid line in Figure 2.7.1.) In order to help the LFM provide severe weather forecasting promptly, the system configuration of the LA has to complete calculations within limited computational time, especially in view of our next plan to upgrade the LA operation on an extended domain as higher frequency of 24 times a day. In addition, the 4D-Var used in the MA(Subsection 2.6.1) is more advanced than the three dimensional variational data assimilation(3D-Var), but the computational time of the 4D-Var is much longer than that of the 3D-Var. Therefore, the LA employs an analysis cycle based on

the 3D-Var scheme(see Subsection 2.7.3 in detail). The 3D-Var is a part of JMA Nonhydrostatic model-based Variational Data Assimilation (JNoVA,Honda *et al.* (2005)).

In this subsection, FT=0(hour) is each LFM initial time. The data cut-off time of the LA is set to FT=0.5. The LA waits for observations to arrive by the data cut-off time, and starts the analysis cycle to assimilate observations from FT=-3.5 to 0.5(Subsection 2.7.4).

The flow of the 3-h analysis cycle of the LA is shown in Figure 2.7.2. In Figure 2.7.2, (a), (c), (e) and (g) are 3D-Var analyses, and (b), (d) and (f) are 1-h JMA-NHM forecasts(LF1). LF1 is made with MSM forecasts as boundary conditions and the previous 3D-Var analysis, and is used as the first guess by the following analysis. The first 3D-Var analysis of the cycle((a) in Figure 2.7.2) uses the latest forecast of the MSM(Subsection 3.5.1) as the first guess. 3D-Var analyses and LF1s are repeated in turn for 3 hours((a)-(g) in Fig.2.7.2). Each analysis assimilates observations within 0.5 hours before and after the analysis time. Quality control is applied on observations before each analysis, using the first guess of the analysis as a reference, and only observations that passes the quality checks are used in each analysis. Hydrometeors are not updated but taken over from the MSM forecasts at the beginning of the analysis cycle and just propagated throughout the cycle. All the processes are accomplished in about 15 minutes.

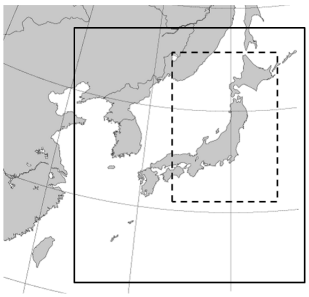

Figure 2.7.1: The domain of LA(bounded by the solid line), that of LFM (bounded by the broken line).

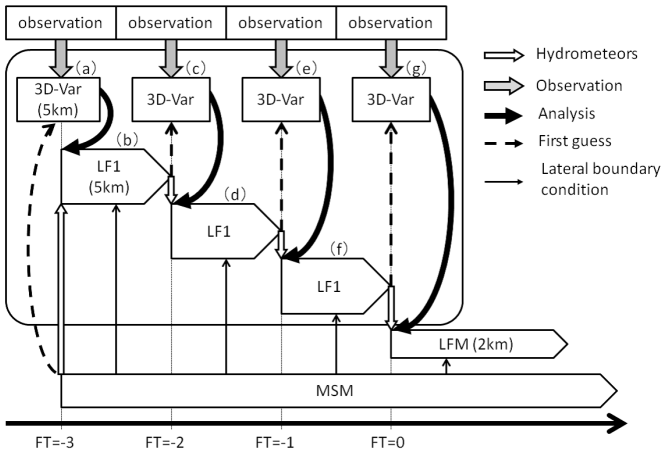

Figure 2.7.2: A schematic figure of the LA analysis cycle.

2.7.3 Basic Formulation

2.7.3.1 Cost Function

The LA uses a 3D-Var scheme for data assimilation. The 3D-Var optimizes the model state $\boldsymbol{x}$ to minimize its deviation from observations $\boldsymbol{y}$ and the first guess $\boldsymbol{x_b}$, measured in terms of a cost function J,

$$J(\boldsymbol{x}) = J_b + J_o = \frac{1}{2}\left(\boldsymbol{x} - \boldsymbol{x}^b\right)^T \mathbf{B}^{-1}\left(\boldsymbol{x} - \boldsymbol{x}^b\right) + \frac{1}{2}\left(H(\boldsymbol{x}) - \boldsymbol{y}\right)^T \mathbf{R}^{-1}\left(H(\boldsymbol{x}) - \boldsymbol{y}\right). \tag{2.7.1}$$

The background term J_b and the observation term J_o measure deviations of the model state $\boldsymbol{x}$ from the first guess $\boldsymbol{x}^b$ and observations $\boldsymbol{y}$, respectively. The observation operator H is a function from the model state space to observation space, and typically consists of collection of conversions from model variables to observed parameters and interpolations from model grid points to observation points. The background and observation error covariance matrices, $\mathbf{B}$ and $\mathbf{R}$, specify error profiles of the first guess and observations, respectively (see Subsection 2.7.3.2 and Subsection 2.7.4).

2.7.3.2 Background Error Covariance

Simplifications of **B** similar to those used in the MA are also applied in the LA. The control variables of the LA are

- u: x-component of horizontal wind
- v: y-component of horizontal wind
- (θ, p_s): potential temperature and surface pressure
- $\tilde{q}_v = q_v/q_v^{bs}$: pseudo relative humidity (q_v: specific humidity, q_v^{bs}: saturation specific humidity of the first guess)
- θ_g : ground potential temperature

In addition to the MA control variables, θ_g is also included, which is found to help appropriately assimilate surface temperature observations. The spatial structure of the background error covariance $\mathbf{B}^\phi$ of a control variable ϕ is modeled as

$$\mathbf{B}^\phi = \mathbf{U}\mathbf{B}_v^{\phi 1/2}\mathbf{C}_h^{\phi 1/2}\mathbf{C}_h^{\phi 1/2T}\mathbf{B}_v^{\phi 1/2T}\mathbf{U}^T \,, \tag{2.7.2}$$

where **U** denotes a vertical coordinate transformation, which is introduced to limit terrain effect of the vertical coordinate within the lower troposphere. As in the MA, assuming the vertical background error covariance, $\mathbf{B}_v^\phi$, is homogeneous over the domain, we introduce a single column vertical covariance $\mathbf{B}_v^{\phi\mathrm{col}}$ (see Eq. (2.6.14)). Using an eigenvalue decomposition of the $\mathbf{B}_v^{\phi\mathrm{col}}$ (see Eq. (2.6.15)), the square root matrix $\mathbf{B}_v^{\phi\mathrm{col}1/2}$ used in the LA is given as

$$\mathbf{B}_v^{\phi\mathrm{col}1/2} = \mathbf{V}\mathbf{D}^{1/2}\mathbf{V}^T \,, \tag{2.7.3}$$

which is taken to be a symmetric square root, compared to Eq. (2.6.16). Using this form of $\mathbf{B}_v^{\phi\mathrm{col}1/2}$, the horizontal background error correlation is specified for each vertical level, instead of each eigenmode. Thus, the horizontal correlation length in x- and y-directions σ_x^k and σ_y^k, corresponding to those in Eq. (2.6.19) are now defined on a vertical level k. In the LA, a recursive filter technique is used in calculation of $\mathbf{C}_{hx}^{\phi 1/2}$ and $\mathbf{C}_{hy}^{\phi 1/2}$ (Purser *et al.* 2003).

The background error covariance **B** in the model state space is similar with that in the MA (Eq. (2.6.21) and Eq. (2.6.22)), and is given as

$$\mathbf{B} = \mathbf{B}^{1/2}\mathbf{B}^{1/2T} \,, \tag{2.7.4}$$

$$\mathbf{B}^{1/2} = \mathbf{K}\,\mathrm{diag}(\mathbf{B}^{u1/2}, \mathbf{B}^{v1/2}, \mathbf{B}^{(\theta,p_s)1/2}, \mathbf{B}^{\tilde{q}_v 1/2}, \mathbf{B}^{\theta_g 1/2}) \,, \tag{2.7.5}$$

where **K** is a linearized transform from the space of control variables to the model state space.

The optimization is performed with respect to $\boldsymbol{\lambda}$ as in the MA (see Eq. (2.6.23), Eq. (2.6.24), and Eq. (2.6.25)),

$$\delta\boldsymbol{x} = \boldsymbol{x} - \boldsymbol{x}^b = \mathbf{B}^{1/2}\boldsymbol{\lambda} \,, \tag{2.7.6}$$

$$J(\boldsymbol{\lambda}) = \frac{1}{2}\boldsymbol{\lambda}^T\boldsymbol{\lambda} + \frac{1}{2}\Big(H(\boldsymbol{x}^b + \mathbf{B}^{1/2}\boldsymbol{\lambda}) - \boldsymbol{y}\Big)^T\mathbf{R}^{-1}\Big(H(\boldsymbol{x}^b + \mathbf{B}^{1/2}\boldsymbol{\lambda}) - \boldsymbol{y}\Big) \,, \tag{2.7.7}$$

$$\nabla_\lambda J = \boldsymbol{\lambda} + \mathbf{B}^{1/2T}\mathbf{H}^T\mathbf{R}^{-1}\Big(H(\boldsymbol{x}^b + \mathbf{B}^{1/2}\boldsymbol{\lambda}) - \boldsymbol{y}\Big) \,, \tag{2.7.8}$$

where $\mathbf{H}^T$ is the adjoint of the observation operator.

The background error statistics, $\mathbf{B}_v^\phi$, $\sigma_x^{\phi k}$ and $\sigma_y^{\phi k}$ are estimated applying the NMC method (Parrish and Derber 1992) to the same data set with that used in the MA. However, the error profiles in lower levels are modified to localize spatial correlations, so that surface observations are assimilated more appropriately. As in the MA, a seasonal variation of the background error statistics is not taken into account.

2.7.4 Observation Terms

2.7.4.1 Observation Data

Assimilated observation types are shown in Table 2.2.1. Brief explanation for each data type and the quality control procedures are found in Section 2.2 and Section 2.3.

2.7.4.2 Observation Error

Observation error covariance matrix **R** in Eq. (2.7.1) is assumed to be a diagonal matrix and the cross correlation between the different observations are not considered. The observation errors (diagonal components of **R**) are the same as those for the Meso-scale Analysis (See Subsection 2.6.4.2).

2.7.4.3 Observation Operator

Observation operator for surface observations is based on the surface diagnostic scheme of the JMA-NHM described in Subsection 3.5.8. Observed parameters such as wind at 10 m height and temperature at 1.5 m height are diagnosed using transfer coefficients based on Beljaars and Holtslag (1991). In the adjoint operator, perturbations of the transfer coefficients are not considered in the diagnostic equations Eq. (3.5.120) and Eq. (3.5.121), but only those of u_a, θ_{va} and θ_{vs} are considered.

2.8 Snow Depth Analysis

The global snow depth analysis is executed every day separately from the global atmosphere analysis. Global snow depth with 1.0° latitude/longitude resolution is analyzed using SYNOP snow depth data on the day.

A two-dimensional optimum interpolation (OI) is employed for the analysis method. The first guess is prepared as follows,

$$G = C + \frac{1}{2}A_C \tag{2.8.1}$$

where G, C and A_C are the first guess, the climatological value interpolated to the analysis day from monthly climatological data, and the analyzed anomaly from the climatological value on the previous day, respectively. The monthly climatological data used from September to June are the climatology compiled by USAF/ETAC (Foster and Davy 1988), and those for July and August are interpolated from the climatology for June and September.

Following type grids are the exception of this analysis; no probability of snow cover, evergreen broadleaves tree vegetation type, and land ice. The snow depth is 0 cm on the first and second type grids, and C is assigned on land ice grids. The snow cover probability is estimated from a past SSM/I observation statistic.

The analyzed snow depth with 1.0° latitude/longitude resolution is interpolated to the resolution of the GSM model grid (TL959), which is converted to snow water equivalent as an initial condition for the land-surface process (SiB) in GSM. In addition, snow water equivalents on Japan land girds are replaced with interpolated latest observation value of AMeDAS snow depth as well as Japanese SYNOP.

2.9 Non-real-time Quality Control

2.9.1 Operational Activities as a GDPFS RSMC

JMA is a Regional Specialized Meteorological Center (RSMC) of the World Meteorological Organization (WMO) Global Data-processing and Forecast System (GDPFS), namely RSMC Tokyo. In March 1991, the Commission for Basic Systems (CBS) of WMO designated RSMC Tokyo as a lead center for monitoring the quality of land surface observations in Region II (Asia). As a part of its operational activities, JMA produces a 6-monthly report containing a consolidated list of stations suspected of reporting low-quality observation data of station level pressure, mean sea level pressure and geopotential height during the 6-month periods ending June and December. The report on the quality of the land surface observations can be obtained from the website of JMA[8].

In addition, RSMC Tokyo produces monthly statistics on the quality of all observations received in time for use in its final global analyses. Copies of these reports are provided to major GDPFS centers and to the WMO Secretariat. The reports are also available in the website of JMA[9].

[8] http://qc.kishou.go.jp/clsf.html
[9] http://qc.kishou.go.jp/mmr.html

The data qualities are evaluated based on the differences between the observations and the first guess fields (3 to 9-hours forecasts) from the global model. These statistics are produced in accordance with the standards for the exchange of monitoring results recommended by WMO CBS.

2.9.2 Operational Activities as a PMOC

The objective of the Data Buoy Cooperation Panel (DBCP) which was established jointly by WMO and the Intergovernmental Oceanographic Commission (IOC) is to improve the quality of buoy data on the Global Telecommunication System (GTS) available to real-time users. DBCP requests some agencies or institutions to volunteer as a Principal Meteorological or Oceanographic Center (PMOC) responsible for controlling Argos GTS data on an operational basis for given variables. JMA as a PMOC undertakes the quality monitoring and makes recommendations on the recalibration and/or removal of buoy sensor data on GTS. The QC information is exchanged with DBCP and other PMOC centers through Internet in a standardized format.

2.9.3 Management of Blacklist

As mentioned in the Section 2.3, the low quality observations can lead the large forecast degradation. The cause of the low quality might be an instrumental failure and the failure can continue long time. Such observations should be excluded in the first step of QC. Blacklist is constructed to meet such a need. Blacklist management is one of the most important activities for QC. The quality for all the observations is evaluated based on the differences between the observations and the first guess fields from the global model (3 to 9-hours forecasts) and the meso-scale model (0 to 3-hours forecasts). The problematic observations are enlisted in the blacklist.

2.10 JMA Climate Data Assimilation System

JMA Climate Data Assimilation System (JCDAS) is an atmospheric global analysis for operational climate use and has been operational since March 2006. It was transitioned from Japanese 25-year Reanalysis (JRA-25) which covered 26 years from 1979 to 2004 and was produced by JMA and the Central Research Institute of Electric Power Industry (CRIEPI) (Onogi *et al.* 2007). JCDAS has been using the same data assimilation system as that of JRA-25. It has a spectral resolution of T106, equivalent to a horizontal grid size around 110 km, and 40 vertical layers with the top level at 0.4 hPa. The data assimilation method of JCDAS is the three dimensional variational (3D-var) assimilation which had been used in the operational global analysis until February 2005. The background error statistics were taken from the operational global analyses as of 2003 which were the latest statistics available at the time when JRA-25 production had started. For surface variables, surface pressure is assimilated simultaneously with upper air variables in the 3D-var; other surface variables of temperature, wind and relative humidity are assimilated separately with a uni-variate 2-dimensional optimal interpolation (2D-OI).

JRA-25 and JCDAS have many advantages. Firstly, predicted 6-hour global total precipitation distribution and amount are well reproduced both in space and time. Especially after July 1987, assimilating retrieved precipitable water from SSM/I radiance data contributed to the good performance. Furthermore, tropical cyclones (TCs) are properly analyzed owing to the assimilation of reconstructed wind profile around TCs.

JRA-25 and JCDAS jointly provide long-term consistent and high quality global analysis fields since 1979. JRA-25 and JCDAS are used to create a new climate normal value and is being used as a basic reference data for operational climate monitoring services. Reanalysis data, produced by the model whose characteristics are the same as the seasonal forecast model, can provide consistent initial field and verification data for the seasonal forecast and hindcast. Consequently the JRA-25 and JCDAS data greatly contributes to the development of the seasonal forecast model.

JMA is conducting the 2nd reanalysis named the Japanese 55-year Reanalysis (JRA-55) (Ebita *et al.* 2011). JRA-55 covers 55 years, extending back to 1958, with the four dimensional variational data assimilation (4D-var). It aims at providing a comprehensive atmospheric climate dataset by producing a more time-consistent dataset for a longer period than JRA-25. JRA-55 will be completed in the first half of 2013 and the current JRA-25 based JCDAS will be replaced with the JRA-55 version in 2014.

Chapter 3

Numerical Weather Prediction Models

3.1 Summary

JMA operates NWP models to meet various kinds of requirements on weather forecasting. The suite of the NWP models covers a wide temporal range of forecast periods from a few hours to two seasons providing a seamless sequence of products for the public.

The Global Spectral Model (GSM) produces 84-hour forecast four times a day (00, 06, 12, 18 UTC) to support the official short-range forecasting (day 3) and to provide the lateral boundary conditions for the Meso-Scale Model (MSM). The GSM forecast at 12 UTC is extended to 11 days to support the official one-week forecasting.

Four ensemble prediction systems are in operation. The one-week ensemble forecast is performed with 51 ensemble members every day at 12 UTC supporting the official one-week forecasting. The typhoon ensemble forecast with 11 ensemble members runs four times a day (00, 06, 12 and 18 UTC) when typhoons exist or are expected to form or to come in the western-north Pacific. The model produces 132-hour forecast and supports activities of the RSMC Tokyo-Typhoon Center. The one-month ensemble forecast with 50 members is carried out once a week (every Wednesday and Thursday) to support the official one-month forecasting, which is issued on Friday. The two-week ensemble forecast is also executed to support early warning information on extreme weather on every Sunday and Monday using the one-month ensemble forecast system. The seasonal ensemble forecast using an atmosphere-ocean coupled model with 51 members is carried out once a month to support the official seasonal forecasting.

MSM is executed eight times a day (00, 03, 06, 09, 12, 15, 18 and 21 UTC). It produces 15-hour forecast from 00, 06, 12 and 18 UTC and 33-hour forecast from 03, 09, 15, 21 UTC, to support the very short-range forecasting and the aviation services. It provides the lateral boundary conditions for the Local Forecast Model (LFM).

LFM produces 9-hour forecast eight times a day (00, 03, 06, 09, 12, 15, 18 and 21 UTC) and supports the weather information regarding to severe weather disturbances and aviation services around Tokyo International Airport.

JMA also operates a global atmospheric transport model to support the RSMC for Emergency Response activities. The model stands ready to run anytime when an environmental emergency situation occurs.

JMA operates three kinds of Chemical Transport Models (CTMs). The Aerosol CTM produces 96-hour forecast to provide Kosa (Aeolian Dust) information, the stratospheric ozone CTM produces 48-hour forecast to support UV index information, and tropospheric-stratospheric ozone CTM produces 72-hour forecast to support the photochemical oxidant information. These CTMs are operated once a day at 12UTC. The radiative transfer model is also used for UV index information.

Table 3.1.1 (global) and Table 3.1.2 (regional) shows specifications of the major NWP models respectively. Details on the NWP models, the ensemble prediction systems, the atmospheric transport model and the chemical transport models are described particularly in the following Section 3.2 - Section 3.8. The operational verification procedure is explained in Section 3.9.

Table 3.1.1: Specifications of the global NWP models at JMA

	Global Spectral Model (GSM)	One-week Ensemble Prediction System (WEPS)	Typhoon Ensemble Prediction System (TEPS)	One-month Ensemble Prediction System
Forecast Range (Initial Time)	84 hours (00, 06, 18UTC) 264 hours (12UTC)	264 hours (12UTC)	132 hours (00,06,12,18UTC)	17 days (12UTC; Sun & Mon) 34 days (12UTC; Wed & Thu)
Horizontal Grids #	$(1920-60)\times 960$	$(640-48)\times 320$		
Truncation Wave #	TL959	TL319		TL159
Grid Spacing	20km	55km		110km
Vertical Layers	60			
Top Layer Pressure	0.1hPa			
Ensemble Size	-	51	11	50
Perturbation Generator	-	Singular Vector method		Combination of BGM method and LAF method (25 BGM and 2 initial dates with 1 day LAF)
Perturbed Area	-	Globe	North-Western Pacific and Vicinities of up to three TCs	Northern Hemisphere and the tropics
Radiation Process	Solar (every hour) Infrared (3 hourly)			
Convective Parametarization	Prognostic Arakawa-Schubert			
Cloud Process	Prognostic cloud water content			
PBL and Surface Fluxes	Mellor-Yamada level 2 Monin-Obukhov similarity			
Gravity Wave Drag	Long wave drag Short wave drag			
Land Surface Model	Simple Biosphere (SiB)			

Table 3.1.2: Specifications of the regional NWP models at JMA

	Meso-Scale Model (MSM)	Local Forecast Model (LFM)
Forecast Range (Initial Time)	15 hours (00,06,12,18UTC) 33 hours (03,09,15,21UTC)	9 hours (00,03,06,09,12,15,18,21UTC)
Forecast Domain	East Asia	Eastern part of Japan
Map Projection	Lambert Conformal	
Horizontal Grids #	721×577	551×801
Grid Spacing	5km	2km
Vertical Layers	50	60
Top Layer Height	21.8km	20.2km
Radiation Process	Solar (every 15 minutes) Infrared (every 15 minutes)	
Convective Parameterization	Kain-Fritsch	(not used)
Cloud Process	3-ice bulk microphysics	
PBL and Surface Fluxes	Mellor-Yamada-Nakanishi-Niino level 3 Monin-Obukhov similarity	
Gravity Wave Drag	(not used)	

3.2 Global Spectral Model (JMA-GSM1212)

3.2.1 Introduction

The Global Spectral Model (GSM) employs primitive equations to express resolvable motions and states of the atmosphere. It also incorporates sophisticated parameterization schemes for physical processes. In the horizontal, prognostic variables are spectrally discretized using triangular truncation at wave number 959 (TL959). The corresponding transform grids cover about 0.1875° in both longitude and latitude. In the vertical, the model has 60 layers up to 0.1 hPa.

JMA has operated GSM since March 1988. The model originally had a horizontal resolution of T63 and 16 vertical layers up to 10 hPa with a sigma coordinate system.

In a model upgrade implemented in November 1989, the truncation wave number and the number of vertical layers were increased to T106 and 21, respectively, and a hybrid η vertical coordinate system was adopted.

In March 1996, the horizontal resolution was doubled to T213 and the number of vertical layers was increased to 30. The cumulus parameterization was changed from a Kuo scheme to a prognostic Arakawa-Schubert scheme.

In December 1999, the physical package underwent extensive refinement. Treatment of cloud water content as a prognostic variable was introduced, and the moist convection process was improved.

In March 2001, the number of vertical layers was increased to 40 and the vertical domain was extended up to 0.4 hPa. The model was highly parallelized to suit massively distributed-memory parallel computer operation.

In February 2005, the Eulerian advection scheme was replaced with a semi-Lagrangian one, and the spectral resolution was increased from T213 (quadratic grid) to TL319 (linear grid). Incremental non-linear normal mode initialization and vertical mode initialization were also introduced.

On 1 March, 2006, operations at 06 and 18 UTC were begun with a forecast time of 36 hours in addition to those conducted at 00 UTC with a forecast time of 90 hours and 12 UTC with a forecast time of 216 hours.

On 21 November, 2007, the horizontal resolution of GSM was enhanced to TL959, while the number of vertical layers was increased to 60 and the vertical domain was extended up to 0.1 hPa (Iwamura and Kitagawa 2008; Nakagawa 2009). The numerical integration scheme was upgraded from the three-time-level leap-frog scheme to a two-time-level scheme. The forecasts run at 00, 06 and 18 UTC were altered to each cover a uniform period of 84 hours. At the same time, the 20-km-resolution Regional Spectral Model (RSM) and the 24-km-resolution Typhoon Model (TYM) were retired from operational use.

On 5 August, 2008, a reduced Gaussian grid was incorporated into GSM as a new dynamical core. This removed redundant grid points at higher latitudes, thereby saving on computational resources (Miyamoto 2006). Incremental non-linear normal mode initialization and vertical mode initialization were eliminated.

On 18 December, 2012, a relative humidity threshold was introduced to the diagnostic stratocumulus scheme.

In March 2013, the coverage period of the forecast run at 12 UTC was extended from 216 hours to 264 hours.

3.2.2 Dynamics

The GSM is based on the framework of a semi-implicit semi-Lagrangian global model. In order to overcome the general shortcomings of semi-Lagrangian models (such as the lack of conservation properties and the high computational cost of three-dimensional interpolations), a vertically conservative semi-Lagrangian scheme is adopted for the GSM.

3.2.2.1 Governing Equations

The GSM is run on an η vertical coordinate system, which is a hybrid between pressure p and σ ($\sigma = p/p_S$, where p_S is surface pressure), implicitly defined as $p = A(\eta) + B(\eta)p_S$. The prognostic variables (wind vector $\boldsymbol{u} = (u, v)$, temperature T, pressure p, specific humidity q and cloud water content q_c) follow the system of primitive equations in the η-coordinate system as follows:

$$\frac{d\mathbf{u}}{dt} = \left(\frac{\partial}{\partial t} + \mathbf{u}\cdot\nabla + \dot{\eta}\frac{\partial}{\partial \eta}\right)\mathbf{u} = -f\mathbf{z}\times\mathbf{u} - (\nabla\Phi + R_d T_V \nabla \ln p) + \mathbf{F}_{\boldsymbol{u}} \tag{3.2.1}$$

$$\frac{dT}{dt} = \frac{\kappa T_V \omega}{\left[1 + \left(C_{pv}/C_{pd} - 1\right) q\right] p} + F_T \tag{3.2.2}$$

$$\frac{dq}{dt} = F_q \tag{3.2.3}$$

$$\frac{dq_c}{dt} = F_c \tag{3.2.4}$$

$$\frac{\partial}{\partial t}\left(\frac{\partial p}{\partial \eta}\right) + \nabla\cdot\left(\mathbf{u}\frac{\partial p}{\partial \eta}\right) + \frac{\partial}{\partial \eta}\left(\dot{\eta}\frac{\partial p}{\partial \eta}\right) = 0 \tag{3.2.5}$$

Here, d/dt is a total derivative and ∇ is a horizontal gradient operator. The other notations used above are conventional: $\mathbf{z}$ is the unit vertical vector, T_V is the virtual temperature, f is the Coriolis parameter, R_d is the gas constant for dry air, and $\kappa = R_d/C_{pd}$. C_{pd} is the the specific heat capacity at the constant pressure of dry air and C_{pv} is the specific heat capacity at the constant pressure of water vapor. $\mathbf{F}_{\boldsymbol{u}}$, F_T, F_q and F_c are tendencies relating to parameterized processes. In addition, $\mathbf{F}_{\boldsymbol{u}}$ and F_T include the effects of horizontal diffusion (to be described later). Integrating Eq. (3.2.5) with respect to η using the boundary conditions of $\dot{\eta} = 0$ at $\eta = 0$ and $\eta = 1$, η-velocity and ω are found:

$$\dot{\eta}\frac{\partial p}{\partial \eta} = -\frac{\partial p}{\partial t} - \int_0^\eta \nabla\cdot\left(\mathbf{u}\frac{\partial p}{\partial \eta'}\right) d\eta' \tag{3.2.6}$$

$$\omega \equiv \frac{dp}{dt} = -\int_0^\eta \nabla\cdot\left(\mathbf{u}\frac{\partial p}{\partial \eta'}\right) d\eta' + \mathbf{u}\cdot\nabla p \tag{3.2.7}$$

The geopotential Φ is given by the following hydrostatic relation:

$$\frac{\partial \Phi}{\partial \eta} = -R_d T_V \frac{\partial \ln p}{\partial \eta} \tag{3.2.8}$$

3.2.2.2 Vertical Finite Difference Scheme

The vertical finite difference scheme is coded according to Simmons and Burridge (1981). The prognostic variables $\mathbf{u}$, T, q and q_c are defined on the full levels, while η (including vertical fluxes) is defined on half-integer levels. Pressure on half-integer levels are expressed as

$$p_{k-1/2} = A_{k-1/2} + B_{k-1/2} p_S \qquad (k = 1, 2, \ldots, \mathrm{kmax}) \tag{3.2.9}$$

Here, the level index k increases with height, $kmax$ is the index of the highest model level, $A_{k-1/2} = A(\eta_{k-1/2})$ and $B_{k-1/2} = B(\eta_{k-1/2})$. $A_{1/2}$ is set to zero so that the lowest level coincides with the ground surface, and values of $B_{k-1/2}$ above 50hPa are set to zero so that these levels coincide with constant pressure surfaces. For intermediate levels, $A_{k-1/2}$ and $B_{k-1/2}$ vary smoothly with k.

From the hydrostatic relation given by Eq. (3.2.8) the finite difference form of geopotential on the full level is chosen as

$$\Phi_k = \Phi_S + \sum_{k'=1}^{k-1} R_d T_{Vk'} \ln\left(\frac{p_{k'-1/2}}{p_{k'+1/2}}\right) + \alpha_k R_d T_{Vk} \tag{3.2.10}$$

$$\alpha_k = \begin{cases} 1 - \dfrac{p_{k+1/2}}{\Delta p_k} \ln\left(\dfrac{p_{k-1/2}}{p_{k+1/2}}\right) & (1 \le k < \mathrm{kmax}) \\ \ln 2 & (k = \mathrm{kmax}) \end{cases} \tag{3.2.11}$$

Here, Φ_S is the geopotential at the surface. The pressure gradient force term in Eq. (3.2.1) and the adiabatic heating rate term in Eq. (3.2.2) can then be written in discretized form as

$$(\nabla\Phi + R_d T_V \nabla \ln p)_k = \nabla\Phi_S + \left[\sum_{k'=1}^{k-1} R_d \nabla T_{Vk'} \ln\left(\frac{p_{k'-1/2}}{p_{k'+1/2}}\right) + \alpha_k R_d T_{Vk}\right] + h_k \nabla p_S$$
$$h_k = \sum_{k'=1}^{k-1} R_d T_{Vk'} \left(\frac{B_{k'-1/2}}{p_{k'-1/2}} - \frac{B_{k'+1/2}}{p_{k'+1/2}}\right) + \frac{R_d T_{Vk}}{p_{k-1/2}} B_{k-1/2} \tag{3.2.12}$$

and

$$\left[\frac{\kappa T_V}{C_p/C_{pd}}\frac{\omega}{p}\right]_k = \frac{\kappa T_{Vk}}{C_{pk}/C_{pd}}\frac{1}{\Delta p_k}\left[\left(\ln\frac{p_{k^-1/2}}{p_{k+1/2}}\right)\left(B_{k+1/2}\mathbf{u}_k\cdot\nabla p_S - \sum_{l=k+1}^{\text{kmax}}\nabla\cdot(\mathbf{u}_l\Delta p_l)\right) - \alpha_k\left(\nabla\cdot\mathbf{u}_k\right)\Delta p_k\right] \tag{3.2.13}$$

respectively. C_p is the specific heat capacity at the constant pressure of moist air. The vertical mass flux in Eq. (3.2.6) is discretized as

$$\left(\dot{\eta}\frac{\partial p}{\partial \eta}\right)_{k-1/2} = -B_{k-1/2}\frac{\partial p_S}{\partial t} - \sum_{l=k}^{\text{kmax}}\nabla\cdot(\mathbf{u}_l\Delta p_l) = B_{k-1/2}\sum_{l=1}^{\text{kmax}}\nabla\cdot(\mathbf{u}_l\Delta p_l) - \sum_{l=k}^{\text{kmax}}\nabla\cdot(\mathbf{u}_l\Delta p_l) \tag{3.2.14}$$

3.2.2.3 Horizontal Grid

To mitigate the overconcentration of grid points at high latitudes and lower the computational cost, a reduced Gaussian grid is adopted for the GSM. The number of east-west grid points at each latitude is determined based on the magnitude of associated Legendre functions, which is negligibly small at high latitudes and in high orders. With this method, the computational cost of Legendre transformation can also be reduced (Juang 2004). The number of east-west grid points is in fact restricted by FFT package specifications, the number of east-west decompositions in parallelization and the interval of coarser radiation grids.

3.2.2.4 Semi-implicit Semi-Lagrangian Formulation

Prior to integration, the forecast equations (Eq. (3.2.1) - Eq. (3.2.5)) are rewritten in the form of $d_H X/dt = \partial X/\partial t + \mathbf{u}\cdot\nabla X = R$ with vertical advection terms incorporated into R on the right-hand side. These equations are integrated with respect to time along the trajectory of the parcel from the departure point D at time t to the arrival point A at time $t + \Delta t$. The linear term L separated from the forcing term R is treated semi-implicitly (i.e. using a trapezoidal rule), and the remaining R, including vertical advection terms, are treated with spatial averaging (Tanguay *et al.* 1992).

The resulting linear terms are slightly amplified by the factor $\beta = 1.2$ for computational stability, and the following is obtained:

$$X^{A+} - X^{D0} = \Delta t\frac{R^{A0} + R^{D(+)}}{2} + \Delta t\beta\left[\frac{L^{A+} + L^{D-}}{2} - \frac{L^{A0} + L^{D0}}{2}\right] \tag{3.2.15}$$

Superscript A represents the arrival point $\mathbf{x}_{ij}$ assumed to be on the Gaussian grid, and D is the departure point $\mathbf{x}_{ij} - \boldsymbol{\alpha}$ (the displacement vector $\boldsymbol{\alpha}$, whose calculation will be described later). The abbreviations used above are the same as those for $X^{A+} = X(\mathbf{x}, t + \Delta t)$, $X^{D0} = X(\mathbf{x} - \boldsymbol{\alpha}, t)$, $R^{A0} = R(\mathbf{x}, t)$, $R^{D(+)} = R(\mathbf{x} - \boldsymbol{\alpha}, t + \Delta t)$ and others. $R^{D(+)}$ is calculated based on extrapolation with respect to time. Rearranging the terms of the above equations gives a system of linear equations for the unknown values X^{A+}:

$$X^{A+} - \frac{\beta\Delta t}{2}L^{A+} = \left[X^0 + \frac{\Delta t}{2}\left\{R^{(+)} - \beta\left(L^0 - L^-\right)\right\}\right]^D + \frac{\Delta t}{2}\left[R^0 - \beta L^0\right]^A \tag{3.2.16}$$

3.2.2.5 Vertically Conservative Semi-Lagrangian Scheme

Yoshimura and Matsumura (2003, 2004) developed a vertically conservative semi-Lagrangian scheme in which vertical advection is treated separately from horizontal advection so that the model preserves conservative vertically integrated quantities such as water vapor under non-dissipative conditions. This separate treatment also reduces the model's cost of interpolation.

Eq. (3.2.16) can be reformulated with flux forms appropriate for a scheme in which vertical advection can retain conservative properties. Beginning with Eq. (3.2.5) and Eq. (3.2.1) - Eq. (3.2.4), rewriting is performed as follows:

$$\frac{d_H}{dt}\frac{\partial p}{\partial \eta} = -D\frac{\partial p}{\partial \eta} - \frac{\partial}{\partial \eta}\left(\dot{\eta}\frac{\partial p}{\partial \eta}\right) \tag{3.2.17}$$

$$\frac{d_H}{dt}\left(X\frac{\partial p}{\partial \eta}\right) = -DX\frac{\partial p}{\partial \eta} - \frac{\partial}{\partial \eta}\left(\dot{\eta}X\frac{\partial p}{\partial \eta}\right) + R_X\frac{\partial p}{\partial \eta} \tag{3.2.18}$$

Here, X represents $\mathbf{u}$, T_V, q and q_c, and $R_X = dX/dt$. The parallel nature of these equations is easily recognizable. The first term on the right hand side of these equations represents the increase caused by horizontal convergence, and the second term is the increase caused by vertical flux convergence. With respect to the latter, where q and q_c being conservative when $R_X = 0$, devising a vertically integrated quantity that remains unchanged in vertical advection appears to be a promising approach. A simple outline of the procedure is given here for specific humidity q without R_q.

Vertical discretization and time integration during the period Δt described earlier give the following equations with the omission of terms related to the semi-implicit method for reasons of simplicity:

$$\begin{aligned}(\Delta p_k)^{A+} = &\left[(\Delta p_k)^0 - \frac{1}{2}(D_k\Delta p_k)^{(+)}\Delta t + \frac{1}{2}\left\{\left(\dot{\eta}\frac{\partial p}{\partial \eta}\right)_{k+1/2} - \left(\dot{\eta}\frac{\partial p}{\partial \eta}\right)_{k-1/2}\right\}^{(+)}\Delta t\right]^D \\ &+\left[-\frac{1}{2}(D_k\Delta p_k)^0\Delta t + \frac{1}{2}\left\{\left(\dot{\eta}\frac{\partial p}{\partial \eta}\right)_{k+1/2} - \left(\dot{\eta}\frac{\partial p}{\partial \eta}\right)_{k-1/2}\right\}^{0}\Delta t\right]^A\end{aligned} \tag{3.2.19}$$

$$\begin{aligned}(q_k\Delta p_k)^{A+} = &\left[(q_k\Delta p_k)^0 - \frac{1}{2}q_k^0(D_k\Delta p_k)^{(+)}\Delta t + \frac{1}{2}\left\{\left(q\dot{\eta}\frac{\partial p}{\partial \eta}\right)_{k+1/2} - \left(q\dot{\eta}\frac{\partial p}{\partial \eta}\right)_{k-1/2}\right\}^{(+)}\Delta t\right]^D \\ &+\left[-\frac{1}{2}q_k^+(D_k\Delta p_k)^0\Delta t + \frac{1}{2}\left\{\left(q\dot{\eta}\frac{\partial p}{\partial \eta}\right)_{k+1/2} - \left(q\dot{\eta}\frac{\partial p}{\partial \eta}\right)_{k-1/2}\right\}^{0}\Delta t\right]^A\end{aligned} \tag{3.2.20}$$

$$p_{k-1/2} = \sum_{k'=k}^{\mathrm{kmax}}\Delta p_{k'}, \quad (k = 1, 2, \ldots, \mathrm{kmax}) \tag{3.2.21}$$

Here, the vertically cumulative quantity Q is defined as follows:

$$Q_{k-1/2} = \sum_{k'=k}^{\mathrm{kmax}}\Delta Q_{k'}, \quad Q_k = q_k\Delta p_k, \quad (k = 1, 2, \ldots, \mathrm{kmax} + 1) \tag{3.2.22}$$

Eq. (3.2.20) rewritten for ΔQ_k is found to be similar to Eq. (3.2.19) for Δp_k, and there is a clear correspondence between Q and p. Computation of Q can therefore be carried out in the five steps outlined below in a fashion parallel to that of p. The first two steps concern the operations inside the square brackets $[\ldots]^D$ in the above equations. The third step involves the calculation of variables at departure points based on interpolation. The fourth and the fifth steps are similar to the first two, but for the operations in the square brackets $[\ldots]^A$.

1. First step: Horizontal divergence is calculated. As the mass of each layer Δp_k varies to $\Delta p'_k$, the half-level pressure values $p_{k-1/2}$ by which layers are bound also shift to $p'_{k-1/2}$, which can be computed using Eq. (3.2.21). The values of q_k remain constant under the horizontal convergence $q'_k = q_k$.

2. Second step: Vertical flux convergence is calculated using Eq. (3.2.14) as in the Eulerian scheme. In the same way as in the first step, $\Delta p'_k$ varies to $\Delta p''_k$, and the values of $p'_{k-1/2}$ shift to $p''_{k-1/2}$ except $k = 1$ ($p'_{1/2} = p''_{1/2}$). In this step, the shift in $Q'_{k-1/2}$ caused by the vertical flux convergence is computed based on interpolation from $Q'_{k-1/2}(p'_{k-1/2})$ using $Q''_{k-1/2} = Q'_{k-1/2}(p''_{k-1/2})$. This procedure ensures the conservation of the total mass-weighted integral $Q'_{1/2} = Q''_{1/2}$, because $p'_{1/2} = p''_{1/2}$ holds and the other values of $p''_{k-1/2}$ ($k = 2, 3, \ldots, kmax$) merely have their intervals changed in the vertical column. New values of q''_k are computed using $\Delta Q''_k$ and $\Delta p''_k$ with Eq. (3.2.22).

3. Third step: Horizontal advection is incorporated by computing $(\Delta p_k)^D$ and q_k^D via quasi-cubic interpolation.

4. Forth step: Vertical flux convergence is calculated at the arrival point via the second step.

5. Fifth step: Horizontal divergence is calculated at the arrival point via the first step.

The time-integration of q and q_c is completed based on these five steps, and that of $\mathbf{u}$, T_V and p_S is followed by the semi-implicit calculation shown in Eq. (3.2.16).

3.2.2.6 Departure Point Determination

The displacement vector $\boldsymbol{\alpha}$ (as yet undetermined) obeys the implicit equation

$$\boldsymbol{\alpha} = \Delta t \left\{ \frac{\mathbf{u}_k(\mathbf{x}_{ij} - \boldsymbol{\alpha},\ t + \Delta t) + \mathbf{u}_k(\mathbf{x}_{ij},\ t)}{2} \right\} \tag{3.2.23}$$

which expresses that the horizontal advection during the time interval Δt is related to the average of future time-step wind value at the departure point and current time-step wind value at the arrival point (SETTLS; Hortal 2002). To improve stability, a method based on wind integrated in a semi-Lagrangian scheme rather than the time extrapolated wind is adopted (Yoshimura 2002). This implicit equation is solved by successive insertions of $\boldsymbol{\alpha}$. For the computation of these vector components, it is considered that the axes of the local coordinates (λ, φ) rotate due to the spherical metric as a parcel advances along a trajectory, as is the case whenever horizontal vector components are interpolated on a sphere. The wind at the departure point is computed from linear interpolation except for the last third of the iteration, for which a quasi-cubic approach is used.

3.2.2.7 Spectral Method and Horizontal Diffusion

Spectral variables (i.e. vorticity $\zeta(= \mathbf{z} \cdot \nabla \times \mathbf{u})$, divergence $D(= \nabla \cdot \mathbf{u})$, T_V and $\ln(p_S)$) are expanded in terms of spherical harmonics with triangular truncation. In accordance with the framework of the semi-Lagrangian scheme, a linear Gaussian transformation grid is used. By solving the semi-implicit equations, horizontal diffusion and variables such as the differentials on the sphere are calculated using the spectral method (Bourke 1974; Hoskins and Simmons 1975). The remaining variables q and q_c are defined only on grid points.

To prevent the accumulation of small scale noise (spectral blocking), fourth-order linear horizontal diffusion is applied to ζ, D and T_V backward and implicitly for the spectral forms in the independent step after semi-implicit time integration:

$$\left(\frac{\partial \zeta}{\partial t}\right)_{\text{hdiff}} = -K\left(\nabla^4 - \frac{4}{a^4}\right)\zeta \tag{3.2.24a}$$

$$\left(\frac{\partial D}{\partial t}\right)_{\text{hdiff}} = -K\nabla^4 D \tag{3.2.24b}$$

$$\left(\frac{\partial T_V}{\partial t}\right)_{\text{hdiff}} = -K\nabla^4\left[T_V - \frac{\partial \bar{T}_V}{\partial \bar{p}}p\right] = -K\nabla^4\left[T_V - \frac{\partial \bar{T}_V}{\partial \bar{p}}B(\eta)p_S\right] \tag{3.2.24c}$$

Here, K is the horizontal diffusion coefficient and a is the radius of the earth. Bars over variables indicate the global average on the η-surface. Angular momentum conservation does not allow the horizontal diffusion

process to work on vorticity with total wave number 1 as shown by Eq. (3.2.24a). Diffusion for virtual temperature is modified to work on the constant pressure surface; otherwise, diffusion on a declining η-surface may produce spurious mixing along steep mountain slopes. The diffusion coefficient is chosen so that the power spectrum of enstrophy coincides with that expected based on two-dimensional turbulence theory. In layers above 100hPa, the coefficient is gradually enhanced with height to simulate a sponge layer that absorbs waves incident upon the upper boundary. Rayleigh friction is also implemented for layers above 50hPa.

3.2.3 Radiation

The radiative heating rate is computed as the divergence of net radiation fluxes F:

$$\left(\frac{\partial T}{\partial t}\right)_{\text{rad}} = \frac{g}{C_p}\frac{\partial F}{\partial p} \tag{3.2.25}$$

where g is the acceleration of gravity and C_p the specific heat at the constant pressure of moist air.

Solving radiative transfer equation is computationally very expensive. In order to reduce computational costs, full radiation computation is performed only every three hours for longwave and hourly for shortwave on a coarser (reduced radiation) grid.

3.2.3.1 Longwave Radiation

The basic framework for longwave flux and cooling rate computation follows the method of Chou *et al.* (2001). Longwave radiation is treated using the broad-band flux emissivity method for nine spectral bands shown in Figure 3.2.1.

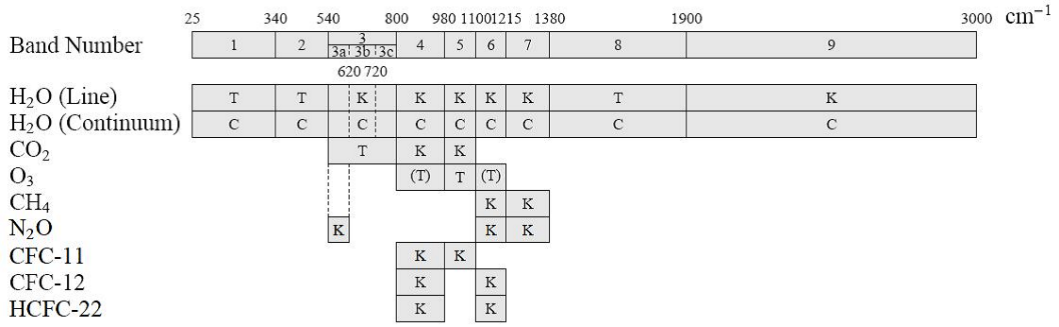

Figure 3.2.1: Spectral regions for evaluation of broad-band transmissivity. Letters represent transmittance calculation methods: K: k-distribution method; T: table look-up method; C: parameterization for water vapor continuum absorption.

Assuming a non-scattering atmosphere, the net longwave radiation flux F can be given by

$$F(p) = C\,(p,\ p_{\text{s}})\,\pi B\,(T_{\text{s}})\,\tau\,(p,\ p_{\text{s}}) + \int_{p_{\text{s}}}^{0} C\,(p,\ p')\,\pi B(T')\frac{\partial \tau\,(p,\ p')}{\partial p'}\,dp' \tag{3.2.26}$$

where p_s is the surface pressure, T_s the surface temperature, and T the air temperature. $\tau\,(p,\ p')$ denotes the band transmissivity between pressures p and p', and $B(T)$ the total Planck function. $C\,(p,\ p')$ is the clear sky fraction between pressures p and p' derived from fractional cloud cover assuming the maximum-random cloud overlap proposed by Geleyn and Hollingsworth (1979). Since clouds are treated as blackbodies, the effective cloudiness of semi-transparent cloud is given by the product of horizontal coverage and emissivity.

Band transmissivity is normalized using the Planck function $B_\nu(T)$ for each absorber in a given spectral region $\Delta\nu$:

$$\tau(p,\, p') = \int_{\Delta\nu} B_\nu(T_0)\tau_\nu(p,\, p')\, d\nu \Big/ \int_{\Delta\nu} B_\nu(T_0)\, d\nu \tag{3.2.27}$$

where T_0 is 250K. Depending on the absorber and the spectral band, band transmissivity is evaluated with three different approaches: the pre-computed table look-up method (Chou and Kouvaris 1991), the *k*-distribution method (Arking and Grossman 1972) for line absorption, and parameterization for water vapor continuum absorption. Gas absorption data are derived from HITRAN2000 (Rothman *et al.* 2003) for water vapor, carbon dioxide, ozone, methane, nitrous oxide and three CFCs. The e-type and P-type continuum absorption by water vapor is treated after the method of Zhong and Haigh (1995) with some refinement. In order to consider the broadening of absorption lines in the *k*-distribution method, the absorption coefficient is adjusted using a pressure scaling technique based on the Line-By-Line calculation. A diffusivity factor of 1.66 is used to approximate integration over the direction of radiance transmission.

3.2.3.2 Shortwave Radiation

Shortwave scattering and absorption are modeled in a two-stream formulation using the delta-Eddington approximation (Joseph *et al.* 1976; Coakley *et al.* 1983). The spectrum is divided into 22 bands based on Freidenreich and Ramaswamy (1999), while absorption by water vapor in the near-infrared region is based on Briegleb (1992). Assuming a plane parallel atmosphere, the diffuse radiance I is governed by the following radiative transfer equation:

$$\mu\frac{dI}{d\delta} + I = \frac{\omega_0}{2}\int_{-1}^{+1} p(\mu,\, \mu')I(\delta,\, \mu')\, d\mu' + \frac{\omega_0}{2}S_0 p(\mu,\, \mu_0)\exp\left(-\frac{\delta}{\mu_0}\right) \tag{3.2.28}$$

where δ is the optical thickness, ω_0 the single scattering albedo, and S_0 the incident solar irradiance in the direction μ_0 (the cosine of the solar zenith angle). The scattering phase function $p(\mu,\, \mu')$ defines the probability that radiation coming from direction μ' is scattered in direction μ. In the delta-Eddington method, the phase function is formed as a linear expression of μ with the fraction of forward-scattering peak f:

$$p(\mu,\, \mu') = 2f\delta(\mu - \mu') + (1 - f)\left(1 + 3\frac{g - f}{1 - f}\mu\mu'\right) \tag{3.2.29}$$

where $\delta(\mu - \mu')$ is the Dirac delta function and g the asymmetry factor.

Considering an atmosphere where the fraction C_{total} (which depends on cloud overlap assumption) is covered by clouds, the total shortwave radiation flux is given as a weighted average of the fluxes in the cloudy and clear sky fractions of the column as follows:

$$F = C_{\text{total}}F_{\text{cloudy}} + (1 - C_{\text{total}})F_{\text{clear-sky}} \tag{3.2.30}$$

The reflectance and transmittance of the cloudy and clear sky fraction of the layer are calculated as functions of the total optical thickness δ_{total}, the total single scattering albedo $\omega_{0\ \text{total}}$ and the total asymmetry factor g_{total} of the layer:

$$\delta_{\text{total}} = \delta_R + \delta_g + \delta_a + \delta_c \tag{3.2.31a}$$

$$\omega_{0\ \text{total}} = \frac{\delta_R + \omega_{0a}\delta_a + \omega_{0c}\delta_c}{\delta_R + \delta_g + \delta_a + \delta_c} \tag{3.2.31b}$$

$$g_{\text{total}} = \frac{g_a\omega_{0a}\delta_a + g_c\omega_{0c}\delta_c}{\delta_R + \omega_{0a}\delta_a + \omega_{0c}\delta_c} \tag{3.2.31c}$$

where the subscripts R, g, a and c denote molecular Rayleigh scattering, gaseous absorption, and Mie scattering/absorption caused by aerosols and cloud droplets, respectively.

The cloud optical properties are parametrized as functions of the cloud water path CWP and the effective radius of liquid droplets or ice particles r_e as follows:

$$\delta_c = \mathrm{CWP}(a + b/r_e) \tag{3.2.32a}$$

$$1 - \omega_{0c} = c + dr_e \tag{3.2.32b}$$

$$g_c = e + fr_e \tag{3.2.32c}$$

where the coefficients $a, \ldots, f$ are specified differently for liquid droplets (Slingo 1989) and for ice particles (Ebert and Curry 1992).

3.2.3.3 Radiatively Active Constituents

Radiatively active gases considered in the scheme are prognostic water vapor, climatological ozone, globally uniform carbon dioxide (at 375ppmv), oxygen (at 209490ppmv), methane (at 1.75ppmv), nitrous oxide (at 0.28ppmv) and CFC-11, CFC-12 and HCFC-22 (at 0.3, 0.5, 0.2ppbv, respectively). Monthly mean concentrations of ozone are specified by three-dimensional Chemical Transport Model calculation(see Subsection 3.8.4). Aerosol optical depth climatology is based on total-column value from Moderate Resolution Imaging Spectroradiometer (MODIS) and Total Ozone Mapping Spectrometer (TOMS) observations with seasonal variation. Other optical properties of aerosols are specified as continental and maritime background values without seasonal variation. The effective radius of cloud liquid droplets is fixed at 13 and 10 micrometers over the ocean and land, respectively. The effective radius of ice particles depends on temperature T and cloud ice content IWC (Wyser 1998) as follows:

$$B = -2 + 10^{-3}(273 - T)^{1.5} \log_{10} \frac{\mathrm{IWC}}{\mathrm{IWC}_0} \tag{3.2.33}$$

$$r_e = 377.4 + 203.3B + 37.91B^2 + 2.3696B^3 \tag{3.2.34}$$

where IWC_0 is $50\mathrm{gm}^{-3}$.

3.2.4 Cumulus Convection

3.2.4.1 Cumulus Model

An economical version of the Arakawa-Schubert scheme (Arakawa and Schubert 1974) developed by JMA is implemented. For economical computation, two simplifications are introduced. First, the vertical profile of the upward mass flux η is assumed to be a linear function of height z, as proposed by Moorthi and Suarez (1992), in the form of $\eta = 1 + \lambda(z - z_b)$, where λ denotes the entrainment rate and z_b is the cloud base height. Secondly, the mass flux at the cloud base is determined by solving a prognostic equation (Randall and Pan 1993) rather than by applying quasi-equilibrium assumption. The cloud base level is fixed near 900 hPa in the model. The moist static energy and other thermodynamic properties of the upward mass flux at the cloud base are given by the grid-scale values at the maximum moist static energy level below the base.

Following the concept of Arakawa and Schubert (1974), the ensemble effect of multiple types of cumuli is considered. Each type is defined by the level of the cloud top, where the updraft cloud mass loses buoyancy and detrainment occurs. The entrainment of the environmental air mass is considered during the upward movement of the cloud air mass. The entrainment rate λ of each cumulus is determined based on a no-buoyancy condition at the cloud top. The upper limit of λ is set to $1 \times 10^{-3}\ \mathrm{m}^{-1}$.

Here it is assumed that all condensed water in the updraft is carried up to the cloud top. Part of this water falls into the environment as rain, and the rest is detrained as cloud water. The ratio of rainwater and cloud water changes linearly with cloud depth. Detrained cloud water is redistributed to layers where the temperature is below freezing point.

3.2.4.2 Upward Mass Flux

The following prognostic equation is used for upward mass flux at the cloud base M_B:

$$\frac{dM_B(\lambda)}{dt} = \max\left(\frac{A(\lambda) - fA_0(\lambda)}{2\alpha},\ 0\right)\min\left(\frac{\lambda}{\lambda_{\min}},\ 1\right)\max\left(\lambda_{\max},\ 0\right)\left(\frac{\Delta p}{\Delta p_{\text{eff}}}\right) - \frac{M_B(\lambda)}{2\tau_d} \tag{3.2.35}$$

where A denotes the cloud work function, A_0 is the average of observed cloud work functions as given by Lord and Arakawa (1980), Δp is the depth of model cloud top layer, Δp_{eff} is the effective depth of the cloud top, and τ_d is the time constant of cumulus kinetic energy decay. The parameter f is introduced to incorporate the effects of grid-scale vertical wind and convective inhibition. This is given by

$$f = \frac{\omega}{\omega_0} + \frac{A_i}{A_{i0}} + c \tag{3.2.36}$$

where ω denotes the vertical pressure velocity at the lowest level, A_i represents the work involved in lifting the parcel to the level of free convection, and ω_0, A_{i0} and c are empirically determined constants. In order to suppress tall cumuli in dry conditions and incorporate the effects of turbulence in the planetary boundary layer, the parameter $\lambda_{\min}$ is defined as follows:

$$\lambda_{\min} = \max\left(\frac{0.9 - \text{RH}}{0.2},\ 10^{-3}\right) \times \frac{0.3}{5l_0} \tag{3.2.37}$$

where RH denotes the vertical mean of relative humidity between the cloud base and the cloud top, and l_0 represents the mixing length of the planetary boundary layer. The parameter $\lambda_{\max}$ is introduced to suppress tall cumuli with unnaturally large entrainment rates, and is defined as

$$\lambda_{\max} = \min\left(\frac{\lambda - \lambda_2}{\lambda_1 - \lambda_2},\ 1\right) \tag{3.2.38}$$

where $\lambda_1 = a_1/(z_t - z_b)$, $\lambda_2 = a_2/(z_t - z_b)$, z_t is the cloud top height, and a_1 and a_2 are empirically determined constants.

3.2.4.3 Convective Downdraft

The convective downdraft associated with cumulus convection affects the environment by reducing the net upward mass flux and detrainment from the downdraft. For reasons of economy, only one type of downdraft is assumed, while many types are considered in the updraft scheme.

The downdraft is initiated at the level where the net upward mass flux is reduced to half of that at the cloud base. The downdraft mass flux M_d at the cloud base is given by

$$M_d = 0.4M_B \tag{3.2.39}$$

Entrainment from the environment is assumed to occur above the cloud base, while detrainment is assumed to occur both above and below it. The entrainment and detrainment rates are set to the same constant value above the cloud base.

3.2.4.4 Triggering Mechanism

The convective triggering mechanism proposed by Xie and Zhang (2000) known as the dynamic CAPE generation rate (DCAPE) is used in the cumulus parameterization. DCAPE is defined as follows:

$$\text{DCAPE} = \left(\text{CAPE}\left(T^*, q^*\right) - \text{CAPE}\left(T, q\right)\right)/\Delta t \tag{3.2.40}$$

where T is the temperature, q is the specific humidity, and (T^*, q^*) are (T, q) plus the change caused by overall large-scale advection over a certain time period Δt (the integration time step used in the model). These values are equivalent to (T, q) just after dynamics calculation. CAPE is defined as

$$\text{CAPE} = \int_{z_{\text{LFC}}}^{z_{\text{LNB}}} g\frac{T_v^u - T_v}{T_v}dz \tag{3.2.41}$$

where z_{LFC} and z_{LNB} are the height of the level of free convection and that of neutral buoyancy, respectively, g is the acceleration of gravity, and T_v is the virtual temperature. The superscript u denotes air parcel lifting. Deep convection is assumed to occur only when DCAPE exceeds an empirically determined critical value.

3.2.4.5 Mid-level Convection

In the extratropics, moist convection does not always arise from the top of the planetary boundary layer. Accordingly, a mid-level convection scheme is incorporated to represent cumulus convection with its roots in the free atmosphere. The cloud base of mid-level convection is given by the maximum moist static energy level in the vertical column. The cloud top is defined as the level where an air mass rising from the cloud base with a constant entrainment rate loses buoyancy. The upward mass flux at the cloud base is given by

$$\frac{dM_B}{dt} = \frac{A}{2\alpha} - \frac{M_B}{2\tau_d} \tag{3.2.42}$$

where A is a cloud work function.

3.2.4.6 Convective Momentum Transport

The parameterization of convective momentum transport follows the scheme proposed by Kershaw and Gregory (1997) and Gregory *et al.* (1997). The horizontal momentum tendency caused by convection is parameterized as

$$\frac{\partial(\rho\overline{\boldsymbol{v}})}{\partial t} = -\frac{\partial M_u}{\partial z}\boldsymbol{v}^u + \frac{\partial}{\partial z}\left(M_u\overline{\boldsymbol{v}}\right) + \frac{\partial M_d}{\partial z}\boldsymbol{v}^d - \frac{\partial}{\partial z}\left(M_d\overline{\boldsymbol{v}}\right) \tag{3.2.43}$$

where $\boldsymbol{v}$ is the horizontal component of the wind vector, ρ is the air density, and M_u and M_d are upward and downward mass fluxes. The overbars denote the average over the horizontal grid, and the superscript $u(d)$ denotes a contribution from the convective upward (downward) domain. Entrainment and detrainment are assumed to occur between the cloud base and the cloud top.

3.2.4.7 Effects on Large-scale Tendencies

The effects of cumulus convection on large-scale tendencies are calculated using large-scale budget equations. The major contributions of such convection are made through 1) compensating downward motion, 2) detrainment of moisture from updraft at the cloud top, 3) detrainment from convective downdraft, and 4) convective momentum transport.

3.2.5 Clouds and Large-scale Precipitation

Clouds are prognostically determined in a fashion similar to that proposed by Smith (1990). The simple statistical approach proposed by Sommeria and Deardorff (1977) is adopted for the calculation of cloud amounts and their water content. In each grid box, the total water content (water vapor and cloud water) and the liquid water temperature are assumed to vary due to unresolved atmospheric fluctuations with uniform probability distribution. The cloud fraction C is given by the part of the grid box where the total water content q_w exceeds the saturation specific humidity q_s:

$$C = \frac{a_L\left(\overline{q}_w - q_s\left(T_L\right)\right) + \Delta q_w}{2\Delta q_w} \tag{3.2.44a}$$

$$a_L = \frac{1}{1 + \frac{L}{C_p}\left(\frac{\partial q_s}{\partial T}\right)_{T=T_L}} \tag{3.2.44b}$$

where L is the latent heat of condensation, C_p is the specific heat at constant pressure, Δq_w is the maximum local deviation from the grid-box mean total water content $\overline{q}_w$, and T_L is the liquid water temperature, defined as

$$T_L = T - \frac{L}{C_p} q_c \tag{3.2.45}$$

where T is the temperature and q_c is the cloud water content. In addition to this, for the representation of marine stratocumulus clouds, the cloud fraction C is diagnosed using the following scheme proposed by Kawai and Inoue (2006) when specific conditions are met:

$$C = 12.0\left(-\frac{\partial\theta}{\partial p} - 0.07\right) \tag{3.2.46}$$

where θ is the potential temperature and p is the pressure. Liquid (ice) cloud is assumed when the temperature is above 0°C (below −15°C). Between −15°C and 0°C, mixed-phase cloud is present and the mixing ratio changes linearly with temperature.

Parameterization for the rate of conversion P from cloud water to precipitation follows the scheme proposed by Sundqvist (1978):

$$P = c_0 q_c \left[1 - \exp\left\{-\left(\frac{q_c}{C q_c^{\mathrm{crit}}}\right)^2\right\}\right] \tag{3.2.47}$$

where $1/c_0$ represents a characteristic time scale for the conversion of cloud droplets into raindrops, and q_c^{crit} is the critical cloud water content at which the release of precipitation becomes efficient. The coalescence process (collection of cloud droplets by raindrops falling through a cloud) and the Bergeron-Findeisen effect (enhancement of precipitation release in clouds containing a mixture of droplets and ice crystals) are modeled following Sundqvist *et al.* (1989).

Based on Kessler (1969) and Tiedtke (1993), the evaporation rate E for large-scale precipitation is parameterized as

$$E = b \times \frac{1}{\tau_e} \times (q_s - q) \times \left\{\left(\frac{p}{p_s}\right)^{1/2} \frac{1}{b} \frac{P_l}{P_{l0}}\right\}^{0.577} \tag{3.2.48}$$

where b is the clear-sky precipitation fraction (set at 0.5), q_s is the saturation specific humidity, p is the pressure, p_s is the surface pressure, and P_l is the local precipitation rate. The values of constants are $1/\tau_e = 5.44 \times 10^{-4}\ \mathrm{s}^{-1}$ and $P_{l0} = 5.9 \times 10^{-3}\ \mathrm{kg\,m^{-2}\,s^{-1}}$. The melting process and snow sedimentation are also considered.

3.2.6 Surface Turbulent Fluxes

Surface turbulent fluxes are formulated with bulk formulae following the Monin-Obukhov similarity theory:

$$\overline{(w'\mathbf{v}')}_s = -C_m|\mathbf{v}_1|\mathbf{v}_1 \tag{3.2.49}$$

$$\overline{(w'\theta')}_s = -C_h|\mathbf{v}_1|(\theta_1 - \theta_s) \tag{3.2.50}$$

$$\overline{(w'q')}_s = -C_h|\mathbf{v}_1|(q_1 - q_s). \tag{3.2.51}$$

Here $\mathbf{v} = (u, v)$ represents horizontal wind, θ is potential temperature and q is specific humidity, and subscripts "1" and "s" indicate variables at the lowest level of the model grid and at the ground surface, respectively.

The bulk Richardson number R_{iB} is defined as

$$R_{iB} = \frac{g z_1(\theta_{v1} - \theta_{vs})}{T_1|\mathbf{v}_1|^2} \tag{3.2.52}$$

where z_1 is the height of the lowest level of the model grid above the ground, and θ_v is the virtual potential temperature.

Using the stability functions proposed by Louis *et al.* (1982), the exchange coefficients can be written as follows:

$$C_m = \begin{cases} \dfrac{\gamma_m}{1 + 10R_{iB}/\sqrt{1 + 5R_{iB}}} & R_{iB} > 0 \\ \gamma_m \left[1 - \dfrac{10R_{iB}}{1 + 75\gamma_m \sqrt{z_1 |R_{iB}|/z_{0m}}} \right] & R_{iB} \leq 0 \end{cases} \tag{3.2.53}$$

$$C_h = \begin{cases} \dfrac{\gamma_h}{1 + 15R_{iB}/\sqrt{1 + 5R_{iB}}} & R_{iB} > 0 \\ \gamma_h \left[1 - \dfrac{15R_{iB}}{1 + 75\gamma_h \sqrt{z_1 |R_{iB}|/z_{0h}}} \right] & R_{iB} \leq 0 \end{cases} \tag{3.2.54}$$

$$\begin{aligned} \gamma_m &= \frac{k^2}{\ln(z_1/z_{0m}) \ln(z_1/z_{0m})} \\ \gamma_h &= \frac{k^2}{\ln(z_1/z_{0m}) \ln(z_1/z_{0h})} \end{aligned} \tag{3.2.55}$$

where k is von Kármán's constant (= 0.4), while z_{0m} and z_{0h} are the surface momentum and heat roughness lengths, respectively.

Over land, surface roughness lengths ($z_{0m} = z_{0h}$) are determined based on vegetation types, and are affected by snow cover. Over ocean, surface wind stress depends on oceanic waves excited by surface winds. Roughness length and wind-induced stress are iteratively calculated in the model. Following the method of Beljaars (1995), surface roughness lengths over ice-free ocean are determined from Charnock's relation (Charnock 1955):

$$\begin{aligned} z_{0m} &= \frac{0.11\nu}{u_*} + \frac{\alpha}{g} u_*^2 \\ z_{0h} &= \frac{0.62\nu}{u_*} \end{aligned} \tag{3.2.56}$$

where $u_* \left(\equiv \left| \overline{(w'\mathbf{v}')_s} \right| \right)$ is the friction velocity, ν is the kinematic viscosity of air (= $1.5 \times 10^{-5} \mathrm{m}^2/\mathrm{s}$) and α the Charnock coefficient (= 0.020). The surface roughness length over sea ice is fixed at 0.001m.

3.2.7 Vertical Turbulent Diffusion

The level 2 turbulence closure scheme of Mellor and Yamada (1974) is used to represent the vertical diffusion of momentum, heat and moisture. The turbulent transports are expressed as

$$\overline{w'\mathbf{v}'} = -K_m \frac{\partial \mathbf{v}}{\partial z} \tag{3.2.57}$$

$$\overline{w's'_L} = -K_h \frac{\partial s_L}{\partial z} \tag{3.2.58}$$

$$\overline{w'q'_w} = -K_h \frac{\partial q_w}{\partial z} \tag{3.2.59}$$

where $s_L (\equiv C_p T + gz - Lq_c)$ is the liquid water static energy and $q_w (\equiv q + q_c)$ is the total water content.

Following the mixing-length theory, the diffusion coefficients can be written as

$$K_m = l^2 \left| \frac{\partial \mathbf{v}}{\partial z} \right| f_m(R_i) \tag{3.2.60}$$

$$K_h = l^2 \left| \frac{\partial \mathbf{v}}{\partial z} \right| f_h(R_i) \tag{3.2.61}$$

where the mixing length l is given according to Blackadar (1962) as;

$$l = \frac{kz}{1 + kz/l_0}. \tag{3.2.62}$$

The asymptotic mixing length l_0 is determined from sub-grid scale orographic variances and the planetary boundary layer depth.

The stability functions f_m and f_h are given following Mellor and Yamada (1982). The gradient Richardson number R_i is defined after the method of Smith (1990),

$$R_i = g \left\{ \tilde{\beta}_s \frac{\partial s_L}{\partial z} + \tilde{\beta}_Q \frac{\partial q_w}{\partial z} \right\} \Big/ \left| \frac{\partial \mathbf{v}}{\partial z} \right|^2 \tag{3.2.63}$$

where $\tilde{\beta}_s$ and $\tilde{\beta}_Q$ are buoyancy parameters in terms of the cloud-conserved quantities s_L and q_w, respectively.

3.2.8 Gravity Wave Drag

The parameterization for the orographic gravity wave drag consists of two components; one for long waves (wavelength > 100km) and the other for short waves (wavelength ≈ 10km). The long waves are assumed to propagate upward until reaching wave-breaking levels mainly in the stratosphere and exert drag there (type A scheme), while short waves are always regarded as trapped and dissipated within the lower troposphere (type B scheme). Therefore the fundamental difference between the two schemes appears in the vertical distribution of the momentum deposit. The type A scheme is based on Palmer *et al.* (1986) with some modifications. Details of type A and B schemes are explained in Iwasaki *et al.* (1989).

In both schemes, the momentum flux $\boldsymbol{\tau}_r$ excited by subgrid-scale variances of topography σ^2 is determined by

$$\boldsymbol{\tau}_r = \min\left(C_{gw}\, \rho_r\, N_r\, v_r\, \sigma^2,\ |\boldsymbol{\tau}_{r,\,sat}| \right) \boldsymbol{v}_r / v_r \tag{3.2.64}$$

where

$$\boldsymbol{\tau}_{r,\,sat} = C_{gw}\, \rho_r\, N_r\, v_r \left(\frac{\nu_r}{2F_c N_r} \right)^2 \boldsymbol{v}_r / v_r \tag{3.2.65}$$

C_{gw} is constant, ρ air density, N Brunt-Väisälä frequency, F_c critical Froude number, $\boldsymbol{v}$ the intrinsic velocity and $v = |\boldsymbol{v}|$. The subscript r denotes the reference level where the gravity wave stresses (momentum fluxes) are generated. There is a maximum of the momentum flux due to the valley blocking phenomenon, which is caused by stagnant flow near bottoms of valleys. This phenomenon occurs when the Froude number is below a critical value. The blocking effectively reduces the amplitudes of gravity waves. The topographic variances σ^2 are derived from the GTOPO30, which is $30'' \times 30''$ geographical data. First, the mean elevation (h_m) and its standard deviation (σ_m) over a $5' \times 5'$ grid box are evaluated from GTOPO30. The standard deviation of $(h_m - h)$ in a Gaussian grid box is regarded as σ in the type A scheme where h denotes the model topography, while the average of σ_m in the Gaussian grid box is regarded as σ in the type B scheme.

In the type A scheme, the momentum deposit is determined by the amplitude saturation hypothesis. The gravity wave stress at the $(k + 1/2)$-th level is given by

$$\boldsymbol{\tau}_{k+1/2} = \min\left(\left| \boldsymbol{\tau}_{k-1/2} \right|,\ |\boldsymbol{\tau}_{sat}| \right) \boldsymbol{\tau}_r / |\boldsymbol{\tau}_r| \tag{3.2.66}$$

where

$$\boldsymbol{\tau}_{sat} = C_{gw}\, \rho\, N \left(\boldsymbol{v} \cdot \frac{\boldsymbol{\tau}_r}{|\boldsymbol{\tau}_r|} \right) \left[\frac{\epsilon}{2F_c N} \left(\boldsymbol{v} \cdot \frac{\boldsymbol{\tau}_r}{|\boldsymbol{\tau}_r|} \right) \right]^2 \frac{\boldsymbol{\tau}_r}{|\boldsymbol{\tau}_r|} \tag{3.2.67}$$

ϵ is a function of the Richardson number

$$R_i = N^2 \Big/ \left[\frac{\partial}{\partial z} \left(\boldsymbol{v} \cdot \frac{\boldsymbol{\tau}_r}{|\boldsymbol{\tau}_r|} \right) \right]^2 \tag{3.2.68}$$

The wave stress of short gravity waves decreases with altitude due to nonhydrostatic effects (*e.g.*, Wurtele *et al.* 1987). In the type B scheme, the wave stress is simply assumed to be a quadratic function of pressure and to vanish around 700hPa as follows:

$$\tau(p) = \begin{cases} \tau(p_s) \cdot \dfrac{(p/p_s - 0.7)^2}{0.3^2} & p/p_s \geq 0.7 \\ 0 & p/p_s < 0.7 \end{cases} \tag{3.2.69}$$

Gravity wave drag is calculated by taking a vertical convergence of gravity wave fluxes as follows:

$$\frac{\partial v}{\partial t} = \frac{1}{\rho}\frac{\partial \tau}{\partial z} \tag{3.2.70}$$

3.2.9 Land Surface Processes

The Simple Biosphere scheme (SiB) developed by Sellers *et al.* (1986), Sato *et al.* (1989a) and Sato *et al.* (1989b) is implemented in the model. Evapotranspiration from dry leaves considerably reduces the Bowen ratio during daylight hours. Figure 3.2.2 shows heat and water flows in the analogy of an electric circuit.

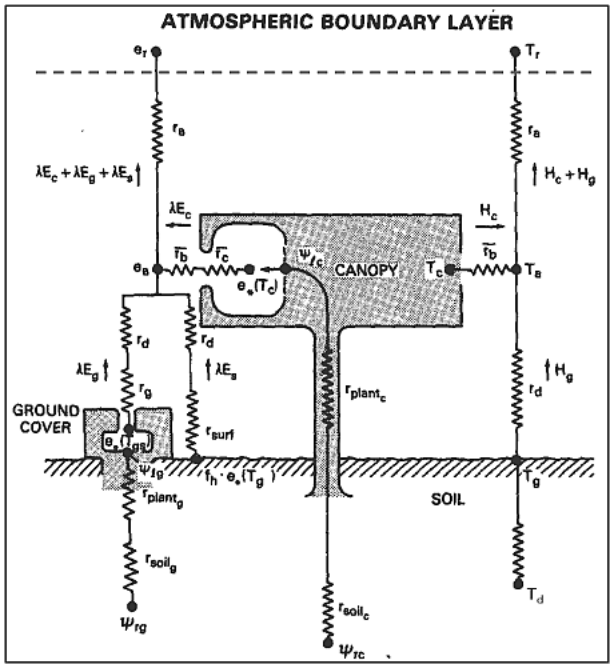

Figure 3.2.2: Schematic illustration of SiB. The temperature T_a and the specific humidity q_a of the canopy space are related to variables at the lowest level of the model grid by the surface boundary layer scheme (Modified from Sellers *et al.* (1986)).

The governing equations for the canopy temperature T_c, the ground surface temperature T_g and the deep soil temperature T_d are

$$C_c \frac{\partial T_c}{\partial t} = R_c^n - H_c - \lambda E_c \tag{3.2.71}$$

$$C_g \frac{\partial T_g}{\partial t} = R_g^n - H_g - \lambda E_g - \frac{2\pi C_g}{\tau_D}\left(T_g - T_d\right) \tag{3.2.72}$$

$$\frac{\partial T_d}{\partial t} = -\frac{2\pi}{\sqrt{365}\,\tau_D}\left(T_d - T_g\right) \tag{3.2.73}$$

where C is heat capacity, R^n is net radiation, H is sensible heat, E is the evapotranspiration rate, λ is the latent heat of evaporation of water, and τ_D is the length of the day. The suffixes c, g and d denote the canopy, the ground/ground grass and the deep soil, respectively. T_g and T_d are predicted using the force-restore method (Deardorff 1978). The initial conditions of T_c, T_g and T_d are those of the first guess, the 6-hour forecast initiated 6 hours before.

Water storage on leaves of the canopy M_c and the ground grass M_g are predicted using

$$\frac{\partial M_c}{\partial t} = P_c - D_c - \frac{E_{wc}}{\rho_w} \tag{3.2.74}$$

$$\frac{\partial M_g}{\partial t} = P_g - D_g - \frac{E_{wg}}{\rho_w} - \delta M_{\mathrm{sn}} \tag{3.2.75}$$

where P represents precipitation over leaves, D is water drainage from leaves, E_w is the evaporation of liquid water on leaves, ρ_w is water density and δM_{sn} is the amount of snow melt. When T_c (T_g) is below the freezing point of water, M_c (M_g) represents ice on canopy leaves (snow water equivalent on the ground).

Soil moisture is predicted in three layers. Vegetation draws water from the soil and transfers it directly to the air. In this relation, stomatal resistance (which depends on soil moisture, humidity and solar radiation intensity) considerably controls transpiration. The prognostic equations used for soil moisture in each layer are as follows:

$$\frac{\partial W_1}{\partial t} = \frac{1}{\delta_s D_1}\left\{P_1 - Q_{1,2} - \frac{1}{\rho_w}E_s\right\} \tag{3.2.76}$$

$$\frac{\partial W_2}{\partial t} = \frac{1}{\delta_s D_2}\left\{Q_{1,2} - Q_{2,3} - \frac{1}{\rho_w}\left(E_{dc,2} + E_{dg,2}\right)\right\} \tag{3.2.77}$$

$$\frac{\partial W_3}{\partial t} = \frac{1}{\delta_s D_3}\left\{Q_{2,3} - Q_3 - \frac{1}{\rho_w}\left(E_{dc,3} + E_{dg,3}\right)\right\} \tag{3.2.78}$$

where W_i is the soil moisture wetness of the i-th soil layer, δ_s is soil porosity, D_i is the thickness of the i-th soil layer, P_1 is infiltration of precipitation, $Q_{i,j}$ is the water flux caused by the difference in matric potential between the i-th and j-th soil layers, Q_3 is gravitational drainage, E_s is evaporation from bare soil, $E_{dc,i}$ is water drawn from the i-th soil layer by canopy transpiration, and $E_{dg,i}$ is that drawn by ground grass transpiration. The first soil layer is the top one. The surface overflow and the gravitational drainage of water are counted as the run-off Q_r as follows:

$$Q_r = P_0 - P_1 + Q_3 \tag{3.2.79}$$

where

$$P_0 = P_{\mathrm{total}} - \left(P_c + P_g\right) + \left(D_c + D_g\right) \tag{3.2.80}$$

P_{total} is total precipitation and P_0 is precipitation reaching the ground. P_1 is limited due to the hydraulic conductivity of saturated soil. The initial condition for soil moisture is based on climatological data published by Willmott *et al.* (1985). Snow depth data from Snow Depth Analysis (see Section 2.8) are used to set the initial value of snow water equivalent M_g, assuming a constant snow density of 200kg/m^3.

SiB is connected to the surface boundary layer scheme through the temperature T_a and the specific humidity q_a of the canopy space. Roughness lengths are based on the vegetation types in the SiB scheme.

3.2.10 Parallelization

In the GSM, Open Multiprocessing (OpenMP) is employed for shared memory parallelization, and a Message Passing Interface (MPI) is used for distributed memory parallelization. A two-dimensional decomposition method is adopted for parallelization among processes.

Figure 3.2.3 shows the schematic design of parallelization. There are five computational stages in the performance of spherical harmonic transformation and the semi-Lagrangian advection scheme, and appropriate decompositions are selected in each stage.

At the grid stage, since all vertical levels exist in a same rank for the computation of physical processes and non-linear terms of dynamical processes, variable arrays are decomposed into east-west and north-south direction. North-south decomposition follows a cyclic order, and is applied in such a way that the order of ranking is reversed alternately. This helps to mitigate load imbalances associated with physical parameterization and the number of grid points, since their computational loads depend mainly on latitudinal zones. At the Fourier stage, since all east-west grid points exist in a same rank for the performance of Fourier transformation, variable arrays are decomposed into north-south and vertical direction. At the Legendre stage, since all north-south grid points exist in a same rank for the performance of Legendre transformation, variable arrays are decomposed into vertical and longitudinal wavenumber direction. At the wavenumber stage, since all vertical levels exist in a same rank for the solution of Helmholtz equations in the semi-implicit scheme, variable arrays are decomposed into longitudinal and total wavenumber direction. Communication among these four stages can be performed independently within each subset based on the provision of two restrictions for the number of decompositions: 1) the number of decompositions for the east-west direction, the vertical direction and the total wavenumber direction must be the same, and 2) the number of decompositions for the north-south direction and the longitudinal wavenumber direction must be the same.

At the horizontal advection stage, variable arrays are decomposed into vertical and north-south direction. To reduce the amount of communication relating to halo regions, the number of decompositions for the north-south direction is made as small as possible. Unlike communication in the stages described above, global communication is required for interaction between the grid stage and the horizontal advection stage.

3.2.11 Surface Boundary Conditions

Model topography is derived from GTOPO30 data, while land-sea distribution is determined in reference to the Global Land Cover Characteristics (GLCC) database compiled by the U.S. Geological Survey (USGS) and others. Vegetation types are based on Dorman and Sellers (1989).

Analyzed daily sea surface temperature (SST) (see Section 5.2) data and sea ice concentration (SIC) are used as initial conditions for the sea surface in the GSM. The amount of change in these variables during the temporal integration of the model is equivalent to the time interpolated variation in monthly climatological data given by the NOAA OI SST (Reynolds and Smith 1994) and the climatological SIC derived using the method of Nomura (1998). A sea area where SIC exceeds 55% is regarded as a sea ice area in the GSM.

3.2.12 Initial Conditions

The initial conditions for zonal wind, meridional wind, temperature, specific humidity and surface pressure are provided from 4D-Var global objective analysis (see Section 2.5). The initial conditions for cloud water content, cloud cover (for radiation), convective mass flux at cloud base, canopy temperature, ground surface temperature and deep soil temperature are those of the first guess. Soil moisture data in the first step are climatological values. The value obtained from snow depth analysis (see Section 2.8) is used to determine the initial snow water equivalent and to adjust the initial ground surface temperature.

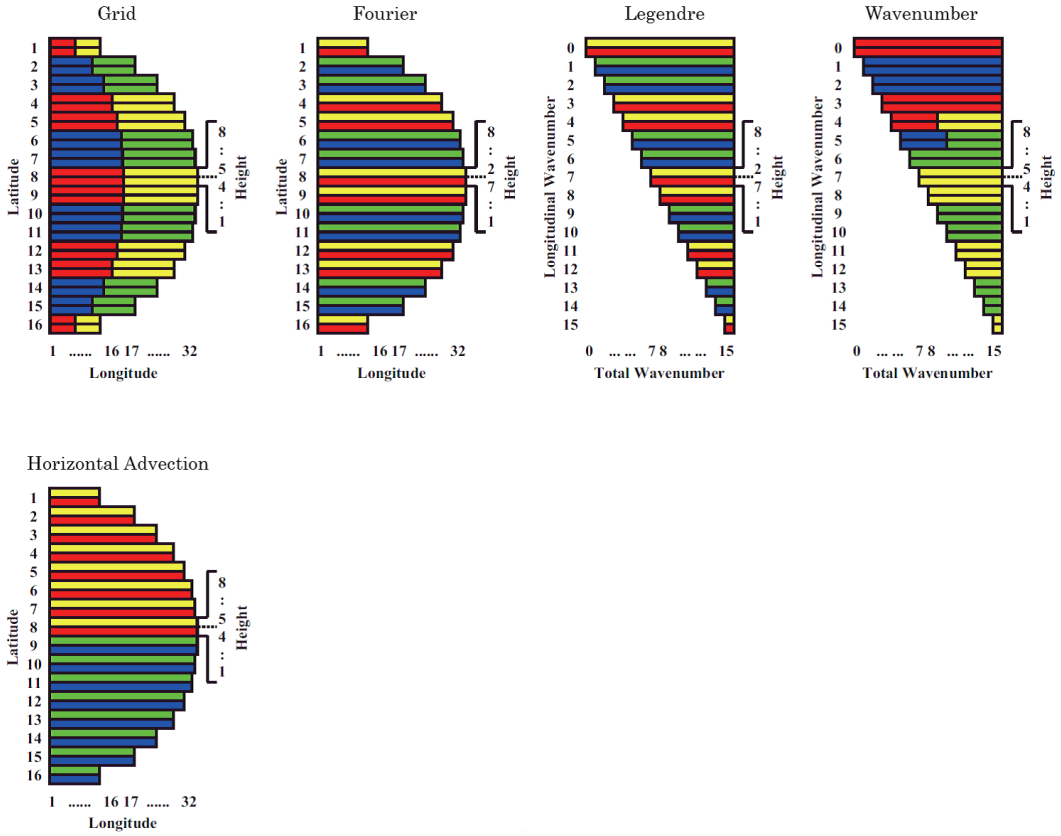

Figure 3.2.3: Schematic design of the parallelization. The number of processes used is assumed to be 4 in this example. Colors in the figure represent the rank for the computation in that area; red is rank 0, yellow is rank 1, blue is rank 2 and green is rank 3.

3.2.13 Forecast Performance

Figure 3.2.4 shows Root Mean Square Error (RMSE) for 24, 72 and 120 hours forecast of 500hPa geopotential height against analysis in the northern hemisphere extra-tropics. Dashed lines indicate the monthly means and solid lines represent 13-month running means. Substantial improvements of the forecast performance are seen at the timing of the upgrades of GSM (see Subsection 3.2.1).

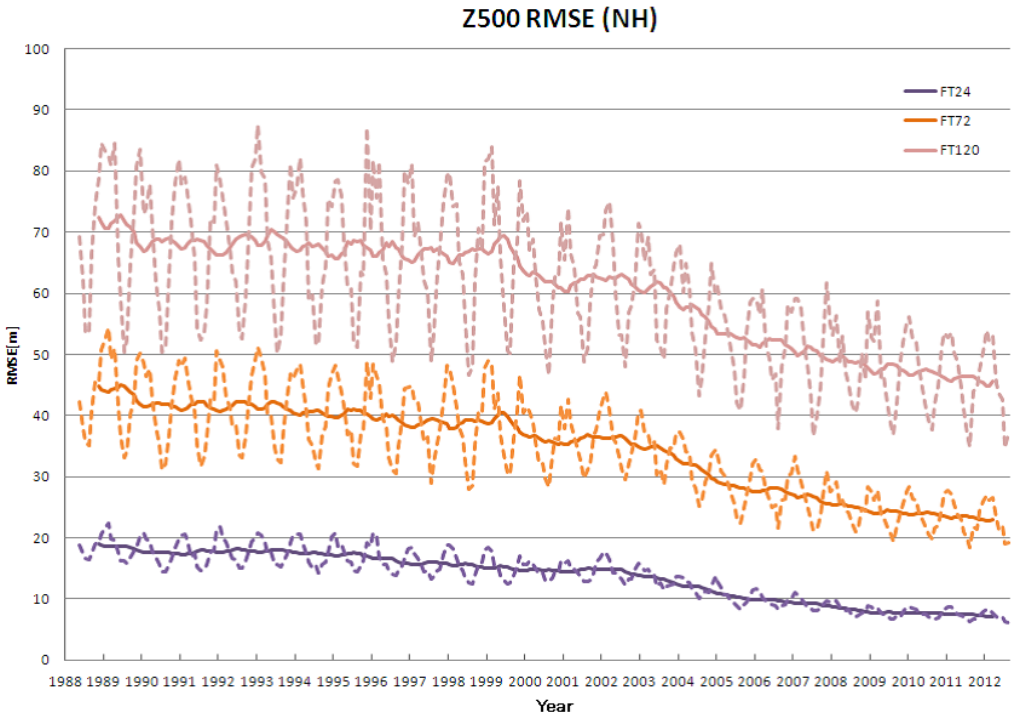

Figure 3.2.4: Root Mean Square Error of GSM 500hPa geopotential height predictions (Z500) against analysis in the northern hemisphere extra-tropics (20°N – 90°N). Dashed lines indicate the monthly means, and solid lines represent 13-month running means.

The predictions of tropical cyclone (TC) track and central pressure are verified against the best track analyzed by the RSMC Tokyo - Typhoon Center in JMA. The mean position error of TC track predictions of GSM in the western North Pacific is shown in Figure 3.2.5. It is found that the mean position error is gradually reduced during the period from 1996 through 2011 corresponding to the improvements of GSM, but with the inter-annual variations of TC occurrences and so on. Figure 3.2.6 shows the bias and Root Mean Square Error (RMSE) of central pressure predictions for 2010 and 2011. The differences of the performance of TC central pressure predictions between 2010 and 2011 appear to be the inter-annual variations.

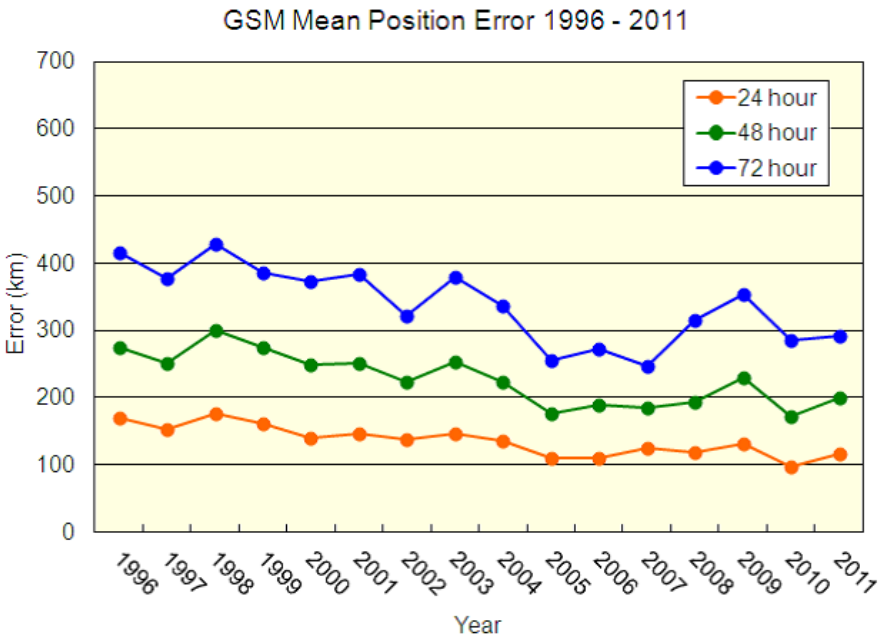

Figure 3.2.5: Mean position error of TC track predictions of GSM in the western North Pacific from 1996 to 2011. The lines represent 24 hours forecast (red), 48 hours forecast (green), and 72 hours forecast (blue), respectively.

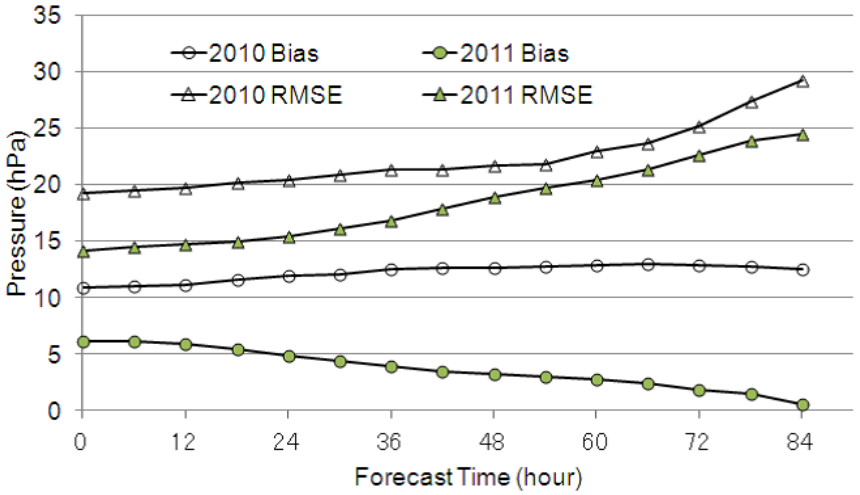

Figure 3.2.6: Bias and RMSE of TC central pressure predictions of GSM in the western North Pacific for 2010 and 2011. The horizontal axis is forecast time, and the vertical axis is TC central pressure. The circles and the triangles indicate bias and RMSE, respectively.

3.3 Ensemble Prediction Systems

3.3.1 Introduction

JMA routinely operates ensemble prediction systems (EPSs) to support forecasting work. As well as covering a wide range of prediction periods from early medium-range to seasonal forecasting, JMA's suite of EPSs supports the issuance of five-day tropical cyclone (TC) track forecasts. Totals of 11, 51 and 50 initial conditions are integrated using a low-resolution version of JMA's Global Spectral Model (GSM) to produce an ensemble of 132-hour forecasts in the Typhoon EPS, 11-day forecasts in the One-week EPS, and 34-day forecasts in the One-month EPS, respectively. In addition, 51 initial conditions are integrated using JMA's coupled Atmosphere-ocean General Circulation Model (CGCM) to produce an ensemble of 120-day forecasts (covering 210 days five times a year) in the Seasonal EPS.

3.3.2 In Operation

3.3.2.1 System Configuration

The specifications of all JMA's operational EPSs are shown in Table 3.3.1.

Table 3.3.1: Specifications of JMA EPSs

		Typhoon EPS	One-week EPS	One-month EPS	Seasonal EPS
Integration	Start of operation	February 2008	March 2001	March 1996	March 2003
	Ensemble size	11	51	50	51
	Initial time	00, 06, 12 and 18 UTC	12 UTC	12 UTC	00 UTC
	Forecast range	132 hours	11 days	17 days on Sundays and Mondays/34 days on Wednesdays and Thursdays	7 months
EPS model	Model type	GSM (an atmospheric general circulation model)			GSM coupled with the Meteorological Research Institute Community Ocean Model (MRI.COM) (a coupled atmosphere-ocean general circulation model)
	Horizontal resolution	TL319[†] reduced Gaussian grid system[‡] roughly equivalent to 0.5625° × 0.5625° (55 km) in latitude and longitude		TL159 reduced Gaussian grid system roughly equivalent to 1.125° × 1.125° (110 km) in latitude and longitude	GSM: TL95 Gaussian grid system roughly equivalent to 1.875° × 1.875° (180 km) MRI.COM: 1.0° × 1.0° in latitude and longitude
	Vertical resolution (model top)	60 levels (0.1 hPa)			GSM: 40 levels (0.4 hPa) MRI.COM: 50 levels
Atmospheric ensemble setting	Initial perturbation generator	Singular vector method		Combination of the breeding of growing modes (BGM) method and the lagged average forecasting (LAF) method (25 BGMs and 2 initial dates with 1-day LAF)	Combination of the BGM method and the LAF method (9 BGMs and 6 initial dates with 5-day LAF)
	Initial perturbed area	Northwestern Pacific (20°N–60°N, 100°E–180°) and the vicinities of up to 3 TCs	Globe	The Northern Hemisphere (20°N–90°N) and the tropics (20°S–20°N)	
	Model ensemble method	Stochastic physics scheme		*Not introduced*	

[†]TL319 is an abbreviation of spectral triangular truncation 319 with a linear grid. The spectral method is described in Subsection 3.2.2.
[‡]The reduced Gaussian grid is described in Subsection 3.2.2.

A low-resolution version of the GSM is used in the Typhoon EPS, the One-week EPS and the One-month EPS. Accordingly, the dynamical framework and physical processes involved are identical to those of the GSM (see Section 3.2) except for the horizontal resolution. Each unperturbed analysis is prepared by interpolating the analyzed field in global analysis (see Section 2.5). The sea surface temperature analysis value (see Section 5.2) is used as a lower boundary condition and prescribed using the persisted anomaly, which means that the anomalies shown by analysis for the initial time are fixed during the time integration. The sea ice concentration analysis value is also prescribed using the persisted anomaly except with the One-month EPS, in which sea ice climatology is adopted as a lower boundary condition.

The CGCM (see Section 3.4) is used in the Seasonal EPS. Unperturbed analysis for this EPS is obtained from the JMA Climate Data Assimilation System (JCDAS) (see Section 2.10) and the ocean data assimilation system (MOVE/MRI.COM-G) (see Section 5.3).

The model's systematic bias is removed from the model results both for One-Month Forecasts and Seasonal Forecasts. The bias is estimated in advance from the mean forecast error obtained from hindcast experiments.

3.3.2.2 Frequency

The frequency of operation differs with each EPS as detailed below.

1. Typhoon EPS

   The Typhoon EPS consists of 11 forecasts run up to four times a day from base times at 00, 06, 12 and 18 UTC with a forecast range of 132 hours. The system is operated when any of the following conditions is satisfied:

   - A TC of tropical storm (TS[1]) intensity or higher is present in the RSMC Tokyo - Typhoon Center's area of responsibility (0°–60°N, 100°E–180°).
   - A TC is expected to reach TS intensity or higher in the area within the next 24 hours.
   - A TC of TS intensity or higher is expected to move into the area within the next 24 hours.

2. One-week EPS

   The One-week EPS consists of 51 forecasts run once a day from a base time at 12 UTC with a forecast range of 11 days.

3. One-month EPS

   The One-month EPS consists of 25 forecasts run four times a week on Sundays, Mondays, Wednesdays and Thursdays from a base time at 12 UTC. The range of the forecasts run on Sundays/Mondays is 17 days, and that of the Wednesday/Thursday forecasts is 34 days. A 50-member lagged ensemble with a forecast range of one month is used for the One-month Forecast issued on Fridays. A 50-member lagged ensemble with a forecast range of two weeks is used for the Early Warning Information on Extreme Weather, which is issued on Tuesdays and Fridays when a high probability of very high or very low seven-day averaged temperatures is predicted in the week starting from five to eight days ahead of the date of announcement.

4. Seasonal EPS

   The Seasonal EPS consists of nine forecasts run every five days from a base time at 00 UTC with a forecast range of seven months. A 51-member lagged ensemble is used for the Three-month Forecast issued every month and for the Warm/Cold Season Forecast issued five times a year (in February, March, April, September and October). The EPS is also used for the El Niño Outlook issued every month.

[1] A TS is defined as a TC with maximum sustained wind speeds of 34 knots or more and less than 48 knots.

Table 3.3.2: SV calculation specifications

	One-week EPS			Typhoon EPS	
Resolution	Spectral triangular truncation 63 (T63), 40 levels				
Norm	Moist total energy				
Target area	Northern Hemisphere (30°N–90°N)	Southern Hemisphere (90°S–30°S)	Tropics (30°S–30°N)	Northwestern Pacific (20°N–60°N, 100°E–180°)	Vicinities of up to 3 TCs in the Typhoon Center's area of responsibility
Physical process	Simplified physics		Full physics	Simplified physics	Full physics
Optimization time	48 hours		24 hours	24 hours	24 hours
Evolved SV	Used			Not used	Not used
Number of perturbations	25			10	10 for each TC

3.3.3 Approach to Ensemble Initial Conditions

Two methods are employed to perturb the initial conditions for the atmosphere. One is the singular vector (SV) method (Buizza and Palmer 1995), which is used for both the One-week EPS and the Typhoon EPS as initial perturbation generators. The other is the breeding of growing modes (BGM) method (Toth and Kalnay 1993, 1997), which is used for both the One-month EPS and the Seasonal EPS. The following subsections describe the specifications of these methods and outline how atmospheric ensemble initial conditions are generated for each EPS.

For the Seasonal EPS, initial perturbations for the ocean are introduced in addition to those for the atmosphere. These values are estimated using the ocean data assimilation system (MOVE/MRI.COM-G) forced with surface heat and momentum fluxes in the atmospheric initial perturbation fields.

3.3.3.1 SV Method

Table 3.3.2 summarizes the specifications of SV calculation for the One-week EPS and the Typhoon EPS. The tangent-linear and adjoint models used for SV computation are lower-resolution versions of those used in 4D-Var (see Section 2.5) until October 2011. The models involve full dynamical core and physical processes including surface fluxes, vertical diffusion, gravity wave drag, large-scale condensation, long-wave radiation and deep cumulus convection. SVs based on tangent-linear and adjoint models incorporating full physical processes are called moist SVs, while those based on models incorporating simplified physical processes involving surface fluxes and vertical diffusion are called dry SVs.

1. SV definition for the One-week EPS

   In the One-week EPS, three targeted areas are used for SV calculation: the Northern Hemisphere (30°N–90°N), the tropics (30°S–30°N) and the Southern Hemisphere (90°S–30°S). Dry SVs with a 48-hour optimization time are computed for the Northern Hemisphere and the Southern Hemisphere, and moist SVs with a 24-hour optimization time are computed for the tropics.

2. Norm of SV calculation for the One-week EPS

   In the One-week EPS, the norm for evaluating the growth rate of dry and moist SVs is based on a total energy norm that includes a specific humidity term (Barkmeijer *et al.* 2001):

$$
\begin{aligned}
(x, Ey) \quad = \quad & \frac{1}{2}\int_0^1 \int_S \left[\nabla\triangle^{-1}\zeta_x \cdot \nabla\triangle^{-1}\zeta_y + \nabla\triangle^{-1}D_x \cdot \nabla\triangle^{-1}D_y + \frac{c_p}{T_r}T_x T_y \right. \\
& \left. + w_q \frac{L_c^2}{c_p T_r} q_x q_y \right] dS \left(\frac{\partial p}{\partial \eta}\right) d\eta + \frac{1}{2}\int_S \left[\frac{R_d T_r}{P_r} P_x P_y \right] dS . \qquad (3.3.1)
\end{aligned}
$$

   Here, ζ_x, D_x, T_x, q_x and P_x are the vorticity, divergence, temperature, specific humidity and surface pressure components of state vector x respectively, and (x, Ey) is an inner product of state vectors x and

y with a norm operator E. c_p is the specific heat of dry air at a constant pressure, L_c is the latent heat of condensation, and R_d is the gas constant for dry air. T_r = 300 K is a reference temperature, P_r = 800 hPa is a reference pressure, and w_q is a constant (here 0.04). $\int dS$ is the horizontal integration for the whole globe, and $\int \left(\frac{\partial p}{\partial \eta}\right) d\eta$ gives the vertical integration from the surface to the model top. In addition, the norm at the initial time is vertically integrated with a weight that depends on the model level; the kinetic energy term and the available potential energy term are multiplied by a factor of 10^3 above the 35th model level, and the specific humidity term is multiplied by a factor of 10^3 above the 9th model level. When the surface pressure is 1,000 hPa, the 35th and 9th model levels correspond to about 10 and 750 hPa, respectively. This suppresses initial perturbation around the model top and confines initial specific humidity perturbation in the lower troposphere.

3. Generation of initial perturbations for the One-week EPS

   The initial conditions of 50 perturbed members are given by adding and subtracting 25 initial perturbations to unperturbed analysis. The initial perturbations are linear combinations of SVs (initial SVs) and evolved SVs. These evolved SVs are calculated by linearly growing previous initial SVs (with an initial time earlier than the current one by an amount equivalent to the optimization time) to the current initial time. A total of 25 initial SVs are created for each targeted area. In this creation procedure, SVs with extremely high growth rates (which will not grow sufficiently in a nonlinear model) and SVs with a high level of similarity to others can be eliminated. Here too, 25 evolved SVs are created for each targeted area. Before the initial and evolved SVs are combined, the evolved ones are approximately orthogonalized with initial SVs and other evolved SVs, and are normalized to a size twice that of the initial SVs. The 25 combined SVs are transformed in a variance minimum rotation (Yamaguchi *et al.* 2009) to generate 25 initial perturbations for each targeted area. The perturbations for the Northern Hemisphere and the Southern Hemisphere are scaled so that their amplitudes of temperature at the 15th model level (or the 6th model level for the tropics) inside the targeted area become 0.3 K. When the surface pressure is 1,000 hPa, the 15th and 6th model levels correspond to about 500 and 850 hPa, respectively. Global perturbations representing linear combinations of the perturbations for the three targeted areas are used as initial perturbations for perturbed members.

4. SV definition for the Typhoon EPS

   Two SV calculations are introduced into the system to efficiently capture the uncertainty of TC track forecasts. One produces dry SVs with a spatial target area fixed on the Northwestern Pacific (20°N–60°N, 100°E–180°), and the other produces moist SVs whose spatial target area can be moved within a 750-km radius of a predicted TC's position in one-day forecasting. Up to three movable areas can be configured for different TCs at one initial time. If more than three TCs are present in the area of responsibility, three are selected in the order of concern as prioritized by the RSMC Tokyo - Typhoon Center.

5. Norm of SV calculation for the Typhoon EPS

   For the Typhoon EPS, the total energy norm is defined by:

$$
\begin{aligned}
(x, Ey) \quad = \quad & \frac{1}{2} \int_0^1 \int_S \left[\nabla\triangle^{-1}\zeta_x \cdot \nabla\triangle^{-1}\zeta_y + \nabla\triangle^{-1}D_x \cdot \nabla\triangle^{-1}D_y + \frac{g\,(\Gamma - \Gamma_d)^{-1}}{T_r} T_x T_y \right. \\
& \left. + w_q \frac{L_c^2}{c_p T_r} q_x q_y \right] dS \left(\frac{\partial p}{\partial \eta}\right) d\eta + \frac{1}{2} \int_S \left[\frac{R_d T_r}{P_r} P_x P_y \right] dS. \qquad (3.3.2)
\end{aligned}
$$

   Here, g is gravity acceleration, Γ_d is the dry adiabatic temperature lapse rate and $\Gamma = \frac{2}{3}\Gamma_d$ is a constant referential temperature lapse rate. Here, w_q = 1. In Eq. (3.3.2), the vertical integration of the kinetic energy term and the available potential energy term is limited to the 26th model level, and the specific humidity term can be limited to the 15th model level. When the surface pressure is 1,000 hPa, the 26th and 15th model levels correspond to about 100 and 500 hPa, respectively. Otherwise, as reported

by Barkmeijer *et al.* (2001), SVs would have a shallow vertical structure in the upper troposphere or a large specific humidity contribution in the upper troposphere where the amount of specific humidity is relatively small. As such SVs have little influence on TC track forecasts, the limit on vertical integration is set as detailed in Eq. (3.3.2).

6. Generation of initial perturbations for the Typhoon EPS

   Initial perturbations are determined by combining dry and moist SVs linearly. Each SV calculation can produce up to 10 SVs depending on how accurate SV estimates are, which makes the maximum number of SVs 40 (i.e., 10 dry SVs for the fixed area and 30 moist SVs for 3 movable areas) for each forecast event. Before the binding coefficients are determined, SVs with structures similar to those of others are eliminated. When the value of the inner product of any two SVs is 0.5 or more, one of them is eliminated from the group of SV candidates to be used for initial perturbations. After this process, the coefficients are determined based on variance minimum rotation, which creates a wide spread in the spatial distributions of the perturbations. If no SVs are eliminated, the number of independent initial perturbations is the same as the number of SVs computed. Five perturbations are randomly selected from the initial perturbations and added to/subtracted from the analysis field to produce 10 perturbed initial conditions. The amplitude of the perturbations is normalized using the moist total energy value.

3.3.3.2 BGM Method

The processes of the BGM method with separate estimation for the Northern Hemisphere (20°N–90°N) and the tropics (20°S–20°N), are described here. First, perturbed and unperturbed initial conditions are integrated up to 12 hours for the Northern Hemisphere and 24 hours for the tropics. Then, the difference between the two fields is normalized so that the area-averaged root mean square of the difference for 500-hPa height over the Northern Hemisphere and 200-hPa velocity potential for the tropics are equal to 14.5 and 20.0 % of the climatological variance, respectively. Third, the normalized perturbations are orthogonalized to each other and added to the analysis to create the next set of initial perturbations. In both the One-month EPS and the Seasonal EPS, the Northern Hemisphere and tropical initial perturbations are combined and added to/subtracted from the analysis.

3.3.4 Model Ensemble Approach

The stochastic physics scheme (Buizza *et al.* 1999) is used in the One-week EPS and the Typhoon EPS in consideration of model uncertainties associated with physical parameterizations. This scheme represents random errors associated with parameterized physical processes as follows:

$$\frac{\partial \mathbf{x}}{\partial t} = F(\mathbf{x}) + \alpha(\lambda, \phi, t)P(\mathbf{x}). \tag{3.3.3}$$

Here t, $\mathbf{x}$, $F(\mathbf{x})$ and $P(\mathbf{x})$ are the time, the set of forecast variables, the total tendency of the forecast model and the tendency of the parameterized physical processes, respectively. λ and ϕ show latitude and longitude; $\alpha(\lambda, \phi, t)$ is a random variable described in a spectral space (Berner *et al.* 2009) featuring spatial correlation with a total wave number of 20 and a time correlation of six hours. The average of α is set to zero. Its value is limited to the range from -0.7 to 0.7 to avoid excess perturbation, and its value in the stratosphere is also set to zero.

3.3.5 Performance

The performance of each EPS product is described below.

3.3.5.1 One-week EPS

The results of verification regarding One-week EPS output are published in the annual WMO Technical Progress Report on the Global Data-processing and Forecasting System (GDPFS). Monthly verification data

are also published on the website of the WMO/CBS Lead Centre for EPS Verification[2].

Figure 3.3.1 shows root mean square errors (RMSEs) for the 500-hPa geopotential height ensemble mean forecast against analysis for the Northern Hemisphere (NH; 20°N–90°N) averaged for the periods of DJF (December/January/February) of 2011/2012 and JJA (June/July/August) of 2012. Figure 3.3.2 compares the monthly-averaged RMSEs of the ensemble means, unperturbed members and the spread of the ensemble. A higher level of skill is observed for ensemble means than for deterministic forecasts, especially for longer lead times. Figure 3.3.3 shows the Brier skill score (BSS) for 500-hPa geopotential height probabilistic forecasts in the NH. The reference forecast for the skill score is the climatological probability given by the frequency derived from the analysis fields for each month. Since the start of its operation, the performance of the One-week EPS has been improved year after year in ensemble mean forecasts and probabilistic forecasts.

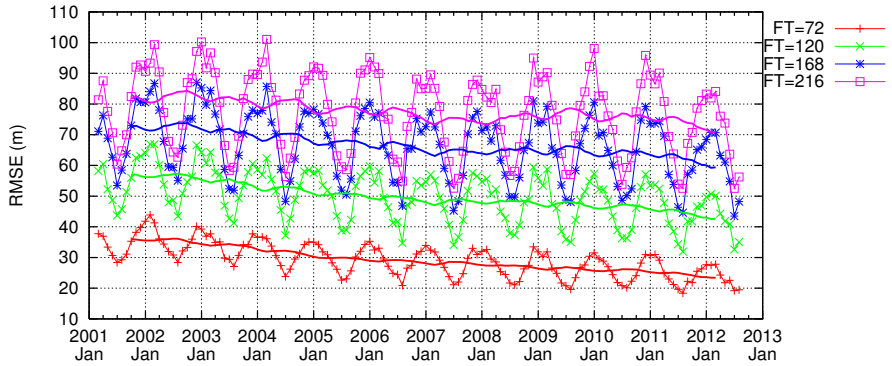

Figure 3.3.1: Time-series representation of ensemble mean scores for JMA's One-week EPS (where the score is the monthly-averaged RMSE of the ensemble mean) for Northern Hemisphere (20°N–90°N) 500-hPa geopotential height forecasts with lead times of 72, 120, 168 and 216 hours from March 2001 to August 2012. The thick lines show 13-month running means.

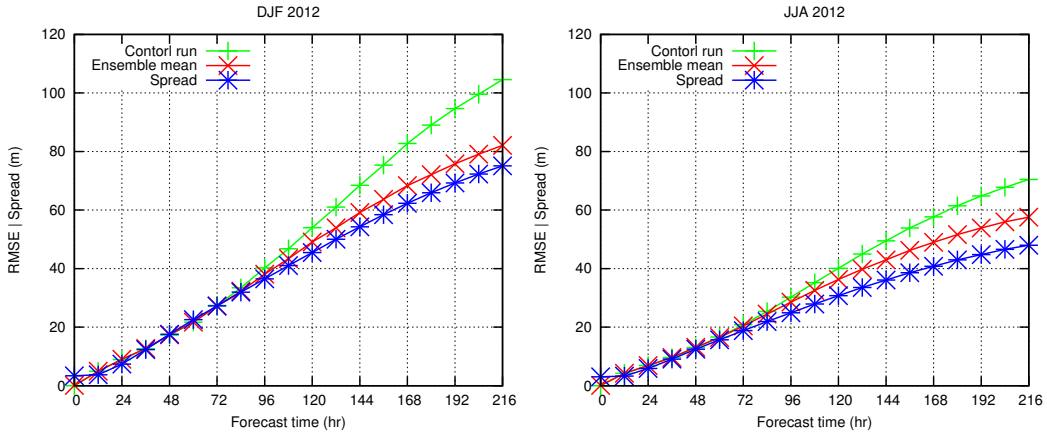

Figure 3.3.2: RMSEs for Northern Hemisphere (20°N–90°N) 500-hPa geopotential height forecasts of the ensemble mean (red) and unperturbed members (green) for DJF and JJA 2012 from JMA's One-week EPS. The spread of the ensemble (blue) is also shown.

[2] http://epsv.kishou.go.jp/EPSv/

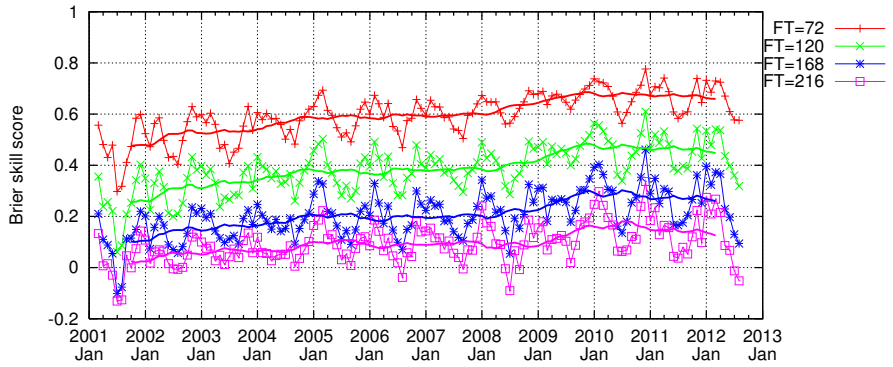

Figure 3.3.3: Time-series representation of Brier skill score for probabilistic forecasts of 500-hPa geopotential height negative anomalies with magnitudes less than one climatological standard deviation over the Northern Hemisphere (20°N–90°N) for lead times of 72 (red), 120 (green), 168 (blue) and 216 (violet) hours from March 2001 to August 2012 from JMA's One-week EPS. The thick lines show 13-month running means.

3.3.5.2 Typhoon EPS

The results of verification regarding Typhoon EPS output are published in the Annual Report on Activities of the RSMC Tokyo - Typhoon Center [3].

Ensemble TC tracks derived from the Typhoon EPS enable JMA forecasters to integrate TC track forecast uncertainty into their operational processes. Strike probability data, which indicate the chances of a TC center passing within 120 km of a grid point, are routinely produced as a form of probabilistic guidance. Figure 3.3.4 shows the reliability of typhoon strike probability data during next five days. The curves for the previous three-year period indicate similar levels of performance. However, the 2008 curve shows relatively high departure from the diagonal, especially in low-probability areas where the forecast frequency is quite large.

3.3.5.3 One-month EPS

The results of prediction skill evaluation based on hindcast experiments and real-time forecasts are available on the Tokyo Climate Center website [4]. To verify performance, hindcast experiments covering a period of 31 years (1979–2009) were conducted under conditions identical to those of the operational system, except with an ensemble size of 5 instead of 50. The skill of ensemble mean forecasts was evaluated using the Anomaly Correlation Coefficient (ACC) and the RMSE for selected areas with respect to several physical variables. Probabilistic forecast skill was also evaluated based on the BSS, the Reliability Skill Score (Brel), the Resolution Skill Score (Bres) and the Relative Operating Characteristics (ROC).

Figure 3.3.5 shows the time-series representation of the NH 500-hPa geopotential height ACC for ensemble mean forecasts averaged over 28 days (the running mean of 52 forecasts) based on operational forecasting conducted from 1996 to 2011. It can be seen that skill in the NH shows a rising trend from 1999 onward. Although ensemble mean skill is sensitive to initial conditions, it is almost consistently higher than that of persistence forecasts. Table 3.3.3 shows ROC areas of 2-m temperature (T2m) and precipitation anomalies based on the outcomes of hindcast experiments covering a 31-year period (1979–2009), and indicates that skill for the tropics is higher than that for the extratropics.

3.3.5.4 Seasonal EPS

The results of prediction skill evaluation based on the WMO Standard Verification System for long-range forecasts (SVS-LRF; WMO 2010b) are available on the Tokyo Climate Center website. To verify performance,

[3] http://www.jma.go.jp/jma/jma-eng/jma-center/rsmc-hp-pub-eg/annualreport.html
[4] http://ds.data.jma.go.jp/tcc/tcc/index.html

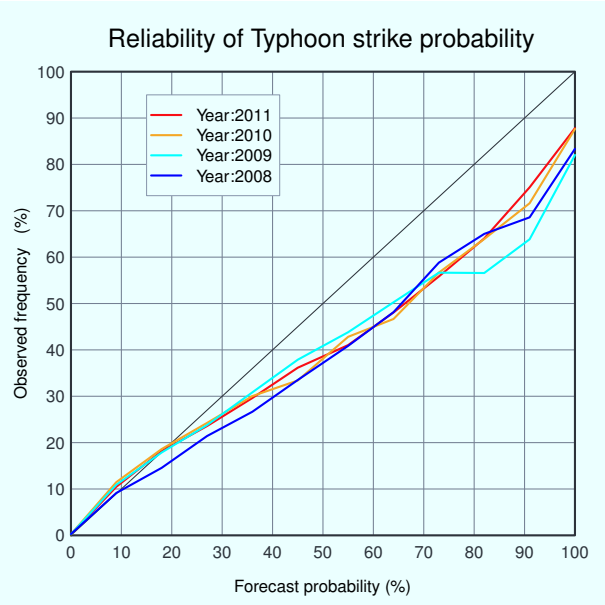

Figure 3.3.4: Reliability diagram for probabilistic verification of typhoon position forecasts as derived from the Typhoon EPS over a four-year period. The target years for verification are 2008 (blue), 2009 (sky blue), 2010 (orange) and 2011 (red). RSMC Tropical Cyclone Best Track information is used as observation data.

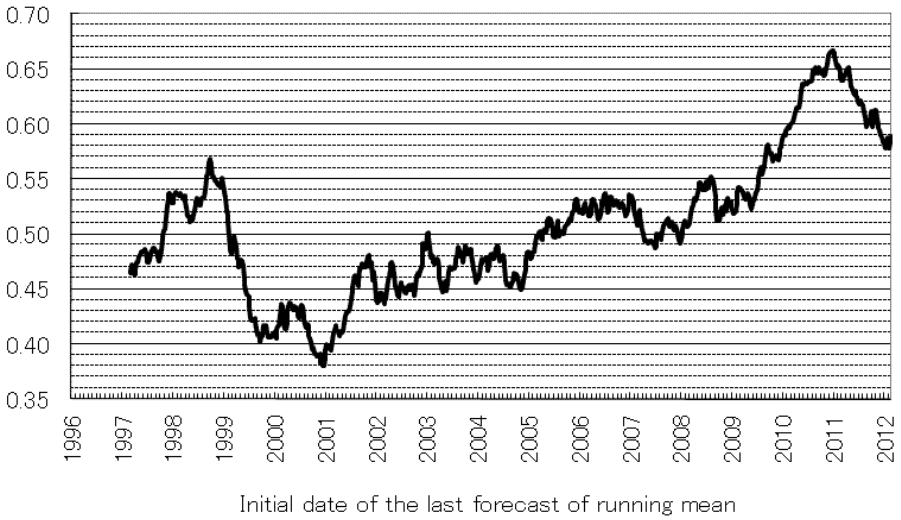

Figure 3.3.5: Time-series representation of the Northern Hemisphere (NH; 20°N–90°N) 500-hPa geopotential height anomaly correlation coefficient in ensemble mean forecasts averaged over 28 days (the running mean of 52 forecasts) based on operational forecasting conducted from 1996 to 2011

Table 3.3.3: ROC areas of 28-day mean 2-m temperature (T2m) and precipitation anomaly prediction for positive anomaly events (upper tercile) in the Northern Hemisphere (NH; 20°N–90°N), the tropics (20°S–20°N), and the Southern Hemisphere (SH; 90°S–20°S) based on hindcast experiments covering a period of 31 years (1979–2009). The figures in the table are multiplied by 100. The initial dates are 31 December for January and 30 June for July.

T2m	NH	Tropics	SH
January(Initial:12/31)	75.9	76.4	69.8
July(Initial:6/30)	71.6	74.3	68.8

Precipitation	NH	Tropics	SH
January(Initial:12/31)	63.0	64.4	56.1
July(Initial:6/30)	58.8	64.0	57.3

hindcast experiments covering a period of 30 years (1979–2008) were conducted under conditions identical to those of the operational system, except with an ensemble size of 10 instead of 51. Figure 3.3.6 shows the ACC between ensemble mean forecasts and observations for SSTs in the NINO3 (5°S–5°N, 150°W–90°W), NINO.WEST (0°–15°N, 130°E–150°E) and IOBW (20°S–20°N, 40°E–100°E) regions. SSTs in these areas are predicted well with the CGCM. Although not shown in Figure 3.3.6, the skill for NINO3.4 SSTs is comparable to those of major state-of-the-art seasonal forecast models (Jin *et al.* 2008). ROC areas of T2m anomalies and precipitation anomalies are shown in Table 3.3.4. The level of skill for T2m is better than that of precipitation in all regions, and skill in the tropics is better than that in the NH and the Southern Hemisphere (SH; 90°S–20°S). These results are consistent with those obtained from studies on the predictability of seasonal mean fields (e.g., Sugi et al. 1997).

Table 3.3.4: ROC areas of three-month means (JJA and DJF) 2-m temperature (T2m) and precipitation anomaly prediction for positive anomaly events (upper tercile) in the Northern Hemisphere (NH; 20°N–90°N), the tropics (20°S–20°N), and the Southern Hemisphere (SH; 90°S–20°S) based on hindcast experiments covering a period of 30 years (1979–2008). The figures in the table are multiplied by 100. The initial dates are 1 May for JJA and 28 October for DJF.

T2m	NH	Tropics	SH
JJA(Initial:5/1)	63.8	73.9	61.3
DJF(Initial:10/28)	63.5	77.1	61.2

Precipitation	NH	Tropics	SH
JJA(Initial:5/1)	52.3	64.9	55.6
DJF(Initial:10/28)	56.0	62.7	53.8

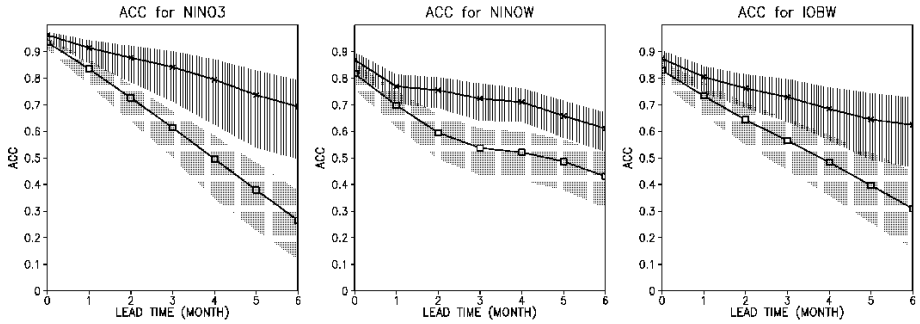

Figure 3.3.6: Anomaly correlations for SSTs over (a) NINO3 (5°S–5°N, 150°W–90°W), (b) NINO.WEST (0°–15°N, 130°E–150°E) and (c) IOBW (20°S–20°N, 40°E–100°E). Crosses indicate scores for CGCM predictions, and squares indicate those for anomaly persistent predictions. Shading indicates a 90% confidence interval as estimated using the bootstrap method.

3.4 Coupled Atmosphere-Ocean General Circulation Model

3.4.1 Model Description

Since July 1998, JMA has used atmosphere-ocean coupled general circulation models (CGCMs) to predict the phenomenon of El Niño-Southern Oscillation (ENSO). The current CGCM (JMA/MRI-CGCM) introduced in February 2008 was developed in collaboration with the Meteorological Research Institute (MRI). In February 2010, the ENSO Prediction System and the Seasonal Prediction System were integrated, and CGCM products have since been commonly used for operational seasonal forecasting and ENSO prediction.

The model consists of atmospheric and oceanic components and a coupler. The atmospheric component is based on a low-resolution version of JMA's Global Spectral Model (GSM0603; JMA 2007), which has a horizontal resolution of TL95 (triangular truncation at total wavenumber 95 with a linear grid) corresponding to 180-km grid spacing and 40 levels in the vertical direction with its top at 0.4 hPa (corresponding to approximately 55 km).

Most physical parameterization schemes relating to atmospheric components remain unchanged unless schemes have resolution dependency or shortcomings in coupled simulations. Several modifications have been made so that the CGCM can better represent atmospheric and oceanic states. Cumulus convection and cloud schemes can be tuned to improve the climatology of precipitation and radiative budgets, and gravity wave drag parameterization can be adjusted to the resolution of the CGCM, whose specifications are summarized in Table 3.4.1.

The effects of greenhouse gas forcing are incorporated via the setting of an increasing atmospheric carbon dioxide (CO_2) trend in the model. In the hindcast covering the period from 1979 to 2007 (Section 3.3), global average CO_2 concentrations during integration are specified as observed values on initial dates based on NASA/Goddard Institute for Space Studies (GISS) data (Hansen and Sato 2004). In hindcasts and real-time forecasts covering the period from 2007 onward, the observed CO_2 trend based on WMO/World Data Centre for Greenhouse Gases (WDCGC) data is added to the 2007 CO_2 value, and the CO_2 concentration specified is fixed throughout each integration. This treatment and the warming trend in ocean analysis contribute to better replication of the global warming trend in seasonal forecasts (e.g., Doblas-Reyes *et al.* 2006).

The oceanic component is the Meteorological Research Institute Community Ocean Model (MRI.COM-G; Tsujino *et al.* 2010), which is a primitive equation ocean general circulation type. The model has a horizontal resolution of $1^\circ \times 1^\circ$ in the extratropics with meridional refinement near the equator to 0.3°, and 50 vertical layers. Sophisticated model parameterizations are adopted, including a vertical diffusion scheme incorporating sea surface wave breaking effects (Noh and Kim 1999) and an isopycnal mixing scheme (Gent and McWilliams 1990). More details are given in Chapter 5.

The atmospheric and oceanic components are coupled every hour with the coupler. These components communicate ocean surface properties such as SSTs, sensible and latent heat fluxes, momentum flux, radiation flux and fresh water flux. Adjustment is applied to heat and momentum fluxes to reduce mean biases.

Atmospheric initial conditions are provided from JRA-25 reanalysis data (Onogi *et al.* 2007) and related real-time analysis from JCDAS (Section 2.10). Oceanic initial conditions are given by an ocean data assimilation system (MOVE/MRI.COM-G, Section 5.3), while land initial conditions are climatologies derived from offline land model simulations forced by ERA-15 reanalysis (Gibson *et al.* 1997). Ensemble perturbations are produced using a combination of the BGM method and the LAF technique. Further details are provided in Section 3.3.

3.5 Meso-Scale Model (JMA-MSM1206)

3.5.1 Introduction

The meso-scale numerical prediction system has been operational since March 2001 to provide information for disaster prevention and aviation safety. In the beginning of its operation, the Meso-Scale Model (MSM) was a hydrostatic spectral model which was also used as a coarser operational model in different configuration. The horizontal resolution of the MSM was 10km and the 40 vertical layers were placed at that time. The MSM produced 18-hour forecasts every 6 hours at 00, 06, 12, 18UTC.

Table 3.4.1: Specifications of the Coupled General Circulation Model

Atmospheric component	Basic equation	Primitive
	Domain	Global
	Resolution	TL95, 40 vertical levels
	Cumulus convection	Prognostic Arakawa-Schubert scheme
	Land surface process	Simple Biosphere (SiB)
	Planetary boundary layer	Mellor & Yamada Level 2
Oceanic component	Basic equation	Primitive, free surface
	Domain	Global (75°S – 75°N)
	Resolution	1°(lon) × 1°(lat), (1°(lon) × 0.3°(lat) near the equator), 50 vertical levels
	Vertical diffusion	Noh and Kim (1999)
Coupling	Frequency	Every hour
	Flux correction	For momentum and heat flux

In September 2004, the hydrostatic spectral model was replaced with a nonhydrostatic grid model. The new MSM employed full-compressible elastic equations including a map factor. The general configurations of the system such as resolution, forecast time, forecast frequency and so on, were kept almost the same to those of the previous system with the hydrostatic model.

In March 2006, simultaneously with installing a new supercomputer system, the resolutions and operation frequency of the MSM were enhanced. The new model with the 5-km horizontal grid spacing and 50 vertical layers produced 15-hour forecasts every 3 hours at 00, 03, 06, 09, 12, 15, 18, 21UTC.

Furthermore, the forecast period was extended to 33 hours four times per day out of the eight-time operations in May 2007. The extension of the forecast period made it possible for the MSM to provide 1-day ahead useful information associated to disaster prevention and aviation operations.

Accompanied with the upgrades of the system configurations such as horizontal and vertical resolution, forecast period, and update frequency, various physical processes were also refined. The improvements contributed to considerable part of the steady progress in accuracy of the forecasts, as shown in Subsection 3.5.11.

3.5.2 General Configurations

The current MSM has been operated 8 times a day and providing 15-hour forecasts at 00, 06, 12, 18 UTC, and 33-hour forecasts at 03, 09, 15, 21UTC. Its forecast domain is a rectangular flat area of 3600km by 2880km covering the Japan and its surroundings with the grid spacing of 5km, which is identical to the domain of the the 4D-Var Meso-scale Analysis (MA; see Section 2.6) as shown in Figure 2.6.2. The rectangular plane is obtained by the Lambert conformal conic map projection of the Earth sphere with the scale factor (map factor) introduced to correct the expanded or shrank distance on the plane through the projection from the sphere.

A hybrid terrain following coordinate is adopted as the vertical coordinate to reduce influences of topography as the height increases (Subsection 3.5.3). The lowest atmospheric layer is placed at the height of 20m above the surface, and the model top is set to 21,801m with 50 layers whose intervals vary linearly from 40m at the bottom to 904m at the top.

A forecast model of the MSM is the JMA nonhydrostatic model (JMA-NHM; Saito *et al.* 2006, 2007). The prognostic variables are horizontal and vertical momentum, potential temperature, pressure, mixing ratios of water vapor and hydrometeors (cloud water, cloud ice, rain, snow and graupel), number concentration of cloud ice, ground temperatures, soil water and four of the second order moments of the turbulent fluctuations (including the turbulent kinetic energy). The model is operated with 20-second time step.

Initial conditions for the model are generated by the MA, and lateral boundary conditions of the model come from forecasts produced by the GSM (Section 3.2). When the operations of the GSM finish and newer forecasts are available, the boundary conditions are updated. The MSM operations initialized with analysis at 03, 09, 15, 21UTC switch the boundary conditions to newer ones (GSM forecasts initialized at 00, 06, 12, 18UTC, respectively) and produce longer period (33 hours) forecasts taking advantage of the new boundary

conditions, while the ones initialized at 00, 06, 12, 18UTC use the same boundary conditions as the previous operation (at 21, 03, 09, 15UTC, respectively) and provide only shorter period (15 hours) forecasts.

The model terrain is set relying on the GTOPO30 data set, which is a global digital elevation model with a horizontal grid spacing of 30 arc seconds and developed by U.S. Geological Survey's EROS Data Center (EDC). In order to avoid computational instability related to steep slopes in the terrain, the terrain is smoothed so that the valid resolution of the terrain adopted in the model is 1.5 times as coarse as the resolution of the model itself.

The Global Land Cover Characteristics (GLCC) data set, again provided by EDC, helps to determine the land-sea attribute of each grid in the model. A grid with the sea fraction over 0.5 is supposed to be located on the sea. The sea fraction on each grid in the model is calculated based on the GLCC data set.

Parameters characterizing surface such as heat capacity, thermal conductivity, albedo, initial values of soil moisture and roughness are decided based on land use described by the GLCC data set as well. The National Land Numerical Information developed by the National-Land Information Office of Japan is also referred to set the parameters over the Japan.

Grids on land are further classified in terms of existence of snow. Similarly, grids on the sea can be covered by ice. It means that there are totally four categories of the surface types: land, land with snow covered, sea, sea with ice covered. Snow covered areas are analyzed with a 5-km horizontal grid spacing using the snow depth data of the Global snow depth analysis (see Section 2.8) and observations obtained through the domestic SYNOP and Automated Meteorological Data Acquisition System (AMeDAS). The snow depth given by the Global snow depth analysis is modified with the denser and frequent domestic observations assuming 60-km correlation radius in the analysis. If the snow depth is greater than 5cm, a corresponding grid is classified to be the land with snow covered. Ice covered areas are identified from the sea ice analysis conducted by the JMA. Over grids with snow or ice covered, surface parameters previously determined based on the GLCC data are modified with the predetermined values.

3.5.3 Dynamics

3.5.3.1 Basic Equations

The governing equations used in the MSM consist of non-hydrostatic, fully compressible equations on a spherical curvilinear orthogonal and a hybrid terrain-following coordinate with the shallow assumption. Details of the derivations of these equations are given in Saito *et al.* (2006).

1. Flux form momentum equations

   The equations of motion are described in the flux form:

$$\frac{\partial U}{\partial t} + \frac{m_1}{m_2}\left(\frac{\partial P}{\partial \hat{x}} + \frac{\partial G^{13} P}{\partial \hat{z}}\right) = -\mathrm{ADV}U + \mathrm{R}U, \tag{3.5.1}$$

$$\mathrm{ADV}U = m_1\left(\frac{\partial Uu}{\partial \hat{x}} + \frac{\partial Vu}{\partial \hat{y}}\right) + \frac{m_3}{m_2}\frac{\partial \hat{W}u}{\partial \hat{z}} - \frac{U}{\rho G^{1/2}}\mathrm{PRC}, \tag{3.5.2}$$

$$\mathrm{R}U = \frac{m_1}{m_2} f_3 V - V\left(v\frac{m_1^2}{m_2^2}\frac{\partial m_2}{\partial \hat{x}} - u\frac{\partial m_1}{\partial \hat{y}}\right) + \mathrm{DIF}.U, \tag{3.5.3}$$

$$\frac{\partial V}{\partial t} + \frac{m_1}{m_2}\left(\frac{\partial P}{\partial \hat{y}} + \frac{\partial G^{23} P}{\partial \hat{z}}\right) = -\mathrm{ADV}V + \mathrm{R}V, \tag{3.5.4}$$

$$\mathrm{ADV}V = m_2\left(\frac{\partial Uv}{\partial \hat{x}} + \frac{\partial Vv}{\partial \hat{y}}\right) + \frac{m_3}{m_v}\frac{\partial \hat{W}v}{\partial \hat{z}} - \frac{V}{\rho G^{1/2}}\mathrm{PRC}, \tag{3.5.5}$$

$$\mathrm{R}V = -\frac{m_2}{m_1} f_3 U - U\left(u\frac{m_2^2}{m_1^2}\frac{\partial m_1}{\partial \hat{y}} - v\frac{\partial m_2}{\partial \hat{x}}\right) + \mathrm{DIF}.V, \tag{3.5.6}$$

$$\frac{\partial W}{\partial t} + \frac{1}{m_3}\frac{\partial}{\partial \hat{z}}\left(\frac{P}{G^{1/2}}\right) + \sigma\frac{gP}{m_3 C_m^2} = \frac{1}{m_3}\mathrm{BUOY} - \mathrm{ADV}W + \mathrm{R}W, \tag{3.5.7}$$

$$\mathrm{BUOY} = \sigma\frac{\rho G^{1/2}\theta'_m}{\theta_m}g - (1-\sigma)\rho' G^{1/2} g, \tag{3.5.8}$$

$$\mathrm{ADV}W = \frac{m_1 m_2}{m_3}\left(\frac{\partial Uw}{\partial \hat{x}} + \frac{\partial Vw}{\partial \hat{y}}\right) + \frac{\partial \hat{W}w}{\partial \hat{z}} - \frac{W}{\rho G^{1/2}}\mathrm{PRC}, \tag{3.5.9}$$

$$\mathrm{R}W = \mathrm{DIF}.W, \tag{3.5.10}$$

where

$$U = \frac{\rho G^{1/2}}{m_2}u, \quad V = \frac{\rho G^{1/2}}{m_1}v, \quad W = \frac{\rho G^{1/2}}{m_3}w, \tag{3.5.11}$$

$$\hat{w} = \frac{1}{G^{1/2}}\left(m_1 G^{1/2} G^{13} u + m_2 G^{1/2} G^{23} v + w\right), \tag{3.5.12}$$

$$\hat{W} = \frac{\rho G^{1/2}}{m_3}\hat{w} = \frac{1}{G^{1/2}}\left\{\frac{m_1 m_2}{m_3}\left(G^{1/2} G^{13} U + G^{1/2} G^{23} V\right) + W\right\}, \tag{3.5.13}$$

$$P = p' G^{1/2}. \tag{3.5.14}$$

Here, u, v and w are the velocity components, m_1 and m_2 are the map factors, m_3 is not a map factor in the z direction but a variable introduced for definition of momentum. ADVs denote the advection terms and DIF.s denote the diffusion terms. Symbols p', ρ and g are the pressure perturbation from the hydrostatic state, density and gravity acceleration, respectively. $G^{1/2}$, G^{13} and G^{23} are the metric tensors, f is the Coriolis parameter. A symbol σ is the switching parameter to choose the way to calculate the buoyancy term. In the MSM, σ is set to zero and buoyancy term is calculated directly from the perturbation of density. A symbol θ_m is the mass-virtual potential temperature (Saito 1997) defined as

$$\theta_m \equiv \theta(1 + 0.608 q_v)(1 - q_c - q_i - q_r - q_s - q_g), \tag{3.5.15}$$

where q is the mixing ratios of water substances and subscripts v, c, i, r, s and g represent water vapor, cloud water, cloud ice, rain, snow and graupel, respectively. A symbol θ'_m is the perturbation of θ_m from 300K. $\hat{W}$ and $\hat{w}$ are vertical momentum and vertical velocity along with $\hat{z}$ coordinate defined below Eq. (3.5.21).

In this model, density is defined by the sum of the masses of moist air and water substances per unit volume as

$$\begin{aligned}\rho &\equiv \rho_d + \rho_v + \rho_c + \rho_i + \rho_r + \rho_s + \rho_g \\ &= \rho_a + \rho_c + \rho_i + \rho_r + \rho_s + \rho_g,\end{aligned} \tag{3.5.16}$$

where ρ_a is the density of air.

PRC is the sum of fallout of precipitable water substances defined by

$$\mathrm{PRC} = \frac{\partial}{\partial \hat{z}}\left(\rho_a V_r q_r + \rho_a V_i q_i + \rho_a V_s q_s + \rho_a V_g q_g\right), \tag{3.5.17}$$

where V_r, V_i, V_s, V_g are the terminal fall velocities of rain, cloud ice, snow and graupel, respectively.

The Lambert conformal projection is employed and the map factors m_1 and m_2, and a variable m_3 are given by

$$m_1 = m_2 = m = \left(\frac{\cos\varphi}{\cos\varphi_1}\right)^{c-1}\left(\frac{1+\sin\varphi_1}{1+\sin\varphi}\right)^{c}, \tag{3.5.18}$$

$$m_3 = 1, \tag{3.5.19}$$

where φ is the latitude of a concerned point, $\varphi_1 = 30°$, $\varphi_2 = 60°$ and c is given by

$$c = \ln\left(\frac{\cos\varphi_1}{\cos\varphi_2}\right)\Bigg/\ln\left\{\frac{\tan\left(45° - \frac{\varphi_1}{2}\right)}{\tan\left(45° - \frac{\varphi_2}{2}\right)}\right\}. \tag{3.5.20}$$

The hybrid terrain-following vertical coordinate which is based on the same approach as the η coordinate (Simmons and Burridge 1981) is adopted to reduce influences of topography as the height increases (Ishida 2007). The vertical coordinate $\hat{z}$ is transformed using the following equation:

$$z = \hat{z} + z_s f(\hat{z}), \tag{3.5.21}$$

where z is the actual height and z_s is the surface height. The function $f(\hat{z})$ is given by,

$$f(\hat{z}) = \frac{c\left\{1 - \left(\frac{\hat{z}}{z_T}\right)^n\right\}}{c + \left(\frac{\hat{z}}{z_T}\right)^n}, \quad c = \frac{\left(\frac{z_l + z_h}{2z_T}\right)^n}{1 - 2\left(\frac{z_l + z_h}{2z_T}\right)^n}, \tag{3.5.22}$$

where z_T is the model top height, $z_l = 1000$, $z_h = 11000$ and $n = 3$ in the MSM. The metric tensors $G^{1/2}$, $G^{1/2}G^{13}$, $G^{1/2}G^{23}$ are written as

$$G^{1/2} = \frac{\partial z}{\partial \hat{z}} = 1 + z_s \frac{-nc(1+c)\left(\frac{\hat{z}}{z_T}\right)^{n-1}}{z_T\left\{c + \left(\frac{\hat{z}}{z_T}\right)^n\right\}^2}, \tag{3.5.23}$$

$$G^{1/2}G^{13} = \frac{\partial z}{\partial \hat{z}}\frac{\partial \hat{z}}{\partial x} = -\frac{\partial z}{\partial \hat{x}} = -\frac{c\left\{1 - \left(\frac{\hat{z}}{z_T}\right)^n\right\}}{c + \left(\frac{\hat{z}}{z_T}\right)^n}\frac{\partial z_s}{\partial \hat{x}}, \tag{3.5.24}$$

$$G^{1/2}G^{23} = \frac{\partial z}{\partial \hat{z}}\frac{\partial \hat{z}}{\partial y} = -\frac{\partial z}{\partial \hat{y}} = -\frac{c\left\{1 - \left(\frac{\hat{z}}{z_T}\right)^n\right\}}{c + \left(\frac{\hat{z}}{z_T}\right)^n}\frac{\partial z_s}{\partial \hat{y}}. \tag{3.5.25}$$

2. Prognostic equation of pressure

The pressure equation is described as follows:

$$\frac{\partial P}{\partial t} + C_m^2(\mathrm{DIVT} - \mathrm{PRC} - \mathrm{PFT}) = 0, \tag{3.5.26}$$

$$\mathrm{DIVT} = m_1 m_2\left(\frac{\partial U}{\partial \hat{x}} + \frac{\partial V}{\partial \hat{y}}\right) + m_3\frac{\partial \hat{W}}{\partial \hat{z}}, \tag{3.5.27}$$

$$\mathrm{PFT} = \frac{\rho G^{1/2}}{\theta_m}\frac{\partial \theta_m}{\partial t}. \tag{3.5.28}$$

Here, C_m is the velocity of sound waves defined by

$$C_m^2 = \frac{C_p}{C_v} R\theta_m \left(\frac{p}{p_0}\right)^{\frac{R}{C_p}}. \tag{3.5.29}$$

C_p and C_v are the specific heat of dry air at constant pressure and constant volume, respectively. R is the gas constant for dry air and $p_0 = 1000$ hPa is a reference pressure. DIVT and PFT are the divergence in $\hat{z}$ coordinate and the thermal expansion of air, respectively.

3. Prognostic equation of potential temperature

   The thermodynamic equation is given by,

$$\frac{\partial \theta}{\partial t} = -\mathrm{ADV}\theta + \frac{Q}{C_p \pi} + \mathrm{DIF}.\theta, \tag{3.5.30}$$

$$\mathrm{ADV}\theta = \frac{1}{\rho G^{1/2}}\left\{ m_1 m_2 \left(\frac{\partial U\theta}{\partial \hat{x}} + \frac{\partial V\theta}{\partial \hat{y}}\right) + m_3 \frac{\partial \hat{W}\theta}{\partial \hat{z}} - \theta \mathrm{DIVT}\right\}, \tag{3.5.31}$$

   where Q is the diabatic heating. π is the Exner function defined by

$$\pi = \left(\frac{p}{p_0}\right)^{\frac{R}{C_p}}. \tag{3.5.32}$$

4. Prognostic equation of water substances

   The prognostic equations of mixing ratios of water substances are given by,

$$\frac{\partial q_n}{\partial t} = -\mathrm{ADV}q_n + Q_n + \mathrm{DIF}.q_n, \tag{3.5.33}$$

$$\mathrm{ADV}q_n = \frac{1}{\rho G^{1/2}}\left\{ m_1 m_2 \left(\frac{\partial U q_n}{\partial \hat{x}} + \frac{\partial V q_n}{\partial \hat{y}}\right) + m_3 \frac{\partial \hat{W} q_n}{\partial \hat{z}} - q_n \mathrm{DIVT}\right\}. \tag{3.5.34}$$

5. State equation

   The state equation is

$$\rho = \frac{p_0}{R\theta_m}\left(\frac{p}{p_0}\right)^{\frac{C_v}{C_p}}. \tag{3.5.35}$$

3.5.3.2 Finite Discretization

The grid structures of the model are the Arakawa C type in the horizontal direction and the Lorenz type in the vertical direction. The fourth-order finite difference scheme is employed to calculate horizontal advection terms, while vertical advection is calculated with the second-order scheme. Considering the staggered grid structure, the fourth-order finite difference is described by

$$\left.\frac{\partial \phi}{\partial x}\right|_i = \frac{9}{8}\frac{\phi_{i+1/2} - \phi_{i-1/2}}{\Delta x} - \frac{1}{8}\frac{\phi_{i+1+1/2} - \phi_{i-1-1/2}}{3\Delta x} + \frac{3}{640}(\Delta x)^4 \frac{\partial^5 \phi}{\partial x^5} + O\left[(\Delta x)^6\right]. \tag{3.5.36}$$

For advection of scalar prognostic variables, the fourth-order finite difference in the flux form is given by

$$\left.\frac{\partial U\theta}{\partial x}\right|_i = \frac{9}{8}\frac{(U\bar{\theta})_{i+1/2} - (U\bar{\theta})_{i-1/2}}{\Delta x} - \frac{1}{8}\frac{(U\bar{\theta})_{i+1+1/2} - (U\bar{\theta})_{i-1-1/2}}{3\Delta x}, \tag{3.5.37}$$

where the second-order interpolation process is used to calculate scalar prognostic variables at the vector points currently. For advection of vector variables,

$$\left.\frac{\partial Uu}{\partial x}\right|_{i+1/2} = \frac{9}{8}\frac{(U\bar{u})_{i+1} - (U\bar{u})_i}{\Delta x} - \frac{1}{8}\frac{(U\bar{u})_{i+2} - (U\bar{u})_{i-1}}{3\Delta x}. \tag{3.5.38}$$

The above higher-order schemes are employed with the modified centered difference advection scheme (Kato 1998), which is a kind of flux limiter and acts as a flux correction scheme.

3.5.3.3 Split Explicit (HE-VI) Scheme

For the temporal discritization, the horizontally explicit, and vertically implicit (HE-VI) scheme is employed. Forward time integrations

$$\frac{U^{\tau+\Delta\tau} - U^\tau}{\Delta\tau} + \frac{m_1}{m_2}\left(\frac{\partial P^\tau}{\partial\hat{x}} + \frac{\partial G^{13}P^\tau}{\partial\hat{z}}\right) = -\mathrm{ADV}U + \mathrm{R}U, \tag{3.5.39}$$

$$\frac{V^{\tau+\Delta\tau} - V^\tau}{\Delta\tau} + \frac{m_2}{m_1}\left(\frac{\partial P^\tau}{\partial\hat{y}} + \frac{\partial G^{23}P^\tau}{\partial\hat{z}}\right) = -\mathrm{ADV}V + \mathrm{R}V, \tag{3.5.40}$$

are used for horizontal momentum equations, where $\Delta\tau$ is the short time step. Backward time integration is employed for vertical momentum equation as

$$\frac{\hat{W}^{\tau+\Delta\tau} - \hat{W}^\tau}{\Delta\tau} + \frac{1}{m_3}\frac{\partial}{\partial\hat{z}}\left(\frac{P^\beta}{G^{1/2}}\right) + \frac{gP^\beta}{m_3C_m^2} = \frac{1}{m_3}\mathrm{BUOY} - \mathrm{ADV}W + \mathrm{R}W + (1-\sigma)\frac{gP^\tau}{m_3C_m^2}, \tag{3.5.41}$$

where

$$P^\beta = \frac{1+\beta}{2}P^{\tau+\Delta\tau} + \frac{1-\beta}{2}P^\tau. \tag{3.5.42}$$

The pressure equation is integrated backward as

$$\frac{P^{\tau+\Delta\tau} - P^\tau}{\Delta\tau} + C_m^2\left\{m_1m_2\left(\frac{\partial U^\gamma}{\partial\hat{x}} + \frac{\partial V^\gamma}{\partial\hat{y}}\right) + m_3\frac{\partial\hat{W}^\beta}{\partial\hat{z}} - \mathrm{PRC} - \mathrm{PFT}\right\} = \mathrm{DIF}.P, \tag{3.5.43}$$

where

$$U^\gamma = \frac{1+\gamma}{2}U^{\tau+\Delta\tau} + \frac{1-\gamma}{2}U^\tau, \quad V^\gamma = \frac{1+\gamma}{2}V^{\tau+\Delta\tau} + \frac{1-\gamma}{2}V^\tau, \quad \hat{W}^\beta = \frac{1+\beta}{2}\hat{W}^{\tau+\Delta\tau} + \frac{1-\beta}{2}\hat{W}^\tau. \tag{3.5.44}$$

Here, β and γ are the implicit factor. $\beta = 1$ and $\gamma = 1$ are employed in the MSM.

Eliminating $\hat{W}^\beta$ from the pressure Eq. (3.5.43) using the vertical momentum Eq. (3.5.41), we obtain the one dimensional Helmholtz type equation

$$-\left(\frac{C_m\Delta\tau(1+\beta)}{2}\right)^2\frac{\partial}{\partial\hat{z}}\left(\frac{1}{G^{1/2}}\frac{\partial}{\partial\hat{z}}\left(\frac{P^\beta}{G^{1/2}}\right)\right) - \left(\frac{C_m\Delta\tau(1+\beta)}{2}\right)^2\frac{\partial}{\partial\hat{z}}\left(\frac{gP^\beta}{C_m^2G^{1/2}}\right) + P^\beta$$
$$= \mathrm{FP.HE.INV} + \mathrm{HP.HE.VAR}, \tag{3.5.45}$$

where

$$\mathrm{FP.HE.INV} = C_m^2 \frac{\Delta\tau(1+\beta)}{2}\left(\mathrm{PRC}^t + \mathrm{PFT}^t + \frac{\mathrm{DIF}.P^t}{C_m^2}\right)$$
$$- C_m^2\left(\frac{\Delta\tau(1+\beta)}{2}\right)^2 m_3 \frac{\partial}{\partial\hat{z}}\left\{\frac{1}{G^{1/2}}\left(\frac{1}{m_3}\mathrm{BUOY}^t - (\mathrm{ADV}W^t - \mathrm{R}W^t) + (1-\sigma)\frac{gP^t}{m_3 C_m^2}\right)\right\}, \quad (3.5.46)$$

$$\mathrm{FP.HE.VAR} = P^\tau - C_m^2 \frac{\Delta\tau(1+\beta)}{2}\left\{m_1 m_2\left(\frac{\partial U^\gamma}{\partial\hat{x}} + \frac{\partial V^\gamma}{\partial\hat{y}} + \frac{\partial}{\partial\hat{z}}(G^{13}U^\beta + G^{23}V^\beta)\right) + m_3\frac{\partial}{\partial\hat{z}}\frac{W^\tau}{G^{1/2}}\right\}. \quad (3.5.47)$$

Considering $(\hat{W}^{\tau+\Delta\tau} - \hat{W}^\tau)/\Delta\tau = 0$ at the upper and lower boundary, upper and lower boundary conditions are given by

$$\frac{1}{G^{1/2}}\frac{\partial}{\partial\hat{z}}\left(\frac{P^\beta}{G^{1/2}}\right) + \frac{gP^\beta}{C_m^2 G^{1/2}} = \frac{m_3}{G^{1/2}}\left\{\frac{1}{m_3}\mathrm{BUOY}^t - \mathrm{ADV}W^t + \mathrm{R}W^t + (1-\sigma)\frac{gP^t}{m_3 C_m^2}\right\}. \quad (3.5.48)$$

3.5.3.4 Divergence Damping

An acoustic filter which is based on the idea of Skamarock and Klemp (1992) is implemented to avoid the computational instability by the sound waves. The gradient of the divergence is added to the momentum equations as

$$\mathrm{R}U \rightarrow \mathrm{R}U + \alpha_H \frac{m_1}{m_2}\left(\frac{\partial G^{1/2}\mathrm{DIVT}}{\partial\hat{x}} + \frac{\partial G^{1/2}G^{13}\mathrm{DIVT}}{\partial\hat{z}}\right), \quad (3.5.49)$$

$$\mathrm{R}V \rightarrow \mathrm{R}V + \alpha_H \frac{m_2}{m_1}\left(\frac{\partial G^{1/2}\mathrm{DIVT}}{\partial\hat{y}} + \frac{\partial G^{1/2}G^{23}\mathrm{DIVT}}{\partial\hat{z}}\right), \quad (3.5.50)$$

$$\mathrm{R}W \rightarrow \mathrm{R}W + \alpha_V \frac{1}{m_3}\frac{\partial}{\partial\hat{z}}\frac{\mathrm{DIVT}}{G^{1/2}}, \quad (3.5.51)$$

where

$$\alpha_H = 0.06\,\frac{1}{\Delta t}\min\left[\left(\frac{\Delta x}{m_1}\right)^2, \left(\frac{\Delta y}{m_2}\right)^2\right], \quad (3.5.52)$$

$$\alpha_V = 0.05\frac{1}{\Delta t}\left(G^{1/2}\Delta\hat{z}\right)^2. \quad (3.5.53)$$

3.5.3.5 Time Splitting of Advection and Gravity Waves

To stabilize the integration in cases where environmental wind is considerably strong and strong inversion layer exists, a new time splitting scheme is implemented (Saito *et al.* 2006). In the scheme, the higher-order advection terms with the modified advection scheme are evaluated at the center of the leapfrog time step, and then the lower-order (second-order) components at each short time step are adjusted only in the latter half of the leapfrog time integration scheme,

$$\mathrm{ADV}^* = \mathrm{ADV} - \mathrm{ADVL} + \mathrm{ADVL}^\tau. \quad (3.5.54)$$

Here, ADV and ADVL are the higher-order advection and the lower-order advection component at a leapfrog time step, respectively, while ADVL^τ is the lower-order advection components at each short time step. This adjustment is performed from $(ns-1)/2+1$ to $ns-1$, where ns is the ratio of $2\Delta t$ and $\Delta\tau$ as shown Figure 3.5.1.

Using this adjustment, the equation of $\hat{W}$ is rewritten as

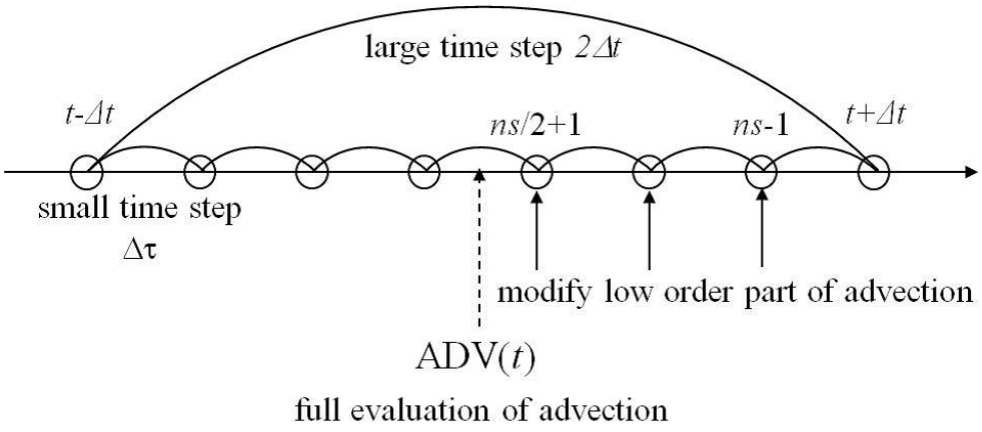

Figure 3.5.1: Time split of advection for case of $ns = 2\Delta t/\Delta\tau = 7$ after Saito *et al.* (2006) Fig. 3.

$$\frac{\hat{W}^{\tau+\Delta\tau} - \hat{W}^{\tau}}{\Delta\tau} + \frac{1}{m_3}\frac{\partial}{\partial\hat{z}}\left(\frac{P^{\beta}}{G^{1/2}}\right) + \frac{gP^{\beta}}{m_3 C_m^2}$$
$$= \frac{1}{m_3}\mathrm{BUOY} - (\mathrm{ADV}W - \mathrm{ADVL}W + \mathrm{ADVL}W^{\tau}) + \mathrm{R}W + (1-\sigma)\frac{gP^{\tau}}{m_3 C_m^2}. \tag{3.5.55}$$

The time splitting of advection of potential temperature using this adjustment is an alternative way to split gravity waves

$$\frac{\theta^{\tau+\Delta\tau} - \theta^{\tau}}{\Delta\tau} = -(\mathrm{ADV}\theta - \mathrm{ADVL}\theta + \mathrm{ADVL}\theta^{\tau}) + \frac{Q}{C_p\pi} + \mathrm{DIF}.\theta, \tag{3.5.56}$$

where ADVLθ is computed by a flux form second-order central difference.

3.5.3.6 Computational Diffusion

A nonlinear damper, a fourth-order linear damper and the Asselin time filter (Robert 1966) are employed to suppress the computational noise. The targeted moisture diffusion is implemented (Saito and Ishida 2005) to control the gridpoint storms and the associated intense grid scale precipitation.

1. Nonlinear damper

   Nonlinear damping (Nakamura 1978),

   $$\mathrm{D}_{NL} = \frac{1}{8m_{NL}\Delta t}\left\{(\Delta x)^3\frac{\partial}{\partial x}\left(\left|\frac{\partial\phi}{\partial x}\right|\frac{\partial\phi}{\partial x}\right) + (\Delta y)^3\frac{\partial}{\partial y}\left(\left|\frac{\partial\phi}{\partial y}\right|\frac{\partial\phi}{\partial y}\right)\right\} \tag{3.5.57}$$

   is added to the diffusion term of ϕ where $m_{NL} = 600$ is used. For two-grid noise of amplitude α, 1/e-folding time is given by $m_{NL}\Delta t/\alpha$. This nonlinear damping sometimes causes the computational instability because of the excessive diffusion. A limit is applied to D_{NL} using the estimated amplitude of the maximum wave number.

2. Fourth-order linear damper

   Fourth-order linear damping,

$$\mathrm{D}_{2D} = \frac{1}{16 m_{2D} \Delta t} \left\{ (\Delta x)^4 \frac{\partial^4 \phi}{\partial x^4} + (\Delta y)^4 \frac{\partial^4 \phi}{\partial y^4} \right\} \tag{3.5.58}$$

is added to the diffusion term of ϕ where $m_{2D} = 600$ is used. 1/e-folding time is given by $m_{2D}\Delta t$.

3. Asselin time filter

   After the time integration, all quantities of prognostic variables are modified following the Asselin time filter,

$$\phi(t) = \phi(t) + 0.5\nu \{\phi(t - \Delta t) - 2\phi(t) + \phi(t + \Delta t)\}, \tag{3.5.59}$$

   where ν is set to 0.2 in the MSM.

4. Targeted moisture diffusion

   A second-order horizontal diffusion is applied to water vapor when strong upward motions exist to selectively damp the gridpoint storms caused by the positive feedback of the latent heat release by condensation and updraft acceleration. In the MSM, water vapor at grid points where the upward velocity exceeds 3.0 ms^{-1} is horizontal diffused with 1/e-folding time of 300 seconds.

3.5.3.7 Boundary Conditions

Rayleigh damping,

$$\mathrm{D}_R = -\frac{\mathrm{D}}{m_R} \{\phi - \phi_{EXT}\} \tag{3.5.60}$$

is added near the lateral and upper boundary to the time tendencies of horizontal and vertical momentum, potential temperature and mixing ratio of water vapor, where ϕ is the prognostic variable and ϕ_{EXT} is the value of the external model. m_R is the coefficient which determines the 1/e-folding time and $m_R = 2400$ is used. D is a function given by of location, where D is unity at boundary and decreases as the grid points are away from boundary.

3.5.4 Cloud Microphysics

An explicit three-ice bulk microphysics scheme (Ikawa and Saito 1991) based on Lin *et al.* (1983) is incorporated. The scheme predicts the mixing ratios of water vapor and five hydrometeors, which are designated by q_x where x denotes categories, defined as v for water vapor, c for cloud water, r for rain, i for cloud ice, s for snow, and g for graupel. Number concentrations of solid hydrometeors (cloud ice N_i, snow N_s, and graupel N_g) are optionally treated as prognostic values in addition to their mixing ratios. Spherical particles are assumed in all categories of hydrometeors. Density is constant in each category (ρ_x). Therefore, the mass-size relation ($m_x(D_x)$) is given by

$$m_x(D_x) = \frac{\pi}{6} \rho_x {D_x}^3, \tag{3.5.61}$$

where D_x is the diameter of the particles. Simple power law is also taken for the fall velocity-size relation ($U_x(D_x)$); therefore, it is given by

$$U_x(D_x) = \alpha_{ux} {D_x}^{\beta_{ux}} \left(\frac{\rho_0}{\rho_a} \right)^{\gamma_{ux}}, \tag{3.5.62}$$

where ρ_a is the density of the air, ρ_0 is the density of the reference air, and α_{ux}, β_{ux} and γ_{ux} are constants in each category of the hydrometeors.

The cloud microphysical processes simulated in this scheme are illustrated in Figure 3.5.2 (see Table 3.5.1 for the list of the symbols used in Figure 3.5.2). In this scheme, some basic cloud microphysical processes (e.g., nucleation of cloud particles, conversion from cloud particles to precipitation particles) are parameterized, because their processes occur in a shorter temporal compared to the integration time-step. However, most

of the cloud microphysical processes can be applied directly to the calculation related to the size distribution assumed in each category of hydrometeors. The number-weighted mean of temporal tendency of one cloud microphysical variable ϕ due to one cloud microphysical process in each particle gives the grid-mean temporal tendency of ϕ as follows:

$$\frac{d\phi}{dt} = \int_0^\infty \frac{d\phi_0}{dt} n(D)\, dD, \tag{3.5.63}$$

where $\frac{d\phi_0(D)}{dt}$ is temporal tendency of ϕ due to one cloud microphysical process in a particle of diameter D, and $n(D)\, dD$ is the number of particles per unit volume of air with diameter D to $D + dD$. Therefore, size distributions of hydrometeors deeply affect time tendency of cloud microphysical variables due to cloud microphysical processes.

The size distributions of rain, snow and graupel are assumed to follow an exponential function:

$$n_x(D_x) = N_{0x} \exp(-\lambda_x D_x), \tag{3.5.64}$$

where N_{0x} is the intercept, and λ_x is the slope parameter of the size distribution. Therefore, the moment formula for rain, snow, and graupel is calculated as the following equation:

$$M_x(p) = \int_0^\infty {D_x}^p n_x(D_x)\, dD_x = N_{0x} \frac{\Gamma(1+p)}{{\lambda_x}^{1+p}}, \tag{3.5.65}$$

where $M_x(p)$ is the p-th moment of $n_x(D_x)$. The number concentration is the zeroth moment of $n_x(D_x)$; therefore, it is calculated as

$$N_x = \int_0^\infty n_x(D_x)\, dD_x = M_x(0) = \frac{N_{0x}}{\lambda_x}. \tag{3.5.66}$$

The mixing ratio ($q_x \equiv \rho_x/\rho_a$) is the third moment of $n_x(D_x)$; therefore, it is also calculated as

$$q_x = \frac{1}{\rho_a} \int_0^\infty m_x(D_x) n_x(D_x)\, dD_x = \frac{\rho_x}{\rho_a} \frac{\pi}{6} M_x(3) = \frac{\rho_x}{\rho_a} \frac{\pi}{6} N_{0x} \frac{\Gamma(4)}{{\lambda_x}^4}. \tag{3.5.67}$$

When the number concentrations for rain, snow, and graupel are not predicted, their intercepts are assumed to be constant; therefore, the following formula is used:

$$N_{0x} = \text{const.}, \quad \lambda_x = \left(\frac{\pi \rho_x N_{0x}}{\rho_a q_x} \right)^{\frac{1}{4}}. \tag{3.5.68}$$

This option is adopted in the MSM.

Cloud water and cloud ice are assumed to be monodisperse; therefore, their size distributions follow the δ-function:

$$n_x(D_x) = N_x \delta(D_x - \overline{D_x}), \tag{3.5.69}$$

where $\delta(x)$ satisfies the following equation: $\int_{-\infty}^{\infty} \delta(x-a) f(x)\, dx = f(a)$, and $\overline{D_x}$ is the diameter of the monodisperse particle. The moment formula for cloud water and cloud ice is given by

$$M_x(p) = N_x \overline{D_x}^p. \tag{3.5.70}$$

The mixing ratio is calculated as

$$q_x = \frac{\rho_x}{\rho_a} \frac{\pi}{6} M_x(3) = \frac{\rho_x}{\rho_a} \frac{\pi}{6} N_x \overline{D_x}^3. \tag{3.5.71}$$

Therefore, their diameter is determined as

$$\overline{D_x} = \left(\frac{6 \rho_a q_x}{\pi \rho_x N_x} \right)^{\frac{1}{3}}. \tag{3.5.72}$$

The number concentration of cloud water (N_c) is always assumed to be constant in this scheme. The number concentration of cloud ice (N_i) can be optionally treated as prognostic value, and this option is adopted in the MSM.

Table 3.5.2 provides the characteristics of each hydrometeor class. More detailed information on the treatment of each cloud microphysical process in this scheme can be found in Ikawa and Saito (1991).

Table 3.5.1: List of symbols in Figure 3.5.2

Notation	Description
	Production terms
p_a_ppp_b	Production of category "a" converted from category "b" through a process "ppp"
p_a_ppp_a_b	Growth of category "a" by capturing category "b" through a process "ppp"
p_a_ppp_b_c	Generation of category "a" by category "b" capturing category "c" through a process "ppp"
	Categories by hydrometeors
v	Water vapor
w	Cloud water
r	Rain
i	Cloud ice
s	Snow
g	Graupel
	Cloud microphysical processes
evp	Evaporation
cnd	Condensation
aut, cn	Conversion
ac	Accretion
mlt	Melting
nud	Nucleation
dep	Deposition/Sublimation
frz	Freezing
spl	Ice splinter multiplication
sed	Sedimentation

Table 3.5.2: Assumed hydrometeor parameters and characteristics.

Variable	Rain q_r(kg kg^{-1})	Snow q_s(kg kg^{-1}) N_s (m^{-3})	Graupel q_g(kg kg^{-1}) N_g (m^{-3})	Cloud water q_c(kg kg^{-1})	Cloud ice q_i(kg kg^{-1}) N_i (m^{-3})
Size distribution (m^{-4})	$n_r(D_r) = N_{r0}\exp(-\lambda_r D_r)$ $N_{r0} = 8.0\times10^6$	$n_s(D_s) = N_{s0}\exp(-\lambda_s D_s)$	$n_g(D_g) = N_{g0}\exp(-\lambda_g D_g)$	$\overline{D_c} = \left[\frac{6q_c\rho_a}{\pi N_c\rho_c}\right]^{\frac{1}{3}}$ $N_c = 1.0\times10^8$	$\overline{D_i} = \left[\frac{6q_i\rho_a}{\pi N_i\rho_i}\right]^{\frac{1}{3}}$
Fall velocity (m s^{-1})	$U_x(D_x) = \alpha_{ux} D_x^{\beta_{ux}} \left(\frac{\rho_0}{\rho_a}\right)^{\gamma_{ux}}$				
	$\alpha_{ur} = 842$ $\beta_{ur} = 0.8$ $\gamma_{ur} = 0.5$	$\alpha_{us} = 17$ $\beta_{us} = 0.5$ $\gamma_{us} = 0.5$	$\alpha_{ug} = 124$ $\beta_{ug} = 0.64$ $\gamma_{ug} = 0.5$	$\alpha_{uc} = 2.98\times10^7$ $\beta_{uc} = 2.0$ $\gamma_{uc} = 1.0$	$\alpha_{ui} = 700$ $\beta_{ui} = 1.0$ $\gamma_{ui} = 0.35$
Density (kg m^{-3})	$\rho_r = 1.0\times10^3$	$\rho_s = 8.4\times10^1$	$\rho_g = 3.0\times10^2$	$\rho_c = 1.0\times10^3$	$\rho_i = 1.5\times10^2$

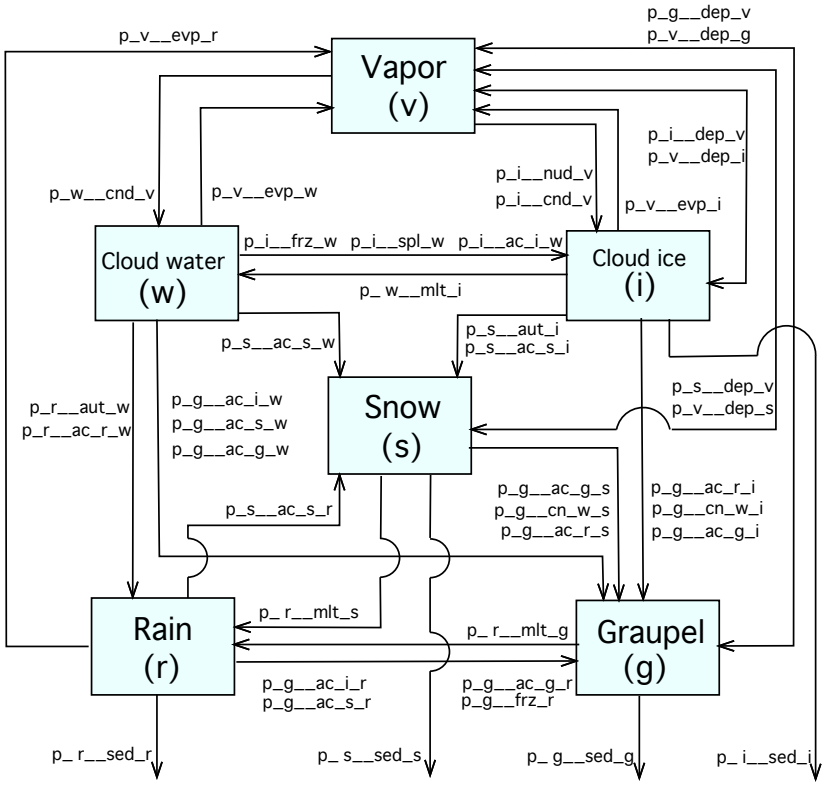

Figure 3.5.2: Cloud microphysical processes in the MSM. For a list of symbols, see Table 3.5.1.

3.5.5 Convective Parameterization

In order to incorporate vertical transport of heat and moisture by subgrid-scale convection, the Kain-Fritsch (KF) convective parameterization (Kain and Fritsch 1990; Kain 2004) has been employed for the MSM.

The KF scheme parameterizes convection using a cloud model based on the one-dimensional entraining/detraining plume model which contains detailed treatment concerning interactions between convective updraft and surrounding air, which are entrainment and detrainment processes. Therefore the subgrid-scale convection parameterized by the KF scheme is sensitive to thermodynamic conditions of the environment. The cloud model consists of a pair of upward and downward mass fluxes. These fluxes and compensating subsidence, which is induced through the mass conservation, transport heat and moisture vertically. Entrainment and detrainment, through which the mass is exchanged between the cumulus and the environment, control the development of the mass fluxes.

The scheme starts from estimation of mass fluxes representing the convection. In that estimation, entrainment and detrainment are calculated as interaction with the environment. The vertical transport of heat and moisture by the fluxes and the compensating subsidence brings modified vertical profiles of temperature and water vapor. Adjusting the mass fluxes to reduce the convective available potential energy (CAPE) results in vertically stabilized atmosphere. To find out grids at which the scheme works, a trigger function is used. As a consequence, temporal tendencies of temperature, water vapor and hydrometeors are obtained by the scheme. Each process is described below in detail.

The upward mass flux is estimated through moving air mass up from the lifting condensation level (LCL) with the conservation of equivalent potential temperature and total amount of water contents in a Lagrangian sense. The initial upward mass flux at the LCL, M_{u0}, is given as follows with the assumption that the vertical velocity is $1\mathrm{ms}^{-1}$ and the initial area occupied by convection is 1% of a grid,

$$M_{u0} = \rho_{u\mathrm{LCL}} \times 0.01\Delta x^2, \tag{3.5.73}$$

where $\rho_{u\mathrm{LCL}}$ is the density of the upward mass flux at the LCL and Δx is the grid size of 5km for the MSM.

While evaluating the updraft, condensate is formed and some of them are glaciated according to the temperature of the updraft at each level, and excess amount of these hydrometeors over a threshold is taken out from the updraft as precipitation via a Kessler type autoconversion scheme. Furthermore, as entrainment and detrainment, the interactions between updraft and the environment as the turbulent mixing are also estimated at each vertical level. It is supposed that the turbulent mixing occurs at very near the periphery of the updraft, then many subparcel-like mixtures of the updraft and the environment are formed at various ratios assuming the Gaussian distribution of the probability such that mixtures at the ratio of fifty-fifty is the most likely. Consequently, the mixtures with positive (negative) buoyancy against the environment entrain into (detrain from) updraft. It means that more moist/warmer condition of the environment favors much developed updraft and that drier/cooler one prevents the updraft from growing. The hydrometeors included in detrainment masses are taken into account as the tendencies for the grid-scale variables. The vertical velocity of the updraft changes by buoyancy and weight of the hydrometeors. The updraft terminates when the upward mass flux has emaciated through detrainment or vertical velocity of the updraft turns into zero.

Entrainment rate, δM_e, which determines amount of entrainment and detrainment, is inversely proportional to radius of the updraft, R,

$$\delta M_e = M_{u0}(0.03\delta P/R), \tag{3.5.74}$$

where δP(Pa) is thickness of vertical grid. The radius of the updraft is used only for the entrainment rate estimation.

The radius R is rendered as a function of larger-scale forcing through the grid-resolved vertical velocity and the height of the LCL (Moriyasu and Narita 2011). In the case that the height of the LCL is lower than 950hPa, R takes 500m. When the height of the LCL is higher than 800hPa, R is determined as follows:

$$R = factor \times \Delta x/\Delta x_0 \times \begin{cases} 1000 & (W_0 < 0\mathrm{ms}^{-1}) \\ 1000(1 + W_0/0.1) & (0\mathrm{ms}^{-1} \leq W_0 \leq 0.1\mathrm{ms}^{-1}) \\ 2000 & (W_0 > 0.1\mathrm{ms}^{-1}), \end{cases} \tag{3.5.75}$$

$$W_0 = \bar{W}_{\mathrm{LCL}} \times \Delta x/\Delta x_0 - W_{\mathrm{KLCL}}, \tag{3.5.76}$$

$$W_{\mathrm{KLCL}} = \begin{cases} 0.02 & (Z_{\mathrm{LCL}} \geq Z_0) \\ 0.02 \times Z_{\mathrm{LCL}}/Z_0 & (Z_{\mathrm{LCL}} < Z_0), \end{cases} \tag{3.5.77}$$

where Δx_0 takes 25km that is the grid size of the original model the KF scheme developed, W_0 indicates the intensity of the updraft depending on the grid-resolved vertical velocity at the LCL, $\bar{W}_{\mathrm{LCL}}$ is a running mean of the grid-resolved vertical velocity at the LCL for 8 timesteps, Z_{LCL} is the height of the LCL, Z_0 takes 2000m and *factor* takes 5 for the MSM. In the case that the height of the LCL is between 950hPa and 800hPa, R is linearly interpolated between both cases above. The gap of the grid size between the MSM and the original model needs the correction term of $\Delta x/\Delta x_0$.

A downward mass flux as a convective downdraft is fueled by evaporation of the hydrometeors that are generated within the updraft. The downdraft starts at the layer of 150hPa above the LCL. With the similar way to the updraft, the mass flux is estimated for the downdraft. Entrainment between the downdraft and the environment is allowed only above the LCL and detrainment only below the LCL.

Parameterized shallow convection is also allowed for any updraft that does not reach the minimum cloud depth for deep convection. The minimum value of cloud depth is a function of temperature at cloud base (LCL).

Adjusting amount of the mass fluxes iteratively in the sense of a 85% reduction of the initial value of CAPE, the stabilized atmosphere succeeds. Differences of the thermodynamic variables of the stabilized atmosphere from that of the initial unstable one is the contributions of the parameterized convection as the goal of the scheme. The differences divided by an advective time period for a column are as the tendencies on each step. In the case of the temperature, T, for example,

$$\left.\frac{dT}{dt}\right|_{\text{convection}} = \frac{T_{\text{stabilized}} - T_{\text{initial}}}{\Delta x/\bar{V}}, \tag{3.5.78}$$

where $\bar{V}$ is an average wind speed at the LCL and 500hPa.

Searching to find out grids which the parameterized convection should occur is repeated in every 5 minutes (*i.e.* 15 timesteps). For picking up the grids, the trigger function is defined as the temperature of a lifted air mass at the LCL with perturbations as a function of the grid-resolved vertical velocity and the relative humidity at the LCL added.

$$\text{Trigger Function} = T_{\text{LCL}} + 0.2 \times \Delta T_{\text{LCL}} + 0.25 \times \Delta T_{\text{RH}}. \tag{3.5.79}$$

The first term of the perturbations represents the dynamical forcing which needs to overcome the convective inhibition.

$$\Delta T_{\text{LCL}} = \max\left[(100W_0)^{\frac{1}{3}}, 0\right]. \tag{3.5.80}$$

And the second term comes from the variance in the relative humidity distribution (Undén *et al.* 2002).

$$\Delta T_{\text{RH}} = \begin{cases} 0 & (RH_{\text{LCL}} < 0.75) \\ 0.25(RH_{\text{LCL}} - 0.75)q/(\partial q^*_{\text{LCL}}/\partial T) & (0.75 \leq RH_{\text{LCL}} \leq 0.95) \\ (1/RH_{\text{LCL}} - 1)q/(\partial q^*_{\text{LCL}}/\partial T) & (0.95 < RH_{\text{LCL}}), \end{cases} \tag{3.5.81}$$

where RH_{LCL} is the grid-resolved relative humidity at the LCL, q is mixing ratio of the water vapor of the lifted source layers and q^*_{LCL} is mixing ratio of the saturated water vapor as grid-resolved value at the LCL. Tuning factors for both the perturbations appear in Eq. (3.5.79) for the MSM.

First, the potential updraft source layer (USL) of the lowest 50hPa depth is lifted adiabatically to its LCL. And then the trigger function to be compared with the environmental temperature represented by a grid-scale value. If $T_{\text{LCL}} + 0.2 \times \Delta T_{\text{LCL}} + 0.25 \times \Delta T_{\text{RH}} > T_{\text{ENV}}$ is met, the USL is regarded to have buoyancy and parameterized convection is initiated at the LCL. If not, the base of the potential USL is moved up 15hPa and the comparison between the trigger function and T_{ENV} is repeated while the base of the potential USL is below the lowest 300hPa of the atmosphere.

3.5.6 Radiation

The radiation process employed in the MSM is almost identical to that in the GSM, as codes of the GSM radiation process was ported into the MSM. The details are described in Subsection 3.2.3. Some differences between them are mentioned below.

A method to evaluate the effective radius of a cloud ice particle in the MSM is based on Ou and Liou (1995) with modification by McFarquhar *et al.* (2003). Following the method, the effective radius $r_{\text{e}}[\mu\text{m}]$ is given as

$$r_{\text{e}} = -1.56 + 0.388D_{\text{e}} + 0.00051{D_{\text{e}}}^2, \tag{3.5.82}$$

$$D_{\text{e}} = 326.3 + 12.42T + 0.197T^2 + 0.0012T^3, \tag{3.5.83}$$

where T [deg. C] is air temperature and D_{e} [μm] is the mean effective size of the particle.

Cloud fraction is diagnosed using the partial condensation method based on Sommeria and Deardorff (1977) which is also employed in evaluating buoyancy flux in the boundary layer scheme (Subsection 3.5.7).

The longwave and shortwave radiation are fully calculated every 15 minutes, while heating rates due to longwave and shortwave radiation are corrected every time step using the surface temperature and the solar zenith angle, respectively.

3.5.7 Boundary Layer

As a boundary layer scheme which represents vertical turbulent transport of momentum, heat and water, the Mellor-Yamada-Nakanishi-Niino Level 3 model (MYNN3) (Nakanishi and Niino 2009) is employed in the MSM.

MYNN3 is the second order turbulent closure model, which assumes that the third order moments of turbulent fluctuation can be depicted by the lower order moments. The full model (called "Level 4") requires too large computational costs because all the second order moments are prognostic variables. In order to reduce the computational costs to run, some terms appeared in the prognostic equations are neglected in terms of the order of anisotropy. In the model called "Level 3" with the boundary layer approximation in which horizontal derivatives are ignored, just only four turbulent prognostic variables, including the turbulent kinetic energy (TKE), are left as

$$\frac{Dq^2}{Dt} = -2\left(\overline{u'w'}\frac{\partial\overline{u}}{\partial z} + \overline{v'w'}\frac{\partial\overline{v}}{\partial z}\right) + 2\frac{g}{\overline{\theta_{\rm v}}}\overline{w'\theta'_{\rm v}} - 2\varepsilon + {\rm dif}.q^2, \tag{3.5.84}$$

$$\frac{D\overline{\theta'^2_{\rm l}}}{Dt} = -2\overline{w'\theta'_{\rm l}}\frac{\partial\overline{\theta_{\rm l}}}{\partial z} - 2\varepsilon_\theta + {\rm dif}.\overline{\theta'^2_{\rm l}}, \tag{3.5.85}$$

$$\frac{D\overline{q'^2_{\rm w}}}{Dt} = -2\overline{w'q'_{\rm w}}\frac{\partial\overline{q_{\rm w}}}{\partial z} - 2\varepsilon_q + {\rm dif}.\overline{q'^2_{\rm w}}, \tag{3.5.86}$$

$$\frac{D\overline{\theta'_{\rm l}q'_{\rm w}}}{Dt} = -\overline{w'\theta'_{\rm l}}\frac{\partial\overline{q_{\rm w}}}{\partial z} - \overline{w'q'_{\rm w}}\frac{\partial\overline{\theta_{\rm l}}}{\partial z} - 2\varepsilon_{\theta q} + {\rm dif}.\overline{\theta'_{\rm l}q'_{\rm w}}, \tag{3.5.87}$$

and the other second order moments are diagnosed as

$$\overline{w'u'} = -q\ell(S_{\rm M2.5} + S'_{\rm M})\frac{\partial\overline{u}}{\partial z}, \tag{3.5.88}$$

$$\overline{w'v'} = -q\ell(S_{\rm M2.5} + S'_{\rm M})\frac{\partial\overline{v}}{\partial z}, \tag{3.5.89}$$

$$\overline{w'\theta'_{\rm l}} = -q\ell(S_{\rm H2.5} + S'_{\rm H})\frac{\partial\overline{\theta_{\rm l}}}{\partial z} = -q\ell\left(S_{\rm H2.5}\frac{\partial\overline{\theta_{\rm l}}}{\partial z} + \Gamma_\theta\right), \tag{3.5.90}$$

$$\overline{w'q'_{\rm w}} = -q\ell(S_{\rm H2.5} + S'_{\rm H})\frac{\partial\overline{q_{\rm w}}}{\partial z} = -q\ell\left(S_{\rm H2.5}\frac{\partial\overline{q_{\rm w}}}{\partial z} + \Gamma_q\right). \tag{3.5.91}$$

Here, $q_{\rm l}$ is mixing ratio of condensed water (including ice phase), and

$$q^2 = 2{\rm TKE} = \left(\overline{u'^2} + \overline{v'^2} + \overline{w'^2}\right), \tag{3.5.92}$$

$$\theta_{\rm l} = \theta - \frac{L}{C_p}\frac{\theta}{T}q_{\rm l}, \tag{3.5.93}$$

$$q_{\rm w} = q_{\rm v} + q_{\rm l}, \tag{3.5.94}$$

with the assumptions that the vertical derivative of the third order moments can reduce to diffusion terms (dif.X denotes a diffusion term on X). The dissipation terms ε_X appeared in the equations are parameterized on the basis of the Kolmogorov's local isotropy assumption as

$$\varepsilon = \frac{q}{B_1\ell}q^2, \quad \varepsilon_\theta = \frac{q}{B_2\ell}\overline{\theta'^2_{\rm l}}, \quad \varepsilon_q = \frac{q}{B_2\ell}\overline{q'^2_{\rm w}}, \quad \varepsilon_{\theta q} = \frac{q}{B_2\ell}\overline{q'_{\rm w}\theta'_{\rm l}}, \tag{3.5.95}$$

with the closure constants B_1, B_2. The mixing length ℓ is given by

$$\frac{1}{\ell} = \frac{1}{L_{\rm S}} + \frac{1}{L_{\rm T}} + \frac{1}{L_{\rm B}}, \tag{3.5.96}$$

where

$$L_{\rm S} = \begin{cases} kz/3.7 & (\zeta \geqq 1) \\ kz(1+2.7\zeta)^{-1} & (0 \leqq \zeta < 1) \\ kz(1-\alpha_4\zeta)^{0.2} & (\zeta < 0) \end{cases}, \tag{3.5.97}$$

$$L_{\mathrm{T}} = \alpha_1 \frac{\int_0^\infty qz\, dz}{\int_0^\infty q\, dz}, \tag{3.5.98}$$

$$L_{\mathrm{B}} = \begin{cases} \alpha_2 q / N_{\mathrm{l}} & (\partial\theta/\partial z > 0, \zeta \geqq 0) \\ \left[\alpha_2 q + \alpha_3 (q_{\mathrm{c}}/L_T N_{\mathrm{l}})^{1/2}\right] / N_{\mathrm{l}} & (\partial\theta/\partial z > 0, \zeta < 0) \\ \infty & (\partial\theta/\partial z < 0) \end{cases}, \tag{3.5.99}$$

with the Brunt-Väisälä frequency N_{l}, von Kármán's constant k, and $\zeta = z/L$ with the Monin-Obukhov length L. Empirical constants α_1, α_2, α_3 and α_4 set to be

$$(\alpha_1, \alpha_2, \alpha_3, \alpha_4) = (0.23, 1.0, 5.0, 100.0). \tag{3.5.100}$$

$S_{\mathrm{M2.5}}$ and $S_{\mathrm{H2.5}}$ are determined by the flux Richardson number and empirical constants appearing in closure assumptions. S'_{M}, S'_{H}, Γ_θ and Γ_q are correction terms induced by the enhancement from level 2.5 (in which only the TKE is treated as a prognostic variable) to level 3. The correction terms depend on the turbulent prognostic variables (q^2, $\overline{\theta_{\mathrm{l}}'^2}$, $\overline{q_{\mathrm{w}}'^2}$ and $\overline{\theta_{\mathrm{l}}' q_{\mathrm{w}}'}$).

Buoyancy flux $(g/\overline{\theta_{\mathrm{v}}})\overline{w'\theta_{\mathrm{v}}'}$ is the important origin of the TKE production. By considering partial condensation effects assuming that fluctuations of θ_{l} and q_{w} from their mean values is depicted by the Gaussian probability density function (PDF) (Sommeria and Deardorff 1977), the width of which depends on $\overline{\theta_{\mathrm{l}}'^2}$, $\overline{q_{\mathrm{w}}'^2}$ and $\overline{\theta_{\mathrm{l}}' q_{\mathrm{w}}'}$, the buoyancy flux can be written as a function of cloud fraction and condensed water obtained as moments of the PDF.

Using local gradient of u, v, θ_{l} and q_{w}, $S_{\mathrm{M2.5}}$ and $S_{\mathrm{H2.5}}$ can be calculated. Once the prognostic equations Eq. (3.5.84), Eq. (3.5.85), Eq. (3.5.86) and Eq. (3.5.87) are integrated, fluxes Eq. (3.5.88), Eq. (3.5.89), Eq. (3.5.90) and Eq. (3.5.91) and tendencies of the turbulent prognostic variables can be calculated. The fluxes give temporal tendency of a variable $\phi(= u, v, \theta_{\mathrm{l}}, q_{\mathrm{w}})$ due to the turbulent transport as follows,

$$\frac{\partial \phi}{\partial t} = -\frac{\partial}{\partial z}\overline{w'\phi'}. \tag{3.5.101}$$

For the details of the formalism, refer to Nakanishi (2001); Nakanishi and Niino (2004, 2006, 2009).

3.5.8 Surface Fluxes

The main procedures around surface processes are evaluation of surface fluxes. It is assumed that the turbulent fluxes are constant with height and equal to the surface values within the surface layer. They can be expressed in term of differences between quantities at the lowest layer of atmosphere (identified by a subscript "a") and surface (identified by a subscript "s") as

$$\overline{u'w'} = -C_{\mathrm{m}} U_{\mathrm{a}} u_{\mathrm{a}}\,, \tag{3.5.102}$$

$$\overline{v'w'} = -C_{\mathrm{m}} U_{\mathrm{a}} v_{\mathrm{a}}\,, \tag{3.5.103}$$

$$\overline{\theta_{\mathrm{v}}'w'} = -C_{\mathrm{h}} U_{\mathrm{a}} (\theta_{\mathrm{va}} - \theta_{\mathrm{vs}})\,, \tag{3.5.104}$$

$$\overline{q_{\mathrm{v}}'w'} = -C_{\mathrm{q}} \beta U_{\mathrm{a}} (q_{\mathrm{va}} - q_{\mathrm{sat}})\,, \tag{3.5.105}$$

where $U_{\mathrm{a}} = \sqrt{u_{\mathrm{a}}^2 + v_{\mathrm{a}}^2}$, q_{sat} is the saturated specific humidity at the ground surface temperature T_1, and β is the evapolation efficiency. Over land, β is estimated with soil moisture

$$\beta = \begin{cases} w_{\mathrm{g}}/0.3 & (w_{\mathrm{g}} \leq 0.3) \\ 1 & (w_{\mathrm{g}} > 0.3) \end{cases}, \tag{3.5.106}$$

where w_{g} is the volumetric water content at the surface, and is predicted by Eq. (3.5.133) (see Subsection 3.5.9). Over the sea, snow, and seaice, β is set equal to 1.

The transfer coefficients C_m, C_h, and C_q can be expressed as

$$C_\mathrm{m} = \frac{\kappa^2}{\left[\ln\frac{z-d_0}{z_{0\mathrm{m}}} - \psi_\mathrm{m}\left(\frac{z-d_0}{L}\right) + \psi_\mathrm{m}\left(\frac{z_{0\mathrm{m}}}{L}\right)\right]^2}, \tag{3.5.107}$$

$$C_\mathrm{h} = \frac{\kappa^2}{\left[\ln\frac{z-d_0}{z_{0\mathrm{m}}} - \psi_\mathrm{m}\left(\frac{z-d_0}{L}\right) + \psi_\mathrm{m}\left(\frac{z_{0\mathrm{m}}}{L}\right)\right]\left[\ln\frac{z-d_0}{z_{0\mathrm{h}}} - \psi_\mathrm{h}\left(\frac{z-d_0}{L}\right) + \psi_\mathrm{h}\left(\frac{z_{0\mathrm{h}}}{L}\right)\right]}, \tag{3.5.108}$$

$$C_\mathrm{q} = \frac{\kappa^2}{\left[\ln\frac{z-d_0}{z_{0\mathrm{m}}} - \psi_\mathrm{m}\left(\frac{z-d_0}{L}\right) + \psi_\mathrm{m}\left(\frac{z_{0\mathrm{m}}}{L}\right)\right]\left[\ln\frac{z-d_0}{z_{0\mathrm{q}}} - \psi_\mathrm{q}\left(\frac{z-d_0}{L}\right) + \psi_\mathrm{q}\left(\frac{z_{0\mathrm{q}}}{L}\right)\right]}, \tag{3.5.109}$$

where ψ_m, ψ_h, and ψ_q are the integrated gradient functions. d_0 is the zero-plane displacement (the MSM assumes $d_0 = 0$). Following Beljaars and Holtslag (1991), they are given as functions of $\zeta = z/L$,

$$\psi_\mathrm{m}(\zeta) = \begin{cases} -b\left(\zeta - \frac{c}{d}\right)\exp(-d\zeta) - a\zeta - \frac{bc}{d} & (\zeta \geq 0) \\ \frac{\pi}{2} - 2\tan^{-1}x + \ln\frac{(1+x)^2(1+x^2)}{8} & (\zeta < 0) \end{cases}, \tag{3.5.110}$$

$$\psi_\mathrm{h}(\zeta) = \begin{cases} -b\left(\zeta - \frac{c}{d}\right)\exp(-d\zeta) - \left(1 + \frac{2}{3}a\zeta\right)^{\frac{3}{2}} - \frac{bc}{d} + 1 & (\zeta \geq 0) \\ 2\ln\frac{1+x^2}{2} & (\zeta < 0) \end{cases}, \tag{3.5.111}$$

where L is the Monin-Obukhov Length, $\kappa = 0.4$ (von Kármán's constant), and $a = 1$, $b = 2/3$, $c = 5$, $d = 0.35$, and $x = (1 - 16\zeta)^{1/4}$. The integrated gradient function for moisture ψ_q is assumed equal to ψ_h. ζ, which required to calculate $\psi_\mathrm{m}(\zeta)$ and $\psi_\mathrm{h}(\zeta)$, satisfies the following equation,

$$Ri_\mathrm{B} = \zeta\frac{\left[\ln\frac{z-d_0}{z_{0\mathrm{h}}} - \psi_\mathrm{h}\left(\frac{z-d_0}{L}\right) + \psi_\mathrm{h}\left(\frac{z_{0\mathrm{h}}}{L}\right)\right]}{\left[\ln\frac{z-d_0}{z_{0\mathrm{m}}} - \psi_\mathrm{m}\left(\frac{z-d_0}{L}\right) + \psi_\mathrm{m}\left(\frac{z_{0\mathrm{m}}}{L}\right)\right]^2}, \tag{3.5.112}$$

which can be solved by iteration such as the Newton's method. Ri_B is the bulk Richardson Number defined by

$$Ri_\mathrm{B} = \frac{gz_\mathrm{a}}{\frac{1}{2}(\theta_\mathrm{va} + \theta_\mathrm{vs})}\frac{(\theta_\mathrm{va} - \theta_\mathrm{vs})}{U_\mathrm{a}^2}. \tag{3.5.113}$$

$z_{0\mathrm{m}}$, $z_{0\mathrm{h}}$, and $z_{0\mathrm{q}}$ are the roughness length for momentum, heat and moisture respectively. The roughness length on land is set depending on the land use of each grid point. Over the sea, following Beljaars (1995) they are expressed by

$$z_{0\mathrm{m}} = a_\mathrm{m}\frac{\nu}{u_*} + a_\mathrm{Ch}\frac{u_*^2}{g}, \tag{3.5.114}$$

$$z_{0\mathrm{h}} = a_\mathrm{h}\frac{\nu}{u_*}, \tag{3.5.115}$$

$$z_{0\mathrm{q}} = a_\mathrm{q}\frac{\nu}{u_*}, \tag{3.5.116}$$

where $a_\mathrm{m} = 0.11$, $a_\mathrm{Ch} = 0.018$, $a_\mathrm{h} = 0.40$, $a_\mathrm{q} = 0.62$, and ν is the kinematic viscosity ($= 1.5 \times 10^{-5}$ m^2 s^{-1}). u_* is the friction velocity defined by

$$u_* = \left(\overline{u'w'}^2 + \overline{v'w'}^2\right)^{\frac{1}{4}}. \tag{3.5.117}$$

An effect of a stomatal resistance is introduced as following. The surface flux of moisture $\overline{q'_v w'}$ is represented with a resistance coefficient r_a,

$$\overline{q'_{\rm v} w'} = -\frac{1}{r_{\rm a}}(q_{\rm va} - q_{\rm sat}), \quad r_{\rm a} \equiv \frac{1}{C_{\rm q}\beta U_{\rm a}} \,. \tag{3.5.118}$$

$r_{\rm a}$ is corrected to $r_{\rm a} + r_{\rm s}$ when an effect of a stomatal resistance $r_{\rm s}$ is incorporated. $r_{\rm s}$ depends on shortwave radiation flux towards surface S

$$r_{\rm s} = r_{\rm s,\,day} + \frac{r_{\rm s,\,night}}{1 + \dfrac{S}{S_0}} \,, \tag{3.5.119}$$

where $S_0 = 1$ W m^{-2}, $r_{\rm s,\,day}$ is set to 30 s m^{-1} from April to October and 60 s m^{-1} in the other month, and $r_{\rm s,\,night} = 300$ s m^{-1}.

The screen level physical quantities such as wind at 10 m height, temperature and dew point at 1.5 m height are diagnosed by interpolation between the lowest model level and surface assuming the same gradient functions as in the scheme of surface process. Wind velocity at z_{10} (10 m height), u_{10}, and virtual potential temperature at $z_{1.5}$ (1.5 m height), $\theta_{\rm v1.5}$ are diagnosed as

$$u_{10} = \sqrt{\frac{C_{\rm m}(z_{\rm a})}{C_{\rm m}(z_{10})}}\, u_{\rm a} \,, \tag{3.5.120}$$

$$\theta_{\rm v1.5} = \theta_{\rm vs} + \frac{C_{\rm h}(z_{\rm a})}{C_{\rm h}(z_{1.5})} \sqrt{\frac{C_{\rm m}(z_{1.5})}{C_{\rm m}(z_{\rm a})}}(\theta_{\rm va} - \theta_{\rm vs}) \,. \tag{3.5.121}$$

3.5.9 Ground Temperature and Soil Moisture

Ground temperature, which is used in evaluating surface fluxes, is predicted by a multi layer model. The basic equation is the heat conduction equation, in which prognostic variables are temperature T,

$$\rho_c \frac{\partial T}{\partial t} = -\frac{\partial G}{\partial z}, \quad G = -\lambda \frac{\partial T}{\partial z} \,, \tag{3.5.122}$$

where G is the ground heat flux, $\rho_{\rm c}$ is the heat capacity, and λ is the coefficient of the thermal conductivity, respectively. By vertically discretizing soil into N layers (is set to 4 in the MSM, as showing Figure 3.5.3),

$$G_{\rm k} = -2\lambda \frac{T_{\rm k} - T_{\rm k-1}}{\Delta z_{\rm k} + \Delta z_{\rm k-1}} \ (k = 2, \ldots, N), \quad \frac{\partial T_{\rm k}}{\partial t} = -\frac{G_{\rm k+1} - G_{\rm k}}{\rho_{\rm c} \Delta z_{\rm k}} \ (k = 1, \ldots, N-1) \,, \tag{3.5.123}$$

where $\Delta z_{\rm k}$ denotes thickness of k-th layer (concretely $\Delta z_1 = 0.04$ m, $\Delta z_2 = 0.15$ m, $\Delta z_3 = 0.40$ m and $\Delta z_4 = 0.60$ m), and $G_{\rm k}(k \geq 2)$ is given as the gradient of temperature between k-th and $(k-1)$-th layer. G_1 is the heat flux towards surface, which is given by

$$G_1 = (1 - \alpha) S_{\downarrow} + L_{\downarrow} - \sigma T_1^4 - H - lE \,, \tag{3.5.124}$$

where $S_{\downarrow}$ and $L_{\downarrow}$ denote fluxes of shortwave and longwave radiation towards surface, σ is the Stefan-Boltzmann constant, and α is the surface albedo. H and lE represent fluxes of sensible heat and latent heat from the surface,

$$H = -c_{\rm p} \rho \, \overline{\theta'_{\rm v} w'} \,, \tag{3.5.125}$$

$$lE = -l\rho \, \overline{q'_{\rm v} w'} \,, \tag{3.5.126}$$

in which $c_{\rm p}$ is the specific heat of dry air at constant pressure, l is the latent heat of vaporization, and ρ is the density of air at the lowest layer of atmosphere. $G_{\rm k}(k \geq 2)$ can be eliminated as:

$$\frac{\partial T_1}{\partial t} = \frac{G_1}{\rho_{\rm c} \Delta z_1} + \frac{2\Lambda(T_2 - T_1)}{\Delta z_1 (\Delta z_2 + \Delta z_1)} \,, \tag{3.5.127}$$

$$\frac{\partial T_{\rm k}}{\partial t} = -\frac{2\Lambda(T_{\rm k} - T_{\rm k-1})}{\Delta z_{\rm k}(\Delta z_{\rm k} + \Delta z_{\rm k-1})} + \frac{2\Lambda(T_{\rm k+1} - T_{\rm k})}{\Delta z_{\rm k}(\Delta z_{\rm k+1} + \Delta z_{\rm k})} \ (k = 2, \ldots, N) \,, \tag{3.5.128}$$

where $\Lambda \equiv \lambda/\rho_{\rm c}$. λ and $\rho_{\rm c}$ are set as to land use and surface type.

For time integration, the trapezoidal implicit method is adopted. Temporally discretized equations are:

$$T_1^{n+1} = T_1^n + \frac{\Delta t}{2}\left[\frac{G_1^{n+1} + G_1^n}{\rho_{\rm c}\Delta z_1} + \frac{2\Lambda(T_2^{n+1} - T_1^{n+1} + T_2^n - T_1^n)}{\Delta z_1(\Delta z_1 + \Delta z_2)}\right] , \tag{3.5.129}$$

$$T_{\rm k}^{n+1} = T_{\rm k}^n + \Delta t\left[-\frac{\Lambda(T_{\rm k}^{n+1} - T_{\rm k-1}^{n+1} + T_{\rm k}^n - T_{\rm k-1}^n)}{\Delta z_{\rm k}(\Delta z_{\rm k} + \Delta z_{\rm k-1})} + \frac{\Lambda(T_{\rm k+1}^{n+1} - T_{\rm k}^{n+1} + T_{\rm k+1}^n - T_{\rm k}^n)}{\Delta z_{\rm k}(\Delta z_{\rm k+1} + \Delta z_{\rm k})}\right] \ (k = 2, \ldots, N-1) \,, \tag{3.5.130}$$

where

$$G_1^{n+1} = G_1^n + \Delta t\left[\frac{\partial G_1}{\partial t}\right]^{n+1/2} = G_1^n + \Delta t\left[\frac{\partial G_1}{\partial T_1}\frac{\partial T_1}{\partial t}\right]^{n+1/2} \cong G_1^n + \left[\frac{\partial G_1}{\partial T_1}\right]^n (T_1^{n+1} - T_1^n) \,. \tag{3.5.131}$$

If $T_{\rm N}$ is given, these elliptic equations can be solved. In the MSM, T_4 is fixed to climatological value during forecasts. The climatological data for the ground temperature were obtained in the following way. Firstly, monthly mean temperatures at standard pressure levels were calculated from the objective analysis during 1985 and 1986. Next, these data were interpolated vertically to the model ground surface. Then, only the annual mean and the first harmonic component of annual change of the surface temperature are extracted to obtain the climatological underground temperature at the k-th ground layer with the following equation.

$$T_{\rm k} = \hat{T} + A\exp\left(-\frac{z_{\rm k}}{d}\right)\cos\left\{\frac{2\pi}{365}(D - P) - \frac{z_{\rm k}}{d}\right\} \,, \tag{3.5.132}$$

where $\hat{T}$ is the mean ground surface temperature, A and P are the amplitude and the phase of the annual component of the surface temperature, respectively, $z_{\rm k}$ is the depth of the k-th ground layer, d(= 2.65 m) is the e-folding depth and D is the number of day from the beginning of the year.

Furthermore, the sea surface temperature is spatially interpolated from the SST analysis at 18UTC (Section 5.2). It is given as T_1, and is kept constant during the forecast.

Soil moisture is also predicted by the force restore method based on Deardorff (1978):

$$\frac{\partial w_{\rm g}}{\partial t} = -\frac{w_{\rm g} - w_2}{\tau_{\rm g}} + F_{\rm g} \,, \tag{3.5.133}$$

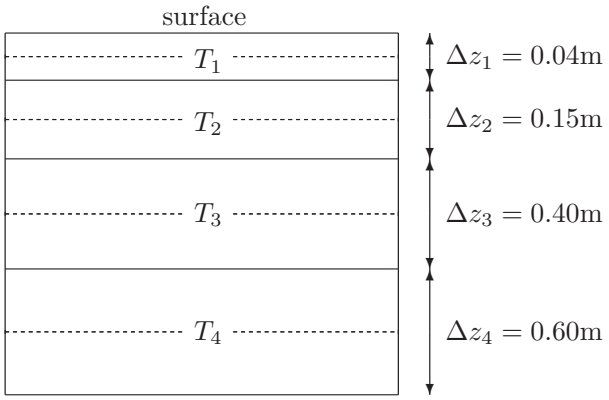

Figure 3.5.3: Structure of the numerical discretization over the layers for the temperatures.

$$\frac{\partial w_2}{\partial t} = F_2 \,, \tag{3.5.134}$$

where w_2 is the mean volumetric water content under the ground, and τ_g is a time constant (= 0.9×86400 s).

Forcing terms F_g and F_2 are given by

$$F_g = -C_g \frac{E - P_r}{\rho_w d_1} \,, \tag{3.5.135}$$

$$F_2 = -\frac{E - P_r}{\rho_w d_2} \,, \tag{3.5.136}$$

where E is the evapolation rate, P_r is the precipitation rate, ρ_w is the density of liquid water, $d_1 = 0.1$ m, and $d_2 = 0.5$ m. C_g is a constant given as following

$$C_g = \begin{cases} 0.5 & \left(\dfrac{w_g}{w_{max}} \geq 0.75\right) \\ 14 - 22.5\left(\dfrac{w_g}{w_{max}} - 0.15\right) & \left(0.15 \leq \dfrac{w_g}{w_{max}} < 0.75\right) \\ 14 & \left(\dfrac{w_g}{w_{max}} < 0.15\right) \end{cases} \,, \tag{3.5.137}$$

where w_{max} is the maximum of volumetric water content (= 0.4).

3.5.10 Parallelization

In order to parallelize computation in the model, the domain is horizontally (two-dimensionally) decomposed into some blocks (Figure 3.5.4) and each of the decomposed blocks is assigned to one process which communicates with other processes through the Message Passing Interface (MPI) (Aranami and Ishida 2004). The processes exchange their data on halo regions when the data on adjacent processes are required for low-order derivatives and interpolation. As the width of the halos is unity, extra halos are temporarily prepared in evaluating the forth order horizontal advection because it requires halos with the width of two or more.

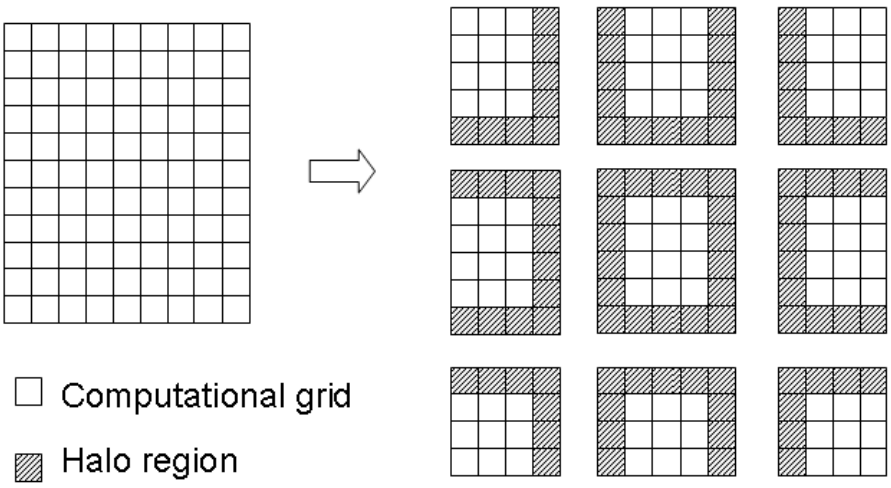

Figure 3.5.4: The whole computational domain (left) and the domain distributed to MPI processes with halo regions (right)

In addition to the processes tied to the decomposed blocks, a special process is exclusively spared to store data into physical disks. As the process can work in background of the main forecasting calculation, time necessary for the output can be hidden and reduced (Figure 3.5.5).

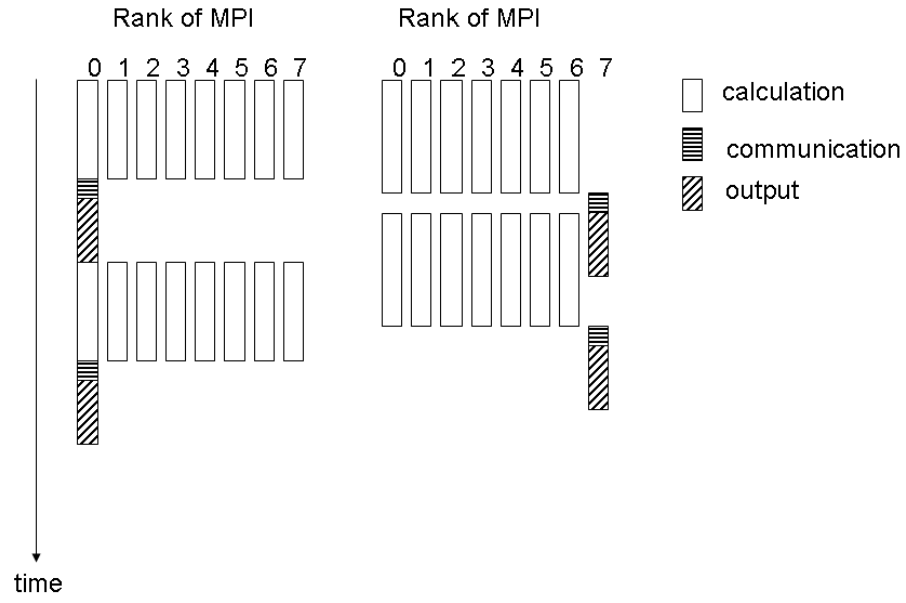

Figure 3.5.5: A diagram of calculation without (left) and with (right) an output process.

Because necessity and sufficiency of conducting MPI communications have been carefully examined, bit-comparable results can be always obtained not depending on the number of processes and how the domain is decomposed. It is very useful and easy to find bugs related to the parallelization.

Within each MPI process, the thread parallelization (SMP) is also applied relying on a function of a Fortran compiler to automatically build parallelized modules.

In the current operation of the MSM, the domain is divided into 17 for x direction and 30 for y direction for the MPI parallelization and additional one process is secured for exclusive data storage. Each MPI process consists of two SMP threads. With this configuration, it takes around 28 minutes to complete 33-hour forecasts of the MSM on Hitachi SR16000/M1 at JMA.

3.5.11 Forecast Performance

Performance of the MSM forecasts has been evaluated by comparing the forecasts with various observations to measure quality of its products and find clues as to further improvements of the model. Especially the accuracy of precipitation forecasts should be emphasized because one of the important purposes of the MSM is to provide information on severe weather phenomena leading to serious disasters.

Figure 3.5.6 and Figure 3.5.7 show time series of threat and bias scores of 3-hour accumulated precipitation forecasts produced by the MSM with the 10-mm threshold from January 2006 to December 2011, respectively. The verification has been performed using "Radar-Raingauge Analyzed Precipitation" (hereafter R/A, see Subsection 4.4.1) as reference observations. (Note that the horizontal resolution of the R/A has been 1-km since March 2006, while the R/A was generated at the 2.5-km resolution until then.) The verification grid size is 20-km, meaning that both the forecasted and observed precipitation over land or sea within 40-km from the coast are averaged over 20-km meshes. Then contingency tables are created by comparing them on each grids.

Figure 3.5.6 and Figure 3.5.7 indicate that the threat score tends to be increasing and the bias score is gradually approaching to unity over the past 6 years. The steady progress has been made by persistent developments of forecast model, data assimilation system, and assimilation method of observation.

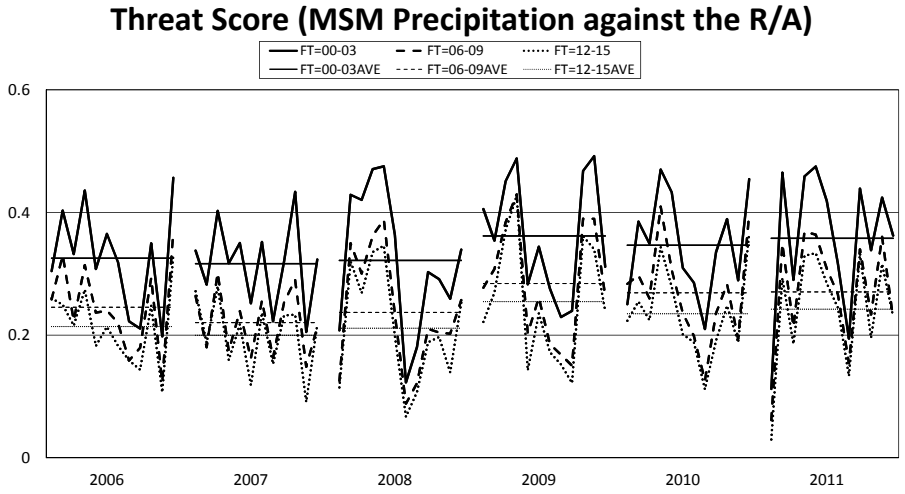

Figure 3.5.6: The monthly threat scores for 3-hour accumulated precipitation by the MSM against the R/A with the threshold of 10mm/3h and within 20km verification grid. The verification period is from January 2006 to December 2011. The thin line means annual average. FT means forecast time from initial time.

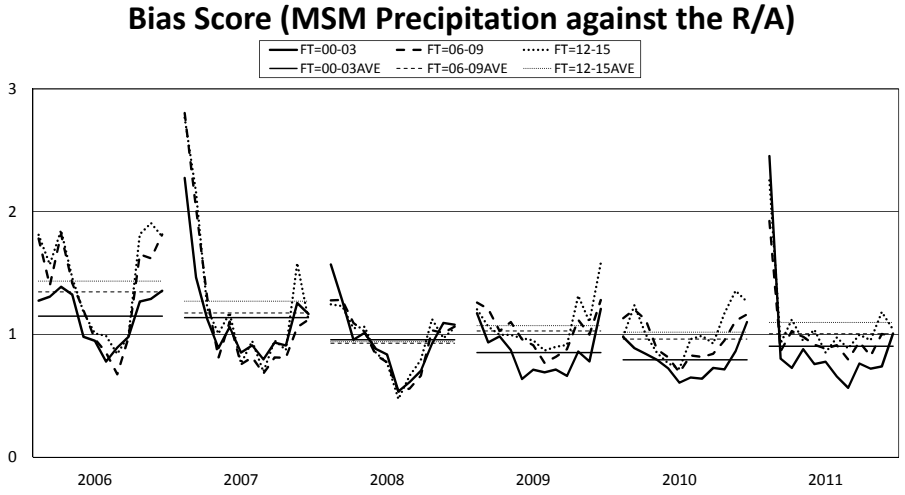

Figure 3.5.7: Same as Figure 3.5.6 but bias scores.

3.6 Local Forecast Model

3.6.1 Introduction

As mentioned in Section 3.5, the Meso-Scale Model (MSM), a numerical weather prediction to provide information on disaster prevention and aviation weather, has been operated since 2001. In its over-ten-year history, horizontal and vertical resolutions have been enhanced: the current MSM covers Japan and its sounding areas with the 5-km grid spacing and places 50 layers in vertical direction up to the height of almost 21.8 km above the surface.

Making use of the new powerful supercomputer system installed in June 2012, operation for a forecast model at an even higher resolution, called the Local Forecast Model (LFM), was launched in August 2012 along with the Local Analysis (LA) described in Section 2.7. The new model has the 2-km horizontal grid spacing and 60 vertical layers up to the height of approximately 20.2km above the surface, and is designed to produce more detailed forecasts with emphasis on predicting localized and short-lived severe events. The LFM focuses on providing very short range forecasts such as 9-hour ahead, and it is intended to quickly and frequently update the forecasts using initial conditions with the latest observations assimilated by the LA.

3.6.2 General Configurations

The LFM has been providing 9-hour forecasts every 3 hours (at 00, 03, 06, 09, 12, 15, 18, 21UTC). The forecast domain covers the eastern part of Japan (shown with the broken line in Figure 2.7.1) with the 2-km horizontal grid spacing.

The LFM employs the identical model to the MSM (the JMA nonhydrostatic model; JMA-NHM) with almost the same configuration mentioned in Section 3.5. Some differences of the configurations between the MSM and the LFM are described below.

- The number and the grid spacings of vertical layers are enhanced in the LFM comparing to those in the MSM. The LFM possesses 60 vertical layers and increases their thicknesses linearly from 40m at the bottom and 678m at the top, while the height of the lowest atmospheric layer is kept the same as that of the MSM. The model top is placed at the height of 20189.5m.

- The LA produces initial conditions with an analysis cycle with hourly 3-dimensional variational method. Boundary conditions are obtained from forecasts performed by the MSM.

- The model is operated with 8-second timestep.

- Strength of the linear and non-linear numerical diffusion should be usually proportional to the horizontal resolution. The time constant for the linear diffusion is set to be 240 seconds as well as that of the non-linear diffusion in the LFM, while both of them are 600 seconds in the MSM.

- The MSM adopts the time splitting of gravity waves (Subsection 3.5.3.5) as the time step (20 seconds) is larger than or comparable to the time scale to propagate the gravity waves (typically 20–30 seconds). Because the time step of the LFM is smaller enough than the time scale, the time splitting is no longer necessary.

- As it is highly expected that considerable part of vertical transport accompanied with convection can be resolved with the grid mean vertical velocity, no convective parameterizations are employed in the LFM. Because convective parameterizations can be the origin of uncertainty of the model, it is preferable to remove them if the resolution is high enough to resolve convective transport.

- As described in Subsection 3.5.6, cloud fraction used in the radiation process is diagnosed considering fluctuations of temperature and water content from their grid mean values over each of the grids. Because the fluctuations are expected to be smaller in higher resolution models, the width of the probability density function depicting behavior of the fluctuation was made smaller.

3.7 Atmospheric Transport Model

3.7.1 Introduction

Since July 1997, JMA has been a Regional Specialized Meteorological Centre (RSMC) with the specialization to provide atmospheric transport model (ATM) products for the environmental emergency response, with responsibility for the Regional Association II (RA-II) of the World Meteorological Organization (WMO). RSMC Tokyo is required to provide advice on the atmospheric transport of pollutants related to nuclear facility accidents and radiological emergencies. The RSMC's ATM products are sent to the National Meteorological Services (NMS) of the WMO Member States in RA-II, and the secretariats of WMO and of the International Atomic Energy Agency (IAEA). The basic procedure of the service is defined in WMO (2010a).

3.7.2 Model

3.7.2.1 Basic Framework

ATM used in JMA is based on Iwasaki *et al.* (1998) with some modifications like one found in Kawai (2002), and it follows a Lagrangian approach, where many tracer particles are released at the time and location of the pollutant emission are displaced due to horizontal and vertical advection and diffusion, and dropped through dry and wet deposition. Advection, diffusion and deposition are computed using 3-hourly model-level outputs from the operational global numerical weather prediction (NWP) model: GSM. The horizontal and vertical displacements during 1 time step δt are given as follows:

$$\delta x = u\delta t + G\sqrt{2k_h\delta t} \tag{3.7.1}$$

$$\delta y = v\delta t + G\sqrt{2k_h\delta t} \tag{3.7.2}$$

$$\delta z = w\delta t + \Sigma G\sqrt{2k_v\delta t'} \tag{3.7.3}$$

where k_h and k_v are horizontal and vertical diffusion coefficients respectively, and Gs are random displacements whose statistical distributions take the Gaussian distribution functions with mean 0 and standard deviation 1. The Monte Carlo method is used to determine displacement of each tracer particle so that it results in a Gaussian distribution. The time step for the integration of the vertical diffusion $\delta t'$ is much less than those for integrations of horizontal diffusion and advection. Tracer particles are also removed from the atmosphere due to dry and wet deposition and radioactive decay.

3.7.2.2 Vertical and Horizontal Diffusion Coefficients

The vertical diffusion coefficient depends on atmospheric vertical profiles. A shorter time step is used so that a vertical displacement due to diffusion becomes smaller than the thickness of the model layer.

The vertical diffusion coefficient k_v is decided referring meteorological parameters on the sigma-pressure hybrid levels by a procedure in the analogous with the molecular diffusion coefficient estimation by Louis *et al.* (1982). The vertical diffusion coefficient is given as follows:

$$k_v = l^2\left|\frac{\partial v}{\partial z}\right|F(R_i) \tag{3.7.4}$$

where the parameters l and R_i are the vertical mixing length of turbulence and the Flux Richardson number, respectively. The similarity function of $F(R_i)$ is taken from Louis *et al*. (1982). The mixing length is written as a function of geometric height z

$$l = \frac{kz}{1 + kz/l_0} \tag{3.7.5}$$

where k is von Kármán's constant and l_0 is the maximum mixing length.

Table 3.7.1: Other Specifications of the ATM

Number of Tracers	100,000
Grid Type for the Calculations of Concentration and Deposition	Lat Lon-grid
Size of the Calculation Grid	(lat) 1.0 × (lon) 1.0 degree

The horizontal diffusion coefficient k_h should be parameterized considering the model resolution and temporal and spatial variations of meteorological fields. An appropriate constant value is set in the model to save computational time.

3.7.2.3 Dry and Wet Deposition

The surface tracer flux F_s due to dry deposition is presented by means of the deposition velocity $V(z_r)$ and concentration $C(z_r)$ at a reference level z_r as

$$F_s \equiv V(z_r)C(z_r) \tag{3.7.6}$$

For simplicity, the deposition rate is set to F_s/z_r according to Kitada *et al.* (1986).

Concerning wet deposition, only wash-out processes are parameterized. The wet deposition rate is approximated as a function of precipitation intensity P(mm/h) predicted by the meteorological model (GSM) with the below-cloud scavenging ratio per hour given by

$$\Lambda \approx 0.1 \times P^{0.75} \tag{3.7.7}$$

according to Kitada (1994). The Monte Carlo method is applied to decide whether each tracer particle is removed from the atmosphere at the above-mentioned dry and wet deposition rates.

Other specifications of the ATM are presented in Table 3.7.1.

3.7.3 Products

The ATM products consist of the charts of 3D trajectories, of the time integrated pollutant concentrations, and of the total depositions. Sample charts are shown in Figure 3.7.1 - Figure 3.7.7. The way to interpret these products is found in Appendix II-7 of WMO (2010).

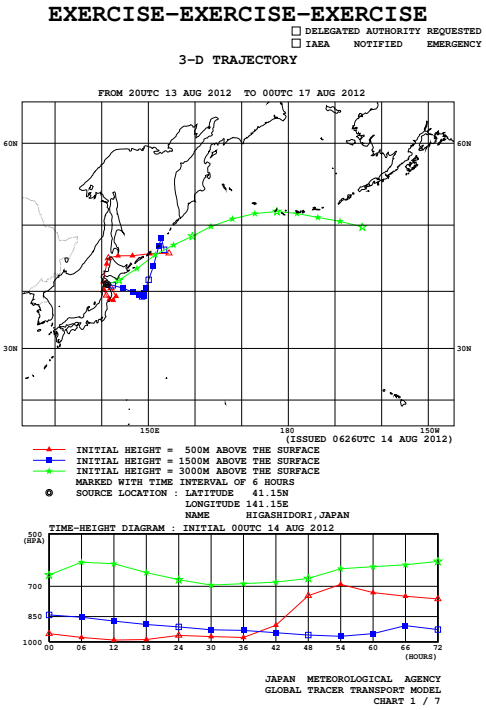

Figure 3.7.1: An example of the 3D trajectories

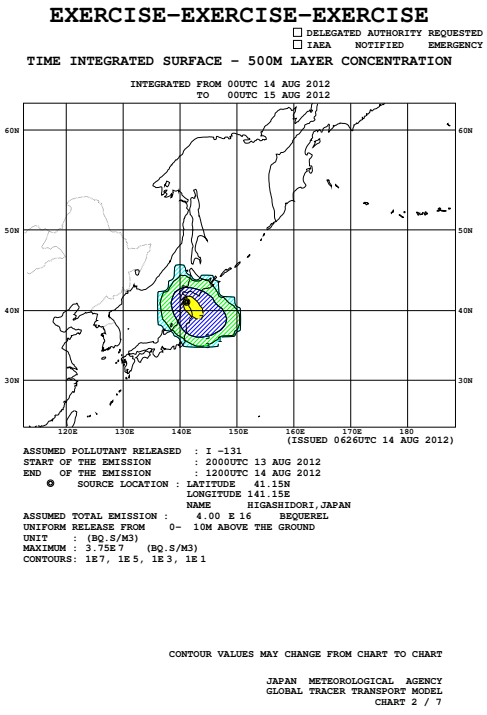

Figure 3.7.2: An example of the time integrated concentration up to 24 hours forecast

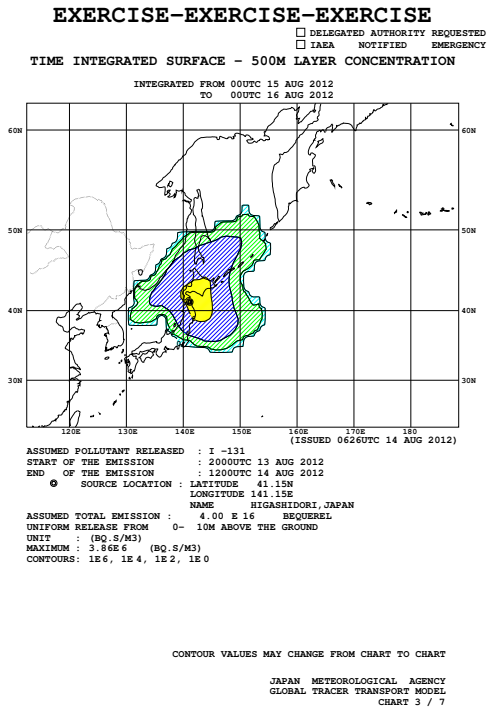

Figure 3.7.3: An example of the time integrated concentration up to 48 hours forecast

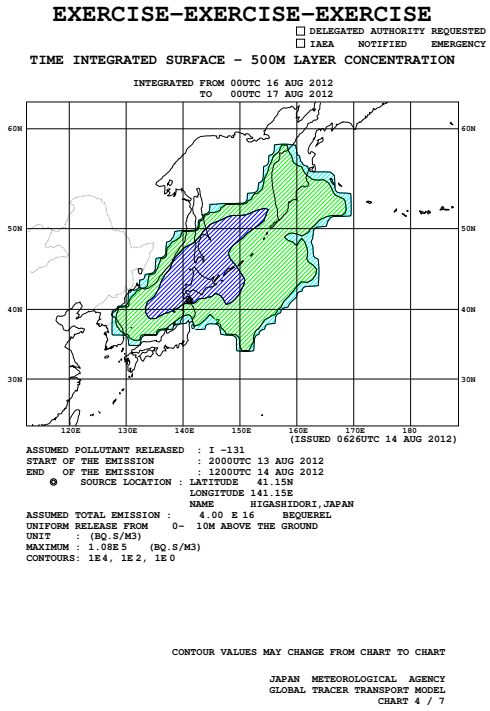

Figure 3.7.4: An example of the time integrated concentration up to 72 hours forecast

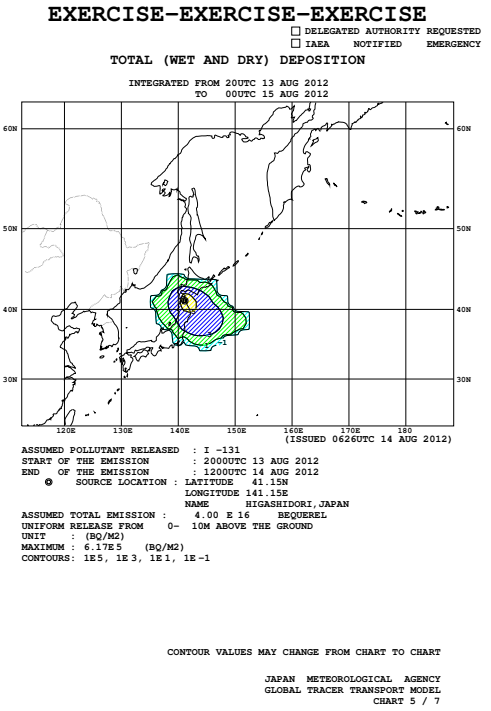

Figure 3.7.5: An example of the total deposition by 24 hours forecast time

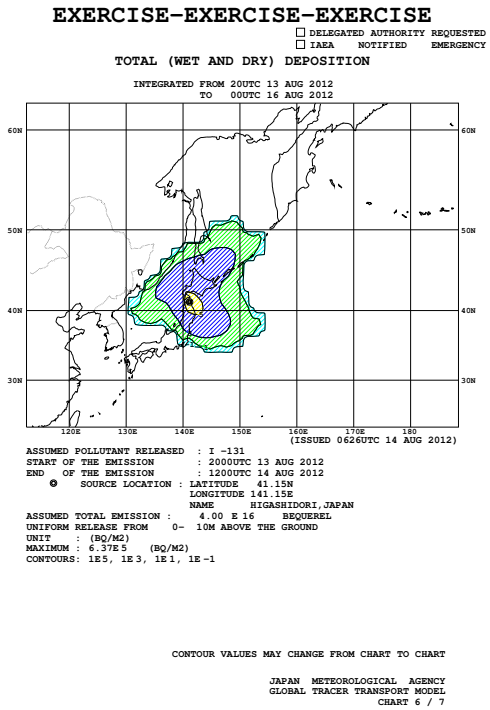

Figure 3.7.6: An example of the total deposition by 48 hours forecast time

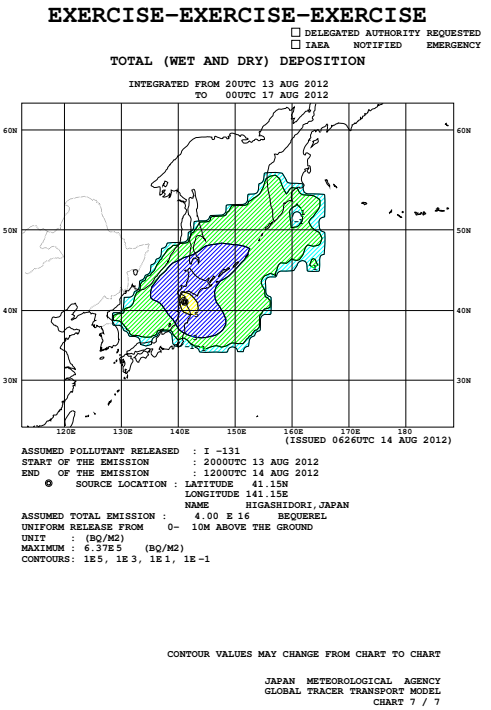

Figure 3.7.7: An example of the total deposition by 72 hours forecast time

3.8 Chemical Transport Model

3.8.1 Introduction

JMA has provided various types of atmospheric environmental information such as a Kosa (Aeolian dust) forecast, UV-index forecast and a photochemical oxidant forecast information through the JMA website (Figure 3.8.1 to Figure 3.8.3), simulated by Chemical Transport Models (CTMs). JMA has operated a Kosa prediction CTM since January 2004, stratospheric ozone CTM for the UV-index prediction system since May 2005 and tropospheric-stratospheric ozone CTM for the photochemical oxidant information since August 2010.

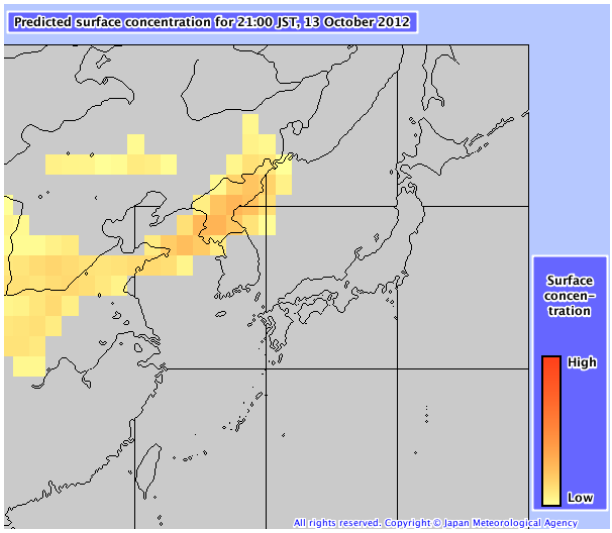

Figure 3.8.1: Kosa information forecast web page(`http://www.jma.go.jp/en/kosafcst/`).

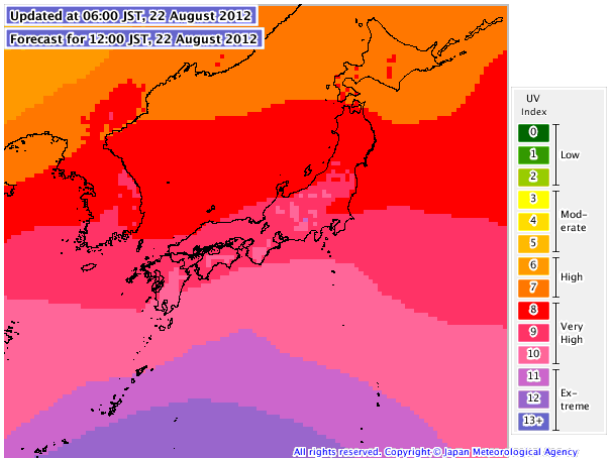

Figure 3.8.2: Clear sky UV index forecast web page(`http://www.jma.go.jp/en/uv/`).

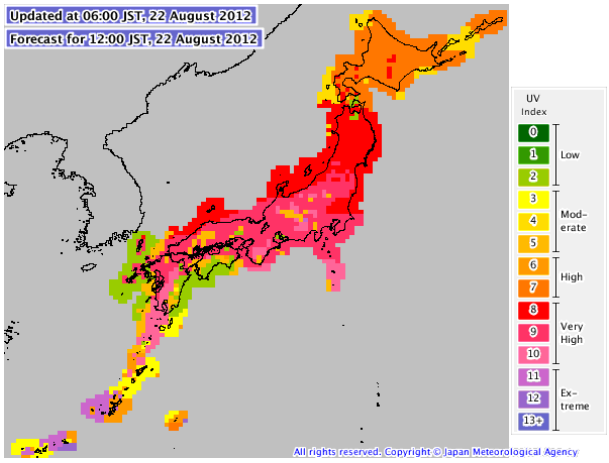

Figure 3.8.3: UV index forecast web page(`http://www.jma.go.jp/en/uv/`).

3.8.2 General Circulation Model

3.8.2.1 Basic Framework

In the CTMs, the chemical modules are directly coupled with a General Circulation Model (MRI/JMA98; Shibata *et al.* (1999)) and use several GCM parameters without any temporal or spatial interpolation. The schematic illustrations of the CTMs structures are shown in Figure 3.8.4 to Figure 3.8.6. The GCM used here is a global spectral model based on an operational weather forecasting model in 1996 (GSM9603) in the JMA, and some improvements are made in physical processes. For example, the solar and terrestrial radiation scheme (Chiba *et al.* 1996) is used to yield temperature distributions in the middle atmosphere with modest accuracy. The soil temperatures are divided into three layers, which are similar to those for soil water, leading to a precise treatment of melting and freezing of water through the consistency between heat and water budgets.

3.8.2.2 Relaxation to Analyzed/Forecasted Field

In general, a CTM needs more computational resources than a GCM because the CTM deals with the more variables and chemical processes than the GCM, and a lower spatial resolution of CTM is adopted for operation. Because of the difference of the resolution and physical and dynamical processes of GCM, the meteorological field will not be consistent with the operational analyzed and forecasted field. To solve this problem, the GCM has a built-in, four-dimensional data assimilation with a nudging scheme incorporating an analyzed and forecasted meteorological field as in Eq. (3.8.1),

$$\left(\frac{\partial x}{\partial t}\right)_{nudging} = -\frac{x - x_{analysis/forecast}}{T} \tag{3.8.1}$$

where x is the dynamical variable, $x_{analysis/forecast}$ is the analyzed/forecasted variable, and T is the time scale of relaxation of 6-24 hours. This scheme enables the CTM to simulate a meteorological field realistically during a forecast period.

3.8.3 Aerosol CTM Used for Kosa Prediction

3.8.3.1 Basic Framework

The Chemical Transport Model used for Kosa prediction was named as a Model of Aerosol Species IN Global Atmosphere (MASINGAR; Tanaka *et al.* (2003)). The MASINGAR consists of transport modules of advective transport (3D semi-Lagrangian scheme), sub-grid scale eddy diffusive and convective transport, and other

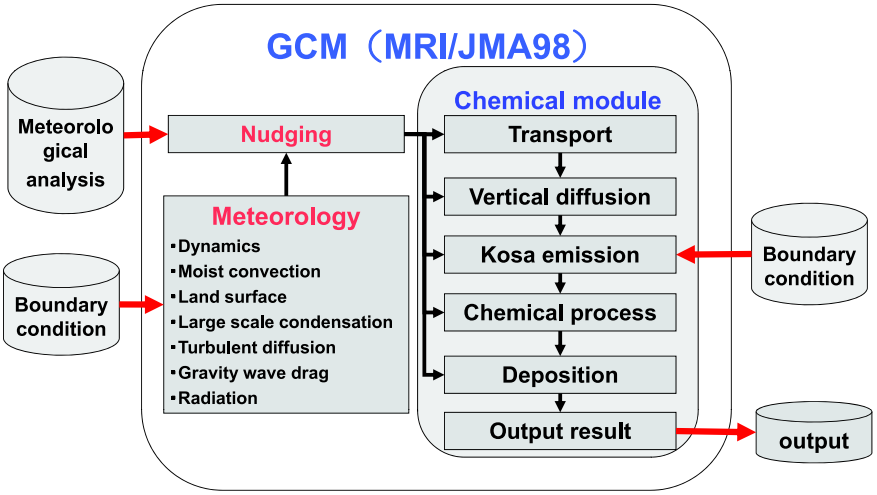

Figure 3.8.4: The schematic illustration of the structure of Kosa CTM.

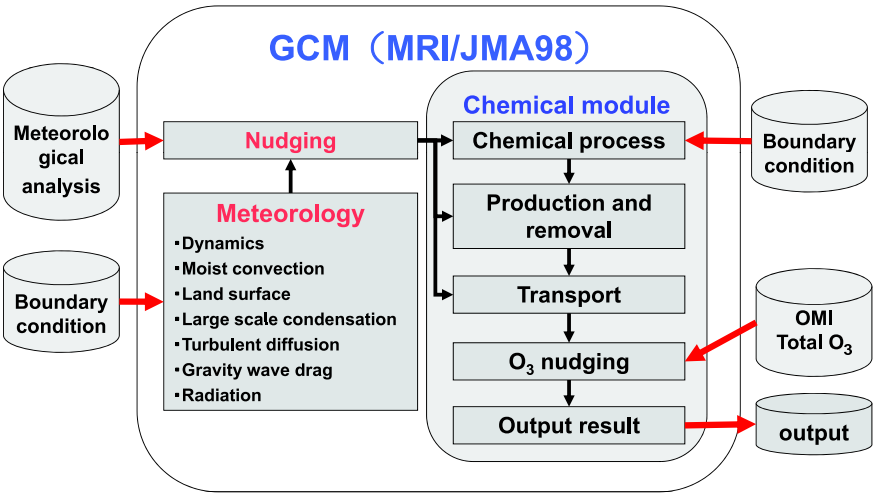

Figure 3.8.5: The schematic illustration of the structure of stratospheric ozone CTM.

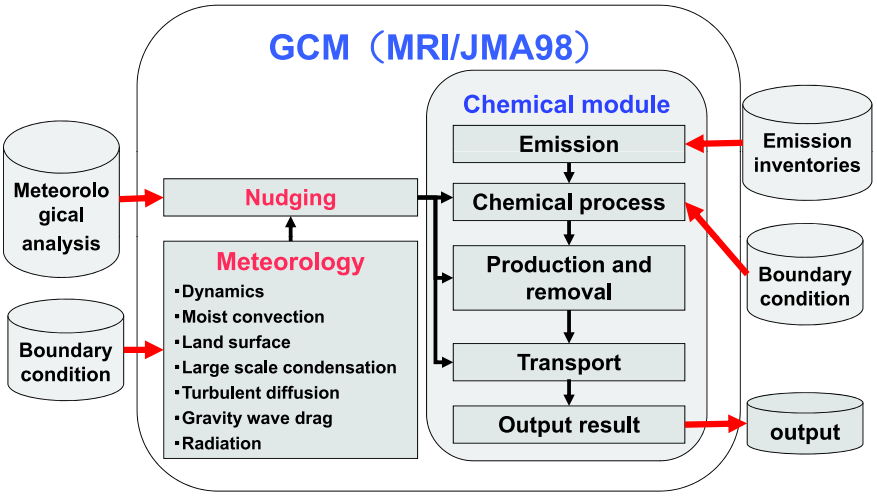

Figure 3.8.6: The schematic illustration of the structure of stratospheric-tropospheric ozone CTM.

modules of surface emission and dry/wet depositions as well as chemical reactions. Although it deals with many types of aerosols such as non-sea-salt sulfate, carbonaceous, mineral dust and sea-salt, only mineral dust aerosol is dealt with in the operational model for Kosa prediction, where the forecast period is 96 hours and the resolution of GCM is T106L30 up to 5 hPa. The vertical resolution of the chemical module is reduced to 20 layers (up to 42 hPa) from 30 of the GCM in order to reduce computational cost. The emission flux of mineral dust aerosol depends on meteorological, geographical and soil surface conditions, such as wind speed, land use, vegetation type, soil moisture and soil types. The dust emission flux F is expressed as a function of dust size and wind speed at 10 m (U_{10}):

$$F = CMA\frac{W_{gt} - W_g}{W_{gt}}\left(U_{10} - U_t\right)U_t^2 \quad \text{for} \quad U_{10} > U_t \text{ and } W_{gt} > W_g \tag{3.8.2}$$

where a threshold wind velocity U_t is set to 6.5 m/s, C is a dimensional factor, M is the mass ratio of dust at a size bin to the total mass, A is the erodible fraction at the surface, W_g is the soil moisture, and W_{gt} is the threshold soil moisture (currently set to 0.3 kg/m^3).

3.8.3.2 Relaxation to Analyzed/Forecasted Field

Due to the lack of real-time and three-dimensional observational data of Kosa aerosol, the chemical module in the MASINGAR is not assimilated with the Kosa aerosol observations. However, because the Kosa emissions are very sensitive to the land surface conditions such as soil water and snow, the chemical module in Kosa prediction model has a nudging system with snow depth analysis. This system improves snow forecast in GCM to be close to the actual snow cover on the surface. The types of datasets used for nudging system in Kosa prediction model is shown in Table 3.8.1.

Table 3.8.1: Types of dataset used for nudging system in Kosa prediction model

	From -24 hour to initial	From initial to 48 hour forecast
Meteorological field	Global analysis	Global forecast
Snow depth	Snow depth analysis	-

Table 3.8.2: Verification indices for categorical forecast

	Observed(ww = 06 – 09, 30 – 35, 98)	Not Observed (ww = 00 – 05)
Forecasted (Surface Kosa concentration is higher than 90μg/m^3)	FO	FX
Not Forecasted (Surface Kosa concentration is lower than 90μg/m^3)	XO	XX

3.8.3.3 Verification

The forecast by the operational Kosa prediction model is verified against the surface synoptic observation (present weather (ww)). We have calculated the model score using categorical verification similar to Appendix A (shown in Table 3.8.2). The threshold value for Kosa forecast is currently set to be 90 μg/m^3. The threat score of the Kosa prediction model at 24 hour forecast in an area of Japan are 0.42, 0.39 and 0.41 in 2009, 2010 and 2011 spring, respectively.

3.8.4 Stratospheric Ozone CTM Used for UV Index Prediction

3.8.4.1 Basic Framework

The stratospheric ozone CTM composed of chemical and transport processes was developed by Shibata *et al.* (2005). The chemical processes, which are based on the family method, contain major stratospheric species, i.e., 34 long-lived species including 7 families and 15 short-lived species with 79 gas phase reactions and 34 photodissociations. The names of these species are shown in Table 3.8.3. The model includes two types of heterogeneous reactions on the surfaces of polar stratospheric clouds (PSCs) and sulfate aerosols. The ozone CTM predicts a 48-hour forecast with a resolution of T42L68 up to 0.01 hPa.

The transport scheme of chemical species adopts a hybrid semi-Lagrangian transport scheme, which is compatibly solved with the continuity equation and has different forms for horizontal and vertical directions (Shibata *et al.* 2005). The horizontal form has an ordinary semi-Lagrangian scheme while the vertical form is equivalent to a mass-conserving flux-form in transformed pressure coordinates specified by the vertical velocity. In addition, the operational global spectral model uses three-dimensional monthly-mean ozone climatology data that were produced by the CTM with nudging towards satellite data (TOMS).

3.8.4.2 Relaxation to Observational Data

The chemical module in the stratospheric ozone CTM has an assimilation system similar to meteorological field (Eq. (3.8.1)), which can assimilate total ozone once a day obtained from the satellite measurement of Ozone Monitoring Instrument (OMI/Aura). The weight of the model guess to OMI data is determined by the ratio of the root mean square errors against the surface observational data. We adopt a third as the ratio of relative contribution of CTM to OMI for nudging. The ozone CTM incorporates a meteorological assimilation system from minus 72 hours to 48 hours with data assimilation to satellite measurements of total ozone, as shown in Table 3.8.4

Table 3.8.3: Names of species used in the stratospheric ozone CTM

Long-lived					
01: N_2O	02: CH_4	03: H_2O	04: NO_y	05: HNO_3	06: N_2O_5
07: Cl_y	08: O_x	09: CO	10: OClO	11: CO_2	12: Aerosols
13: HCl	14: $ClONO_2$	15: HOCl	16: Cl_2	17: H_2O_2	18: $ClNO_2$
19: HBr	20: $BrONO_2$	21: NO_x	22: HO_2NO_2	23: ClO_x	24: BrO_x
25: Cl_2O_2	26: HOBr	27: CCl_4(CFC-10)	28: $CFCl_3$(CFC-11)	29: CF_2Cl_2(CFC-12)	30: Br_y
31: CH_3Cl	32: CH_3Br	33: CF_2ClBr (Halon1211)	34: CF_3Br (Halon1301)		
O_x = O_3 + O(3P) + O(1D)					
ClO_x = Cl + ClO	Cl_y = ClO_x + OClO + $2Cl_2O_2$ + HCl + $ClONO_2$ + HOCl + $2Cl_2$ + $ClNO_2$ + BrCl				
NO_x = NO + NO_2 + NO_3	NO_y = NO_x + N + HNO_3 + $2N_2O_5$ + HO_2NO_2 + $ClONO_2$ + $ClNO_2$ + $BrONO_2$				
BrO_x = Br + BrO + BrCl	Br_y = BrO_x + HBr + HOBr + $BrONO_2$				
Short-lived					
01: O(1D)	02: OH	03: Cl	04: O(3P)	05: O_3	06: HO_2
07: NO_2	08: NO	09: Br	10: N	11: ClO	12: BrO
13: NO_3	14: BrCl	15: H			

Table 3.8.4: Types of datasets used for nudging system in stratospheric ozone CTM

	From -72 hour to initial	From initial to 48 hour forecast
Meteorological field	Global analysis	Global forecast
Total ozone	OMI daily data	-

3.8.4.3 Verification

The predictability of CTM on total ozone was investigated for up to 4 weeks from 1997 to 2000 (Sekiyama and Shibata 2005). Root-mean-square errors (RMSEs) of the control run for the hindcast experiments range from 10 to 30 DU in the whole earth and global average of RMSEs are approximately 10 DU (3% of total ozone) throughout the year. The anomaly correlation between the 5-day forecasts and satellite measurements is approximately 0.6 throughout the year in the extratropical regions in the both hemispheres, suggesting that the model utilizes total ozone forecasts up to 5 days. Furthermore, in the extratropical regions, the model can produce better total ozone forecasts up to 2 weeks.

3.8.4.4 Radiative Transfer Model for UV Index Prediction Using Look-Up Table Method

The surface UV dose is calculated under clear-sky conditions by the radiative transfer model (Aoki *et al.* 2002) in an area from 122°E to 149°E and from 24°N to 46°N with a grid resolution of 0.25° x 0.20°. A Look-Up Table (LUT) method is used to reduce the computational cost. The basic parameters of LUT for the clear-sky UV are the solar zenith angle and the total ozone predicted by the CTM. The clear-sky UV index is derived from clear-sky UV dose corrected by climatological aerosol, distance from the sun, altitude, and climatological surface albedo. The forecast UV index is corrected by a categorization of weather forecast.

The clear sky UV index calculated by the LUT is verified against the observed UV index. The result is shown in Figure 3.8.7. The mean error of the calculated clear sky UV index is 0.0 and the RMSE is 0.5. We find that modeled UV indices are well simulated to observed ones.

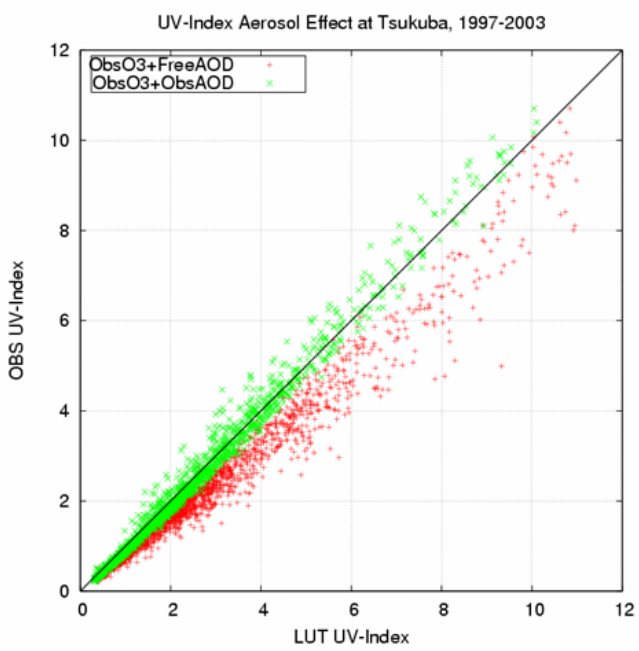

Figure 3.8.7: Relationship between the observed and calculated UV indices. The green cross marks show the UV index with the correction of measured aerosol optical depth and the red-plus marks show the UV index without aerosol correction.

3.8.5 Tropospheric-Stratospheric Ozone CTM Used for Photochemical Oxidant Information

3.8.5.1 Basic Framework

JMA has provided photochemical oxidant information by a CTM for the whole of Japan since August 2010. The information is produced by combining a global tropospheric-stratospheric ozone CTM (MRI-CCM2; Deushi and Shibata (2011)) incorporating chemical transport processes of photochemical oxidants in the troposphere/stratosphere and statistical guidance induced from model outputs associated with past events. The framework of this model is similar to that of the stratospheric ozone CTM (MRI-CCM: referred in Subsection 3.8.4). The MRI-CCM2 was produced to add detailed tropospheric chemistry to the MRI-CCM in order to treat ozone chemistry in both the troposphere and stratosphere seamlessly. The chemistry module includes 90 chemical species (64 for the long-lived species and 26 for the short-lived species) with 172 gas-phase reactions, 59 photolysis reactions and 16 heterogeneous reactions. The names of these species are shown in Table 3.8.5. The forecast period is 72 hours and the resolution is T106L30 up to 0.4 hPa. The model adopted the improved grid-scale transport with a semi-Lagrangian scheme, sub grid-scale convective transport and turbulent diffusion, dry and wet deposition, and emissions of trace gases from various sources.

As for the emission of the trace gases imposed at the surface, we use the statistical inventories shown in Table 3.8.6.

The dynamical module in the MRI-CCM2 also has an assimilation system in the meteorological field. Types of datasets used for nudging system in tropospheric and stratospheric ozone prediction model are shown in Table 3.8.7.

3.8.5.2 Verification

We compared the simulated ozone field to the observation. The simulated seasonal cycle of the ozone mixing ratio at 800 hPa reproduces the observed seasonal cycle at ozonesonde measurement stations (Deushi and

Table 3.8.5: Names of species used in the tropospheric-stratospheric ozone CTM

Long-lived			
01: N_2O	02: CH_4	03: H_2O	04: NO_y
05: HNO_3	06: N_2O_5	07: Cl_y	08: O_x
09: CO	10: OClO	11: CO_2	12: Passive tracer
13: HCl	14: $ClONO_2$	15: HOCl	16: Cl_2
17: H_2O_2	18: $ClNO_2$	19: HBr	20: $BrONO_2$
21: NO_x	22: HO_2NO_2	23: ClO_x	24: BrO_x
25: Cl_2O_2	26: HOBr	27: CCl_4(CFC-10)	28: $CFCl_3$(CFC-11)
29: CF_2Cl_2(CFC-12)	30: Br_y	31: CH_3Cl	32: CH_3Br
33: CF_2ClBr (Halon1211)	34: CF_3Br (Halon1301)	35: COF_2	36: HF
37: CH_2O	38: CH_3OOH	39: C_2H_6	40: CH_3CHO
41: C_2H_5OOH	42: PAN ($CH_3C(O)OONO_2$)	43: $CH_3C(O)OOH$	44: C_3H_8
45: ACET ($CH_3C(O)CH_3$)	46: C_3H_7OOH	47: HACET ($CH_3C(O)CH_2OH$)	48: MGLY ($CH_3C(O)CHO$)
49: C_2H_4	50: GLY ALD ($HOCH_2CHO$)	51: GPAN ($HOCH_2C(O)OONO_2$)	52: GC(O)OOH ($HOCH_2C(O)OOH$)
53: C_3H_6	54: ONIT ($CH_3C(O)CH_2ONO_2$)	55: POOH (HOC_3H_6OOH)	56: C_4H_{10}
57: C_5H_8 (isoprene)	58: MACR	59: ISON	60: ISOPOOH
61: NALD	62: MACROOH	63: MPAN	64: $C_{10}H_{16}$ (terpenes)
Short-lived			
01: O(1D)	02: OH	03: Cl	04: O(3P)
05: O_3	06: HO_2	07: NO_2	08: NO
09: Br	10: N	11: ClO	12: BrO
13: NO_3	14: BrCl	15: H	16: CH_3O_2
17: $C_2H_5O_2$	18: $CH_3C(O)O_2$	19: $C_3H_7O_2$	20: $ACETO_2$ ($CH_3C(O)CH_2O_2$)
21: EO_2 ($HOC_2H_4O_2$)	22: EO (HOC_2H_4O)	23: $GC(O)O_2$ ($HOCH_2C(O)O_2$)	24: PO_2 ($HOC_3H_6O_2$)
25: $ISOPO_2$	26: $MACRO_2$		
Chemical families			
O_x = O_3 + O(3P) + O(1D)			
ClO_x = Cl + ClO			
Cl_y = ClO_x + OClO + $2Cl_2O_2$ + HCl + $ClONO_2$ + HOCl + $2Cl_2$ + $ClNO_2$ + BrCl			
NO_x = NO + NO_2 + NO_3			
NO_y = NO_x + N + HNO_3 + $2N_2O_5$ + HO_2NO_2 + $ClONO_2$ + $ClNO_2$ + $BrONO_2$ + PAN + GPAN + ONIT + ISON + NALD + MPAN			
BrO_x = Br + BrO + BrCl			
Br_y = BrO_x + HBr + HOBr + $BrONO_2$			

Table 3.8.6: The emission inventories of trace gases used in the MRI-CCM2

name	emission sources	coverage
EDGAR v2.0 (Olivier *et al.* 1996)	anthropogenic	global
GEIA (Guenther *et al.* 1995)	natural	global
REAS1.1 (Ohara *et al.* 2007)	anthropogenic	East Asia

Table 3.8.7: Types of datasets used for nudging system in tropospheric-stratospheric ozone CTM

	From -24 hour to initial	From initial to 48 hour forecast
Meteorological field	Global analysis	Global forecast

Shibata 2011). At the Naha station which is located in the East China Sea, the model captures well the observed summertime minimum due to the evolution of continental air mass to a maritime one, which implies that the chemical destruction of O_x in the summer maritime air mass is adequately simulated (Figure 3.8.8).

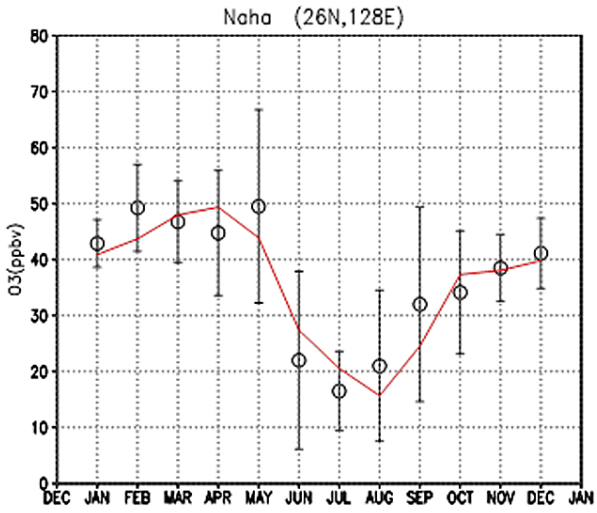

Figure 3.8.8: Annual cycle of observed ozone mixing ratios (in ppb by volume) (open circles) with standard deviations (error bars) at Naha station for the 800 hPa level by ozonesonde measurements, and the simulated mixing ratios (red line) of the FREE-run averaged over 10 years at the corresponding location (Deushi and Shibata 2011).

3.9 Verification

In JMA, the forecast results of the Numerical Weather Prediction (NWP) models are operationally verified against observations and/or analyses. The results of the verification are used for the reference of research and development of the NWP models. The verification results of GSM are exchanged between JMA and the other NWP centers through the Global Data-processing and Forecasting System (GDPFS) of Commission for Basic Systems (CBS) in World Meteorological Organization (WMO), based on the Manual on the GDPFS (WMO 2010a). The standard procedure of the verifications for the deterministic NWP model is coordinated in the Coordination Group on Forecast Verification (CG-FV), CBS (WMO 2012). In this section, the operational verifications for GSM, MSM and One-week EPS are summarized.

The specifications of the verifications for GSM and MSM against analysis are shown in Table 3.9.1. Although the operation of the Regional Spectral Model (RSM) for the east Asian area was discontinued in November 2007, the RSM core region is used for the continuity of the verification. The scores used for the verifications indices are presented in Appendix A. The adjacent zones to the boundaries are excluded from the verification for MSM, because the limited area models such as MSM have lateral boundaries and the adjacent zones to the boundaries are strongly affected by an outer coarse mesh model such as GSM. The remaining areas are called core regions. The forecast performance of GSM including typhoon forecast are described in Subsection 3.2.13. The results of the categorical verification for precipitation forecasts of MSM are presented in Subsection 3.5.11. As mentioned in Section 3.6, LFM was put into operation in August 2012, and the verification results are to be prepared.

Radiosonde data are used for the verification against observations. The specifications of the verification against radiosonde data for GSM and MSM are shown in Table 3.9.2. All of the radiosonde data that have passed quality control are used for the verification for GSM and MSM. The stations of which radiosonde data is to be used in the verification for GSM are selected according to the recommendation of CBS.

Table 3.9.1: Operational Verification against Analysis

	GSM	MSM
Verification Grid Size	2.5°	40km
Element	Z, U, V, T and wind speed at 850, 500 and 250hPa Psea; RH at 850 and 500hPa; total precipitable water	
Score	mean error, root mean square error, anomaly correlation, standard deviation, S1 score	
Time Interval	6 hours	6 hours
Verification Area	NH(90°N – 20°N), SH(20°S – 90°S), TR(20°N – 20°S), RSM core region	MSM core region

Table 3.9.2: Operational Verification against Radiosonde Data

	GSM	MSM
Verification Grid Size	2.5°	40km
Element	Z, U, V, T and wind speed at 850, 500 and 250hPa; RH at 850hPa and 500hPa	
Score	mean error, root mean square error, standard deviation	
Time Interval	12 hours	6 hours
Verification Area	NH,SH,TR, North America, Europe, Asia, Australia, RSM core region	MSM core region

The specifications of the verification against the surface observations for GSM and MSM are shown in Table 3.9.3, Table 3.9.4, and Table 3.9.5. JMA operates a surface observation network with high spatial resolution called Automated Meteorological Data Acquisition System (AMeDAS), which consists of about 1300 stations with raingauges, about 310 stations with snowgauges, and about 840 stations with thermometer, aerovanes and heliographs in Japan. The average intervals of the AMeDAS stations are about 17 km for raingauges and about 21km for the others. The AMeDAS data are used for the verification of forecast performance on both precipitation and temperature at the surface. The observation data are converted into a set of grid mesh data with a uniform spatial resolution of 80 km to be compared with the forecasts and to reduce sampling error of observation. As a consequence, the continuity for the verification is kept, even if the resolutions of models are changed.

The network of C-band Doppler radars (with a wavelength of 5.6 cm) covers most of Japan's territory, and observes rainfall intensity and distribution. Radar data are digitized to produce special radar-echo composite maps every five minutes for the purpose of monitoring precipitation throughout the country. The data are also calibrated with raingauge data of AMeDAS, and are used for a precipitation analysis over the coverage in Japan. Table 3.9.6 shows the specifications of the verification for GSM and MSM against Radar-Raingauge Analyzed Precipitation. Since the precipitation analysis provides very dense (about 1km) information making up for the raingauge data, it is capable to evaluate forecast skills on meso-scale disturbances. It is also used for the verification of typhoon forecast, along with the best track of TC track and central pressure analyzed by the RSMC Tokyo - Typhoon Center in JMA.

A low-resolution version of GSM is used for the operational EPSs (see Section 3.3), which are also verified operationally. The specifications of the verification for One-week EPS are shown in Table 3.9.7. The probabilistic forecasts for the verification is defined as the ratio of the number of ensemble members occurred in an event to the ensemble size at every grid. The verification results for One-week EPS are described in Section 3.3.

Table 3.9.3: Operational Verification against AMeDAS Raingauge Observation (quantitative)

	GSM	MSM
Verification Grid Size	80km	
Score	mean of observation, mean of forecast, root mean square error, correlation, standard deviation of observation, forecast and error	
Time Interval	12 hours	3, 6 and 12 hours
Verification Area	whole and 6 districts of Japan	

Table 3.9.4: Operational Verification against AMeDAS Raingauge Observation (categorical)

	GSM	MSM
Verification Grid Size	80km	
Score	threat score, bias score	
Time Interval	12, 24 hours	3, 6 and 12 hours
Threshold	1, 5, 20, 50mm	
Verification Area	whole and 6 districts of Japan	

Table 3.9.5: Operational Verification against AMeDAS Temperature Observation

	GSM	MSM
Verification Grid Size	80km	
Score	mean error, root mean square error	
Time Interval	3 hours maximum, minimum	3 hours maximum, minimum
Verification Area	whole and 6 districts of Japan	

Table 3.9.6: Operational Verification against Radar-Raingauge Analyzed Precipitation (categorical)

	GSM	MSM
Verification Grid Size	20, 40 and 80km	5, 10, 20, 40 and 80km
Score	threat score, bias score	
Time Interval	3 and 6 hours	1, 3 and 6 hours
Threshold	1, 5, 10, 20mm	1, 5, 10, 20, 50mm
Verification Area	whole of Japan	

Table 3.9.7: Operational Verification for One-week EPS

	Deterministic Verification	Probabilistic Verification	
Analysis	Global analysis on $2.5^\circ \times 2.5^\circ$ grid	Global analysis on $2.5^\circ \times 2.5^\circ$ grid	
Forecast	Ensemble mean and all members	Probability	
Climatology	Climatological fields and standard deviations are calculated from JRA-25. The climatological probability is given by the monthly frequency derived from analysis fields.		
Element	Z at 1000 and 500hPa; T at 850 and 500hPa; U and V at 850 and 250hPa; Psea	Anomalies of Z at 500hPa, T at 850hPa and Psea with thresholds of ±1, ±1.5, and ±2 climatological standard deviation; Anomalies of Z at 500hPa with thresholds of ±25m and ±50m; Psea with thresholds of 1000hPa; Wind speed at 850hPa with thresholds of 10, 15, and 25m/s	Z at 500hPa; T at 850hPa; U and V at 850 and 250hPa; Wind speed at 850hPa; Psea
Score	Mean error, root mean square error, and anomaly correlation	Brier (skill) score, ROC-area (skill) score, and relative economic value	Continuous rank probability score
Time Interval	12 hours	24 hours	
Verification Area	NH extra-tropics, East Asia, Japan, Tropics, Western Pacific, SH extra-tropics, NH, SH, North America, Europe, and Asia		

Chapter 4

Application Products of NWP

4.1 Summary

The results of NWP are indispensable elements to weather forecasting both for general public and for special purposes, and therefore JMA disseminates them in real time to the local offices of JMA, private companies, and related organizations both in Japan and abroad. Although facsimile charts have been the primary means of distributing NWP output for a long time, at the present time dissemination in the form of Grid Point Values (GPV) is the essential method with the progress of telecommunication infrastructure and sophisticated visualization systems.

In addition to the raw NWP data, value-added products derived from NWP output are also disseminated. One example of such products is information on parameters not explicitly calculated in NWP models, such as probabilistic forecasts and turbulence potential for aviation. Another is error-reduced estimation of NWP output parameters, with statistics of the relationship between NWP output and the corresponding observation. JMA has been disseminating Very-short-range (6 hour) Forecast of Precipitation and the Hourly Analysis of horizontal wind and temperature field, a three-dimensional variational (3D-Var) method is utilized for Hourly Analysis. To support middle to long-range forecasting, JMA has been disseminating various kind of forecast charts and Grid Point Value for one-week forecast and one-month and seasonal forecast.

In the following sections, specification of Application Products of NWP and their utilization in the JMA offices are demonstrated.

4.2 Weather Chart Services

Facsimile chart is a conventional service to disseminate the result of NWP in a graphical form. The JMA's facsimile charts are sent to national meteorological services via the Global Telecommunication System (GTS) and to ships via the shortwave radio transmission (call sign JMH).

Table 4.2.1 and Figure 4.2.1 give summaries of weather charts easily accessible for international users, namely charts served through GTS and JMH.

The Web is emerging alternative to complement and innovate above services. A number of projects are running worldwide. JMA takes part in international projects such as Project on the Provision of City-Specific Numerical Weather Prediction (NWP) Products to Developing Countries via the Internet in the WMO Regional Association II (RA II) or the Severe Weather Forecast Demonstration Project (SWFDP) in WMO RAs II and V. There are also JMA's own projects, such as JMA Pilot Project on EPS Products or SATAID Services on the WMO Information System.

Table 4.2.1: List of facsimile charts provided through GTS and radio facsimile JMH. Symbols for vertical level: Surf: surface, Trop: tropopause, numbers (850, 700, ... 100): level of pressure in hPa; Symbols for contours: D: dewpoint depression ($T - T_d$), E: precipitation (over past 12h for 24h forecast, or past 24h for others), H: geopotential height, J: wave height, O: vertical velocity (ω), P: MSL pressure, T: temperature, W: wind speed (isotach), Z: vorticity, μ: time average, δ: time average and anomaly from climatology; Symbols for other drawings: a: wind arrow from GPV, b: observation plots, d: hatch for area $T - T_d < 3$K, g: arrow for prevailing wave direction, j: jet axis, m: wave period, t: temperature numbers, x: streamlines; Symbols for dissemination and temporal specialty: ': sent to GTS, *: sent to JMH, §: only for 12 UTC, †: average over pentad, sent only for 00 UTC five-daily, ‡: average over month, sent only for 00 UTC monthly.

Model	Area (see Figure 4.2.1)	Forecast Time						
		Analysis	12h	24h	36h	48h 72h	96h 120h	144h 168h 196h
GSM	A' (Far East)	500 (H, Z)' 850 (T; a)+700 (O)'		500 (T)+700 (D)'* 500 (H, Z)'* 850 (T, W)+700 (O)'* Surf(P, E; a)'*				
	C (East Asia)	300 (H, W; a, t, b)'* 500 (H, T; a, b)' 700 (H, T; b, d)' 850 (H, T; b, d)'*		Surf(P, E)'		500 (H, Z)' 850 (T, W)+700 (O)'§ Surf(P, E)'*	Surf(P, E)*§	
	O (Asia)						500 (H, Z)'§ Surf(P)+850 (T)'§	
	Q (Asia-Pacific)	200 (H, W; t, a, j)+Trop(H)' 250 (H, W; t, a)'		250 (H, W; t, a)' 500 (H, W; t, a)'				
	Q (NW Pacific)	200 (x)' 850 (x)'		200 (x)' 850 (x)'				
	D (N Hem.)	500 (H, T)'						
Ocean Wave	X (Japan)	Surf(J; b, g, m)'*						
	C" (NW Pacific)	Surf(J; b, g, m)'*	Surf(J; g, m)*			Surf(J; g, m)*		
JCDAS	D' (N.Hem.)	100 (μH, δH)'† 500 (μH, δH)'† 500 (μH, δH)'‡ Surf(μP, δP)'‡						

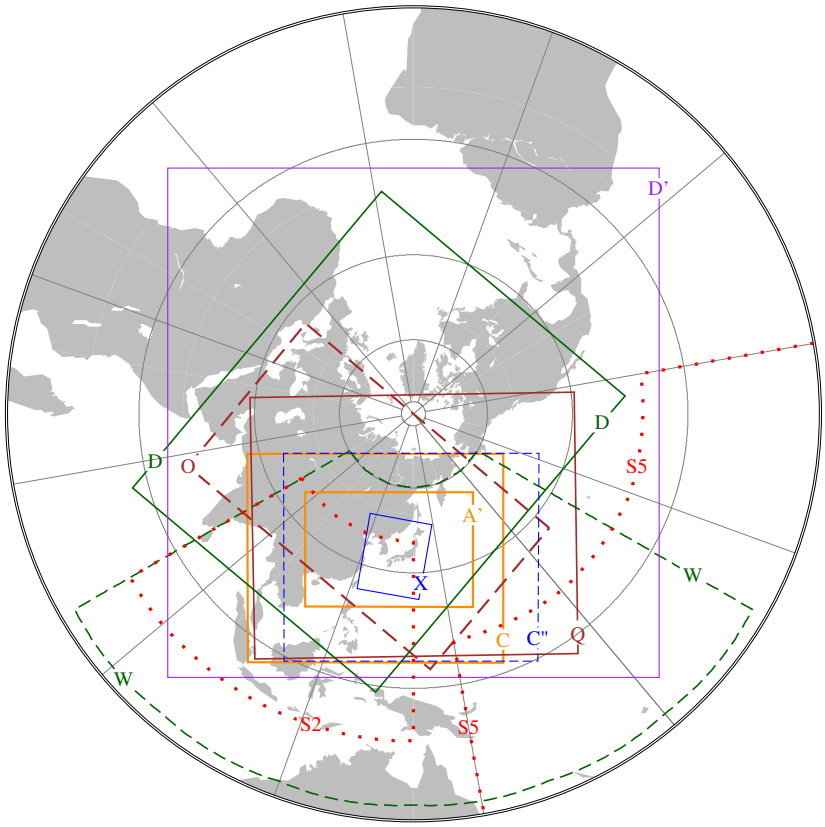

Figure 4.2.1: Areas for charts disseminated through GTS and radio facsimile JMH (symbols A', C, C", D, D', O, Q, W, and X). Dotted boxes labeled S2 and S5 are areas of SWFDP products for WMO Regional Associations II and V, respectively (for information).

4.3 GPV Products

As a part of JMA's general responsibility of meteorological information service, the grid point values (GPV) products are distributed to domestic and international users. In conformance to requirement of the WMO Information System (WIS), this data service utilizes both dedicated and public (i.e. the Internet) network infrastructure.

The dedicated infrastructure consists of an international part called GTS, together with domestic parts inside JMA (including the Meteorological Satellite Center and the Meteorological Research Institute) and toward government agencies and Meteorological Business Support Center, which is in charge of managed service for general users including the private sector.

The portal to JMA's international services over the Internet is the website of Global Information System Centre (GISC) Tokyo [1]. The WMO Distributed Data Bases (DDBs) and RSMC Data Serving System (RSMC DSS) are integrated into GISC Tokyo. Currently the international service of GPV products includes GSM, One-week EPS, and Ocean Wave Model, as listed in Table 4.3.1.

4.4 Very-short-range Forecasting of Precipitation

JMA has been routinely operating a fully automated system for semi-hourly analysis and very-short-range forecasting of precipitation since 1988 to provide products for monitoring and forecasting local severe weather. The products are :

1. Analysis of precipitation called the "Radar-Raingauge Analyzed Precipitation" (hereafter R/A) based on the radar observations operated by JMA and the other organization and the raingauge measurements operated by JMA(the Automated Meteorological Data Acquisition System, hereafter AMeDAS) and the other organizations,

2. Semi-hourly forecasts of 1-hour accumulated precipitation called the "Very-Short-Range-Forecasting of Precipitation" (hereafter VSRF) based on extrapolation and forecast by the Meso-scale Model (MSM, see Section 3.5). The forecast time of VSRF is from 1 to 6 hour.

The spatial resolution of these products are 1km. These products are made available in about 20 minutes after observation time every half hour. They are transmitted to local meteorological observatories, and the local governments and broadcasting stations which are responsible for disaster prevention.

4.4.1 Analysis of Precipitation (R/A)

R/A uses data of 46 radars (JMA 20, the other organization 26) and up to about $10,000$ raingauges (AMeDAS $1,300$, the other organizations $8,700$). These data are combined to benefit from advantages of both facilities: the advantage of the radar is its high resolution in space and that of raingauge is its high accuracy of precipitation measurement.

The one-hour accumulated precipitation amounts estimated using radar observation are usually different from those observed with raingauges. The radar precipitation amounts are calibrated into more accurate precipitation using the raingauge precipitation data (Makihara 2000). First, calibration factors over the entire detection range of each radar are calculated by comparing the radar precipitation of the multiple radars and raingauge data. When comparing radar precipitation, the difference of radar beam height is taken into account. Then the estimated calibration factor is further modified using raingauge data to estimate local heavy precipitation more accurately at each grid which contains raingauges. For the grid has no raingauges, the modified calibration factors is calculated with weighted interpolation of the calibration factors of the surrounding grids that contain raingauges. Composition of all radar's calibrated precipitation into a nationwide chart is made by the maximum value method, in which the largest value is selected if a grid has several data observed by multiple radars. A schematic diagram of this procedure is shown in Figure 4.4.1.

[1] http://www.wis-jma.go.jp

Table 4.3.1: List of GPV products transmitted through GTS and GISC Tokyo website. Symbols for contents: C_L: low cloud amount, C_M: middle cloud amount, C_H: high cloud amount, D: dewpoint depression ($T - T_d$), E: precipitation (from initial time), G: prevailing wave direction, H: geopotential height, J: wave height, M: wave period, N: total cloudiness, O: vertical velocity (ω), P: MSL pressure, P_S: surface pressure, R: relative humidity, T: temperature, U: eastward wind speed, V: northward wind speed, X: stream function, Y: velocity potential, Z: vorticity, μ: average over ensemble, σ: standard deviation over ensemble. Symbols °, *, ¶, §, †, ‡are notes on availability, and are explained inside the table.

Model	GSM	GSM	GSM	GSM
Service Channel	GISC	GTS and GISC	GTS and GISC	GISC
Code form	GRIB Edition 1	GRIB Edition 1	GRIB Edition 1	GRIB Edition 2
Area	Whole Globe	20°S–60°N 60°E–160°W	Whole Globe	Whole Globe and also 5°S–90°N, 30°E–165°W
Resolution	1.25° × 1.25°	1.25° × 1.25°	2.5° × 2.5°	0.5° × 0.5° (0.25° × 0.25° for surface)
Contents 10, 20 hPa	H, U, V, T	H, U, V, T	H*, U*, V*, T*	H, U, V, T, R, O
30, 50, 70, 100 hPa	H, U, V, T	H, U, V, T	H°, U°, V°, T°	H, U, V, T, R, O
150 hPa	H, U, V, T	H, U, V, T	H*, U*, V*, T*	H, U, V, T, R, O
200 hPa	H, U, V, T, X, Y	H§, U§, V§, T§, X, Y	H, U, V, T	H, U, V, T, R, O, X, Y
250 hPa	H, U, V, T	H, U, V, T	H°, U°, V°, T°	H, U, V, T, R, O
300 hPa	H, U, V, T, R, O	H, U, V, T, D	H, U, V, T, D*‡	H, U, V, T, R, O
400 hPa	H, U, V, T, R, O	H, U, V, T, D	H*, U*, V*, T*, D*‡	H, U, V, T, R, O
500 hPa	H, U, V, T, R, O, Z	H§, U§, V§, T§, D§, Z	H, U, V, T, D*‡	H, U, V, T, R, O, Z
600 hPa	H, U, V, T, R, O			H, U, V, T, R, O
700 hPa	H, U, V, T, R, O	H§, U§, V§, T§, D§, O	H, U, V, T, D	H, U, V, T, R, O
800 hPa				H, U, V, T, R, O
850 hPa	H, U, V, T, R, O, X, Y	H§, U§, V§, T§, D§, O, X, Y	H, U, V, T, D	H, U, V, T, R, O
900 hPa				H, U, V, T, R, O
925 hPa	H, U, V, T, R, O	H, U, V, T, D, O		H, U, V, T, R, O
950, 975 hPa				H, U, V, T, R, O
1000 hPa	H, U, V, T, R, O	H, U, V, T, D	H, U*, V*, T*, D*‡	H, U, V, T, R, O
Surface	P, U, V, T, R, E†	P¶, U¶, V¶, T¶, D¶, E¶	P, U, V, T, D‡, E†	P, U, V, T, R, E†, P_S, N, C_L, C_M, C_H
Forecast time range (*from–until/interval*)	0–84h/6h †: except for analysis	0–84h/6h	0–72h/24h *: Analysis only	0–84h/3h
Extension on 12UTC	96–192h/12h	§: 96–192h/24h ¶: 90–192h/6h	96–192h/24h °: 96–120h/24h	90–216h/6h
Initial times	00UTC and 12UTC	00UTC and 12UTC	00UTC and 12UTC ‡: 00UTC only	00, 06, 12, 18UTC

Model	One-week EPS	Ocean Wave Model
Service Channel	GTS and GISC	GISC
Code form	GRIB Edition 1	GRIB Edition 1
Area	Whole Globe	75°S–75°N, 0°E–358.75°E
Resolution	2.5° × 2.5°	1.25° × 1.25°
Contents 250 hPa	μU, σU, μV, σV	
500 hPa	μH, σH	
850 hPa	μU, σU, μV, σV, μT, σT	
1000 hPa	μH, σH	
Surface	μP, σP	J, M, G
Forecast time range	0–192h/12h	0–84h/6h
Extension on 12UTC	(none)	96–192h/12h
Initial times	12UTC only	00UTC and 12UTC

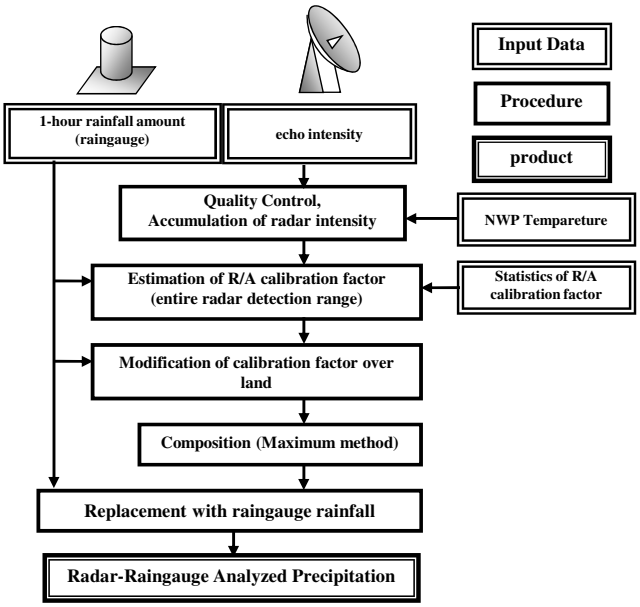

Figure 4.4.1: A flow chart of the "Radar- Raingauge Analyzed Precipitation"

4.4.2 Forecasting of Precipitation (VSRF)

Two methods are used for VSRF. One is the extrapolation of movements of the analyzed precipitation systems. In the course of extrapolation, development and decay of the precipitation systems due to the orographic effects and the echo intensity trends are taken into account. The other is the precipitation forecast of MSM, which is available in about two hours later from its initial time, eight times a day (every three hours). The extrapolation forecasts are more skillful than the MSM forecasts at first, but they rapidly lose skill. On the other hand, the skill of the MSM forecasts degrades gradually and becomes comparable with the extrapolation forecasts after a few forecasting hours. Therefore the so-called "merging technique" was introduced. It is essentially the weighted-averaging of those two precipitation forecasts. For the first one hour, the merging weights are set nearly zero for the MSM forecasts, so the products are almost the same as the extrapolation forecasts. After that, the merging weights for the MSM forecasts increase with forecast time. The merging weights are determined by comparing skills of the MSM forecasts and the extrapolation forecasts. A schematic diagram of this procedure is shown in Figure 4.4.2.

4.4.2.1 Extrapolation Forecasts

The calibrated precipitation intensity, which is obtained in the course of the precipitation analysis (Subsection 4.4.1), is used as the initial value of the forecast. A time step of the forecast is two or five minutes and the forecasted precipitations are accumulated to produce hourly forecasts up to six hours.

The extrapolation vectors (the movement vectors of precipitation systems) are evaluated by a generalized cross correlation method, comparing the location of the precipitation systems at the initial time with those at 0.5, 1, 2 and 3 hours before.

As the seeder-feeder mechanism is assumed to work in the regions of orographic updraft, the precipitation systems are allowed to develop in the course of extrapolation over such regions. Precipitation systems that have passed across mountains higher than its echo top height are decayed, when the following two conditions are satisfied:

1. orographic downslope motion of the rain system is expected from the low-level wind of MSM,

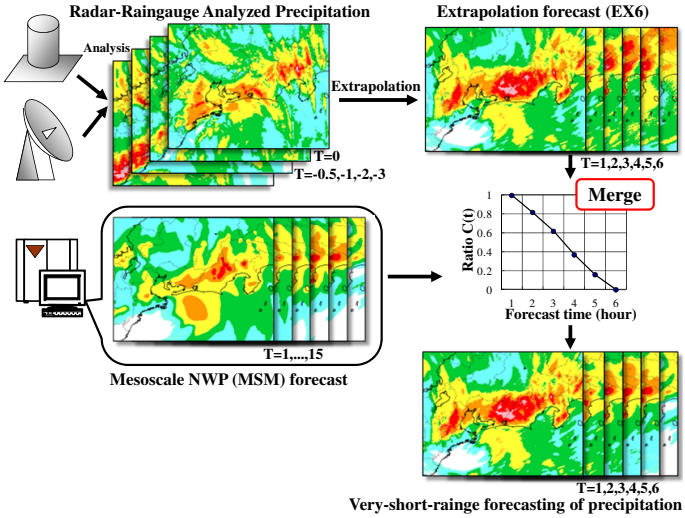

Figure 4.4.2: A schematic diagram of the very-short-range forecasting of precipitation

2. the direction of the rain system movement or that of 700hPa wind by MSM is nearly parallel to that of 900hPa wind by MSM.

And the echo intensity trends can be obtained by comparing the current area average of the echo intensity to the past one. The movement vectors for the intensity trends are calculated in addition to the extrapolation vectors. The vectors move the echo intensity trends and the trends change the forecasted precipitations.

4.4.2.2 Merging Technique

First, the relative skill of the extrapolation forecast and the MSM forecast are estimated. The extrapolation forecast from three hours before is verified against the current analysis. For the MSM forecast, the latest available forecast is verified with the current analysis. The relative reliability coefficient C_{RR} is defined as follows:

$$C_{RR} = \min\left(1, \frac{D_{EX}}{D_{MSM}}\right) \tag{4.4.1}$$

where D_{EX} is the 2-dimensional pattern distance, or 2-dimensionally extended Levenshtein distance, between the extrapolation forecast and the analysis, and D_{MSM} is the 2-dimensional pattern distance between the MSM forecast and the analysis.

Then, the relative weight of the extrapolation forecast $C_{EX}(T)$ is determined by C_{RR} and the statistically determined function $C(T)$ indicated at merge process in Figure 4.4.2, where T denotes the forecast time in hour:

$$C_{EX}(T) = 1 - C_{RR} \cdot (1 - C(T)) \tag{4.4.2}$$

Finally the merged forecast $R_{MRG}(T)$ is calculated with the following equation:

$$R_{MRG}(T) = C_{EX}(T) \cdot R_{EX}(T) + (1 - C_{EX}(T)) \cdot R_{MSM}(T) \tag{4.4.3}$$

where $R_{EX}(T)$ denotes the extrapolation forecasts of precipitation at the forecast time T, and $R_{MSM}(T)$ denotes the MSM forecasts of precipitation from the latest initial time at the same valid time T.

4.4.3 Example and Verification Score

An example of the R/A and VSRF is shown in Figure 4.4.3. The R/A in the Kyushu region, southwestern area of Japan at 20UTC 23 June 2012 is shown in the left panel (a), and the 3-hour forecast of VSRF at the same valid time, i.e. its initial time is at 17UTC 23 June 2012, is shown in the right panel (b). The intense rain band is well forecasted.

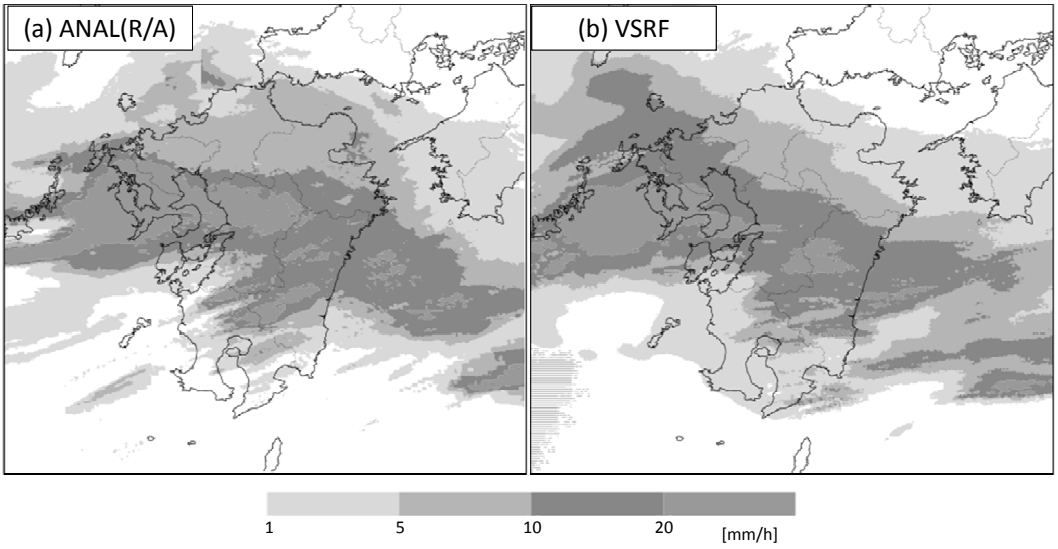

Figure 4.4.3: An example of (a) the Radar-Raingauge Analyzed Precipitation at 20UTC 23 June 2012 and (b) the 3-hour forecast of precipitation of VSRF at the same valid time

The accuracy of VSRF has been statistically verified with the Critical Success Index (CSI)[2]. Forecasts are compared with precipitation analysis after both fields are averaged in 20km $\times$ 20km grids. The threshold value is set as 1mm/hr. Indices from 1-hour to 6-hour forecasts for June 2012 are shown in Figure 4.4.4, together with those of the extrapolation, MSM, and the persistence forecasts.

It can be seen that the scores get worse as forecast time gets longer. Up to three hours, the extrapolation forecast keeps its superiority to MSM, but the relationship of them becomes reverse after four hours, while VSRF behaves best performance through all forecast times.

4.5 Hourly Analysis

The hourly analysis provides grid point value data of three-dimensional temperature and wind analysis every hour, assisting forecasters in monitoring the atmosphere. Imagery products are also available to users in the aviation sector through a meteorological information web page.

The configuration of the hourly analysis system is listed in Table 4.5.1. The hourly analysis uses an objective analysis scheme of a 3-dimensional variational (3D-Var) method, which is implemented as a part of the "JMA Nonhydrostatic model"-based Variational Analysis Data Assimilation (JNoVA; Honda *et al.* 2005). The analysis uses the latest Meso-scale Model (MSM, Section 3.5) forecast as the first guess (a 2-4 hour forecast depending on the analysis time). The domain of the hourly analysis is the same as that of the MSM (MA) (Figure 2.6.2), covering Japan and its surrounding area (3,600 km by 2,880 km) at the same horizontal resolution as that in the MSM (with a grid spacing of 5 km). The hourly analysis has fifty vertical layers defined in the z*-coordinate, with the top of the domain at 21,801 m.

[2]The CSI is the number of correct "yes" forecasts divided by the total number of occasions on which that event was forecast and/or observed. It is also cited as "Threat Score".

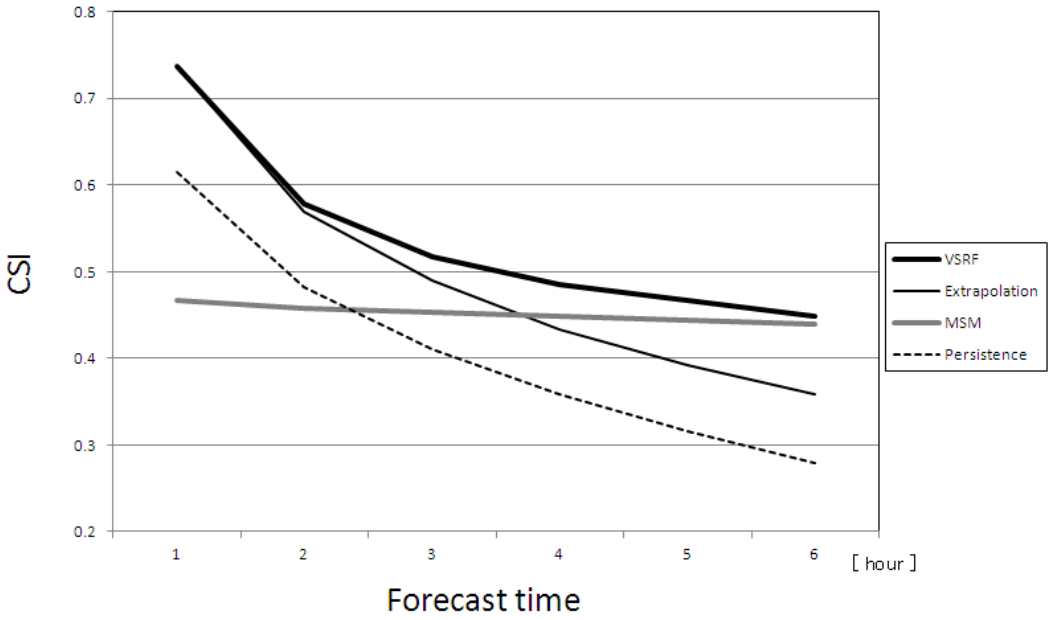

Figure 4.4.4: CSI of the very-short-range forecasting (VSRF) of precipitation averaged within the 20km×20km grids for June 2012, together with that of the extrapolation, MSM, and the persistence forecast. Threshold value is 1mm/hr.

The observations assimilated in the analysis are from wind profilers (wind), Doppler radars (radial velocity), ACARS (Aircraft Communications Addressing and Reporting System, wind and temperature), satellite AMV (Atmospheric Motion Vector, wind), and AMeDAS (Automated Meteorological Data Acquisition System, surface station data over Japan, wind and temperature). The data cut-off time is set to 20 minutes past the hour to enable the product to be distributed before 30 minutes past the hour.

In order to obtain a good fit to the surface observations on land, the 3D-Var analysis uses a short background error correlation distance and a small observation error on the surface. Thus, the surface field on land has typically large increments. The followings are modifications of the 3D-Var scheme and additional post-processings introduced to handle this situation appropriately.

Table 4.5.1: Configuration of the hourly analysis system.

analysis scheme	3D-Var
analysis time	every hour (on the hour)
observation	wind profilers (wind), Doppler radars (radial velocity), ACARS (wind and temperature), satellite AMV (wind), AMeDAS (wind and temperature)
cut-off time	20 minutes past the hour
first guess	the latest MSM forecast (forecast time = 2-4h)
analysis variable	horizontal wind (u and v components), temperature
domain	the MSM domain (3,600km by 2,880 km, grid spacing 5km), 50 vertical layers
product distribution	around 30 minutes past the hour

- In the 3D-Var analysis, the surface and the upper air fields are treated as uncorrelated. Thus, the surface observations only have contribution to analysis increments on the surface, but not to those in the upper air. Analysis increments on the surface and in the upper air are not consistent at this point.
- After the 3D-Var analysis is completed, a surface filter is applied on the surface temperature and wind fields. This filter is designed to attenuate the surface increments over the sea with distance from the coastline, reducing excessive increments in sea regions near the coastline located within the range of correlation from the land observations.
- After applying the surface filter, the increments on the surface and in the upper air are merged in each vertical column within the boundary layer of the first guess. This makes the surface and the upper air increments consistent. The weight of the surface increment attenuates with height above the ground, and approaches to zero at about the height of the boundary layer.

4.6 Guidance for Short-range Forecasting

4.6.1 Overview

To provide the first guess of forecast target to forecasters, various kinds of forecast guidance are produced from the output of the NWP models. The parameters of the guidance for short-range (up to 84 hours) forecasting are listed in Table 4.6.1.

Table 4.6.1: Parameters of the guidance products for short-range forecasting

Parameters	Target		Model	Forecast hour	Method*
Categorized weather over 3 hours (fair, cloudy, rainy, sleety, snowy)	Grids	20km	GSM	KT=6,9,12,. . .,81,84	NRN
		5km	MSM	KT=3,6,9,. . .,30,33	
Mean precipitation amount over 3 hours	Grids	20km	GSM	KT=6,9,12,. . .,81,84	KF & FBC
		5km	MSM	KT=3,6,9,. . .,30,33	
Maximum precipitation amount over 1, 3 and 24 hours	Grids	20km	GSM	KT=6,9,12,. . .,81,84	KF & NRN
		5km	MSM	KT=3,6,9,. . .,30,33	
Probability of precipitation over 6 hours > 1mm/6h	Grids	20km	GSM	KT=9,15,21,. . .,75,81	KF
		5km	MSM	KT=6,12,18,. . .,24,30	
Maximum temperature in the daytime (09-18 local time)	Points	AMeDAS	GSM	Today to 3 days after	KF
			MSM	Today and tomorrow	
Minimum temperature in the morning (00-09 local time)	Points	AMeDAS	GSM	Today to 3 days after	KF
			MSM	Today and tomorrow	
Time-series temperature	Points	AMeDAS	GSM	KT=3,4,5,. . .,81,84	KF
			MSM	KT=1,2,3,. . .,32,33	
Wind speed and direction	Points	AMeDAS	GSM	KT=3,6,9,. . .,81,84	KF & FBC
			MSM	KT=1,2,3,. . .,32,33	
Maximum wind speed and direction over 3hours	Points	AMeDAS	GSM	KT=3,6,9,. . .,81,84	KF & FBC
			MSM	KT=3,6,9,. . .,30,33	
Daily minimum humidity	Points	SYNOP	GSM	Today to 3 days after	NRN
			MSM	Today and tomorrow	
Snowfall amount over 12 hours	Points	AMeDAS	GSM	KT=24,36,48,60,72	NRN
Maximum snowfall amount over 3,6,12 and 24 hours	Grids	5km	GSM	KT=6,9,12,. . .,81,84	DIAG
			MSM	KT=3,6,9,. . .,30,33	
Probability of thunderstorm over 3 hours	Grids	20km	GSM	KT=6,9,12,. . .,81,84	LGR
			MSM	KT=6,9,12,. . .,30,33	

∗ KF: Kalman Filter, NRN: Neural Network, LGR: Logistic Regression, FBC: Frequency Bias Correction, DIAG: Diagnostic method

The first objective of the guidance is to reduce forecast errors, mainly bias errors, of NWP output such as in surface temperature. The second objective is to derive quantitative values of parameters not directly calculated in the NWP models, such as probability of precipitation.

To cope with frequent model upgrades, JMA developed methods of adaptively correcting the statistics of the relationship between NWP output and the corresponding observation. The methods, based on Kalman Filter and Neural Network, were put into operational use for the first time in 1996. Since then the adaptive

methods have been applied to most of the parameters, replacing the formerly used non-adaptive multivariate regression method.

In the following subsections, Kalman Filter and Neural Network used in the guidance system are explained in Subsection 4.6.2 and Subsection 4.6.3, respectively, and the utilization of the guidance in forecasting offices is summarized in Subsection 4.6.4.

4.6.2 Guidance by Kalman Filter

4.6.2.1 Kalman Filter

As a statistical post-processing method of NWP output, Kalman Filter (KF) was developed in JMA on the basis of earlier works of Persson (1991) and Simonsen (1991). The notation of KF, which basically follows that of Persson (1991), is as follows:

y: predictand (target of forecast)

$\boldsymbol{c}$: predictors ($1 \times n$ matrix)

$\boldsymbol{X}$: coefficients ($n \times 1$ matrix)

$\boldsymbol{Q}$: covariance of $\boldsymbol{X}$ ($n \times n$ matrix)

τ: sequence number of NWP initial times

First, the observation equation, which is a linear model for relating the predictand with the pre-selected predictors, and the system equations are given as:

$$y_\tau = \boldsymbol{c}_\tau \boldsymbol{X}_\tau + v_\tau \tag{4.6.1}$$

$$\boldsymbol{X}_{\tau+1} = \boldsymbol{A}_\tau \boldsymbol{X}_\tau + \boldsymbol{u}_\tau \tag{4.6.2}$$

where v_τ is the observational random error whose variance is D_τ, and $\boldsymbol{u}_\tau$ is the random error vector of the system, whose covariance matrix is $\boldsymbol{U}_\tau$. The matrix $\boldsymbol{A}_\tau$ describes the evolution of the coefficients in time and is set to the unit matrix in this case;

$$\boldsymbol{A}_\tau \equiv \boldsymbol{I} \tag{4.6.3}$$

The objective of KF is to obtain the most likely estimation of the coefficients $\boldsymbol{X}_{\tau+1/\tau}$, whose subscripts denote that this is an estimate using the observation corresponding to the forecast at τ and used for the prediction at $\tau + 1$. In contrast, single subscripts in Eq. (4.6.1) and Eq. (4.6.2) denote the "true" values at τ. $\boldsymbol{X}_{\tau+1/\tau}$ is obtained from the previous estimate $\boldsymbol{X}_{\tau/\tau-1}$ and the forecast error:

$$\boldsymbol{X}_{\tau+1/\tau} = \boldsymbol{X}_{\tau/\tau} \tag{4.6.4}$$

$$= \boldsymbol{X}_{\tau/\tau-1} + \delta_\tau (y_\tau - \boldsymbol{c}_\tau \boldsymbol{X}_{\tau/\tau-1}) \tag{4.6.5}$$

where

$$\delta_\tau = \boldsymbol{Q}_{\tau/\tau-1} \boldsymbol{c}_\tau^{\mathrm{T}} (\boldsymbol{c}_\tau \boldsymbol{Q}_{\tau/\tau-1} \boldsymbol{c}_\tau^{\mathrm{T}} + D_\tau)^{-1} \tag{4.6.6}$$

$\boldsymbol{Q}$, the covariance of $\boldsymbol{X}$, is updated as follows:

$$\boldsymbol{Q}_{\tau+1/\tau} = \boldsymbol{Q}_{\tau/\tau} + \boldsymbol{U}_\tau \tag{4.6.7}$$

$$= \boldsymbol{Q}_{\tau/\tau-1} - \delta_\tau \boldsymbol{c}_\tau \boldsymbol{Q}_{\tau/\tau-1} + \boldsymbol{U}_\tau \tag{4.6.8}$$

Eq. (4.6.4) and Eq. (4.6.7) are derived from Eq. (4.6.2) and Eq. (4.6.3).

Finally, the forecast value is calculated with the updated coefficients and predictors at $\tau + 1$;

$$y_{\tau+1/\tau} = \boldsymbol{c}_{\tau+1}\boldsymbol{X}_{\tau+1/\tau} \tag{4.6.9}$$

For some forecast parameters, temperature for example, the predictand y is the difference between the NWP output and the observation, while for the others, precipitation amount for example, y is the observation itself.

In the forecast guidance system with KF, D_τ in Eq. (4.6.6) and $\boldsymbol{U}_\tau$ in Eq. (4.6.8) are treated as empirical parameters of controlling the adaptation speed.

4.6.2.2 Frequency Bias Correction

With KF, the most likely estimation of the predictand which minimizes the expected root-mean-square error is obtained. However, the output has a tendency of lower frequency of forecasting rare events, such as strong wind and heavy rain, than the actual. To compensate this unfavorable feature, a frequency bias correction scheme is applied to the KF output of some parameters.

The basic idea is to multiply the estimation of KF, y, by a correction factor $F(y)$ to get the final output y^b:

$$y^b = y \cdot F(y)$$

To determine $F(y)$, a number of thresholds t^i are chosen to span the given observation data set first. Then corresponding thresholds f^i for the forecast data set are adjusted so that the number of observation data smaller than t^i should approximate to that of forecast data smaller than f^i. Finally the correction factors are computed as follows:

$$F(f^i) = t^i/f^i$$
$$F(y) \text{ for } f^i < y < f^{i+1} \text{ is linearly interpolated between } F(f^i) \text{ and } F(f^{i+1}).$$

Since KF is an adaptive method, f^i is also updated each time the observation y_τ corresponding to the estimates of KF $y_{\tau/\tau-1}$ is available. The update procedure is as follows:

$$f^i_{\tau+1} = \begin{cases} f^i_\tau(1+\alpha) & \text{if} \quad y_\tau < t^i \quad \text{and} \quad y_{\tau/\tau-1} > f^i \\ f^i_\tau(1-\alpha) & \text{if} \quad y_\tau > t^i \quad \text{and} \quad y_{\tau/\tau-1} < f^i \\ f^i_\tau & \text{otherwise} \end{cases}$$

where α is an empirical parameter to determine the adaptation speed. This frequency bias correction is applied to the guidance for wind and precipitation amount.

4.6.2.3 An Example of the Guidance by Kalman Filter (3-hour Precipitation Amount)

In this guidance, the predictand is the observed 3-hour accumulated precipitation amount averaged within a 20km × 20km square, and the following nine parameters derived from GSM forecast are used as predictors.

1. NW85: NW − SE component of wind speed at 850hPa
2. NE85: NE − SW component of wind speed at 850hPa
3. SSI: Showalter's stability index
4. OGES: Orographic precipitation index
5. PCWV: Precipitable water contents × wind speed at 850hPa × ascending speed at 850hPa
6. QWX: Σ (Specific humidity × ascending speed × relative humidity) between 1000 and 300hPa
7. EHQ: Σ (Depth of wet layer × specific humidity) between 1000 and 300hPa
8. DXQV: Precipitation index on winter synoptic pattern

9. FRR: Precipitation by the model (GSM)

Figure 4.6.1 is an example of precipitation forecasts. The model(GSM) (C) predicted very little or no precipitation in the area M, where the observation (A) shows weak precipitation. On the other hand, the guidance (B) predicted weak precipitation in this area, showing better results. Examination of the coefficient values shows orographic effect by OGES enhanced precipitation amount in this area.

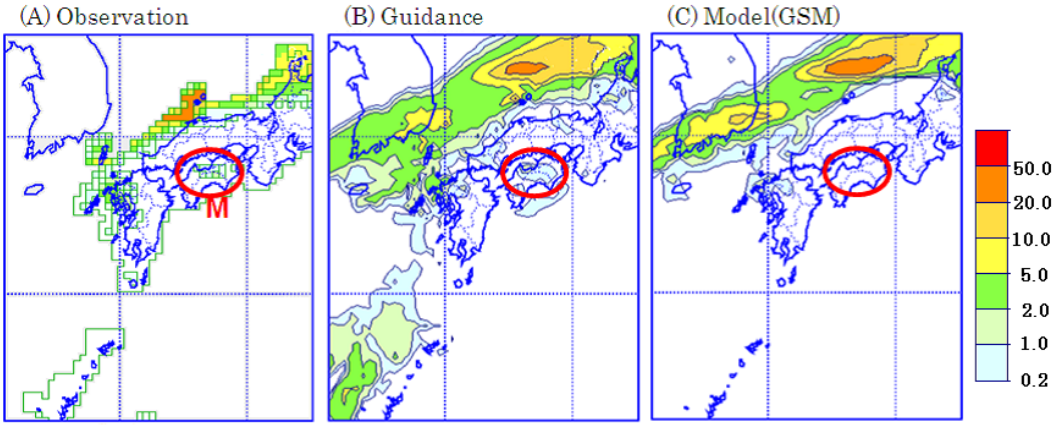

Figure 4.6.1: Mean precipitation amount over 3 hours. (A) Observation. (B) Forecast by the Guidance. (C) Forecast by the Model (GSM).

4.6.3 Guidance by Neural Network

4.6.3.1 Neural Network

The Neural Network (NRN) is one of the artificial intelligence methods and is an effective technique to analyze non-linear phenomena (Yanagino and Takada 1995). Its basic element is called a "neuron", and multiple neurons are linked together to construct a hierarchical neural network, as shown in Figure 4.6.5. The first layer is called the "input layer", the last layer is called the "output layer", and the layers between them are called "hidden layers".

When a signal is put into the input layer, it is propagated to the next layer through the interconnections between the neurons. Simple processing is performed on this signal by the neurons of the receiving layer prior to its propagation to the next layer. This process is repeated until the signal reaches the output layer.

A schematic diagram of a neuron is shown in Figure 4.6.2. The input of each neuron is a weighted sum of the outputs of other neurons, and the output is a function of its input. This function is called an "activation function", and a sigmoid function shown in Figure 4.6.3 is usually used.

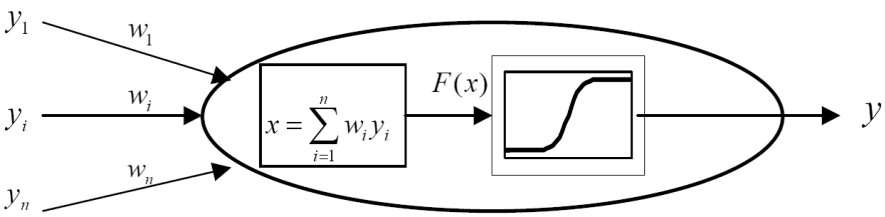

Figure 4.6.2: A schematic diagram of the neuron

$$F(x) = \frac{1}{1 + e^{-(2/c)x}}$$

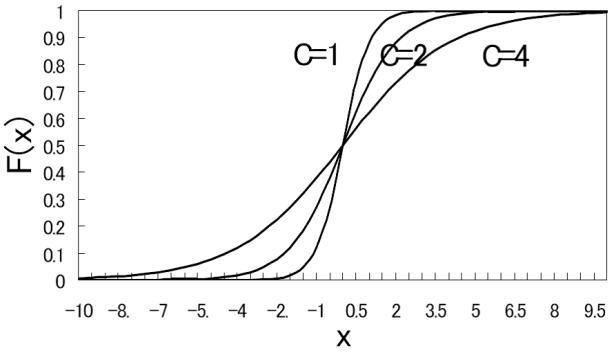

Figure 4.6.3: Examples of the sigmoid function

The weights of NRN are iteratively adjusted through learning numerous sets of input/output data. The most popular way to adjust weights is the "back propagation of error" algorithm described as follows:

1. At first, weights are initialized with randomized values.
2. The NRN gets a set of input values and calculates output.
3. The weights are adjusted to make the NRN output approach the "supervisor data" (correct values of the output variable).
4. Processes of 2 and 3 are iterated until the error measure falls below a specified value or a specified maximum number of iterations is reached.

4.6.3.2 An Example of the Guidance by Neural Network (Categorized Weather)

In the forecast guidance system, a Neural Network model is constructed at each grid or observation point from the sets of NWP output and observed weather elements. Categorized weather is one of the forecast guidance parameters to which NRN is applied. Figure 4.6.4 shows an output example of categorized weather guidance. In this guidance, a NRN model is used to derive sunshine duration, which is used to determine the non-precipitating weather categories (fair or cloudy). The NRN is constructed at each AMeDAS station, and output values (3-hourly sunshine duration) are interpolated to grid points. The precipitating weather categories (rain, sleet, snow) are determined from the KF-based precipitation amount guidance described in Subsection 4.6.2 and another NRN. The constitution of the sunshine duration NRN model is shown in Figure 4.6.5, and its characteristics are summarized as follows:

1. It is a 3-layered Back Propagation Network.
2. As an activation function of each neuron, a linear function is used in the input and output layer, and a sigmoid function is used in the hidden layer.
3. In learning processes, NWP output is used as input data, and sunshine duration observed at each AMeDAS point is used as supervisor data.
4. The weights of the network are modified at every time when the observation corresponding to the forecast is obtained.

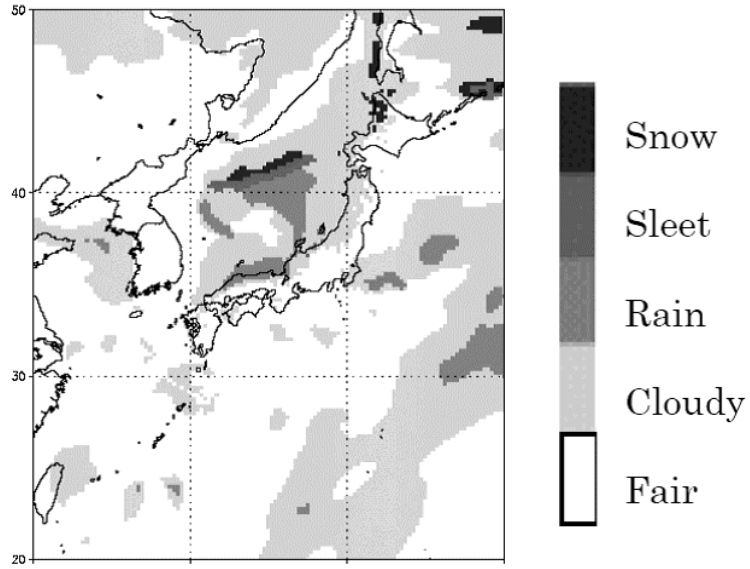

Figure 4.6.4: An example of output of the categorized weather guidance

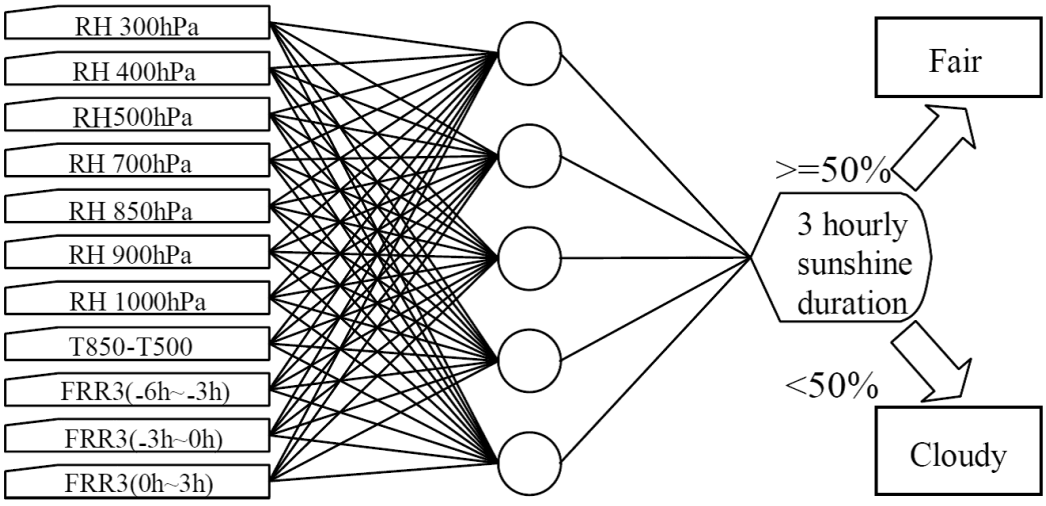

Figure 4.6.5: Neural Network for fair/cloudy determination. RH: Relative Humidity, FRR3: Precipitation over 3 hours.

4.6.4 Utilization of the Guidance at Forecasting Offices

The forecast guidance products are disseminated to forecasting offices and used as a draft of a weather forecast in the forecast editing software. Figure 4.6.6 shows an example of its data entry screen. The forecasters revise elements (time series data of categorized weather, PoP, temperature etc.) on the display considering the current weather condition and empirical knowledge. The processed data are then composed to the forecast bulletin and disseminated to the users.

To make a draft of the weather forecast bulletin automatically, an algorithm shown bellow is used:

1. 3-hourly dominant weather categories are derived from the majority of the categorized weather on the grids in the forecast area .
2. The draft of the weather forecast bulletin for a day is derived from the sequence of 3-hourly dominant weather categories over the forecast area. Some examples of the algorithm are shown in Table 4.6.2.

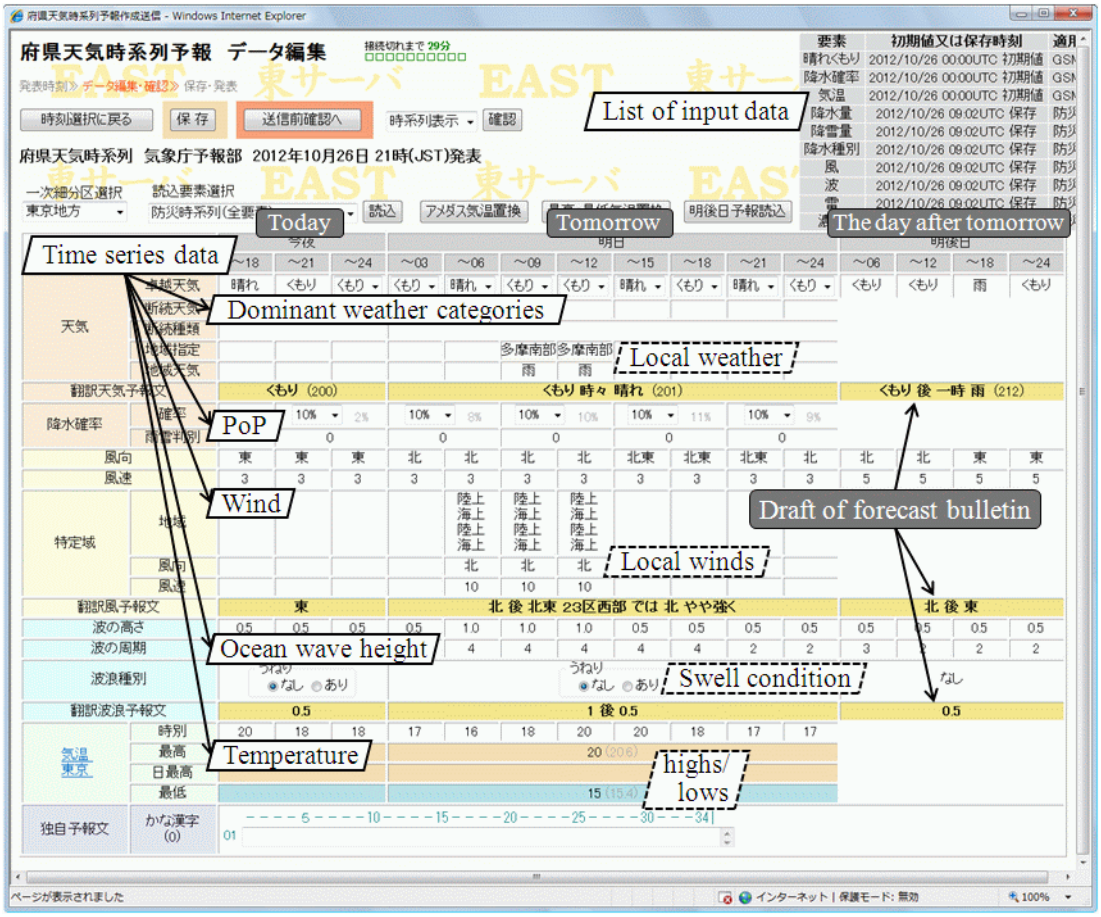

Figure 4.6.6: An example of a data entry screen of the forecast editing software

Table 4.6.2: Examples of the algorithm for making a draft of the weather forecast bulletin

Sequence of 3-hourly categorized weather*								Draft of a weather forecast bulletin
0 - 3	3 - 6	6 - 9	9 -12	12-15	15-18	18-21	21-24	
F	F	F	F	C	F	F	F	Fair
R	R	R	R	R	S	S	S	Rain, snow from the evening
C	R	F	R	C	F	R	C	Cloudy, occasional rain
C	R	C	C	C	C	R	C	Cloudy, rain in the morning and the evening

* F:Fair C:Cloudy R:Rain S:Snow

4.7 Application Products for Aviation Services

4.7.1 Aerodrome Forecast Guidance

The Terminal Area Forecast guidance for Long range flight (TAF-L guidance) and that for Short range flight (TAF-S guidance) were integrated to the guidance for Terminal Area Forecast (TAF guidance) in May 2007. The TAF guidance is derived from the output of MSM 8-times a day and gives hourly predictions upto 33 hours (03, 09, 15, 18UTC initial times) and upto 15 hours (00, 06, 12, 18UTC initial times). The predicted parameters of these guidances are listed in Table 4.7.1.

Table 4.7.1: Parameters of Aerodrome Forecast Guidance. (for 91 airports in Japan)

Parameters	TAF guidance
Visibility	Minimum visibility during an hour Probability of minimum visibility during 3 hours < 5km and 1.6km
Cloud	Cloud amount and height of 3 layers at minimum ceiling during an hour Probability of minimum ceiling during 3 hours < 1000ft and 600ft
Weather	Categorized weather every hour
Temperature	Maximum temperature in the daytime, minimum temperatures in the morning and temperatures every hour
Wind	Wind speed and direction every hour Wind speed and direction of hourly maximum peak wind
Gust	Probability of gust during 3 hours Gust speed and direction of hourly maximum peak gust
Thunder	Probability of thunder during 3 hours

4.7.1.1 Visibility

The minimum visibility and the probability of minimum visibility in TAF guidance (VIS) use statistical interpretation of the model output. The VIS is calculated by linear equations whose coefficients are adapted by Kalman filter (see Subsection 4.6.2.1) with the predictors and METAR reports. The VIS consists of three linear equations classified by weather (rain, snow, no precipitation). The following predictors from the output of MSM are used for each equation.

- no precipitation: $(1 - Rh)^{1/2}$,$Qc^{1/2}$,where Rh is surface relative humidity ($0 \sim 1$), Qc is cloud water content near surface(kg/kg).
- rain: $RR^{1/2}$, $(1 - Rh)^{1/2}$,$Qc^{1/2}$,where RR is precipitation amount (mm).
- snow: $RR^{1/2}$, $(1 - Rh)^{1/2}$, $VV * T$,where VV is surface wind speed (m/s), T is surface temperature (°C, only < 0)

Frequency bias correction (see Subsection 4.6.2.2) is applied to parameters calculated by three equations. After that one parameter is chosen depend on weather category, which is predicted by weather guidance(described later).

4.7.1.2 Cloud

The TAF cloud guidance uses statistical interpretation of the model output. First, each cloud amount at 38 layers (0, 100, ..., 1000, 1500, ..., 5000, 6000, ..., 10000, 12000, ..., 30000 ft) is calculated by neural net (see Subsection 4.6.3), then three cloud layers are searched upward from surface like METAR reports. The input data (predictors) are relative humidity at three model levels, temperature lapse rate between surface and 925hPa from MSM. The utilization of neural net was introduced in March 2006, improved forecast score.

The TAF probability of minimum ceiling guidance uses statistical interpretation of the model output. It predicts probability of minimum ceiling during 3 hours becomes below 1000ft and below 600ft. The predictors are precipitation amount during 3 hours (rain,snow,hail), precipitation amount during 3 hours (snow), temperature lapse rate between surface and 925hPa, relative humidity, E-W component of wind speed, S-N component of wind speed, cloud amount, cloud ice content, cloud water content at 1000ft and 600ft from the height of airport. The logistic regression (Agresti 2002) was introduced to predict probability of minimum ceiling in December 2010.

4.7.1.3 Weather

The weather guidance predicts categorized weather (fine, cloudy, rainy, snowy and the intensity of precipitation). The TAF weather guidance uses diagnostic method to interpret MSM output into categorized weather (JMA 1997). But only to determine precipitation type (rain or snow), instead of MSM temperature the hourly temperature guidance is used, which improves accuracy of precipitation type prediction.

4.7.1.4 Wind and Temperature

The wind and temperature guidance are calculated with the same methods as the guidance for short-range forecasting (see Section 4.6).

4.7.1.5 Gust

The TAF gust guidance predicts the probability of gust during 3 hours and the speed and direction of the hourly maximum peak gust. It utilized Kalman Filter and Frequency Bias Correction. Predictors are gust speed predicted by MSM, surface wind speed, maximum wind speed in boundary layer. The TAF gust guidance was introduced in December 2012.

4.7.1.6 Thunder

The Probability of Thunder(PoT) guidance predicts the probability of thunder during 3 hours around airport. It utilizes logistic regression and 6 predictors are used in 12 potential predictors, especially SSI, CAPE and precipitation amount during 3 hours are always used for predictor. The TAF PoT guidance was introduced in May 2007.

4.7.2 Products for Domestic Area Forecast

4.7.2.1 Grid-point Values of Significant Weather

Aviation impact variables derived from the MSM output are calculated at model vertical layers and interpolated to flight levels. It is used to produce domestic area forecast in JMA. This purely aviation-oriented dataset is called SIGGPV (Grid-Point Values of Significant weather), whose specifications are listed in Table 4.7.2. The parameter Vws, which is an indicator of Clear Air Turbulence (CAT), is calculated as vertical wind shear between the model levels in kt/1000ft. The parameter TBindex (Kudo 2011) is a combined index of multiple turbulence indices derived from MSM, which is an indicator of various kind of turbulence, i.e. CAT, mountain-waves and cloud related turbulences. The parameters Csig and Cbtop are indicator of cumulonimbus amount and height of cumulonimbus cloud, they are calculated based on Kain-Fritsch convective scheme which is used in the MSM. The parameter Icing is an indicator of aircraft icing. It is derived from empirical equation,

which is consists of temperature and dew-point temperature. As illustrated in Figure 4.7.1, SIGGPV, which is distributed as binary data and can be visualized on terminals at aviation forecast offices, is also used for production of the following fax-charts.

Table 4.7.2: Specifications of SIGGPV

Base model	MSM
Forecast time	T=0-15, 1 hourly (initial = 00, 06, 12, 18 UTC) T=0-33, 1 hourly (initial = 03, 09, 15, 21 UTC)
Grid coordinate	Polar Stereographic (60°N, 140°E), 40km, 83 × 71
Parameters	U, V, T, Rh, Psea, Rain, Csig, Cbtop, Trpp[surface] U, V, T, W, Rh, Icing, Vws, TBindex[1,000 - 55,000 ft / every 2,000 ft]

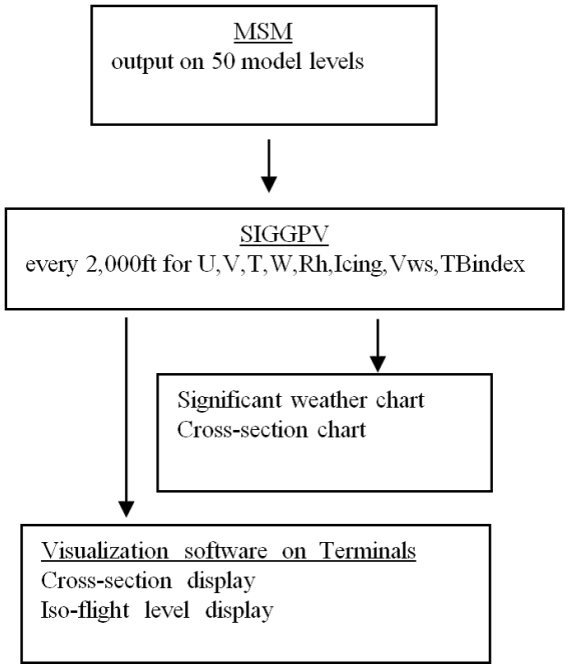

Figure 4.7.1: Data flow of products for domestic area forecast

4.7.2.2 Domestic Significant Weather Chart

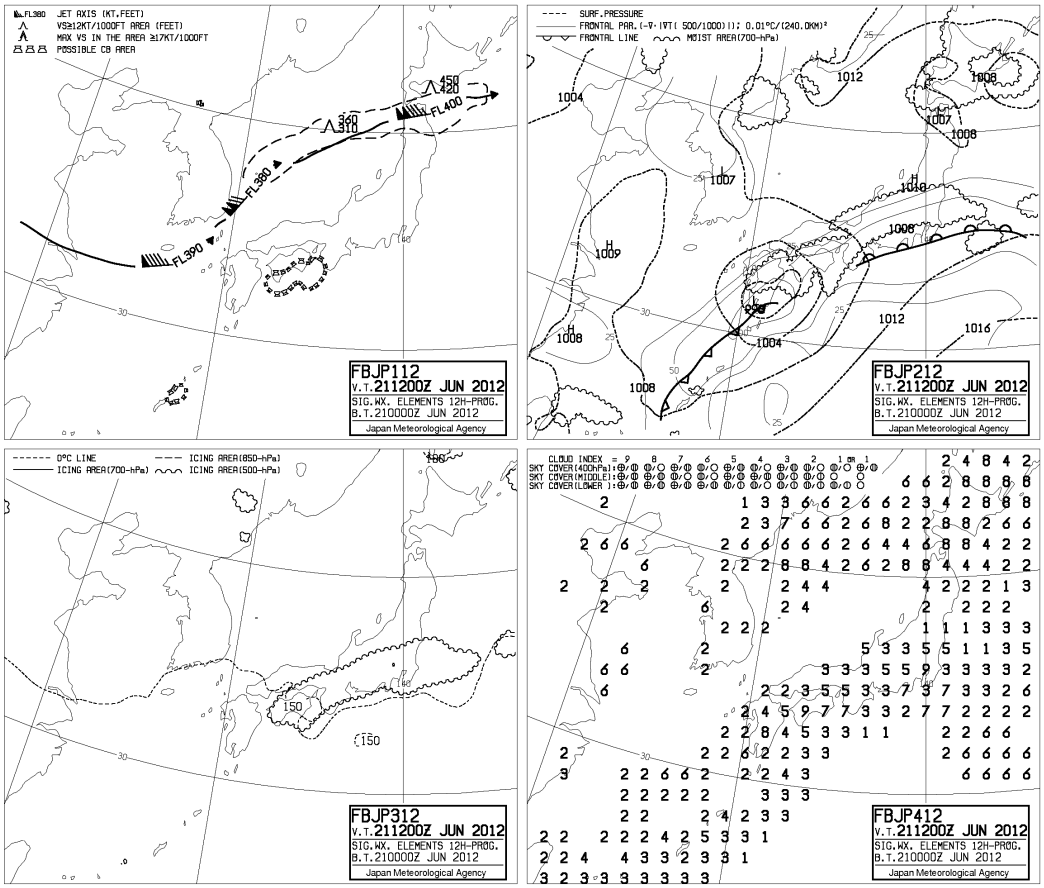

Figure 4.7.2: An example of the domestic significant weather chart

This chart shows 12- hour forecast fields of the parameters listed below in four panels: (Figure 4.7.2)

- Upper-left:
  - Jet stream axes.
  - Possible CAT areas.
  - Possible Cb areas.
- Lower-left:
  - Contours of 0°C height.
  - Possible icing areas at 500, 700 and 850hPa based on the -8 D method (Godske 1957)
- Upper-right:
  - Contours of sea level pressure.
  - Moist areas at 700 hPa.
  - Front parameters $DDT = -\nabla_n|\nabla_n T|$, where T is mean temperature below 500hPa and ∇_n denotes the horizontal gradient perpendicular to the isotherms.

– "NP fronts" drawn along the maxima of DDT.

- Lower-right:
  - Cloud indices indicating the low, middle and upper cloud amount.

4.7.2.3 Domestic Cross-section Chart

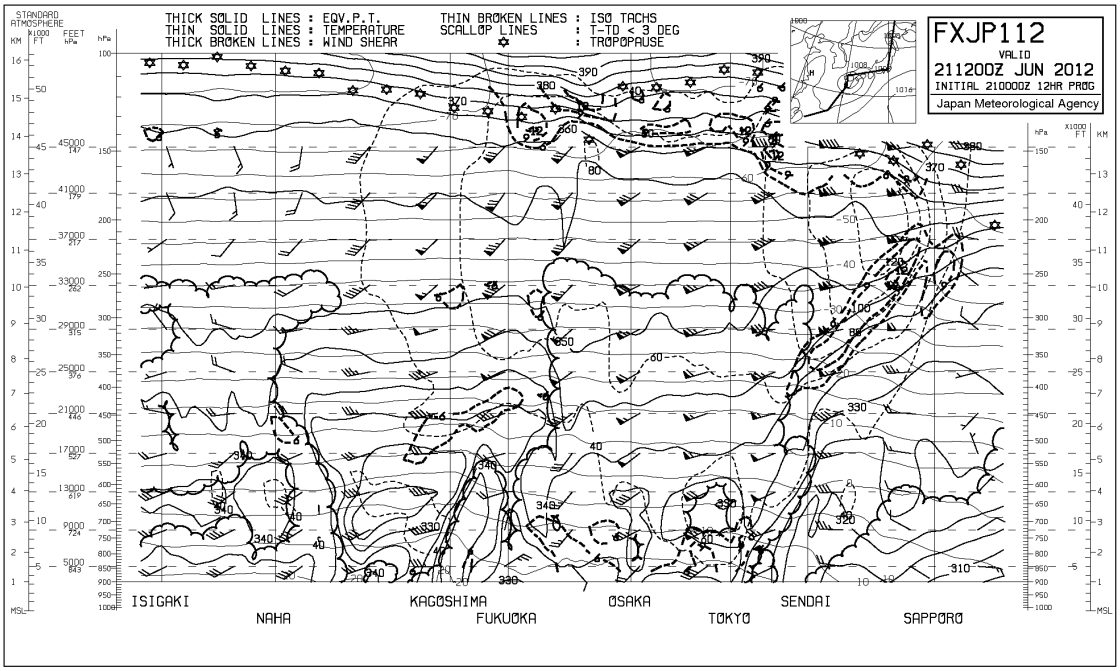

Figure 4.7.3: An example of the domestic cross-section chart. Only the lower part of the fax, corresponding to 12- hour forecast, is shown.

This chart shows 6- and 12-hour forecast fields along the major domestic route. The information drawn is: temperature, equivalent potential temperature, wind barbs and isotachs, moist areas, vertical wind shear and tropopause height (Figure 4.7.3).

4.7.3 Products for International Area Forecast

Global Grid Point Values are derived from the GSM four times a day and distributed in thinned GRIB codes, a format compatible with the products from the World Area Forecast Centers (WAFC). In addition to the parameters included in the WAFC products, Vws, an indicator of CAT and Cbtop, pressure of the top of Cb areas are derived with the same method as that in domestic SIGGPV (see Subsection 4.7.2).

JMA produces 13 Significant weather (SIGWX) charts and 18 Wind and temperature (WINTEM) charts, they are based on the WAFS Significant weather data provided form the World Area Forecast Centers (WAFCs).

4.8 Products of Ensemble Prediction System

4.8.1 Products of the EPS for One-week Forecasting

To assist forecasters in issuing one-week weather forecasts, some products of ensemble mean are made from output of the EPS.

An example of ensemble average chart of mean sea level pressure and precipitation is shown in Figure 4.8.1.

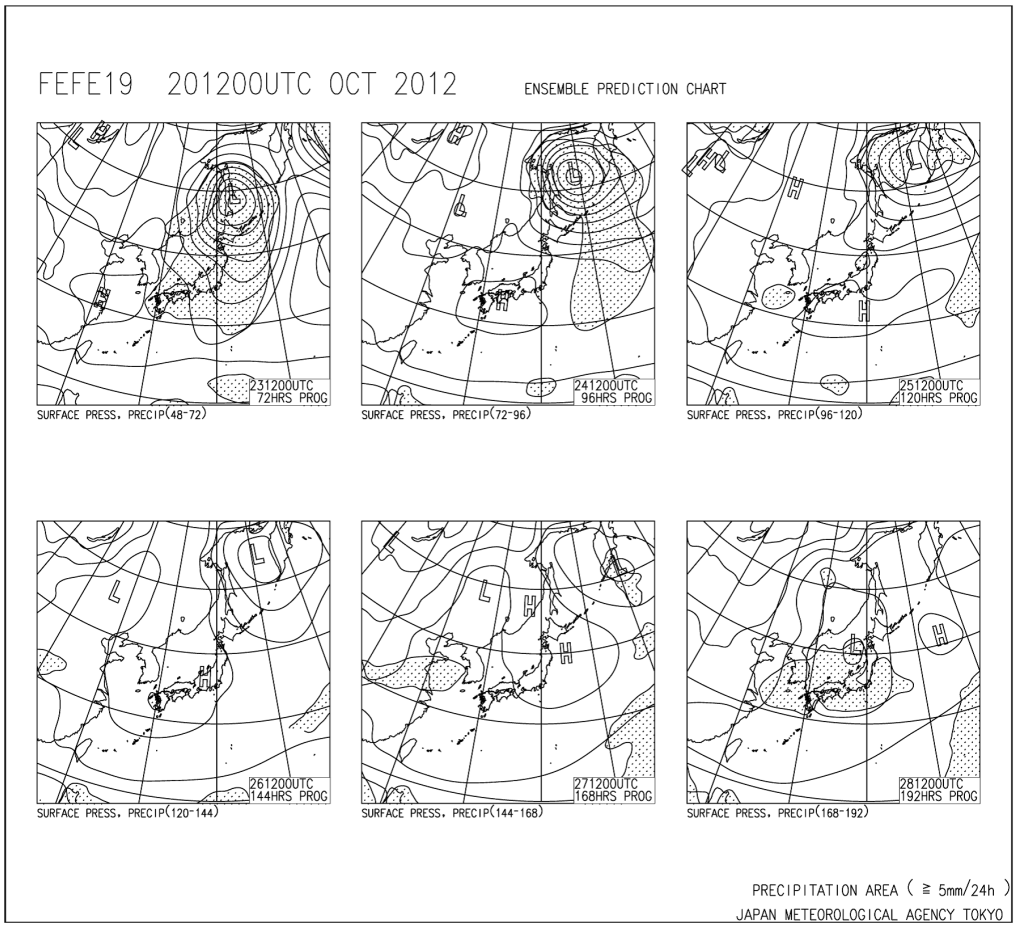

Figure 4.8.1: Ensemble average chart of mean sea level pressure and precipitation from day 2 to 7. This schematic chart is produced by averaging over all members.

4.8.2 Products of the One-month and Seasonal EPSs

4.8.2.1 Forecast Maps and Diagrams

Various kinds of forecast maps and diagrams are produced using the direct outputs from the operational EPSs. Major contents are as follows:

- Ensemble mean maps
- Ensemble spread maps

- Diagrams of time series of varies indices calculated from the ensemble mean and the individual member forecasts (for domestic users only)
- Outlook of sea surface temperature deviations for Ninõ regions to support monthly El Ninõ outlook (Figure 4.8.2)

4.8.2.2 Gridded Data

Gridded data of the model output has been provided via the TCC (the Tokyo Climate Center) website. The products are as follows:

- One-month EPS
  - Daily mean ensemble statistics
  - Daily mean forecast of the individual ensemble member
- Seasonal EPS
  - Monthly mean ensemble statistics
  - Monthly mean forecast of the individual ensemble member

4.8.2.3 Probabilistic Forecast Products

Probabilistic forecasts of three-category (e.g., above-, near-, below-normal) and probabilistic distribution functions are produced using the direct model outputs and hindcast datasets (Figure 4.8.3).

4.8.2.4 Hindcast Dataset and Verification Results

A hindcast is a long set of systematic forecast experiments for past cases, and is performed using forecast models identical to the current operational version. JMA provides not only the operational products but also the hindcast dataset. The Hindcast datasets are used statistically to calibrate real-time forecasts and to evaluate the prediction skill of models.

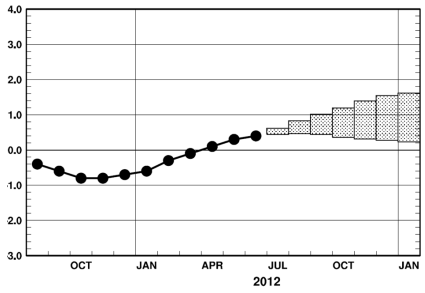

Figure 4.8.2: Outlook of the SST deviation for NINO.3 by the seasonal EPS. The thick line with closed circles denotes the observed SST deviation available at the time of issuance, and the boxes denote the prediction. (ensemble mean collected systematic biases). Each box denotes the range of SST anomaly with the probability of 70% estimating with hindcast results.

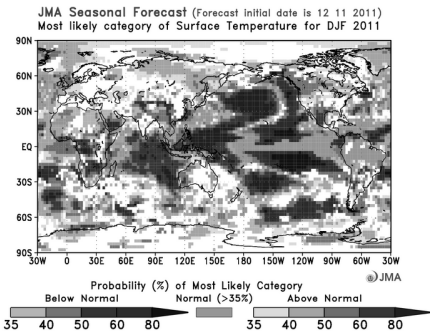

Figure 4.8.3: Probabilistic forecast map of surface air temperature for seasonal prediction. Probability is estimated using a numerical guidance, which applies the Model Output Statistics (MOS) technique based on hindcast result. This figure is monochrome, but it is color illustration in actual.

4.9 Atmospheric Angular Momentum Functions

The Atmospheric Angular Momentum (AAM) functions were proposed to evaluate the earth rotational variation by precisely estimating the variation of the atmospheric angular momentum. To monitor the atmospheric effect on the earth rotation, JMA sends the AAM products to NCEP which is the sub-bureau of International Earth Rotation Service (IERS) through GTS. The AAM functions are expressed as follows (Barnes *et al.* 1983).

$$\chi_1 = -1.00\left[\frac{r^2}{(C-A)g}\right]\int P_S \sin\phi\cos\phi\cos\lambda\, dS - 1.43\left[\frac{r}{\Omega(C-A)g}\right]\iint (u\sin\phi\cos\lambda - v\sin\lambda)\, dPdS, \tag{4.9.1}$$

$$\chi_2 = -1.00\left[\frac{r^2}{(C-A)g}\right]\int P_S \sin\phi\cos\phi\sin\lambda\, dS - 1.43\left[\frac{r}{\Omega(C-A)g}\right]\iint (u\sin\phi\sin\lambda + v\cos\lambda)\, dPdS, \tag{4.9.2}$$

$$\chi_3 = -0.70\left[\frac{r^2}{Cg}\right]\int P_S \cos^2\phi\, dS - 1.00\left[\frac{r}{\Omega Cg}\right]\iint u\cos\phi\, dPdS. \tag{4.9.3}$$

In Eq. (4.9.1) to Eq. (4.9.3), P is the pressure, $\int dS$ is the surface integral over the globe, $(\phi,\ \lambda)$ are latitude and longitude, u, v are the eastward and northward components of the wind velocity, P_S is the surface pressure, g is the mean acceleration of gravity, r is the mean radius of the earth, C is the polar moment of inertia of the solid earth, A is the equatorial moment of inertia, and Ω is the mean angular velocity of the earth.

Functions χ_1 and χ_2 are the equatorial, and function χ_3 is the axial component. Every component is non-dimensional. The first term of each component is a pressure-term, which is related to the redistribution of the air masses. The second term is a wind-term, which is related to the relative angular momentum of the atmosphere.

The variation of the AAM functions calculated from the JMA global analysis data has been reported to well correspond to the variation of the earth rotation. Figure 4.9.1 shows the seasonal variation of the observed earth rotation and the calculated atmospheric relative angular momentum (the wind term of χ_3). The calculation was carried out by National Astronomical Observatory of Japan (Naito and Kikuchi 1992).

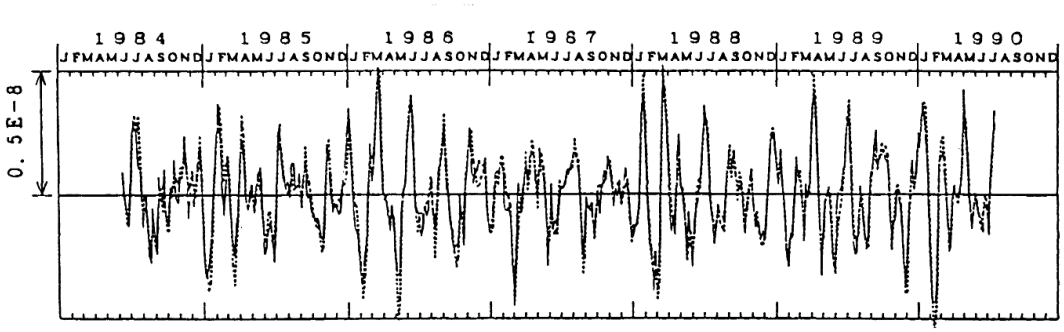

Figure 4.9.1: Seasonal variations of the observed earth rotation (solid line) and the calculated atmospheric angular momentum (broken line). Both data are 150 days' high-pass filtered.

Since early 1993, the AAM functions calculated from the JMA global analysis data at 00UTC, 06UTC, 12UTC and 18UTC have been provided operationally. Now, the AAM functions calculated from the JMA global 8-day forecast data at 12UTC also have been provided operationally.

The AAM functions which are calculated in a test period between 21 June and 30 September 1992 are shown in Figure 4.9.2. In this figure, day 1 - 102 corresponds to 21 June - 30 September 1992. Each term of

the AAM functions is multiplied by 10^7. The broken line shows the 6-hourly values of the AAM functions (difference from the period mean values), and the solid line shows the 5-10 days' band-pass filtered values. It can be noticed that an oscillation that has a 5-10 day period is remarkable in each term of the each component, which implicitly means that there is a 5-10 day period oscillation in the global scale atmosphere.

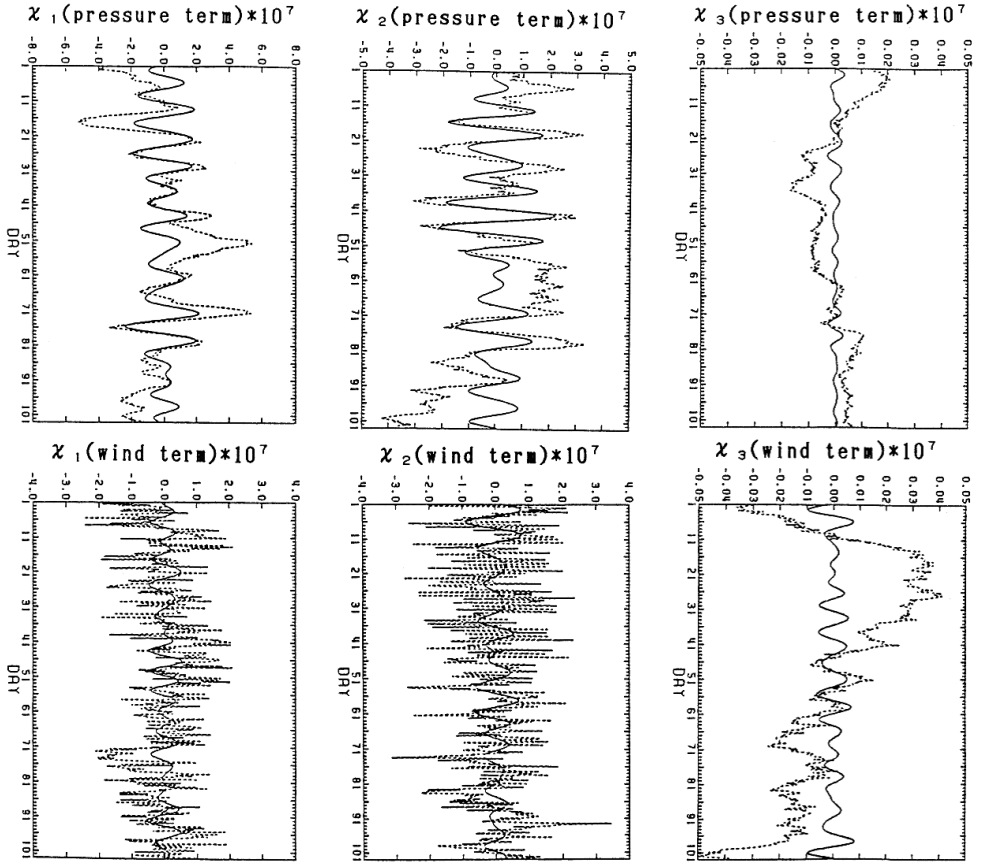

Figure 4.9.2: Pressure terms (top) and wind terms (bottom) of the AAM functions. The left panels are the χ_1 component, the center ones are the χ_2 and the right ones are the χ_3. Day 1 - 102 corresponds to 21 June - 30 September 1992. The broken line shows the 6-hourly values of the AAM functions, and the solid line shows the 5-10 days' band-pass filtered values. Each value is multiplied by 10^7.

Chapter 5

Sea State Models

5.1 Summary

(i) Two types of sea surface temperature analysis systems are operated at JMA. One is a high resolution analysis using satellite remote sensing data and *in-situ* observation data to provide real-time ocean information. The other is an analysis based on *in-situ* observation data to monitor long-term variations in the ocean such as El Niño events and global warming.

(ii) A global ocean data assimilation system (MOVE/MRI.COM-G) has been operated at JMA since 2008 for the monitoring of El Niño and the Southern Oscillation (ENSO). MOVE/MRI.COM-G consists of an ocean general circulation model (MRI.COM) and an objective analysis scheme. The output of MOVE/MRI.COM-G, along with the atmospheric analysis, is given to a coupled ocean-atmosphere model for ENSO prediction and seasonal forecast of climate in Japan.

(iii) Another ocean data assimilation system for the Western North Pacific (MOVE/MRI.COM-WNP) has been operated since 2008, aiming to analyze and predict variations of sea-water temperature, salinity and current associated with eddy-scale oceanic phenomena, such as the Kuroshio, Oyashio and mid-scale eddies in the seas adjacent to Japan.

(iv) JMA operates three wave models: the Global Wave Model (GWM), the Coastal Wave Model (CWM), and the Shallow-water Wave Model (SWM). The GWM and CWM, for the seas around Japan, are based on the MRI-III, which is developed in the Meteorological Research Institute (MRI) of JMA. The SWM, which is applied to several bays and seas near shore, is based on the WAM, which is a well known wave model and used in many organizations.

(v) JMA has operated storm surge models. One model is for Japan region and predicts storm surges generated by tropical and extra-tropical cyclones. The model runs eight times a day and provides 33or 30 hours forecasts for 385 points along Japanese coastlines. The other is for Asian region, which is developed in the framework of the Storm Surge Watch Scheme of WMO. The model runs four times a day and predicts up to 72 hours forecast, and horizontal storm surge map and time series at selected points are issued to the members of Typhoon Committee.

(vi) A numerical sea ice model has been operated at JMA to support sea ice forecast for the southern part of the Sea of Okhotsk. The model forecasts distributions and concentrations of sea ice for one week based on dynamic and thermodynamic equations in the winter season.

(vii) An oil spill prediction model has been ready for operation at JMA since 1999. The model is an advection-diffusion model to predict distributions of spilled oil. The operation is triggered when a large-scale oil spill occurs in the offshore seas. Effects of transport by sea surface winds, ocean waves and sea surface currents, turbulent diffusion, evaporation and emulsification are considered in the model.

5.2 Sea Surface Temperature Analysis

5.2.1 Merged Satellite and *In-situ* Data Global Daily Sea Surface Temperature

High-resolution daily sea surface temperatures (SSTs) in the global ocean on a grid of $0.25° \times 0.25°$ are objectively analyzed for ocean information services and for providing boundary conditions of the atmospheric short and medium range prediction models and the North Pacific Ocean models (see Section 3.2, Section 3.5 and Section 5.5; Kurihara *et al.* (2006)). SSTs obtained from the infrared radiometer of AVHRRs on the NOAA and MeTop polar orbiting meteorological satellites are used together with *in-situ* SST observations. While a major portion of the *in-situ* data are obtained through the Global Telecommunication System, still many are obtained from domestic organizations via facsimile, e-mail and postal mail.

Satellite-derived SST anomalies (SSTA) from daily SST climatologies are decomposed into two temporal-scale and three spatial-scale components: long and short timescales with a cutoff period of 53 days, and large, middle and small scales with cutoff wavelengths of 580km and 143km. The middle scale is aimed to represent the SST signals caused by eddy-scale phenomena. The small scale is aimed to represent meso-scale signals. The signals varying with a period shorter than 27 days are cut off, because the noise of the data in this range is considerably large. The long timescale signals represent the intra-seasonal variation, and the short timescale signals represent variation influenced by atmospheric condition, such as a tropical cyclone reducing SSTs.

The large-scale and long-timescale components of SSTAs from AVHRR are calibrated with *in-situ* SSTAs using Poisson's equation (Reynolds (1987)). The space-time optimum interpolation (OI) is applied to each component. Zero value is adopted as the first guess. The space-time correlation coefficients and the RMS values of the first guess error and the satellites' observation errors were statistically estimated a priori from the satellites' data themselves, using the method of Kuragano and Kamachi (2000). Daily SST is a sum of the components of interpolated SSTAs and the daily climatologies (Figure 5.2.1).

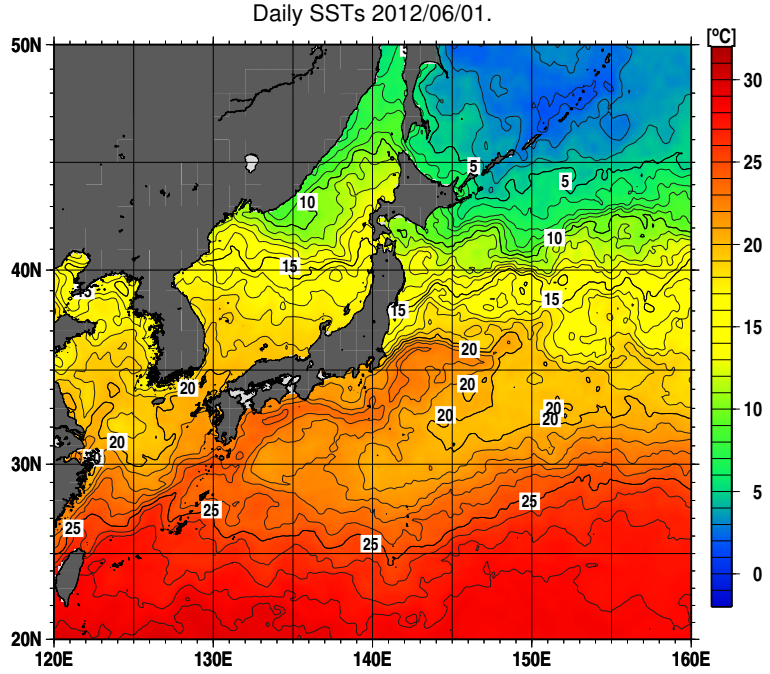

Figure 5.2.1: An example of analyzed SSTs

5.2.2 Daily Sea Surface Analysis for Climate Monitoring and Predictions

The Sea Surface Temperature (SST) analysis for climate monitoring at JMA is based on the method described in Ishii *et al.* (2005), which is summarized in the following.

The SST analysis has a resolution of 1° latitude and 1° longitude. The east-west grid points start at 0.5°E and end at 0.5°W. The north-south grid points start at 89.5°S, and end at 89.5°N. The analysis uses optimum interpolation method. The deviation of the previous day's analysis from normal is multiplied by 0.95 and is used as a first guess. The analysis is performed daily and uses the marine meteorological data for 7 days centered at the day of interest. The observed data in a day are averaged in $1.5^\circ \times 1.5^\circ$ box before analyzing data by optimum interpolation method to save the processing time of analysis.

The bias corrections for the past SST observation reports were performed by the way of Folland and Parker (1995). The quality control of observed data is performed by checking ship tracks, dates and positions of reports, and then erroneous data are automatically corrected in compiling marine meteorological data in JMA. Moreover, with observed data deviations from climatological values during the three months including the day of interest, biases of the data having the same ship call signs are estimated, and call signs having large biased data are listed automatically in a blacklist through the daily analysis. The daily analysis (final analysis) is performed with delay of 31 days from real time to allow delayed observations to be used sufficiently. Additionally as quick look analyses for the real time utilization, the analyses for the 30-day period following the final analysis are done every day.

The information of sea ice concentration is made use of in estimating SSTs in the polar oceans.

The daily updated operational SST data are utilized as follows with historical ones.

1. Monitoring of equatorial Pacific SSTs, El Niño/ La Niña evolutions and global warming over 100 years.
2. Input of the operational Ocean Data Assimilation System (MOVE/MRI.COM-G) and historical oceanic analysis (see Section 5.3).
3. Input of the JMA Climate Data Assimilation System (JCDAS) and Japanese 25-year Re-analysis (see Section 2.10).
4. Input of Ensemble Prediction Systems for one-month forecasts (see Section 3.3).

The monthly averaged SST data are made available through the Tokyo Climate Center web site[1] and characteristics of the data are described in Japan Meteorological Agency (2006) which is available in the Web page of Tokyo Climate Center[2].

5.3 Ocean Data Assimilation System

Following successful development of a ocean data assimilation system (MOVE/MRI.COM) by the Meteorological Research Institute (MRI) of JMA, JMA has been operating two types of the MOVE/MRI.COM since 2008. One is the global system (MOVE-G) for the monitoring of El Niño and the Southern Oscillation (ENSO), which replaced JMA-ODAS described in the previous report. The other is the Western North Pacific system (MOVE-WNP) for analyzing eddy-scale oceanic phenomena in the seas adjacent to Japan, which is a successor of COMPASS-K described in the previous report. In the following subsections, firstly a brief outline of the MOVE/MRI.COM is provided. Secondly, some examples of the MOVE-G and MOVE-WNP are presented.

5.3.1 Ocean General Circulation Model and Objective Analysis Scheme

The MOVE/MRI.COM consists of an ocean general circulation model (MRI.COM) and an objective analysis scheme (MOVE). The details of MOVE/MRI.COM are described in Usui et al. (2006).

MRI.COM (Ishikawa *et al.* 2005) is a multilevel model that solves primitive equations under the hydrostatic and the Boussinesq approximation. The σ-z vertical coordinate is adopted with which the layer thickness

[1] http://ds.data.jma.go.jp/tcc/tcc/products/elnino/cobesst/cobe-sst.html
[2] http://ds.data.jma.go.jp/tcc/tcc/library/MRCS_SV12/index_e.htm

near the surface follows the surface topography to allow the freely elevating surface (Hasumi 2006). For the nonlinear momentum advection, the generalized enstrophy-preserving scheme (Arakawa 1972) and the scheme that contains the concept of diagonally upward/downward mass momentum fluxes along the sloping bottom are applied. The vertical viscosity and diffusivity are determined by the turbulent closure scheme of Noh and Kim (1999). In MOVE-G, isopycnal mixing (Gent and McWilliams 1990) is used for horizontal turbulent mixing, and harmonic viscosity with the parameterization of Smagorinsky (1963) is used for momentum. In MOVE-WNP, on the other hand, a biharmonic operator is used for horizontal turbulent mixing, and a biharmonic friction with a Smagorinsky-like viscosity (Griffies and Hallberg 2000) is used for momentum. The values of wind stress, heat and fresh water fluxes to drive the model are produced with the routinely operated JMA Climate Data Assimilation System (JCDAS; see Section 2.10), which is almost the same system as the Japanese 25-year Re-Analysis (JRA25; Onogi *et al.* 2007).

The analysis scheme adopted in MOVE is a multivariate three-dimensional variational (3DVAR) analysis scheme with vertical coupled Temperature-Salinity (T-S) Empirical Orthogonal Function (EOF) modal decomposition (Fujii and Kamachi 2003). Amplitudes of the T-S EOF modes above 1500 m are employed as control variables and the optimal temperature and salinity fields are represented by the linear combination of the EOF modes. In this system, the model domain is divided into several subregions and vertical T-S EOF modes are calculated from the observed T-S profiles for each subregion. The 3DVAR results are inserted into the model temperature and salinity fields above 1500 m by the incremental analysis updates (Bloom *et al.* 1996).

These in-situ observations are reported from ships, profiling floats and moored or drifting buoys through the GTS and other communication systems. In MOVE/MRI.COM, not only in-situ observations of subsurface temperature and salinity, but also satellite altimeter data are assimilated into the model. The results of sea surface temperature analysis, which are analyzed independently from the MOVE/MRI.COM, are also assimilated as observational data; the COBE-SST (see Subsection 5.2.2) grid-point values are used for MOVE-G, and the MGDSST (see Subsection 5.2.1) grid-point values are used for MOVE-WNP.

5.3.2 Ocean Data Assimilation System for Global ocean (MOVE-G)

The horizontal resolution is 1.0° latitude and 1.0° longitude except for the 15°S-15°N band, where the latitudinal grid spacing decreases to the minimum of 0.3° between 6°S and 6°N (see Figure 5.3.1). The model has 50 vertical levels, 24 of which are placed above 200 meters (see Figure 5.3.2). The model has realistic bottom topography, and the maximum depth of the bottom is set to 5000 meters. The computational domain is global, excluding the higher latitudes than 75°S and 75°N. With regard to sea ice, daily climatological data are applied to MRI.COM. Additionally, the deviation of the model sea surface temperature (SST) from the daily analyzed SST for climate (COBE-SST; Ishii *et al.* 2005) is referred to in calculating long-wave radiation to keep the model SST closer to the observation.

The latest assimilation results are obtained once in five days, and the targeted term is 3-7 days before the assimilation is carried out. The assimilation data for the same term are updated every five days using additional delayed-mode observation data until the term reaches 39-43 days before the final assimilation.

The output from MOVE-G is used in various forms for the monitoring of ENSO at JMA, and some products for the equatorial Pacific region are distributed in a couple of publications, namely, "Monthly Highlights on Climate System" and "El Niño Outlook". Figure 5.3.3 is one of such charts of the MOVE-G, which shows the depth-longitude sections of temperature and its anomalies. The charts in the reports are also made available through the Tokyo Climate Center Web page[3].

5.3.3 Ocean Data Assimilation System for the Western North Pacific (MOVE-WNP)

The model domain spans from 117°E to 160°W zonally and from 15°N to 65°N meridionally. The horizontal resolution is variable: it is 1/10° from 117°E to 160°E and 1/6° from 160°E to 160°W, and 1/10° from 15°N to 50°N and 1/6° from 50°N to 65°N. There are 54 levels in the vertical direction with thickness increasing 1 m at the surface to 600 m near the bottom (see Figure 5.3.4). Oceanic states at the side boundaries are replaced by those from a North Pacific model with a horizontal resolution of 1/2° (one-way nesting). A sea ice model

[3] http://ds.data.jma.go.jp/tcc/tcc/index.html

with the thermodynamics of Mellor and Kantha (1989) and the elastic-viscous-plastic rheology of Hunke and Dukowicz (1997) is also applied.

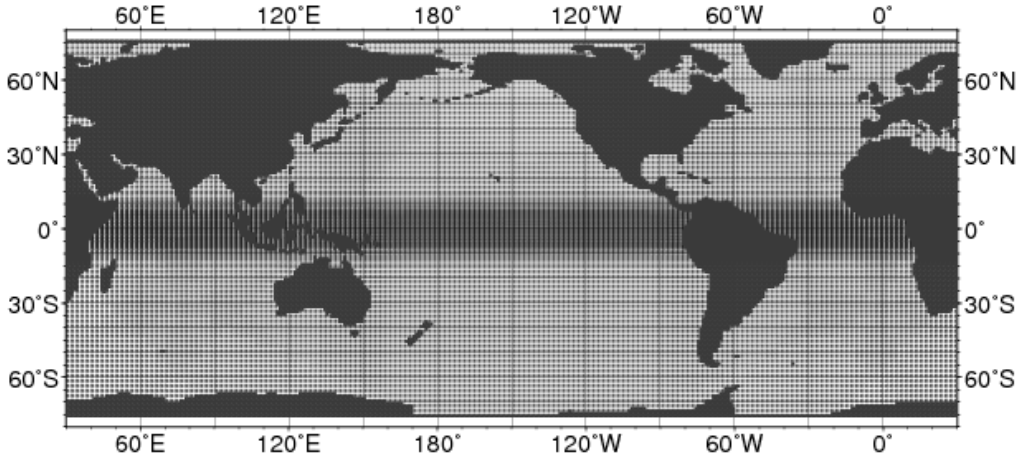

Figure 5.3.1: The MOVE-G horizontal grids

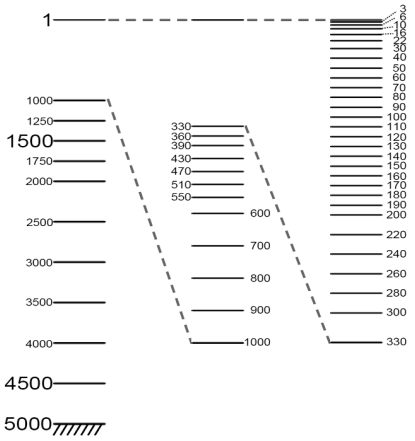

Figure 5.3.2: The MOVE-G vertical levels which indicate depths in meter

Figure 5.3.5 shows the predicted ocean current fields at a depth of 50m, which was calculated by the forecast run from the initial condition of 1 May 2012. The assimilated fields are also shown in the figure. The figure shows that the undulation of the Kuroshio path was successfully predicted in the forecast run. The assimilation run is implemented every five days. The output from MOVE-WNP is used as initial condition of the ocean forecasting model with one month prediction period. The results of the operational assimilation, nowcast and forecast runs are provided on JMA's web site and those of assimilation and nowcast runs are available on the NEAR-GOOS RRTDB[4].

[4] http://goos.kishou.go.jp/

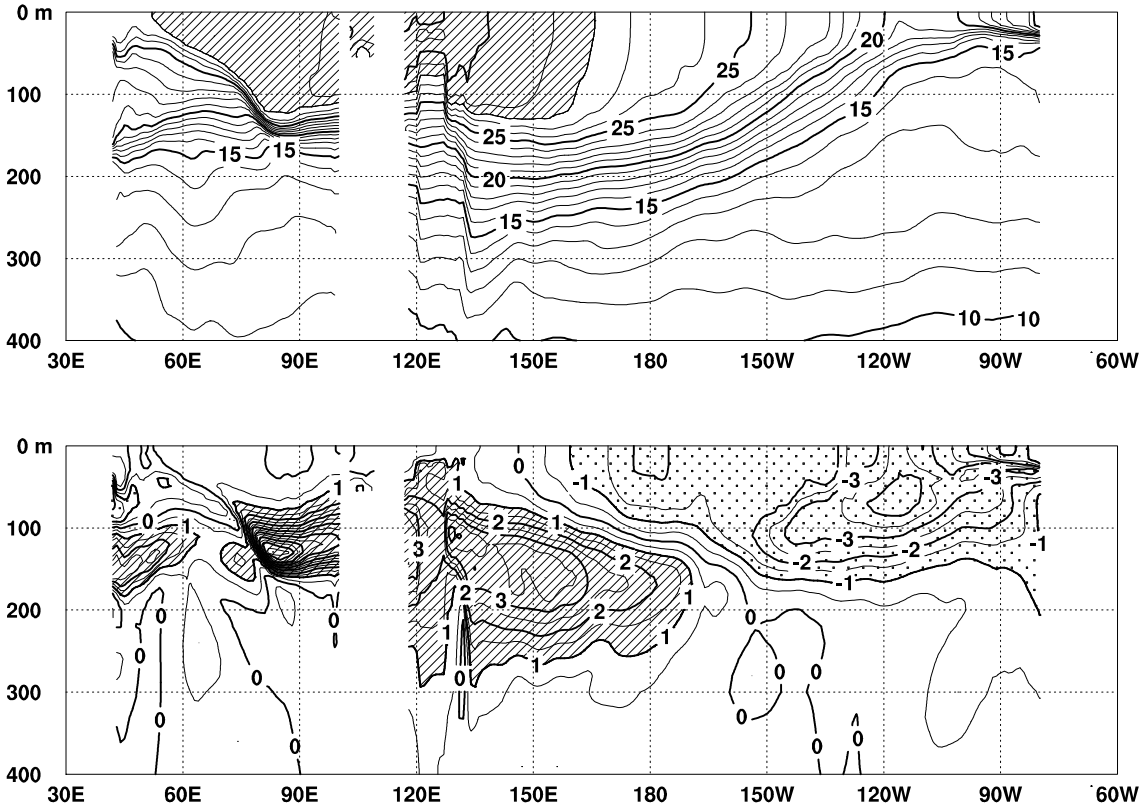

Figure 5.3.3: Depth-longitude cross sections of monthly mean temperature and temperature anomalies along the equator in the Indian and Pacific Ocean for November 2010 by MOVE-G. Base period for normal is 1981-2010.

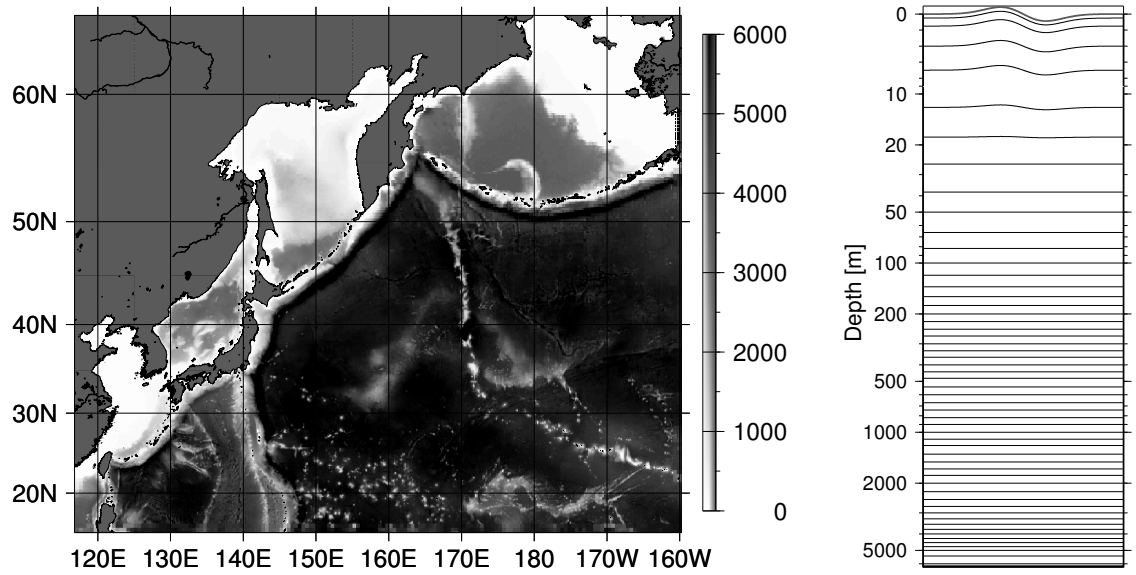

Figure 5.3.4: Bottom topography (left panel) and vertical levels (right panel) of OGCM for the Western North Pacific.

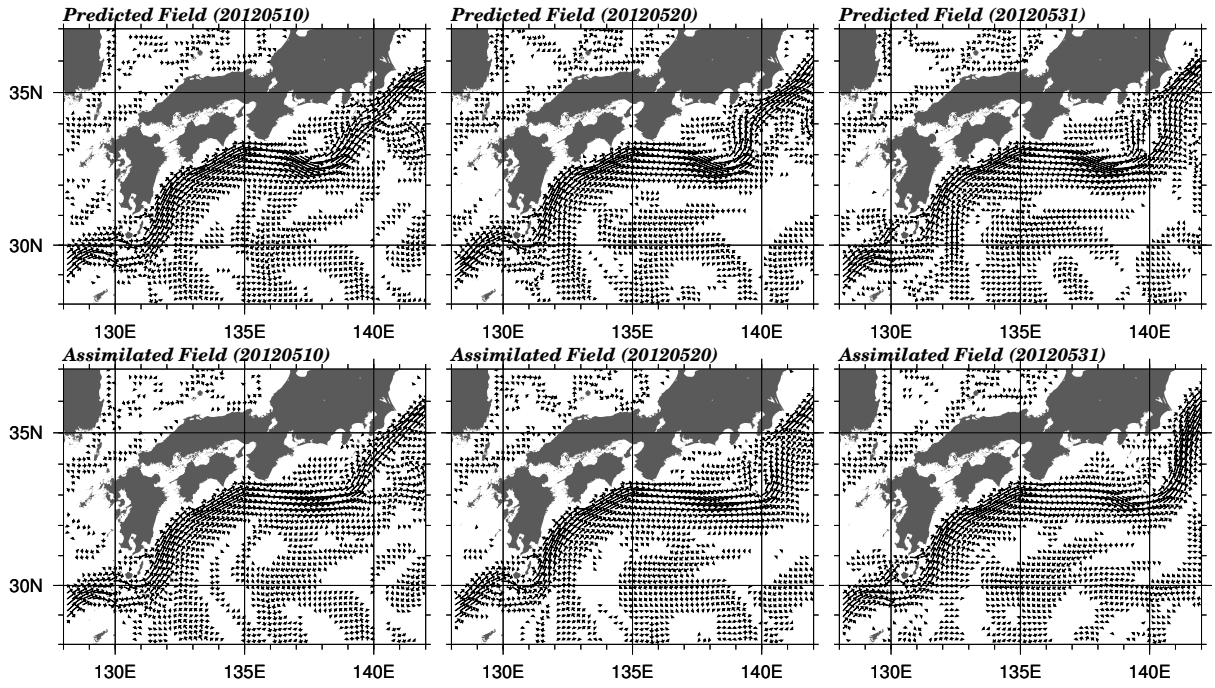

Figure 5.3.5: Horizontal current fields around 50m depth. Upper panels show the results of prediction using the initial condition of 1 May 2012. Lower panels are depicted using assimilation results.

5.3.4 Future plan

The Meteorological Research Institute (MRI) of JMA is now in process of developing a new ocean data assimilation system which is composed of a new version of MRI.COM (Tsujino *et al.* 2010) and the improved MOVE system. The new model will cover the global ocean including the Arctic Ocean, and its resolution will be higher than the present model. Introduction of an active sea-ice model is under consideration.

While the MOVE-WNP is aimed at monitoring sub meso-scale features such as a variation of the Kuroshio path, demands for information on smaller scale phenomena (e.g. the Kuroshio frontal waves) are increasing. JMA/MRI is now developing a new ocean model, which has higher horizontal resolution and schemes considering tidal effect.

5.4 Ocean Wave Models

5.4.1 Introduction

The Japan Meteorological Agency (JMA) operates three wave models: the Global Wave Model (GWM), the Coastal Wave Model (CWM) and the Shallow-water Wave Model (SWM), all of which are classified as the third-generation wave model.

The GWM and the CWM are based on the MRI-III, which was originally developed in the Meteorological Research Institute of JMA. The current versions of the GWM and the CWM, which only consider deep water waves, have been in operations since May 2007. The specifications of the GWM and the CWM are given in Table 5.4.1 and the model domains are shown in Figure 5.4.1.

The SWM is based on the WAM (The WAMDI Group 1988), but was modified at the National Institute for Land and Infrastructure Management of the Ministry of Land, Infrastructure, Transport, and Tourism (MLIT) and was put into operation under a cooperative framework with MLIT's Water and Disaster Management Bureau. The specifications of the SWM are given in Table 5.4.2. The SWM has high resolution of 1 minute,

Table 5.4.1: Specifications of the Global Wave Model and the Coastal Wave Model.

Model name	Global Wave Model	Coastal Wave Model
Type of wave model	spectral model (third-generation wave model, MRI-III)	
Area	global 75°N – 75°S 180°W – 0° – 180°E	coastal sea of Japan 50°N – 20°N 120°E – 150°E
Grid size	0.5° × 0.5° (720 × 301)	0.05° × 0.05° (601 × 601)
Time step (advection term) (source term)	 10 minutes 30 minutes	 1 minutes 3 minutes
Calculated time (from 00UTC, 06UTC, 18UTC) (from 12UTC)	 84 hours 264 hours	 84 hours 84 hours
Spectral component	900 components 25 frequencies from 0.0375 to 0.3 Hz (logarithmically partitioned) 36 directions	
Initial condition	hindcast	
Boundary condition		Global Wave Model
Wind field	Global Spectral Model (GSM)	
	Fujita's empirical formula and a corresponding gradient wind for a typhoon	

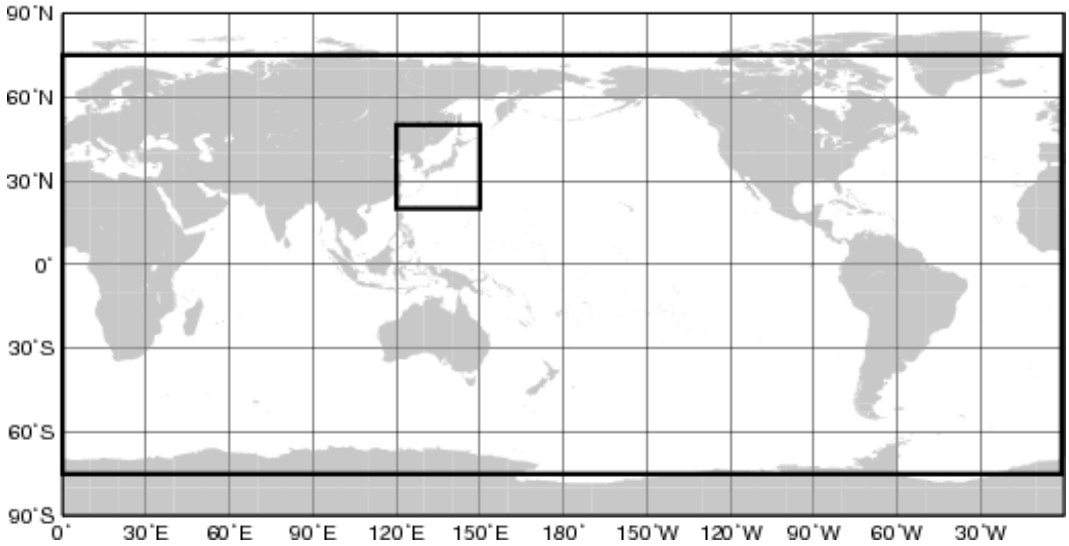

Figure 5.4.1: The calculation area of the Global Wave Model (outer thick line) and the Coastal Wave Model (inner thick line).

Table 5.4.2: Specifications of the Shallow-water Wave Model.

Type of wave model	spectral model (third-generation wave model, WAM)		
Areas	Domain name	Grid size	Integration domain
	Off Tomakomai	121 × 43	42.70°N – 42.00°N 141.00°E – 0° – 143.00°E
	Sendai Bay	37 × 43	38.45°N – 37.75°N 140.90°E – 0° – 141.50°E
	Tokyo Bay	37 × 43	35.75°N – 35.05°N 139.55°E – 0° – 140.15°E
	Ise Bay	61 × 43	35.05°N – 34.35°N 136.45°E – 0° – 137.45°E
	Harima-Nada Osaka Bay	79 × 49	34.85°N – 34.05°N 134.15°E – 0° – 135.45°E
	Suo-Nada Iyo-Nada Aki-Nada	109 × 67	34.40°N – 33.30°N 131.00°E – 0° – 132.80°E
	Ariake Sea	43 × 49	33.25°N – 32.45°N 130.05°E – 0° – 130.75°E
	Off Niigata	55 × 37	38.40°N – 37.80°N 138.35°E – 0° – 139.25°E
Grid resolution	1′ × 1′		
Time step (advection term) (source term)	 1 minutes 1 minutes		
Calculated time	33hours		
Spectral component	1260 components 35 frequencies from 0.0418 to 1.1 Hz (logarithmically partitioned) 36 directions		
Initial condition	hindcast		
Boundary condition	Coastal Wave Model		
Wind field	Meso-Scale Model (MSM)		
	Fujita's empirical formula and a corresponding gradient wind for a typhoon		

including shallow water effects. However, the SWM is applied to only limited areas, as shown in Figure 5.4.2. The products of the SWM are only used within JMA and MLIT's Regional Development Bureaus.

5.4.2 Structure of the Ocean Wave Models

All of the wave models are spectral model which is usually used in operational forecasts. The physical element is wave energy density (spectrum) of each frequency and direction, namely two-dimensional (directional) wave spectrum. The basic equation is the energy balance equation

$$\frac{\partial F}{\partial t} + \nabla(C_g \cdot F) = S_{net} = S_{in} + S_{nl} + S_{ds} + S_{btm} \tag{5.4.1}$$

where $F(f, \theta, x, t)$ is the two dimensional spectrum dependent on the frequency f and the wave direction θ, $C_g(f, \theta, x)$ is the group velocity, which becomes simply $C_g(f)$ for deep water waves. S_{net} is the net source function which consists of four terms: S_{in}, S_{nl}, S_{ds}, and S_{btm}. The four terms are briefly explained as follows. The model numerics of the MRI-III are described since those of the WAM has many references (Janssen 2004).

1. S_{in}: the energy input from wind. The S_{in} is generally expressed as the form $S_{in} = A + BF$, where A shows linear wave growth and BF exponential growth. In the MRI-III, the formula of Cavaleri and Rizzoli (1981) is used for linear growth

$$A = 1.5 \times 10^{-3} \left(u_*^4 / 2\pi g^2\right) \exp[-(f_{PM}/f)^4] \, (\max(0, \cos(\theta - \theta_W))^4 \tag{5.4.2}$$

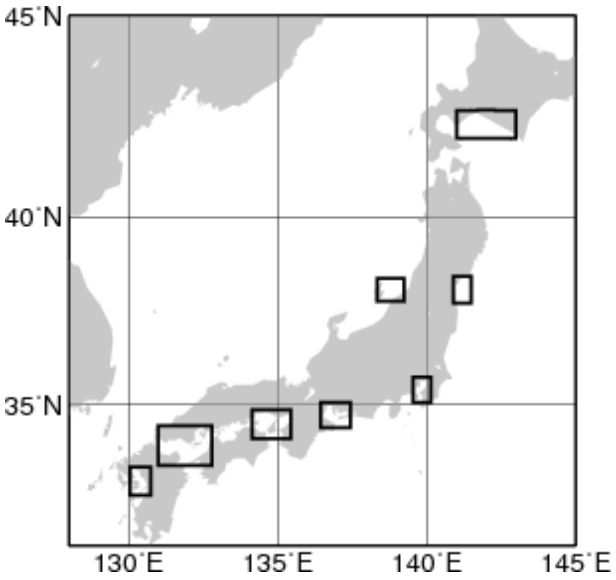

Figure 5.4.2: The calculation area of the Shallow-water Wave Model.

where θ is a direction of wave spectrum, u_* the friction velocity of wind, θ_W the wind direction, g the gravitational acceleration. In general, this term has little influence on wave growth except very early stage. On the other hand, the exponential term BF has a key role in wave growth. In the MRI-III, The B is expressed as

$$B(f, u_*, \theta_W - \theta) = c_{in}\left(\frac{u_*}{C_p}\right)^2 \cos^3(\theta_W - \theta)/|\cos(\theta_W - \theta)|. \tag{5.4.3}$$

where C_p is the phase speed of deep water waves, namely $C_p = \dfrac{g}{\omega} = \dfrac{g}{2\pi f}$.

This expression is based on Mitsuyasu and Honda (1982) and Plant (1982).

2. S_{nl}: the nonlinear energy transfer by resonant interaction. Because the rigorous calculation requires much computation time, a practical scheme, the Discrete Interaction Approximation (DIA) (Hasselmann *et al.* 1985), was developed. This scheme uses only one parameter for the set of four resonant waves and is widely used in many third-generation wave models.

$$\left.\begin{array}{l} f_1 = f_2 = f, \\ f_3 = f(1+\lambda) = f_+, \\ f_4 = f(1-\lambda) = f_-, \\ \theta_1 = \theta_2 = \theta, \\ \theta_3 - \theta = \pm\cos^{-1}\left\{\left(1 + 2\lambda + 2\lambda^3\right)/(1+\lambda)^2\right\}, \\ \theta_4 - \theta = \mp\cos^{-1}\left\{\left(1 - 2\lambda - 2\lambda^3\right)/(1-\lambda)^2\right\}. \end{array}\right\} \tag{5.4.4}$$

$$\left\{\begin{array}{c} \delta S_{nl} \\ \delta S^+_{nl} \\ \delta S^-_{nl} \end{array}\right\} = \left\{\begin{array}{c} -2(\Delta f \Delta\theta)/(\Delta f \Delta\theta) \\ (1+\lambda)(\Delta f \Delta\theta)/(\Delta f_+ \Delta\theta) \\ (1-\lambda)(\Delta f \Delta\theta)/(\Delta f_- \Delta\theta) \end{array}\right\}$$

$$\times C f^{11} g^{-4}\left[F^2\left\{\frac{F_+}{(1+\lambda)^4} + \frac{F_-}{(1-\lambda)^4}\right\} - 2\frac{FF_+F_-}{(1-\lambda^2)^4}\right] \tag{5.4.5}$$

where $F \equiv F(f,\theta)$, $F_+ \equiv F(f_+,\theta_3)$, $F_- \equiv F(f_-,\theta_4)$. The coefficient C is determined to be fitted to the exact calculation. Hasselmann *et al.* (1985) defined the parameters as $\lambda = 0.25$ which corresponds to $\theta_3 - \theta = \pm 11.5°$, $\theta_4 - \theta = \mp 33.6°$, and $C = 3 \times 10^7$. It is turned out that the DIA calculation gives much accurate estimation by multiplying the parameters. In the MRI-III, S_{nl} is calculated by DIA scheme but with three configurations. The used parameters are $\lambda_1 = 0.19 (C_1 = 1.191 \times 10^7)$, $\lambda_2 = 0.23 (C_2 = 6.835 \times 10^6)$, and $\lambda_3 = 0.33 (C_3 = 1.632 \times 10^6)$.

3. S_{ds}: the energy dissipation due to wave breaking and so on. In the MRI-III, dissipation terms are expressed as local energy dissipation proposed by Ueno (1998).

$$S_{ds} = -c_b \frac{u_*}{g^3} f^7 \left(F(f,\theta)\right)^2 \tag{5.4.6}$$

where c_b is a coefficient and determined to fit with wave generation. In the MRI-III, swell decay process which is slightly artificial is also included.

$$S_{sds} = -2.96 \times 10^{-6} \tanh\left[4 \left(f_s - f\right) / f_p\right] F(f,\theta), \tag{5.4.7}$$

Where $f_p = 0.156 g / U_{10N}$ stands for the peak frequency of the Pierson-Moskowitz (PM) spectrum from the 10m height wind speed U_{10N}. This decay function is applied to the spectrum whose frequency is smaller than $f_s = 1.8 f_p$ and only when significant wave height is larger than 1.5m.

4. S_{btm}: the energy loss by bottom friction. This term is not yet included in the MRI-III which deal with only deep water.

5.4.3 Wind Field

Wind fields for the GWM and the CWM are given by the Global Spectral Model (GSM), while the SWM uses Meso-Scale Model (MSM) winds. In all the models, wind fields around typhoons were modified with an empirical method. Typhoons are one of major sources to produce extremely high waves in the western North Pacific, and accurate wave forecasts are crucial to prevent shipwreck and coastal disasters. Since the NWP models sometimes do not predict correct typhoon conditions such as intensity or location, wind fields by operationally analyzed / forecasted typhoon are implanted onto the NWP winds (what we call "bogus wind") , when a typhoon exists in the western North Pacific. Moreover, the change of a typhoon course may drastically change the wave field especially in small region of the SWM. Therefore, wave fields are also predicted in five cases when typhoon is assumed to move the successive path of five points (center, faster, slower, right end and left end) on the typhoon forecast error circle.

The bogus winds are made as the following way. Sea level pressure distribution near a typhoon is assumed to have a profile of Fujita's empirical formula (Fujita 1952)

$$P(r) = P_\infty - \frac{P_\infty - P_0}{\sqrt{1 + (r/r_0)^2}} \tag{5.4.8}$$

where P_∞, P_0 and r_0 denote the ambient pressure, the central pressure of the typhoon, and the scaling factor of the radial distribution of the pressure, respectively. Surface winds near the typhoon are estimated from the pressure field by assuming the gradient wind balance with modifications based on the typhoon movement and surface friction effects.

5.4.4 Initial Condition

The initial conditions for the wave models are given by the 6-hour forecast of the previous initial run. Wind fields for the initial conditions are given by the GSM and the MSM initiated 6 hours before. An assimilation scheme (Kohno *et al.* 2011) for the GWM and the CWM has just been introduced in October 2012. In this system, initial conditions (wave spectra) are modified based on the significant wave heights by the Objective Wave Analysis System (Kohno *et al.* 2009), which automatically analyzes wave heights with observations by

radar altimeters of satellites, buoys, coastal wave recorders and ships. This change will improve the prediction of ocean wave field, especially in shorter forecast time.

5.4.5 Examples of Wave Prediction

Figure 5.4.3 is an example of the 24-hour prediction of wave fields by GWM. The chart contains contours of significant wave heights and mean wave direction at selected grid points.

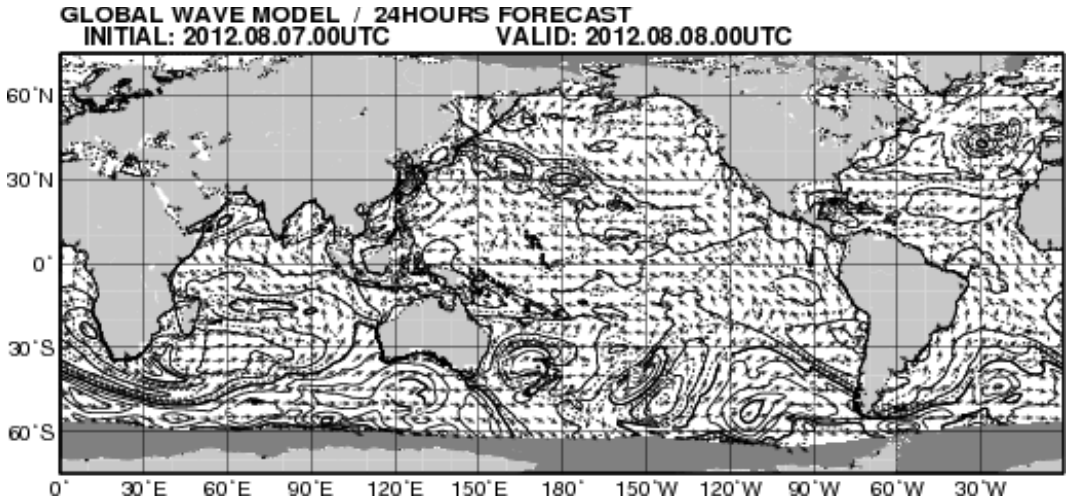

Figure 5.4.3: An example of 24-hour prediction of ocean wave by the Global Wave Model with the initial time of 00UTC 7 August 2012. Significant wave heights are contoured with dashed lines for half a meter, solid lines for every meter and thick solid lines for every 4 meters. Wave directions are represented by arrows for selected grid points. Area of sea ice is dark-shaded.

Figure 5.4.4 is a chart of the 24-hour prediction of wave fields by CWM.

5.4.6 Improvement and Development

The new assimilation scheme has just been introduced and is needed to be improved, as well as the MRI-III model numerics improvements.

The target area of the SWM is going to be added in due course. Furthermore, new version of MRI-III, including shallow water effects, has been developed to be used as the SWM.

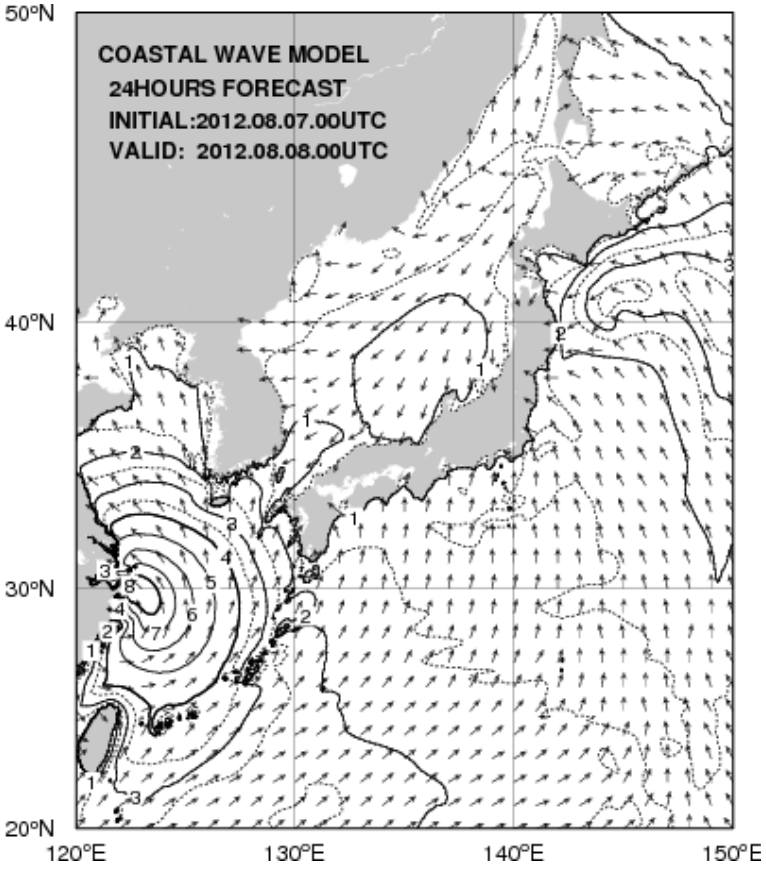

Figure 5.4.4: An example of 24-hour prediction around Japan by the Coastal Wave Model with the initial time of 00UTC 7 August 2012. Notations are the same as in Figure 5.4.3. The high wave was predicted around a tropical cyclone in the East China.

5.5 Storm Surge Model

5.5.1 Japan Area Storm Surge Model

5.5.1.1 Introduction

Since Japan has suffered from many storm surge disasters over the years, accurate and timely forecasts and warnings are critical to mitigating the threat to life and property from such storm surges.

Japan Meteorological Agency (JMA), which is responsible for issuing storm surge warnings, has operated a numerical storm surge model since 1998 to provide basic information for the warnings.

Numerical storm surge prediction started in July 1998 only when a typhoon exists. The storm surge model has been modified in enlarging the model domain, prediction for the extratropical cyclone case, extending of forecast time and adding advection terms, etc. Since May 2010, for more detailed information and warnings, a new storm surge model with higher resolution (approximately 1 km mesh) and the gridded astronomical tide analysis method have been operated.

5.5.1.2 Dynamics

Storm surges are mainly caused by the effect of wind setup due to strong onshore winds on sea surface and inverse barometer effect associated with pressure drop in a low pressure system. The effect of wind setup is proportional to the square of wind speed and inversely proportional to water depth, and related with the coastal topography, that is, it is amplified in a bay opened against the wind.

The storm surge model operated in the JMA is almost the same as the one described in Higaki *et al.* (2009). This model includes the ocean model and the part which makes the meteorological fields that drive the ocean model. To predict the temporal and spatial variations of sea level in response to such meteorological disturbances, the storm surge model utilizes two-dimensional shallow water equations. The shallow water equations consist of vertically integrated momentum equations in two horizontal directions:

$$\frac{\partial U}{\partial t} + u\frac{\partial U}{\partial x} + v\frac{\partial U}{\partial y} - fV = -g(D+\eta)\frac{\partial(\eta-\eta_0)}{\partial x} + \frac{\tau_{\mathrm{sx}}}{\rho_w} - \frac{\tau_{\mathrm{bx}}}{\rho_w} \tag{5.5.1a}$$

$$\frac{\partial V}{\partial t} + u\frac{\partial V}{\partial x} + v\frac{\partial V}{\partial y} + fU = -g(D+\eta)\frac{\partial(\eta-\eta_0)}{\partial y} + \frac{\tau_{\mathrm{sy}}}{\rho_w} - \frac{\tau_{\mathrm{by}}}{\rho_w} \tag{5.5.1b}$$

and the continuity equation:

$$\frac{\partial \eta}{\partial t} + \frac{\partial U}{\partial x} + \frac{\partial V}{\partial y} = 0 \tag{5.5.2}$$

where U and V are volume fluxes in the x- and y-directions, defined as:

$$U \equiv \int_{-D}^{\eta} u\,dz \tag{5.5.3a}$$

$$V \equiv \int_{-D}^{\eta} v\,dz \tag{5.5.3b}$$

f is the Coriolis parameter; g is the gravity acceleration; D is the water depth below mean sea level; η is the surface elevation; η_0 is the inverse barometer effect converted into the equivalent water column height; ρ_w is the density of water; τ_{sx} and τ_{sy} are x- and y-components of wind stress on sea surface; and τ_{bx} and τ_{by} are stresses of bottom friction, respectively.

The equations are solved by numerical integration using an explicit finite difference method. Regarding grid system, the staggered (or Arakawa-C) grid (Arakawa and Lamb 1977) is adopted.

5.5.1.3 Meteorological Forcing

The fields of surface wind and atmospheric pressure predicted by the Meso-Scale Model (MSM) are required as external forcing for the storm surge model. When a tropical cyclone (TC) exists around Japan, a simple parametric TC model is also used.

The simple parametric TC model (or referred to as bogus) is introduced in order to take into account the error of TC track forecast and its influence on storm surge forecasting. To consider the influence of TC track uncertainty on the occurrence of storm surge, we conduct five runs of the storm surge model with five possible TC tracks. These TC tracks are prescribed at the center and at four points on the forecast circle within which a TC is forecasted to exist with a probability of 70% (Figure 5.5.1):

1. Center track
2. Fastest track
3. Rightward biased track
4. Slowest track
5. Leftward biased track

and used to make meteorological fields with the parametric TC model.

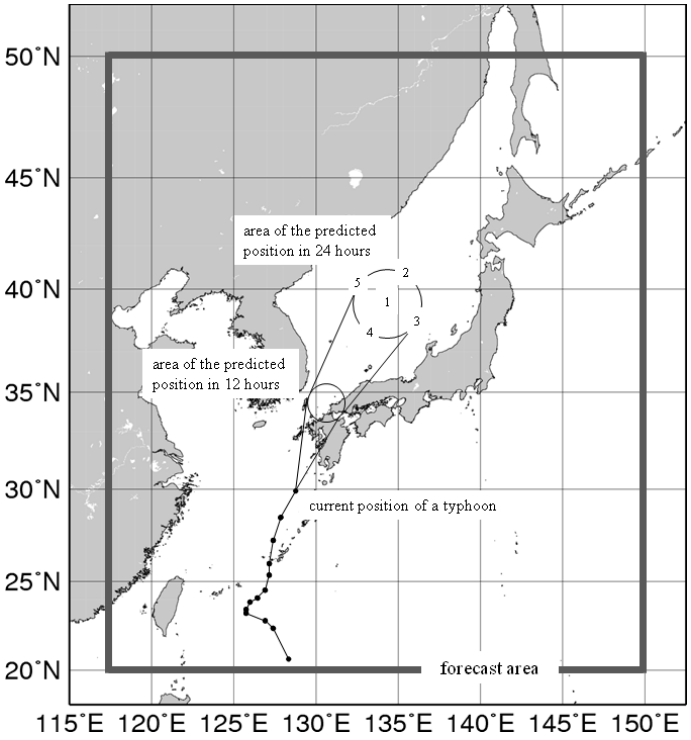

Figure 5.5.1: TC tracks of bogus and the domain of the Japan area storm surge model

The simple parametric TC model utilizes the Fujita's formula (Fujita 1952) that represents the radial pressure distribution in a TC:

$$P = P_\infty - \frac{P_\infty - P_c}{\sqrt{1 + (r/r_0)^2}} \tag{5.5.4}$$

and the gradient wind relation:

$$-\frac{v_g^2}{r} - f v_g = -\frac{1}{\rho}\frac{\partial P}{\partial r} \tag{5.5.5}$$

In Eq. (5.5.4), P is an atmospheric pressure at distance r from the center of a TC, P_∞ is the atmospheric pressure at an infinitely distant point, P_c is the pressure at TC center and r_0 is the scaling factor of the radial distribution of the pressure. In Eq. (5.5.5), ρ is the density of air, v_g is the gradient wind.
To represent the asymmetry of wind field **w** in a TC, the moving velocity vector of the TC multiplied by a weight that decays exponentially with the distance from TC center is added to the gradient wind:

$$\mathbf{w} = C_1 \left\{ \mathbf{v_g} + \mathbf{C} \cdot \exp\left(-\pi \frac{r}{r_e}\right) \right\} \tag{5.5.6}$$

C is the the moving velocity vector of the TC, r_e is the coefficient of decay.

Analysis and forecast information on TC, such as center position, central pressure and maximum wind are applied to these formulas to synthesize the wind and pressure fields (Konishi 1995).

5.5.1.4 Specifications of the Model

Table 5.5.1 gives the specifications of the storm surge model. The finest horizontal resolution of the model is $45''$(lon) $\times$ $30''$(lat) (approximately 1km mesh). The model domain covers the entire Japan.

Table 5.5.1: Specifications of the Japan area storm surge model

Model	2-dimensional model
Grid	Lat-Lon Arakawa-C grid
Region	20°N - 50°N, 117.5°E - 150°E
Resolution	approximately 1, 2, 4, 8, 16 km (Adaptive mesh)
Time step	4 seconds
Initial time	00, 03, 06, 09, 12, 15, 18, 21 (UTC)
Forecast time	00, 06, 12, 18 (UTC): 30 hours 03, 09, 15, 21 (UTC): 33 hours
Member	TC case: 6 members (MSM+5 bogus) no TC case: 1 member (MSM)

Since the storm surge is the shallow water long wave, its phase speed is proportional to the square root of water depth. It is inefficient to set all grids with the same resolution from a viewpoint of computer resources. Therefore, the adaptive mesh refinement (Berger and Oliger 1984) in which the mesh is fine over the shallow water and coarse over the deep water is adopted. The resolution is varied for 5 levels (1, 2, 4, 8 and 16 km) with the water depth (Figure 5.5.2). This method makes the storm surge calculations more efficient than the normal lat-lon grid system.

The storm surge model runs 8 times a day (every 3 hours) and calculates storm surge predictions up to 30 or 33 hours ahead. Initial values are generated by a previous calculation using the newest MSM prediction as the forcing (hindcast). Since the initial values are not so important as the one in atmospheric models, assimilation of observation data is not conducted.

The model computes only storm surges, i.e. anomalies from the level of astronomical tides. However, storm tides (storm surge plus astronomical tide) are also needed in issuing a storm surge warning. Astronomical tides are predicted by using harmonic analyses of sea level observations. The JMA developed the gridded astronomical tide method which calculates the astronomical tide even on the no-observation grid (Subsection 5.5.3). After the computation of the storm surge model, the level of astronomical tide for the coastal area is added to the predicted storm surge.

Then the results are sent to Local Meteorological Observatories that issue storm surge warnings to their responsible areas.

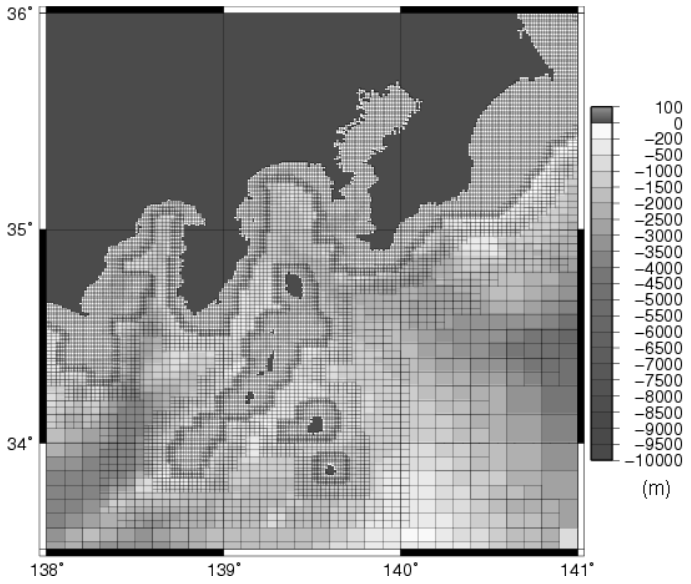

Figure 5.5.2: Horizontal grid system and water depth of the storm surge model (around Kanto region)

5.5.1.5 Verification

Accuracy of the storm surge prediction depends on accuracy of the storm surge model itself and atmospheric model. We investigated the accuracy of the storm surge model itself using the storm surge predictions driven by the atmospheric analysis data.

Figure 5.5.3 shows a scatter diagram of the predicted storm surges against the observed values. The statistical period is from 2004 to 2008. Observation from 120 tide stations, which are managed by the JMA, the Japan Coast Guard and the Geographical Survey Institute, are used. The figure shows that most errors of storm surge predictions lie in the range of ± 50 cm. It is supposed that the large errors mainly result from the factors which are not included in the storm surge model, i.e., the effect of wave setup, ocean currents and sea water stratification, etc.

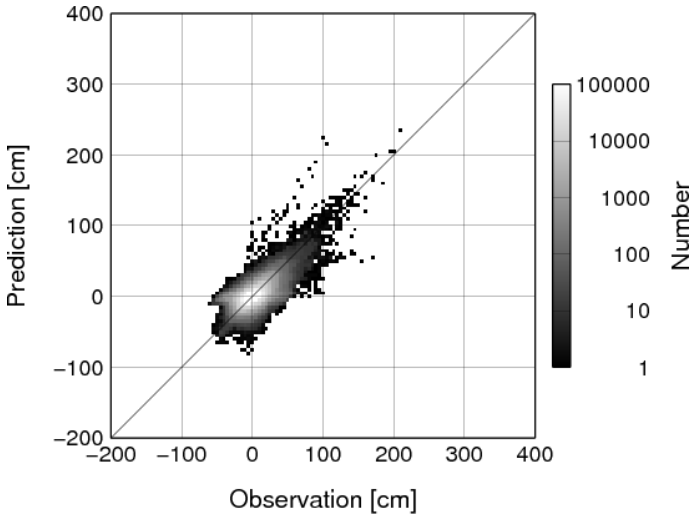

Figure 5.5.3: Scatter diagram of predicted storm surges against observed values

Figure 5.5.4 shows the best track of typhoon MELOR (T0918). The typhoon MELOR passed the eastern part of Japan and caused storm surge disasters especially in Mikawa bay on 8 October 2009. Figure 5.5.5 (a) shows the distributions of storm surge around Mikawa bay. The model well predicted the extreme storm surges by the wind setup in closed-off section of Mikawa bay. Figure 5.5.5 (b) shows the time series of storm surge at the port of Mikawa. Though the peak surge was slightly underestimated, the time of peak surge was exactly predicted.

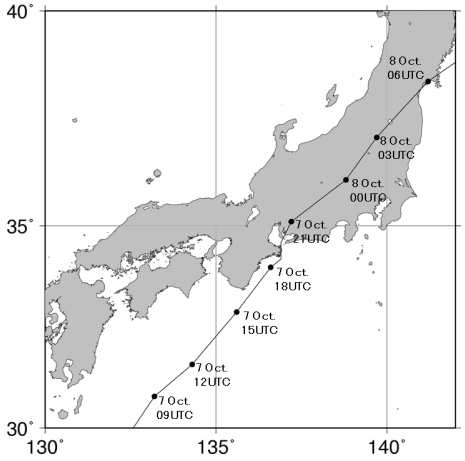

Figure 5.5.4: The best track of typhoon MELOR (T0918)

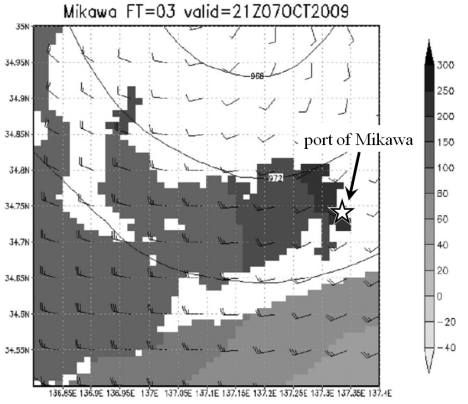

(a) Distribution of storm surge at 21UTC 8 October around Mikawa bay predicted by the storm surge model

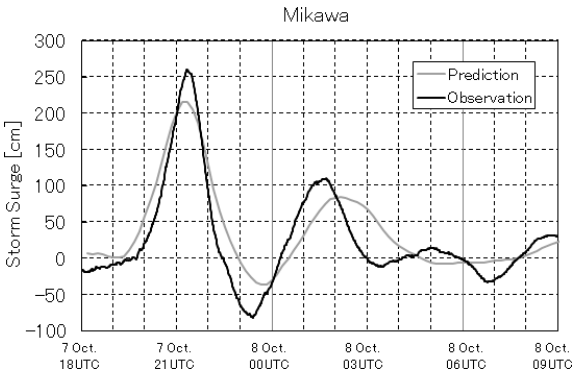

(b) Time series of storm surge at the port of Mikawa

Figure 5.5.5: Distribution of storm surge and timeseries at the port of Mikawa

5.5.2 Asia Area Storm Surge Model

5.5.2.1 Introduction

In recent years, heavy storm surge disasters occurred worldwide, such as the one in the coast of the Gulf of Mexico caused by Hurricane Katrina in 2005, the one in the coast of Bangladesh by Cyclone Sidr in 2007, and the one in the coast of Myanmar by Cyclone Nargis in 2008. By these storm surges more than thousands of people suffered. The countermeasures for storm surges and inundation are crucial.

In response to a request by the WMO Executive Council (60th session, June 2008), WMO initiated the development of a regional Storm Surge Watch Scheme (SSWS) in regions affected by tropical cyclones. In relation to the western North Pacific and the South China Sea, the ESCAP/WMO Typhoon Committee (41st session, January 2009) endorsed a commitment by the RSMC Tokyo - Typhoon Center to prepare storm surge forecasts with the aim of strengthening the storm surge warning capabilities of National Meteorological and Hydrological Services (NMHSs) in the region. JMA began development of a storm surge model for the Asia region in 2010, in collaboration with Typhoon Committee Members who provide sea level observation and sea bathymetry data. Horizontal distribution maps of predicted storm surges and time series charts have been published on JMA's Numerical Typhoon Prediction website (Hasegawa *et al.* 2012).

5.5.2.2 Dynamics

The basic equations of the Asia area storm surge model are nearly the same as those of the Japan area storm surge model (Subsection 5.5.1) except that advection terms are omitted. The equations of the model incorporate vertically integrated momentum fluxes under the influence of the earth's rotation with gravity acceleration:

$$\frac{\partial U}{\partial t} - fV = -g(D+\eta)\frac{\partial(\eta-\eta_0)}{\partial x} + \frac{\tau_{\mathrm{sx}}}{\rho_w} - \frac{\tau_{\mathrm{bx}}}{\rho_w} \tag{5.5.7a}$$

$$\frac{\partial V}{\partial t} + fU = -g(D+\eta)\frac{\partial(\eta-\eta_0)}{\partial y} + \frac{\tau_{\mathrm{sy}}}{\rho_w} - \frac{\tau_{\mathrm{by}}}{\rho_w} \tag{5.5.7b}$$

and the continuity equation:

$$\frac{\partial \eta}{\partial t} + \frac{\partial U}{\partial x} + \frac{\partial V}{\partial y} = 0 \tag{5.5.8}$$

Definitions of each variables and constants are the same as those of the Japan area storm surge model. The wind stresses are expressed as:

$$\tau_{\mathrm{sx}} = c_d \rho_a W u_w \tag{5.5.9a}$$

$$\tau_{\mathrm{sy}} = c_d \rho_a W v_w \tag{5.5.9b}$$

where c_d is the drag coefficient, ρ_a is the density of air, $W \equiv \sqrt{u_w^2 + v_w^2}$ is the wind speed, and (u_w, v_w) is the wind velocity. The drag coefficient is set from the results of Smith and Banke (1975) and Frank (1984):

$$c_d = \begin{cases} (0.63 + 0.066W) \times 10^{-3} & (W < 25 m/s) \\ \{2.28 + 0.033(W-25)\} \times 10^{-3} & (W \geq 25 m/s) \end{cases} \tag{5.5.10}$$

5.5.2.3 Data

The bathymetry data for the storm surge model is mainly made from the 2-minute Global Gridded Elevation Data (ETOPO2) of NGDC/NOAA (Figure 5.5.6). The bathymetry data was partly modified with local bathymetry data provided by the Typhoon Committee Members, which enable more accurate forecast.

The astronomical tides are determined by harmonic analysis using the past tide observation data provided by the Typhoon Committee members.

5.5.2.4 Meteorological Forcing

In the operation of the Asia area storm surge model, two kinds of meteorological forcing field are used. One is a simple parametric TC model, and the other is the products of the JMA operational Global Spectral Model (GSM). The simple parametric TC model of the Asia area storm surge model is the same one as of the Japan area storm surge model (Subsection 5.5.1).

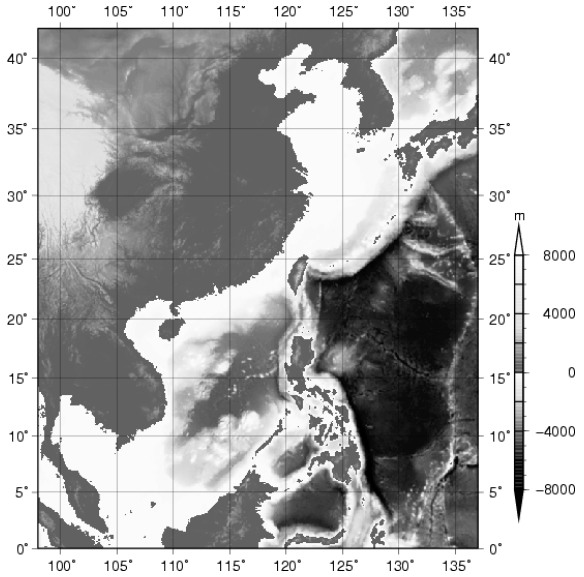

Figure 5.5.6: Model domain and topography of the Asia area storm surge model

5.5.2.5 Specifications of the Model

Table 5.5.2 shows the outline of the specifications of the Asia area storm surge model. The horizontal grid resolution is 2 minutes, corresponding to a distance of about 3.7 km. The model covers almost all areas in the RSMC Tokyo - Typhoon Center area of responsibility (Figure 5.5.6). It runs four times a day (every 6 hours), and calculates storm surge predictions up to 72 hours ahead. Each calculation takes about 10 minutes, and storm surge distribution maps are created using the results. When no typhoon is expected nor exist during the forecast time, the model calculates the hindcast only for the next run, and no distribution maps are produced.

The 3-hourly distribution maps of the whole domain and enlarged versions showing only the areas around typhoon are available up to 72 hours. The time series charts include predicted/astronomical tide, storm surge, sea level pressure and surface wind.

Table 5.5.2: Specifications of the Asia area storm surge model

Model	2-dimensional linear model
Grid	Lat-Lon Arakawa-C grid
Region	0° - 42°N, 98°E - 137°E
Resolution	2-minutes mesh (approximately 3.7 km mesh)
Time step	8 seconds
Initial time	00, 06, 12, 18 (UTC)
Forecast time	72 hours
Member	1 member

5.5.2.6 Verification

To examine the performance of the Asia area storm surge model, we verified the model accuracy by comparing predicted values with observed ones. In this verification, hourly storm surge predictions were compared with observations at seven tide stations. The predictions are calculated by the GSM analysis data (Sep. 2007 to Dec. 2010) and the parametric TC model with typhoon best track data made by RSMC Tokyo - Typhoon Center.

Figure 5.5.7 shows a scatter diagram of the predicted storm surges against the observed values. The predicted values include all those for 1-hour through 72-hour forecast time. The figures show that the surge predictions lie in the range of 100 cm.

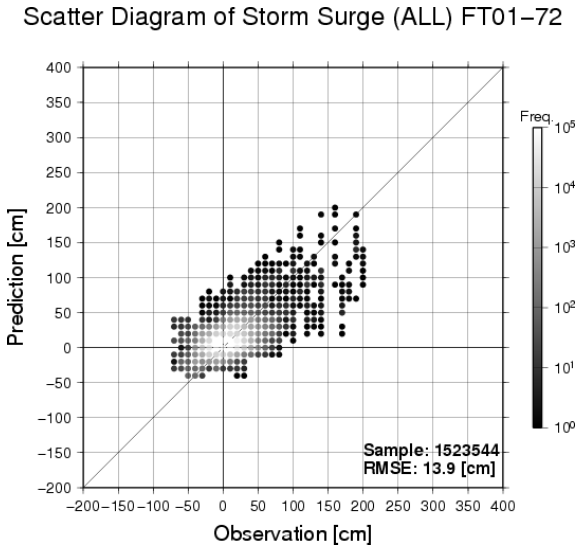

Figure 5.5.7: Scatter diagram of predicted storm surges against observed values

Figure 5.5.8 shows a storm surge distribution map for Typhoon KOPPU (T0915), which generated extremely high storm surges in Hong Kong and Macao and made landfall on the coast of southern China, and a time series chart at Macao. The extremely high storm surges are well represented by the Asia area storm surge model.

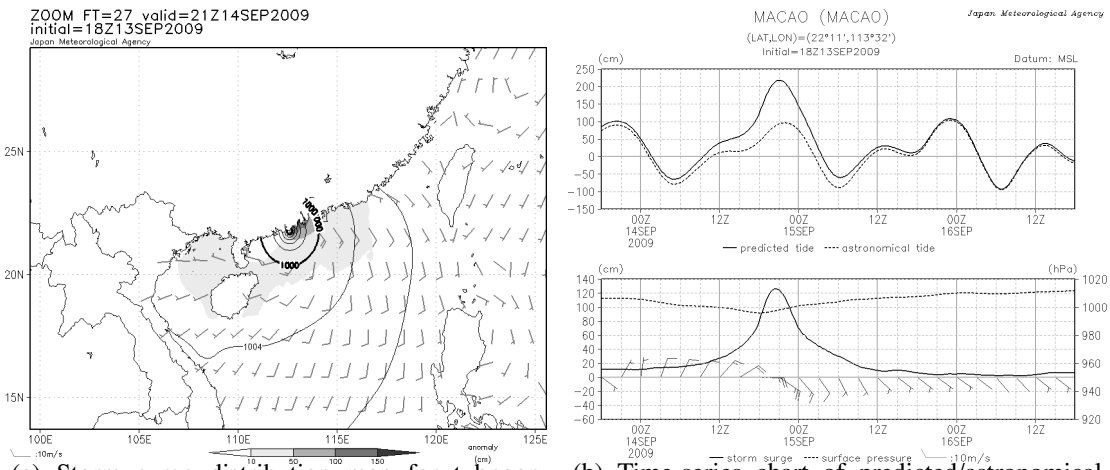

(a) Storm surge distribution map for tyhpoon KOPPU (T0915)

(b) Time-series chart of predicted/astronomical tides and storm surge at Macao

Figure 5.5.8: Distribution of storm surge and timeseries at Macao

5.5.3 Astronomical Tide Analysis

5.5.3.1 Introduction

The model explained in Subsection 5.5.1 only calculates storm surges, in other words, anomalies from the level of the astronomical tides. But, prediction of storm tides, which are storm surges plus the astronomical tides, are needed for issuing storm surge warnings. Since 2010, JMA issues storm surge warnings for all coastal areas in Japan. Therefore the analyses of astronomical tides at any Japanese coast are required. JMA developed a new analysis method of astronomical tides for the coastal seas around Japan.

5.5.3.2 Analysis Method

The variation of tides is expressed as a composition of periodic oscillations in various frequencies such as semi-diurnal, diurnal and annual tides. Semi-diurnal and diurnal tides are caused by gravitational forces of the moon and the sun. Annual tides are brought by seasonal variation of seawater temperature and sea surface pressure. Harmonic constants which are the sets of amplitudes and phases for each tidal constituent are derived by harmonic analysis. As for tide station, they are derived by analyzing hourly tidal observation data. But, it is impossible to gain the harmonic constants at arbitrary coastal points by using this method.

In order to analyze astronomical tides at any point, we calculate the first guess and assimilate the harmonic constants at tide stations. The procedures of analysis for short-period tides (semi-diurnal and diurnal tides) and long-period tides (annual tides) are described below. The schematic diagram is shown in Figure 5.5.9. Constituents used in this method are shown on Table 5.5.3.

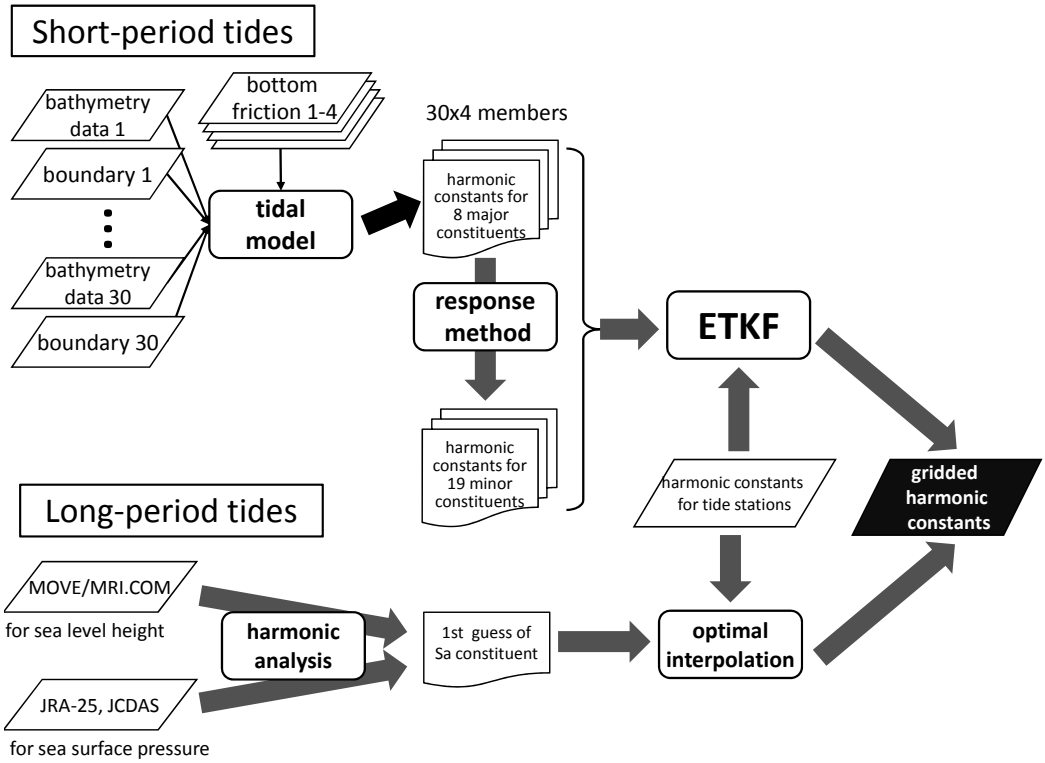

Figure 5.5.9: Schematic flow chart of astronomical tide analysis

Table 5.5.3: List of constituents used in astronomical tide analysis. "Major" and "minor" mean constituents estimated by a tidal model, and those estimated by the response method using major constituents, respectively.

Name	Type	Major/Minor	Name	Type	Major/Minor
S_a	annual	-	θ_1	diurnal	minor
$2Q_1$	diurnal	minor	J_1	diurnal	minor
σ_1	diurnal	minor	OO_1	diurnal	minor
Q_1	diurnal	major	$2N_2$	semi-diurnal	minor
ρ_1	diurnal	minor	μ_2	semi-diurnal	minor
O_1	diurnal	major	N_2	semi-diurnal	major
MP_1	diurnal	minor	ν_2	semi-diurnal	minor
M_1	diurnal	minor	M_2	semi-diurnal	major
χ_1	diurnal	minor	λ_2	semi-diurnal	minor
π_1	diurnal	minor	L_2	semi-diurnal	minor
P_1	diurnal	major	T_2	semi-diurnal	minor
K_1	diurnal	major	S_2	semi-diurnal	major
ψ_1	diurnal	minor	R_2	semi-diurnal	minor
ϕ_1	diurnal	minor	K_2	semi-diurnal	major

5.5.3.3 Short-period Tides

Constituents which amplitude is relatively large (major 8 constituents) are estimated using a tidal model of Oregon State University Tidal Inversion Software (OTIS) package (Egbert and Erofeeva 2002). OTIS consists of three components: the data preparation, the ocean dynamics and the data assimilation. We only use the linearized version of the ocean dynamics (tidal model) in which Fourier transform is applied to eliminate time variable:

$$i\omega U - fV + gH\frac{\partial \zeta}{\partial x} + \kappa U = F_U \tag{5.5.11}$$

$$i\omega V + fU + gH\frac{\partial \zeta}{\partial y} + \kappa V = F_V \tag{5.5.12}$$

$$\left(\frac{\partial U}{\partial x} + \frac{\partial V}{\partial y}\right) + i\omega\zeta = 0 \tag{5.5.13}$$

where ω is frequency of a tidal constituent, U and V are x and y components of current integrated from sea surface to bottom, respectively, f is Coriolis parameter, g is acceleration of gravity, H is depth, ζ is the anomaly from mean sea level, κ is dissipation coefficient of bottom friction, F is tide-generating force.

We use Ensemble Transform Kalman Filter (ETKF) (Bishop *et al.* 2001) to assimilate harmonic constants at tide stations. Since the model result has errors due to the resolution and accuracy of bathymetry data and lateral boundary conditions, perturbations are added to bathymetry and boundary condition in order to create an ensemble. We have prepared 120 ensemble members which are combinations of 30 different data sets of bathymetry including random errors and boundary condition generated by blending the results of tidal models and 4 bottom friction data. The tidal models used are NAO.99Jb (Matsumoto *et al.* 2000), FES2004 (Lyard *et al.* 2006), GOT00.2 (an update to Ray (1999)), and TPXO (Egbert and Erofeeva 2002). Minor 19 constituents are estimated from major constituents of similar frequency using the response method (Munk and Cartwright 1966).

5.5.3.4 Long-period Tides

The first guess of annual constituents (S_a) is derived from the result of harmonic analysis of reanalyzed sea level height from MOVE/MRI.COM (see Section 5.3 and Usui *et al.* (2006)) corrected with sea surface pressure

from Japanese 25-year Reanalysis (JRA-25) and JMA Climate Data Assimilation System (JCDAS) (see Section 2.10 and Onogi *et al.* (2007)) assuming hydrostatic balance. This is modified using harmonic constants at tide stations by optimal interpolation (OI) method.

5.5.3.5 Verification

To verify the astronomical tides analyzed by the described method, we compared them with those from harmonic constants at tide stations. Figure 5.5.10 shows the distribution of root mean square error (RMSE) of the analysis compared with those from harmonic constants of tide stations. At most of the stations, RMSE is less than 3cm, while at some stations especially in bays and inland sea, RMSE is relatively large.

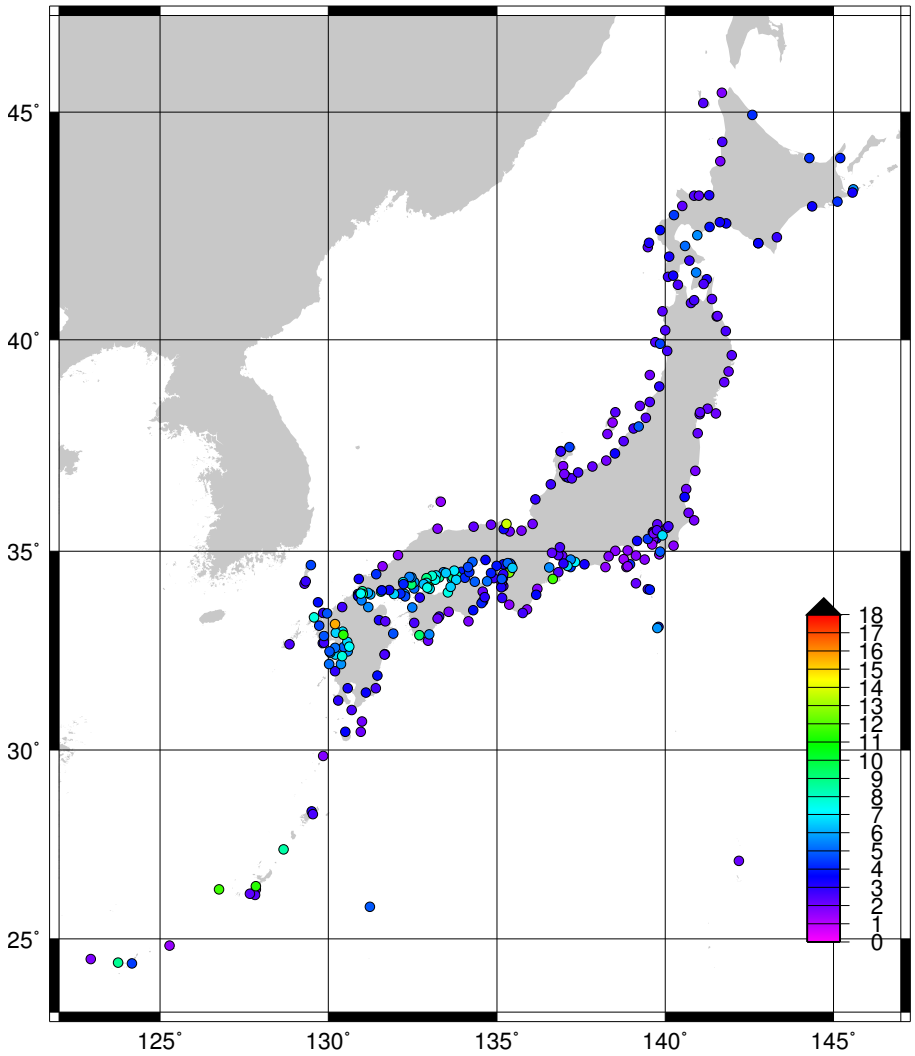

Figure 5.5.10: Distribution of RMSE of astronomical tide analysis. The unit is cm.

5.6 Sea Ice Model

5.6.1 Introduction

The Japan Meteorological Agency (JMA) has operated a numerical sea ice model since December 1990 to support sea ice forecasting for the southern part of the Sea of Okhotsk in the winter season. The sea ice model based on dynamics and thermodynamics forecasts distribution and concentration of sea ice for the next 7 days.

Outputs of the model have been operationally disseminated twice a week for the duration of sea ice around Hokkaido, the northern island of Japan, via internet[5] and through JMH broadcast system.

5.6.2 Model Structure

5.6.2.1 Forecast Area

Figure 5.6.1 shows the forecast area with 71×71 square grids with intervals of 12.5km. The model calculates 4 physical elements (volume, concentration, velocity and thickness (=volume/concentration)) of sea ice at each grid by using initial data of sea ice concentration and sea surface temperature (SST), meteorological forecast data and statistics of ocean current.

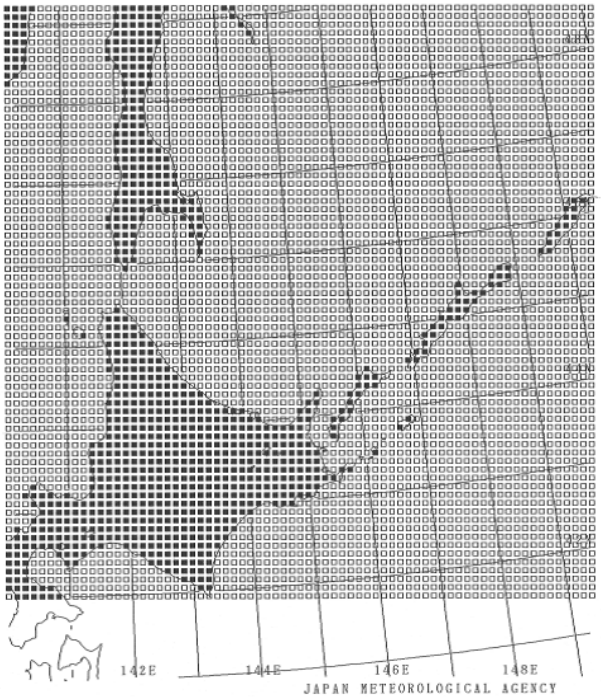

Figure 5.6.1: Forecast area of the sea ice model. ■: a land grid □: a sea grid

5.6.2.2 Calculation of Sea Ice Condition

The volume (M_i) and the concentration (A_i) of sea ice at each grid are governed by the following equations:

$$\frac{\partial M_i}{\partial t} = -\mathrm{div}(M_i V_i) + P_M$$

[5] `http://www.data.kishou.go.jp/kaiyou/db/seaice/forecast/nsif.html` (in Japanese) and `http://www.jma.go.jp/jmh/jmhmenu.html` (in Japanese)

$$\frac{\partial A_i}{\partial t} = -\mathrm{div}(A_i V_i) + P_A + D_A \tag{5.6.1}$$

where V_i is the sea ice velocity, which is determined in the dynamical process described in Subsection 5.6.2.3. P_M and P_A denote the change of the volume and the concentration, respectively, due to the growth or the melting of sea ice and snowfall. They are determined in the thermodynamic process described in Subsection 5.6.2.4. D_A is a term related to the development of hummock due to the convergence of sea ice. D_A is given by calculating the convergence of V_i : (Udin and Ullerstig 1976)

$$D_A = \begin{cases} \mathrm{div}(A_i V_i) & A_i = 1 \quad \text{and} \quad \mathrm{div}(V_i) < 0 \\ 0 & 0 < A_i < 1 \quad \text{or} \quad \mathrm{div}(V_i) \geq 0. \end{cases} \tag{5.6.2}$$

5.6.2.3 Dynamical Processes

A momentum equation of sea ice is described as follows: (Hibler 1979)

$$\rho_i H_i \frac{\partial V_i}{\partial t} = \tau_a(V_a) + \tau_w(V_w, V_i) + C(V_i) + G(V_w) + F_i \tag{5.6.3}$$

τ_a : wind stress,
τ_w : water stress,
C : Coriolis force,
G : pressure gradient force due to tilting sea surface,
F_i : internal ice stress.

Here ρ_i and H_i ($=M_i / A_i$) are sea ice density and thickness, respectively. V_a, V_w, and V_i denote the velocity of wind, ocean current and sea ice, respectively. Due to the fact that the left-hand side term of Eq. (5.6.3) is smaller than the other terms by more than one order of magnitude, V_i can be derived approximately on the assumption that the terms on the right-hand side terms of Eq. (5.6.3) are in balance. V_a is given by Global Spectral Model (GSM, see Section 3.2) and V_w is given by climatology described in Subsection 5.6.3.3. We simplified Hibler's viscous-platic method to calculate F_i because F_i is such a quite complex term that we used a lot of computational resources. The alternate method is that a provisional sea ice velocity calculated by the assumption that the first 4 terms of Eq. (5.6.3) are balanced is modified by the non-slip condition at the coastal square grids.

5.6.2.4 Thermodynamic Processes

The thermodynamic processes in the model effect the growth or the melting of sea ice by heat exchange among atmosphere, ocean and sea ice. In sea ice area, heat exchange between atmosphere and sea ice causes the change of sea ice thickness. A heat balance equation on the sea ice surface is as follows (Semtner 1976):

$$(1 - Al)R_s \downarrow + R_a \downarrow + SH(T_i) \downarrow + LH(T_i) \downarrow - FL(T_i, H_i) \downarrow - R_i(T_i) \uparrow = 0 \tag{5.6.4}$$

R_s : solar radiation,
Al : albedo of sea ice or snowfall,
R_a : atmospheric radiation,
SH : sensitive heat flux,
LH : latent heat flux,
FL : vertical heat flux in sea ice,
R_i : radiation emitted from sea ice,
T_i : surface temperature of sea ice.

R_s and R_a are given by GSM. T_i can be calculated from Eq. (5.6.4). If $T_i < -1.8°C$, sea ice gains the thickness whose increment is estimated from FL. If $T_i > 0°C$, sea ice loses the thickness whose negative increment is estimated from the sum of all the terms on the left-hand side of Eq. (5.6.4) after T_i is set to 0°C. If $-1.8°C \leq T_i \leq 0°C$, sea ice remains unchanged.

In open water area, heat exchange between atmosphere and ocean causes change of sea water temperature that affects melting sea ice. The ocean in the model consists of a thin surface layer and a mixed layer. The amount of heat exchange between the ocean and the atmosphere at each grid is described as follows:

$$Q_w \downarrow = (1 - Al_w)R_s \downarrow + R_a \downarrow + SH(T_s) \downarrow + LH(T_s) \downarrow - R_w(T_s) \uparrow \tag{5.6.5}$$

Here R_w denotes the radiation emitted from sea surface and Al_w is the albedo of sea water. T_s is the sea water temperature of the surface layer. We assume that the heat exchange between the sea surface layer and the mixed layer is calculated as follows:

$$T_s = \frac{(T_s - T_f)D_s + (T_m - T_f)D_m}{D_s + D_m} + T_f \tag{5.6.6}$$

Here D_s and D_m denote the depth of the surface layer and the mixed layer, respectively, and are fixed at each sea grid. T_m is the sea water temperature of the mixed layer, and T_f is the freezing point (−1.8°C) of sea water. Here, the change of sea water temperatures is calculated on the two assumptions that direct heat exchange between sea ice and sea water occurs only through the surface layer and that the heat exchange between sea ice and the surface layer occurs to drive T_s to the melting point (0°C).

5.6.3 Data Used in the Model

5.6.3.1 Initial Data of Sea Ice and Sea Surface Temperature

Initial fields of sea ice and sea surface temperature are derived from data as follows: Initial fields of sea ice concentration is subjectively estimated on the basis of data from satellites (mainly MTSAT and NOAA), aircraft, ships and coastal observations; An initial field of sea ice thickness is derived from the previous forecast; Daily SST analysis data in the seas around Japan given by MGDSST, which is described in Subsection 5.2.1, are used for an initial field of SST.

5.6.3.2 Meteorological Data

Air pressure, air temperature, wind, dew point, solar radiation, atmospheric radiation and precipitation on the sea surface at each grid are given by the interpolation of the predictions by the atmospheric numerical model (GSM).

5.6.3.3 Ocean Current Data

The distribution of the ocean currents used in the model is obtained from Japan Maritime Safety Agency (1983) and shown in Figure 5.6.2. It is fixed throughout the winter season.

5.6.4 Example of the Results of the Numerical Sea Ice Model

An example of the results of the 7-day forecast is shown in Figure 5.6.3. In this example the model forecasts that sea ice will move southward and be on the coast of the Hokkaido Island facing the Sea of Okhotsk.

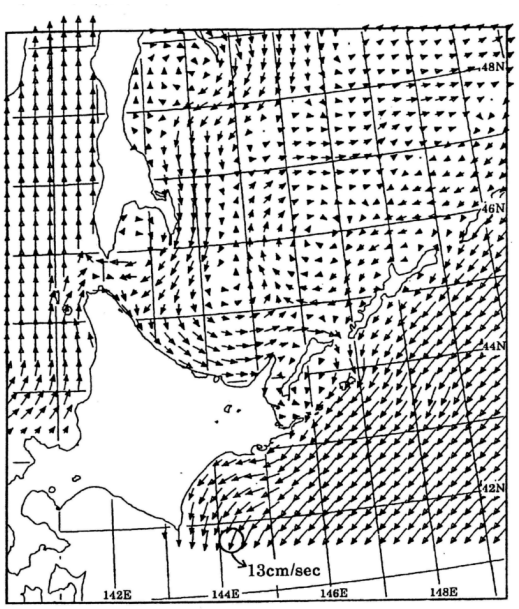

Figure 5.6.2: The ocean currents used in the model.

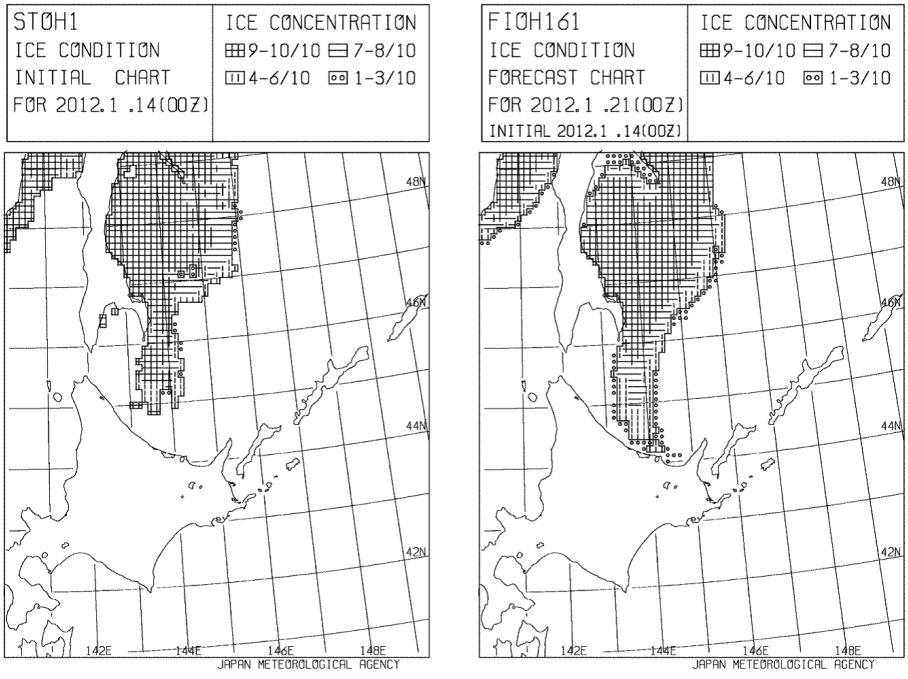

Figure 5.6.3: An example of the results of the model.

5.7 Oil Spill Prediction Model

5.7.1 Introduction

In 1990s, large-scale oil spill incidents frequently occurred in the world. Around Japan, a wrecked Russian tanker "Nakhodka" brought about a severe oil spill incidents in the Sea of Japan in January 1997, which led to heavy damage to the environment along the western coastline of the Japan. After the incident, countermeasures against large-scale oil spill events were considered in the Japanese Government, and JMA developed an Oil Spill Prediction Model, and the model has been put into operational mode since October 1999.

The model predicts large scale behavior of spilled oil in offshore seas where tidal current is negligible. Getting accident information from the Japan Coast Guard, JMA operates the Oil Spill Prediction Model to get up to 192 hours forecast, and results are transferred to the staff who is responsible for emergency response operations.

The prediction model is applicable to the entire western North Pacific. The domain of calculation is selected from prepared seven settings from $0.8^\circ \times 0.8^\circ$ to $12^\circ \times 12^\circ$ in latitude and longitude, by considering of the incident condition.

5.7.2 Basic Equation

An oil spill prediction model is generally described in the following equation including the terms of advection and diffusion,

$$\frac{dC}{dt} = \frac{\partial C}{\partial t} + \mathbf{V} \cdot \nabla C = \nabla \cdot (K \nabla C) + S \tag{5.7.1}$$

where C is the concentration of the pollutant, t is time, $\mathbf{V}$ the advection velocity, K the turbulent diffusion coefficient, and S (called the source term) represents processes to change the total amount of the spilled oil through the change of oil properties.

To solve the equation (5.7.1) with a computer, there are two common ways: one is to calculate C values directly by the finite difference method; the other is to simulate the behaviors of many 'particles' which are supposed to be the components of oil. The Oil Spill Prediction Model in JMA uses the latter method. The spilled oil is expressed by many particles $C_n (n = 1, 2, \cdots)$ as,

$$C_n \{\mathbf{x}(t + \delta t), s(t + \delta t); t + \delta t\} = \Phi[C_n (\mathbf{x}(t), s(t); t)] \tag{5.7.2}$$

where $\mathbf{x} = (x, y, z)$ indicates the position of each particle, s is the chemical status of oil. Φ is a general function which describes the oil property change in time.

In the advection term, effects of the surface wind, the ocean wave, and the ocean current could be major processes to be taken into account. Ekman drift current is generated by the sea surface wind, which is well-known as "3% rule". In the JMA model, the surface flows are determined as 2.5% of the wind speed with an angle of 15° clockwise with respect to the wind direction. The Stokes drift is a forwarded movement of particles at the sea surface to the wave direction by the wave motion back and forth in each wave cycle. This effect becomes important if high waves exist and the effect is independent of wind when swell is predominant. Therefore, Stokes drift is included explicitly and calculated from the wave condition predicted by JMA wave models. Ocean currents are provided by the JMA Ocean Data Assimilation System for the Western North Pacific (MOVE-WNP).

The three dimensional diffusion of oil is basically calculated by the sheer diffusion treatment by Elliott (1986). The surface flow is supposed to have a logarithmic profile in vertical, and spilled oil is assumed to be carried by horizontal speed at each water level. The sheer mechanism considers the vertical diffusion too. The spilled oil is divided into many oil droplets, which get the buoyancy according to their size. By considering the buoyancy and the present depth of oil drop, the oil motion in vertical, whether it remains in surface or not, is determined.

In addition to the above sheer diffusion process, there may be isotropic diffusion generated by small scale eddies and so on. This effect is estimated by the constant diffusion coefficient $K_h = 95.0 m^2/s$. In the condition

Table 5.7.1: Specification of the oil spill prediction model

Applicable area		10°S – 65°N, 120°E – 180°E
Domain of calculation		7 options ($0.8^\circ \times 0.8^\circ - 12^\circ \times 12^\circ$)
Grid spacing		7 options (2 – 30km), according to the domain of calculation
Number of grids		41×41
Prediction period		192 hours
Physical and chemical process	Advection	Ekman drift (estimated from wind field of Global Spectrum Model) Stokes drift (estimated from wave field of Global/Coastal Wave Models) Ocean current (MOVE/MRI.COM-NWP)
	Diffusion	Elliott (1986) etc.
	Evaporation	Fingas (1997)
	Emulsification	Reed (1989)

of strong winds or high ocean waves, diffusion may be enlarged. Therefore, these diffusions are parameterized with additional diffusion coefficients:

$$\begin{cases} waves : K_{wv} = 500.0 H_w^2 / T_w \\ winds : K_{wnd} = 5.0 W^5 / g \end{cases} \tag{5.7.3}$$

where H_w and T_w are wave height and period, W is wind speed, and g is the gravitational acceleration.

The additional diffusion of oil parcels are estimated by the total value of the diffusion coefficients (K_h, K_{wv}, and K_{wnd}). The concrete values are calculated by the random walk method and this diffusion is supposed to be horizontal.

Since the behavior of spilled oil is quite complicated, it is difficult to consider all of the chemical processes. We only consider a few of major processes, that is, evaporation and emulsification. The evaporation is estimated by the Fingas's empirical formulae (Fingas 1997). According to Fingas (1997), the evaporation rate $E_v(\%)$ of most oils can be expressed by the form of either the logarithmic or root profile in time.

$$E_v = \begin{cases} (a + b \cdot T) \ln t \\ (a + b \cdot T) \sqrt{t} \end{cases} \tag{5.7.4}$$

The constant coefficients a and b were determined by experiments and are listed in the oil data catalogue by Environment Canada. T stands for the temperature of oil which is supposed to have the same value of the Sea Surface temperature (SST), t is the elapsed time (in minute) after the spill.

The emulsification is calculated by the formula of Reed (1989), which estimates the water content F_{wc} by

$$\frac{dF_{wc}}{dt} = 2.0 \times 10^{-6} (W + 1)^2 \cdot \left(1 - \frac{F_{wc}}{C_3}\right) \tag{5.7.5}$$

where $W(m/s)$ is wind speed. C_3 is a constant parameter for the upper limit of water content, which differs among the oil types. The density of oil is also calculated with the water content, which can change the behaviour of oil.

Specifications of the Oil Spill Prediction Model and process methods used in the model are summarized in Table 5.7.1

5.7.3 Products

The model is to be operated in the case of a large-scale oil spill in the offshore deep water seas where tidal currents in short time can be negligible. The result of oil spill prediction is provided to the Japanese Government and/or the Japan Coast Guard with the other various marine meteorological charts. An example of the prediction is shown in Figure 5.7.1.

5.7.4 Development Plan

The current model is going to be replaced by a new version written in fortran90. In the current version, the model domain and resolution must be chosen from seven options, because of the restriction of setting in FORTRAN77. On the other hand, dynamic array allocation is available in fortran90. Therefore, in the new version, the model domain and grid resolution can be set freely, so as to be suitable for the incident condition.

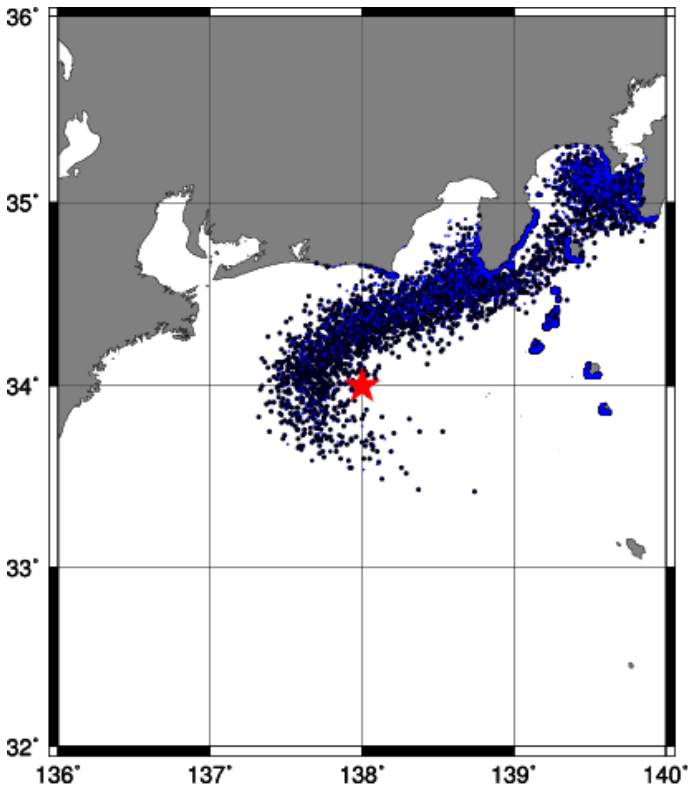

Figure 5.7.1: An example of a test simulation case in the sea south of Japan. The star shows the locations of the accident. The area and amount of the spilled oil is indicated by dot distribution.

Appendix A

Verification Indices

In this appendix, a number of verification indices used in this document are presented for reference. The indices are also used in the international verification through the Global Data-processing and Forecasting System (GDPFS) of the World Meteorological Organization (WMO 2010a, 2012).

A.1 Basic Verification Indices

A.1.1 Mean Error

Mean Error (ME), also called Bias, represents the mean value of deviations between forecasts and verification values, and is defined by

$$\mathrm{ME} \equiv \left(\sum_{i=1}^{n} w_i D_i \right) \Big/ \sum_{i=1}^{n} w_i, \tag{A.1.1a}$$

$$D_i = F_i - A_i, \tag{A.1.1b}$$

$$w_i = \frac{1}{n} \text{ (or } \cos\phi_i \text{, and so on)}, \tag{A.1.1c}$$

where F_i, A_i, and D_i represent forecast, verifying value, and the deviation between forecast and verifying value, respectively. Also, w_i represents weighting coefficient, n is the number of samples, and ϕ_i is latitude. In general, observational values, initial values, or objective analyses are often used as the verifying values. When the forecast is perfectly correct, called *perfect forecast*, ME is equal to zero.

In calculating the average in a wide region, *e.g.* the Northern hemisphere, the average should be evaluated with the weighting coefficients, taking into account the differences of areas due to the latitudes. For example, in order to evaluate objective analysis in equirectangular projection, the weighting coefficient "$w_i = 1/n$" is often replaced with cosine of latitude "$\cos\phi_i$" (see WMO (2012)). The other indices in Section A.1 will be dealt with in the same manner.

A.1.2 Root Mean Square Error

Root Mean Square Error (RMSE) is often used for representing the accuracy of forecasts, and is defined by

$$\mathrm{RMSE} \equiv \sqrt{\sum_{i=1}^{n} w_i D_i^2} \Big/ \sqrt{\sum_{i=1}^{n} w_i}, \tag{A.1.2}$$

where D_i represents the deviation between forecast and verifying value in Eq. (A.1.1b), w_i represents the weighting coefficient in Eq. (A.1.1c), and n is the number of samples. If RMSE is closer to zero, it means that

the forecasts are closer to the verifying values. For perfect forecast, RMSE is equal to zero. By separating the components of ME and random error, RMSE is expressed as follows:

$$\mathrm{RMSE}^2 = \mathrm{ME}^2 + \sigma_{\mathrm{e}}^2, \tag{A.1.3}$$

where σ_e represents Standard Deviation (SD) for the deviation D_i, and is given by

$$\sigma_e^2 = \left(\sum_{i=1}^{n} w_i (D_i - \mathrm{ME})^2 \right) \Big/ \sum_{i=1}^{n} w_i. \tag{A.1.4}$$

A.1.3 Anomaly Correlation Coefficient

Anomaly Correlation Coefficient (ACC) is one of the most widely used measures in the verification of spatial fields (Jolliffe and Stephenson 2003), and is the correlation between anomalies of forecasts and those of verifying values with the reference values, such as climatological values. ACC is defined as follows:

$$\mathrm{ACC} \equiv \frac{\sum_{i=1}^{n} w_i \left(f_i - \overline{f}\right)(a_i - \overline{a})}{\sqrt{\sum_{i=1}^{n} w_i \left(f_i - \overline{f}\right)^2 \sum_{i=1}^{n} w_i \left(a_i - \overline{a}\right)^2}}, \quad (-1 \le \mathrm{ACC} \le 1), \tag{A.1.5}$$

where n is the number of samples, and f_i, $\overline{f}$, a_i and $\overline{a}$ are given by the following equations:

$$f_i = F_i - C_i, \quad \overline{f} = \left(\sum_{i=1}^{n} w_i f_i \right) \Big/ \sum_{i=1}^{n} w_i, \tag{A.1.6a}$$

$$a_i = A_i - C_i, \quad \overline{a} = \left(\sum_{i=1}^{n} w_i a_i \right) \Big/ \sum_{i=1}^{n} w_i, \tag{A.1.6b}$$

where F_i, A_i, and C_i represent forecast, verifying value, and reference value such as climatological value, respectively. Also, $\overline{f}$ is the mean of f_i, $\overline{a}$ is the mean of a_i, and w_i represents the weighting coefficient in Eq. (A.1.1c). If the variation pattern of the anomalies of forecast is perfectly coincident with that of the anomalies of verifying value, ACC will take the maximum value of 1. In turn, if the variation pattern is completely reversed, ACC takes the minimum value of -1.

A.1.4 Ensemble Spread

Ensemble Spread is a familiar measure which represents the degree of the forecast uncertainty in the ensemble forecast. It is the standard deviation of the ensembles, and is defined by

$$\text{Ensemble Spread} \equiv \sqrt{\frac{1}{N} \sum_{i=1}^{N} \left(\frac{1}{M} \sum_{m=1}^{M} (F_{m,i} - \bar{F}_i)^2 \right)}, \tag{A.1.7}$$

where M is the number of ensemble members, N is the number of samples, $F_{m,i}$ represents the forecast of the mth member, and $\bar{F}_i$ is the ensemble mean, defined by

$$\bar{F}_i \equiv \frac{1}{M} \sum_{m=1}^{M} F_{m,i}. \tag{A.1.8}$$

Table A.2.1: Schematic contingency table for categorical forecasts of a binary event. The numbers of outcomes in each category are indicated by FO, FX, XO and XX, and N is the total number of events.

	Observed	Not Observed	Total
Forecasted	FO (hits)	FX (false alarms)	$FO + FX$
Not Forecasted	XO (misses)	XX (correct rejections)	$XO + XX$
Total	M	X	N

A.1.5 S1 Score

S1 Score is often used to measure the degree of error in the depiction of forecast pressure field, and is defined by

$$\mathrm{S1} \equiv 100 \times \frac{\sum_{i=1}^{n} w_i \left\{ |\partial_x D_i| + \left|\partial_y D_i\right| \right\}}{\sum_{i=1}^{n} w_i \left[\max\left(|\partial_x F_i|, |\partial_x A_i|\right) + \max\left(\left|\partial_y F_i\right|, \left|\partial_y A_i\right|\right) \right]}, \tag{A.1.9}$$

where F_i and A_i represent forecast and verifying value, respectively. D_i is the deviation between forecast and verifying value in Eq. (A.1.1b), w_i is the weighting coefficient in Eq. (A.1.1c), and the subscript x or y denotes the differential with respect to x or y, as shown in the forms:

$$\partial_x X = \frac{\partial X}{\partial x}, \quad \partial_y X = \frac{\partial X}{\partial y}. \tag{A.1.10}$$

The lower S1 Score is, the better the forecast is.

A.2 Verification Indices for Categorical Forecasts

Many meteorological phenomena can be regarded as simple binary events, and forecasts or warnings for these events are often issued as unqualified statement that they will or will not take place (Jolliffe and Stephenson 2003). In the verification of the forecasts for binary events, the outcomes for an event on the targeted phenomenon are distinguished in terms of the correspondence between forecasts and observations, using 2×2 contingency table as shown in Table A.2.1.

A.2.1 Contingency Table

In the contingency table, the categorical forecasts of a binary event are divided into four possible outcomes, namely, hits, false alarms, misses, and correct rejections (or correct negatives). The numbers of the possible outcomes are indicated with the notations, FO, FX, XO, and XX, respectively. The total number of events is the sum of numbers of all outcomes, given by $N = FO + FX + XO + XX$. The numbers of observed events and not observed events are $M = FO + XO$, and $X = FX + XX$, respectively.

A.2.2 Proportion Correct

Proportion Correct (PC) is the ratio of the number of correct events $FO + XX$ to the total number of events N, and is defined by

$$\mathrm{PC} \equiv \frac{FO + XX}{N}, \qquad (0 \leq \mathrm{PC} \leq 1). \tag{A.2.1}$$

The larger PC means the higher accuracy of the forecasts.

A.2.3 False Alarm Ratio

False Alarm Ratio (FAR) is the ratio of the number of false alarm events FX to the number of forecasted events $FO + FX$, and is defined by

$$\mathrm{FAR} \equiv \frac{FX}{FO + FX}, \qquad (0 \leq \mathrm{FAR} \leq 1). \tag{A.2.2}$$

The smaller FAR is, the less the number of false alarm events is. In some cases, the total number N is used as the denominator in Eq. (A.2.2), instead of $FO + FX$.

A.2.4 Undetected Error Rate

Undetected Error Rate (Ur) is the ratio of the number of miss events XO to the number of observed events M, and is defined by

$$\mathrm{Ur} \equiv \frac{XO}{M}, \qquad (0 \leq \mathrm{Ur} \leq 1). \tag{A.2.3}$$

The smaller Ur is, the less the number of miss events is. In some cases, the total number N is used as the denominator in Eq. (A.2.3), instead of M.

A.2.5 Hit Rate

Hit Rate (Hr) is the ratio of the number of hit events FO to the number of observed events M, and is defined by

$$\mathrm{Hr} \equiv \frac{FO}{M}, \qquad (0 \leq \mathrm{Hr} \leq 1). \tag{A.2.4}$$

The larger Hr is, the less the number of miss events is. Hit Rate is used for the plot of ROC curve, described in Subsection A.3.5.

A.2.6 False Alarm Rate

False Alarm Rate (Fr) is the ratio of the number of false alarm events FX to the number of not observed events X, and is defined by

$$\mathrm{Fr} \equiv \frac{FX}{X}, \qquad (0 \leq \mathrm{Fr} \leq 1). \tag{A.2.5}$$

The smaller Fr means that the number of false alarm events is less and the accuracy of the forecasts is higher. It is noted that the denominator of False Alarm Rate is different from that of False Alarm Ratio (see Subsection A.2.3). False Alarm Rate is also used for the plotting of the ROC curve, described in Subsection A.3.5.

A.2.7 Bias Score

Bias Score (BI) is the ratio of the number of forecasted events $FO + FX$ to the number of observed events M, and is defined by

$$\mathrm{BI} \equiv \frac{FO + FX}{M}, \qquad (0 \leq \mathrm{BI}). \tag{A.2.6}$$

If the number of forecasted events $FO + FX$ is equal to the number of observed events M, BI will be unity. If BI is larger than unity, the frequency of events is overestimated. Conversely, if BI is smaller than unity, the frequency of events is underestimated.

A.2.8 Climatological Relative Frequency

Climatological Relative Frequency (P_c) is the probability of occurrence of the events estimated from the samples, and is defined by

$$\mathrm{P}_c \equiv \frac{M}{N}, \tag{A.2.7}$$

where M is the number of observed events to occur, and N is the total number of events. P_c is derived from the number of observed events, and independent of the accuracy of forecast.

A.2.9 Threat Score

Threat Score (TS) is the index focused on the hit event. TS is the ratio of the number of hit events FO to the number of events except for the correct rejections events $FO + FX + XO$, and is defined by

$$\mathrm{TS} \equiv \frac{FO}{FO + FX + XO}, \qquad (0 \leq \mathrm{TS} \leq 1). \tag{A.2.8}$$

If the number of observed events is extremely small, i.e. $N \gg M$, and $XX \gg FO$, FX, or XO, Proportion Correct (PC) will be close to unity because of the the major contribution from the number of not observed events. TS is applicable to validate the accuracy of forecasts without the contribution from the correct rejections events. The accuracy of forecasts is higher as TS approaches to the maximum value of unity. TS is often affected by Climatological Relative Frequency, so that it is not applicable to compare the accuracy of forecasts validated under different conditions. In order to avoid this problem, Equitable Threat Score is often used for the validation.

A.2.10 Equitable Threat Score

Equitable Threat Score (ETS) is similar to the threat score, but removed the contribution from hits by chance in *random forecast*, and is defined by

$$\mathrm{ETS} \equiv \frac{FO - S_f}{FO + FX + XO - S_f}, \qquad (-\frac{1}{3} \leq \mathrm{ETS} \leq 1), \tag{A.2.9}$$

and

$$S_f = P_c(FO + FX), \quad P_c = \frac{M}{N}, \tag{A.2.10}$$

where P_c is Climatological Relative Frequency, and S_f is the number of hit events in being forecasted randomly at $FO + FX$ times. The closer to the maximum value of unity, the higher the accuracy of forecast is. In the case of random forecast, ETS is zero. ETS has the minimum value of $-1/3$, if $FO = XX = 0$ and $FX = XO = N/2$.

A.2.11 Skill Score

Skill Score, also called Heidke Skill Score, is used to remove the effect of the difficulties in individual forecasts, taking in to account the number of correct events in random forecast estimated from climatological probabilities, and defined by

$$\text{Skill} \equiv \frac{FO + XX - S}{N - S}, \qquad (-1 \leq \text{Skill} \leq 1), \tag{A.2.11}$$

$$S = P_c(FO + FX) + Px_c(XO + XX), \tag{A.2.12}$$

and

$$P_c = \frac{M}{N}, \quad Px_c = \frac{X}{N} = 1 - P_c, \tag{A.2.13}$$

where P_c and Px_c are the climatological relative frequencies of observed events and not observed events in random forecast, respectively. The closer to the maximum value of unity, the higher the accuracy of forecast is. Skill score is zero in random forecast and unity in perfect forecast. Skill score has the minimum value of -1, if $FO = XX = 0$ and $FX = XO = N/2$.

A.3 Verification Indices for Probability Forecasts

A.3.1 Brier Score

Brier Score (BS) is a basic verification index for the probability forecasts, and is defined by

$$\text{BS} \equiv \frac{1}{N}\sum_{i=1}^{N}(p_i - a_i)^2, \quad (0 \leq \text{BS} \leq 1), \tag{A.3.1}$$

where p_i is the forecast probability of occurrence of an event ranging from 0 to 1 in probability forecasts, a_i indicates the observations with binary values, i.e. 1 for observed or 0 for not observed, and N is the number of samples. The smaller BS is, the higher the accuracy of forecasts is. In the perfect forecast, BS has the minimum value of 0 for the deterministic forecast, in which p_i is equal to 0 or 1.

Brier Score for *climatological forecast* (BS_c), in which the climatological relative frequency $P_c = M/N$ is always used as the forecast probability p_i, is defined by

$$\text{BS}_c \equiv P_c(1 - P_c), \tag{A.3.2}$$

Since the Brier Score is influenced by the climatological frequency of the event in the verification sample, it is not applicable to compare the accuracy of the forecast with different sets of samples and/or different phenomena. For example, BS_c can be different with the different value of P_c even if the forecast method is same such as climatological forecast, because of its dependence on P_c. In order to reduce this effect, Brier Skill Score is often used for the verification with the improvement from the climatological forecast (see Subsection A.3.2).

A.3.2 Brier Skill Score

Brier Skill Score (BSS) is an index based on the Brier Score, indicating the degree of forecast improvements in reference to climatological forecast. BSS is defined by

$$\text{BSS} \equiv \frac{\text{BS}_c - \text{BS}}{\text{BS}_c}, \quad (\text{BSS} \leq 1), \tag{A.3.3}$$

where BS is Brier Score, and BS_c is the Brier Score for climatological forecast. BSS is unity for perfect forecast, and zero for the climatological forecast. BSS has a negative value if the forecast error is more than that of climatological forecast.

A.3.3 Murphy's Decompositions

In order to provide a deeper insight on the relation between Brier Score (BS) and the properties of the probability forecasts, Murphy (1973) decomposed the Brier Score into three terms, i.e. reliability, resolution, and uncertainty. This is called Murphy's Decompositions.

Consider the probability of forecasts classified to L intervals. Let the sample number in the lth interval be N_l, and also the number of observed events in N_l be M_l. It follows that $N = \sum_{l=1}^{L} N_l$ and $M = \sum_{l=1}^{L} M_l$. Therefore, BS can be represented with Murphy's Decompositions as follows:

$$\text{BS} = \text{Reliability} - \text{Resolution} + \text{Uncertainty}, \tag{A.3.4a}$$

$$\text{Reliability} = \sum_{l=1}^{L} \left(p_l - \frac{M_l}{N_l} \right)^2 \frac{N_l}{N}, \tag{A.3.4b}$$

$$\text{Resolution} = \sum_{l=1}^{L} \left(\frac{M}{N} - \frac{M_l}{N_l} \right)^2 \frac{N_l}{N}, \tag{A.3.4c}$$

$$\text{Uncertainty} = \frac{M}{N} \left(1 - \frac{M}{N} \right), \tag{A.3.4d}$$

where p_l is the representative value in the lth interval of the predicted probability. Reliability becomes the minimum value of zero when p_l is equal to the relative frequency of the observed events M_l/N_l. If the distance between $M/N\,(=\ P_c)$ and M_l/N_l is longer, Resolution will have a large value. Uncertainty depends on the observed events, regardless of forecast methods. When $P_c = 0.5$, Uncertainty will have the maximum value of 0.25. Uncertainty is equal to the Brier Score for climatological forecast (BS_c). In this regard, Brier Skill Score (BSS) can be written as

$$\text{BSS} = \frac{\text{Resolution} - \text{Reliability}}{\text{Uncertanity}}. \tag{A.3.5}$$

A.3.4 Reliability Diagram

The performance for the probability forecasts is often evaluated using Reliability Diagram, also called Attributes Diagram, which is a chart with the relative frequencies of observed events P_{obs} as the ordinate and the probability of the forecasted events to occur P_{fcst} as abscissa, as shown in Figure A.3.1. The plot is generally displayed as a curve, called Reliability Curve.

The properties of Reliability Curve can be related to Reliability and Resolution in Murphy's Decompositions. Contribution to Reliability (or Resolution) for each value of P_{fcst} is associated with the squared distance from a point on Reliability Curve to the line $P_{\text{obs}} = P_{\text{fcst}}$ (or $P_{\text{obs}} = P_c$), and is derived from its weighted mean using the number of samples as weights. The contributions are the same for both Reliability and Resolution on the line $P_{\text{obs}} = (P_{\text{fcst}} + P_c)/2$, called no-skill line, and the contribution to Brier Score becomes zero on this line. The gray meshed area surrounded by the no-skill line, the line $P_{\text{fcst}} = P_c$ and the axes in Figure A.3.1 indicates the area with positive contributions to BSS, since the contribution to Reliability is larger than that to Resolution. For further details on Reliability Diagram, please refer to Wilks (2006).

In the climatological forecast (see Subsection A.3.1) as the special case, the Reliability Curve corresponds to a point $(P_{\text{fcst}},\ P_{\text{obs}}) = (P_c,\ P_c)$. The probability forecasts which indicate the following properties will have higher accuracy.

- Reliability Curve is close to the linear line $P_{\text{obs}} = P_{\text{fcst}}$ (Reliability is close to zero),
- Points with the large number of samples on Reliability Curve is distributed apart from the point of the climatological forecast $(P_{\text{fcst}},\ P_{\text{obs}}) = (P_c,\ P_c)$ (around the lower left or the upper right in Reliability Diagram), with higher Resolution.

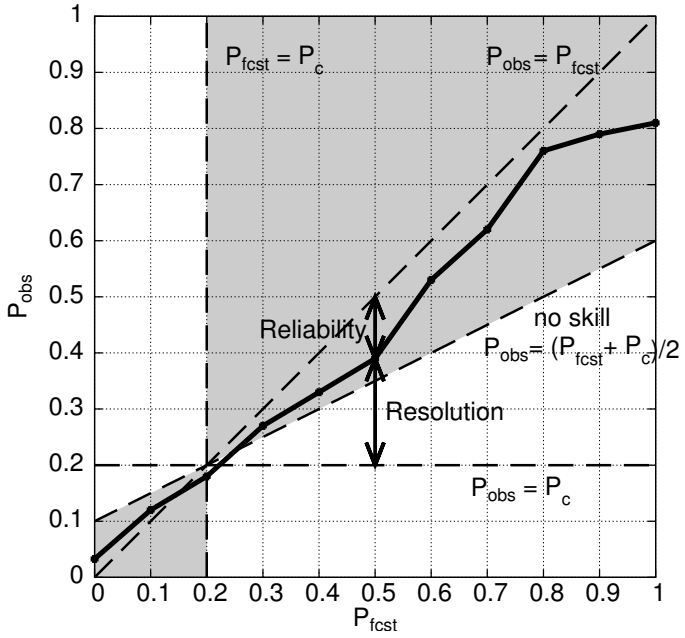

Figure A.3.1: Reliability Diagram. The ordinate is the relative frequencies of observed events P_{obs}, the abscissa is the probability of the forecasted events to occur P_{fcst}, and the solid line is Reliability Curve. The gray meshed area indicates the existence of the positive contributions to BSS.

A.3.5 ROC Area Skill Score

If two alternatives in a decision problem, whether the event occur or not, must be chosen on the basis of a probability forecast for a dichotomous variable, the determination which of the two alternatives will depend on the probability threshold. Relative Operating Characteristic (ROC) curve is often used to evaluate such decision problem. ROC curve is a schematic diagram whose ordinate and abscissa are Hit Rate (Hr) and False Alarm Rate (Fr), respectively, and made from the contingency tables with variations of the threshold values, as shown in Figure A.3.2.

The threshold value is lower around the upper right in the diagram, and higher around the lower left. The probability forecast is more accurate when the curve is more convex to the top because Hit Rate is more than False Alarm Rate, i.e. $Hr > Fr$ around the upper left. Therefore, the area below ROC curve filled in gray, called ROC area (ROCA), will be wider with the higher value of information in the probability forecasts. For further details on ROC curve, please refer to Wilks (2006).

ROC Area Skill Score (ROCASS) is a validation index in reference to the probability forecasts with no value of information, i.e. $Hr = Fr$, and defined by

$$\text{ROCASS} \equiv 2(\text{ROCA} - 0.5), \quad (-1 \leq \text{ROCASS} \leq 1). \tag{A.3.6}$$

ROCASS is unity for perfect forecast, and zero for the forecast with no value of information, *e.g.* the forecast with a uniform probability which is randomly sampled from the range [1, 0].

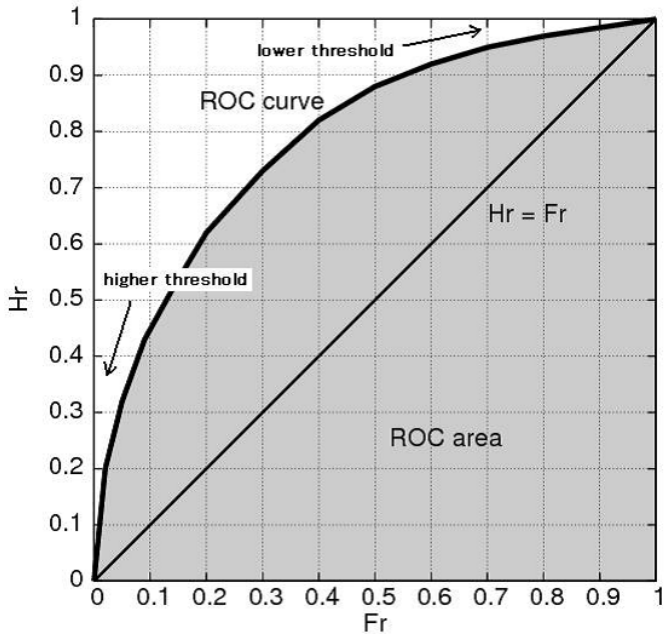

Figure A.3.2: Schematic Diagram of ROC Curve. The ordinate of the diagram is Hr and the abscissa is Fr. The gray area indicates ROC area.

References

Agresti, A., 2002: *Categorical Data Analysis, 2nd ed.* New York: Wiley, 734pp.

Andersson, E. and H. Järvinen, 1999: Variational Quality Control. *Quart. J. Roy. Meteor. Soc.*, **125**, 697–722.

Aoki, Te., Ta. Aoki, M. Fukabori, and T. Takao, 2002: Characteristics of UV-B irradiance at Syowa Station, Antarctica: Analyses of the measurements and comparison with numerical simulations. *J. Meteor. Soc. Japan*, **80**, 161–170.

Arakawa, A., 1972: Design of the UCLA general circulation model. Numerical simulation weather and climate, Tech. Rep. 7, Dept. of Meteorology, University of California, Los Angeles. 116pp.

Arakawa, A. and V. R. Lamb, 1977: Computational design of the basic dynamical processes of the UCLA general circulation model. *Methods in Computational Physics*, **17**, 174–265, Academic Press.

Arakawa, A. and W. H. Schubert, 1974: Interaction of a cumulus cloud ensemble with the large-scale environment, Part I. *J. Atmos. Sci.*, **31**, 674–701.

Aranami, K. and J. Ishida, 2004: Implementation of two dimensional decomposition for JMA non-hydrostatic model. *CAS/JSC WGNE Res. Activ. Atmos. Oceanic Modell.*, **34**, 03.01–03.02.

Arking, A. and K. Grossman, 1972: The influence of line shape and band structure on temperatures in planetary atmospheres. *J. Atmos. Sci.*, **29**, 937–949.

Barkmeijer, J., R. Buizza, T. N. Palmer, K. Puri, and J.-F. Mahfouf, 2001: Tropical singular vectors computed with linearized diabatic physics. *Quart. J. Roy. Meteor. Soc.*, **127**, 685–708.

Barnes, R. T. H., R. Hide, A. A. White, and C. A. Wilson, 1983: Atmospheric angular momentum fluctuations, length-of-day change and polar motion. *Proc. R. Soc.*, **A387**, 31–73.

Beljaars, A. C. M., 1995: The parameterization of surface fluxes in large-scale models under free convection. *Quart. J. Roy. Meteor. Soc.*, **121**, 255–270.

Beljaars, A. C. M. and A. A. M. Holtslag, 1991: Flux parameterization over land surfaces for atmospheric models. *J. Appl. Meteor.*, **30**, 327–341.

Berger, M. J. and J. Oliger, 1984: Adaptive mesh refinement for hyperbolic partial differential equations. *J. Comp. Phys.*, **53**, 484–512.

Berner, J., G. J. Shutts, M. Leutbecher, and T. N. Palmer, 2009: A Spectral Stochastic Kinetic Energy Backscatter Scheme and Its Impact on Flow-Dependent Predictability in the ECMWF Ensemble Prediction System. *J. Atmos. Sci.*, **66**, 603–626.

Bishop, C. H., B. J. Etherton, and S. J. Majumdar, 2001: Adaptive Sampling with the Ensemble Transform Kalman Filter. Part I : Theoretical Aspects. *Mon. Wea. Rev.*, **129**, 420–436.

Blackadar, A. K., 1962: The vertical distribution of wind and turbulent exchange in a neutral atmosphere. *J. Geophys. Res.*, **67**, 3095–3102.

Bloom, S. C., L. L. Takacs, A. M. da Silva, and D. Ledvina, 1996: Data assimilation using incremental analysis updates. *Mon. Wea. Rev.*, **124**, 1256–1271.

Bourke, W., 1974: A multi-level spectral model. I. Formulation and hemispheric integrations. *Mon. Wea. Rev.*, **102**, 687–701.

Briegleb, B. P., 1992: Delta-Eddington Approximation for Solar Radiation in the NCAR Community Climate Model. *J. Geophys. Res.*, **97**, 7603–7612.

Buizza, R., 1998: Impact of Horizontal Diffusion on T21, T42, and T63 Singular Vectors. *J. Atmos. Sci.*, **55**, 1069–1083.

Buizza, R., M. Miller, and T. N. Palmer, 1999: Stochastic representation of model uncertainties in the ECMWF Ensemble Prediction System. *Quart. J. Roy. Meteor. Soc.*, **125**, 2887–2908.

Buizza, R. and T. N. Palmer, 1995: The Singular-Vector Structure of the Atmospheric Global Circulation. *J. Atmos. Sci.*, **52**, 1434–1456.

Caumont, O., V. Ducrocq, É. Wattrelot, G. Jaubert, and S. Pradier-vabre, 2010: 1D+3DVar assimilation of radar reflectivity data: a proof of concept. *Tellus*, **62A**, 173–187.

Cavaleri, L. and P. M. Rizzoli, 1981: Wind wave prediction in shallow water: Theory and applications. *J. Geophys. Res.*, **86**, 10 961–10 973.

Charnock, H., 1955: Wind stress on a water surface. *Quart. J. Roy. Meteor. Soc.*, **81**, 639–640.

Chiba, M., K. Yamazaki, K. Shibata, and Y. Kuroda, 1996: The description of the MRI atmospheric spectral GCM (MRI-GSPM) and its mean statistics based on 10-year integration. *Pap. Meteor. Geophys.*, **47**, 1–45.

Chou, M.-D. and L. Kouvaris, 1991: Calculations of transmission functions in the infrared CO_2 and O_3 bands. *J. Geophys. Res.*, **96**, 9003–9012.

Chou, M.-D., M. J. Suarez, X.-Z. Liang, and M. M.-H. Yan, 2001: A thermal infrared radiation parameterization for atmospheric studies. Technical report series on global modeling and data assimilation, NASA/TM-2001-104606, 19, NASA Goddard Space Flight Center, 56 pp.

Coakley, J. A., R. D. Cess, and F. B. Yurevich, 1983: The effect of tropospheric aerosols on the earth's radiation budget: a parameterization for climate models. *J. Atmos. Sci.*, **40**, 116–138.

Courtier, P., J.-N. Thépaut, and A. Hollingsworth, 1994: A strategy for operational implementation of 4D-Var, using an incremental approach. *Quart. J. Roy. Meteor. Soc.*, **120**, 1367–1387.

Deardorff, J. W., 1978: Efficient prediction of ground surface temperature and moisture, with inclusion of a layer of vegetation. *J. Geophys. Res.*, **83**, 1889–1903.

Deardorff, J. W., 1980: Stratocumulus-capped mixed layers derived from a three-dimensional model. *Bound.-Layer Meteor.*, **18**, 495–527.

Dee, D. P., 2004: Variational bias correction of radiance data in the ECMWF system. *Proceedings of the ECMWF workshop on assimilation of high spectral resolution sounders in NWP*, Reading, UK, 28 June - 1 July 2004, 97–112.

Derber, J. and F. Bouttier, 1999: A reformulation of the background error covariance in the ECMWF global data assimilation system. *Tellus*, **51A**, 195–221.

Derber, J. C. and W.-S Wu, 1998: The use of TOVS cloud-cleared radiances in the NCEP SSI analysis system. *Mon. Wea. Rev.*, **126**, 2287–2299.

Desroziers, G., L. Berre, B. Chapnik, and P. Poli, 2005: Diagnosis of observation, background and analysis-error statistics in observation space. *Quart. J. Roy. Meteor. Soc.*, **131**, 3385–3396.

Deushi, M. and K. Shibata, 2011: Development of a Meteorological Research Institute Chemistry-Climate Model version 2 for the study of tropospheric and stratospheric chemistry. *Pap. Meteor. Geophys.*, **62**, 1–46.

Doblas-Reyes, F. J., R. Hagedorn, T. N. Palmer, and J.-J. Morcrette, 2006: Impact of increasing greenhouse gas concentrations in seasonal ensemble forecasts. *Geophys. Res. Lett.*, **33**, L07 708.

Dorman, J. and P. J. Sellers, 1989: A global climatology of albedo, roughness length and stomatal resistance for atmospheric general circulation models as represented by the Simple Biosphere model (SiB). *J. Appl. Meteor.*, **28**, 833–855.

Ebert, E. E. and J. A. Curry, 1992: A parameterization of ice cloud optical properties for climate models. *J. Geophys. Res.*, **97**, 3831–3836.

Ebita, A., S. Kobayashi, Y. Ota, M. Moriya, R. Kumabe, K. Onogi, Y. Harada, S. Yasui, K. Miyaoka, K. Takahashi, H. Kamahori, C. Kobayashi, H. Endo, M. Soma, Y. Oikawa, and T. Ishimizu, 2011: The Japanese 55-year Reanalysis "JRA-55": An Interim Report. *SOLA*, **7**, 149–152.

Egbert, G. D. and S. Y. Erofeeva, 2002: Efficient Inverse Modeling of Barotropic Ocean Tides. *J. Atmos. Oceanic Technol.*, **19**, 183–204.

Ehrendorfer, M., R. M. Errico, and K. D. Raeder, 1999: Singular-vector perturbation growth in a primitive equation model with moist physics. *J. Atmos. Sci.*, **56**, 1627–1648.

Elliott, A. J., 1986: Shear diffusion and the spread of oil in the surface layers of the North Sea. *Dt. Hydrogr. Zeit.*, **39**, 113–137.

Fingas, M. F., 1997: Studies on the evaporation of crude oil and petroleum products: I. The relationship between evaporation rate and time. *J. Hazrd. Mater.*, **56**, 227–236.

Folland, C. K. and D. E. Parker, 1995: Correction of instrumental biases in historical sea surface temperature data. *Quart. J. Roy. Meteor. Soc.*, **121**, 319–367.

Foster, D. J. and R. D. Davy, 1988: Global Snow Depth Climatology. Tech. Rep. USAF-ETAC/TN-88/006, Scott Air Force Base, Illinois. 48pp.

Frank, W. M., 1977: The structure and energetics of the tropical cyclone I. Storm structure. *Mon. Wea. Rev.*, **105**, 1119–1135.

Frank, W. M., 1984: A composite analysis of the core of a mature hurricane. *Mon. Wea. Rev.*, **112**, 2401–2420.

Freidenreich, S. M. and V. Ramaswamy, 1999: A new multiple-band solar radiative parameterization for general circulation models. *J. Geophys. Res.*, **104**, 31 389–31 409.

Fujii, Y. and M. Kamachi, 2003: A reconstruction of observed profiles in the sea east of Japan using vertical coupled temperature-salinity EOF modes. *J. Oceanogr.*, **59**, 173–186.

Fujita, T., 1952: Pressure Distribution within Typhoon. *Geophys. Mag.*, **23**, 437–451.

Gauthier, P. and J.-N. Thépaut, 2001: Impact of digital filter as a weak constraint in the preoparational 4DVAR assimilation system of Météo-France. *Mon. Wea. Rev.*, **129**, 2089–2102.

Geleyn, J.-F. and A. Hollingsworth, 1979: An economical analytical method for the computation of the interaction between scattering and line absorption of radiation. *Contrib. Atmos. Phys.*, **52**, 1–16.

Gent, P. R. and J. C. McWilliams, 1990: Isopycnal mixing in ocean circulation models. *J. Phys. Oceanogr.*, **20**, 150–155.

Gibson, J. K., P. Kållberg, S. Uppala, A. Hernandez, A. Noumura, and E. Serrano, 1997: *ERA Description*, Re-Analysis (ERA) Project Report Series, Vol. 1. European Centre for Medium-Range Weather Forecasts, Reading, UK, 77pp.

Godske, C. L. et al., 1957: *Dynamic Meteorology and Weather Forecasting*, chap. 18. Amer. Met. Soc.

Gregory, D., R. Kershaw, and P. M. Inness, 1997: Parameterization of momentum transport by convection. II: Tests in single-column and general circulation models. *Quart. J. Roy. Meteor. Soc.*, **123**, 1153–1183.

Griffies, S. M. and R. W. Hallberg, 2000: Biharmonic friction with a Smagorinsky-like viscosity for use in large-scale eddy-permitting ocean models. *Mon. Wea. Rev.*, **128**, 2935–2946.

Guenther, A., C. N. Hewitt, D. Erickson, R. Fall, C. Geron, T. Graedel, P. Harley, L. Klinger, M. Lerdau, W. A. McKay, T. Pierce, B. Scholes, R. Steinbrecher, R. Tallamraju, J. Taylor, and P. Zimmerman, 1995: A global model of natural volatile organic compound emissions. *J. Geophys. Res.*, **100**, 8873–8892.

Hansen, J. and M. Sato, 2004: Greenhouse gas growth rates. *Proc. Natl. Acad. Sci.*, **101**, 16 109–16 114.

Hasegawa, H., N. Kohno, and H. Hayashibara, 2012: JMA's Storm Surge Prediction for the WMO Storm Surge Watch Scheme (SSWS). *RSMC Tokyo-Typhoon Center Technical Review*, **14**, 13–24.

Hasselmann, S., K. Hasselmann, J. H. Allender, and T. P. Barnett, 1985: Computations and parameterizations of the nonlinear energy transfer in a gravity-wave spectrum. Part II: Parameterizations of the nonlinear energy transfer for application in wave models. *J. Phys. Oceanogr.*, **15**, 1378–1391.

Hasumi, H., 2006: CCSR Ocean Component Model (COCO) Version 4.0. CCSR Report 25, Center for Climate System Research, The University of Tokyo. 103pp.

Hibler, W. D., 1979: A dynamic thermodynamic sea ice model. *J. Phys. Oceanogr.*, **9**, 815–846.

Higaki, M., H. Hayashibara, and F. Nozaki, 2009: Outline of the storm surge prediction model at the Japan Meteorological Agency. *RSMC Tokyo-Typhoon Center Technical Review*, **11**, 25–38.

Holmlund, K., 1998: The utilization of statistical properties of satellite-derived atmospheric motion vectors to derive quality indicators. *Wea. Forecasting*, **13**, 1093–1104.

Honda, Y., M. Nishijima, K. Koizumi, Y. Ohta, K. Tamiya, T. Kawabata, and T. Tsuyuki, 2005: A pre-operational variational data assimilation system for a non-hydrostatic model at the Japan Meteorological Agency: Formulation and preliminary results. *Quart. J. Roy. Meteor. Soc.*, **131**, 3465–3475.

Hortal, M., 2002: The development and testing of a new two-time-level semi-Lagrangian scheme (SETTLS) in the ECMWF forecast model. *Quart. J. Roy. Meteor. Soc.*, **128**, 1671–1687.

Hoskins, B. J. and A. J. Simmons, 1975: A multi-layer spectral model and the semi-implicit method. *Quart. J. Roy. Meteor. Soc.*, **101**, 637–655.

Hunke, E. C. and J. K. Dukowicz, 1997: An elastic-viscous-plastic model for sea ice dynamics. *J. Phys. Oceanogr.*, **27**, 1849–1867.

Ikawa, M. and K. Saito, 1991: Description of a nonhydrostatic model developed at the Forecast Research Department of the MRI. *Tech. Rep. MRI*, **28**, 238pp.

Ikuta, Y. and Y. Honda, 2011: Development of 1D+4DVAR data assimilation of radar reflectivity in JNoVA. *CAS/JSC WGNE Res. Activ. Atmos. Oceanic Modell.*, **41**, 01.09–01.10.

Ishida, J., 2007: Development of a hybrid terrain-following vertical coordinate for JMA Non-hydrostatic Model. *CAS/JSC WGNE Res. Activ. Atmos. Oceanic Modell.*, **37**, 03.09–03.10.

Ishihara, M., Y. Kato, T. Abo, K. Kobayashi, and Y. Izumikawa, 2006: Characteristics and Performance of the Operational Wind Profiler Network of the Japan Meteorological Agency. *J. Meteor. Soc. Japan*, **84**, 1085–1096.

Ishii, M., A. Shouji, S. Sugimoto, and T. Matsumoto, 2005: Objective Analyses of Sea-Surface Temperature and Marine Meteorological Variables for the 20th Century using ICOADS and the Kobe Collection. *Int. J. Climatol.*, **25**, 865–879.

Ishikawa, I., H. Tsujino, M. Hirahara, H. Nakano, T. Yasuda, and H. Ishizaki, 2005: Meteorological Research Institute Community Ocean Model (MRI.COM) manual. *Technical Reports of the Meteorological Research Institute*, **47**, 189pp., (in Japanese).

Ishikawa, Y. and K. Koizumi, 2002: Meso-scale analysis. *Outline of the operational numerical weather prediction at the Japan Meteorological Agency. Appendix to WMO Technical Progress Report on the Global Data-processing and Forecasting System*, Tokyo, Japan, Japan Meteorological Agency, 26–31.

Iwamura, K. and H. Kitagawa, 2008: An upgrade of the JMA Operational Global NWP Model. *CAS/JSC WGNE Res. Activ. Atmos. Oceanic Modell.*, **38**, 06.3–06.4.

Iwasaki, T., T. Maki, and K. Katayama, 1998: Tracer transport model at Japan Meteorological Agency and its application to the ETEX data. *Atmos. Env.*, **32**, 4285–4295.

Iwasaki, T., S. Yamada, and K. Tada, 1989: A parameterization scheme of orographic gravity wave drag with two different vertical partitionings, Part I: Impact on medium-range forecasts. *J. Meteor. Soc. Japan*, **67**, 11–27.

Janssen, P., 2004: *The Interaction of Ocean Waves and Wind*. Cambridge Univ. Press, 308pp.

Japan Maritime Safety Agency, (Ed.) , 1983: *Nihonkinkai Kairyu Tokeizu (Statistical charts of ocean currents around Japan)*. Japan Maritime Safety Agency, (in Japanese).

Japan Meteorological Agency, 2006: Characteristics of Global Sea Surface Temperature Analysis Data (COBE-SST) for Climate Use. *Monthly Report on Climate System Separated Volume*, **12**, 116pp.

Jin, E. K., J. L. Kinter III, B. Wang, C.-K. Park, I.-S. Kang, B. P. Kirtman, J.-S. Kug, A. Kumar, J.-J. Luo, J. Schemm, J. Shukla, and T. Yamagata, 2008: Current status of ENSO prediction skill in coupled ocean-atmosphere models. *Clim. Dyn.*, **31**, 647–664.

JMA, 1997: Objective Interpretation of NWP Products. *Outline of the operational numerical weather prediction at the Japan Meteorological Agency. Appendix to WMO Technical Progress Report on the Global Data-processing and Forecasting System*, Japan Meteorological Agency, Tokyo, Japan, 123–124.

JMA, 2002: *Outline of the operational numerical weather prediction at the Japan Meteorological Agency. Appendix to WMO Technical Progress Report on the Global Data-processing and Forecasting System*. Japan Meteorological Agency, Tokyo, Japan.

JMA, 2007: *Outline of the operational numerical weather prediction at the Japan Meteorological Agency. Appendix to WMO Technical Progress Report on the Global Data-processing and Forecasting System and Numerical Weather Prediction Research*. Japan Meteorological Agency, Tokyo, Japan.

Jolliffe, I. T. and D. B. Stephenson, 2003: *Forecast Verification: A Practitioner's Guide in Atmospheric Science*. Wiley, 254pp.

Joseph, J. H., W. J. Wiscombe, and J. A. Weinman, 1976: The delta-Eddington approximation for radiative flux transfer. *J. Atmos. Sci.*, **33**, 2452–2459.

Juang, H.-M. H., 2004: A Reduced Spectral Transform for the NCEP Seasonal Forecast Global Spectral Atmospheric Model. *Mon. Wea. Rev.*, **132**, 1019–1035.

Kadowaki, T. and K. Yoshimoto, 2012: A new inner model with a higher horizontal resolution (TL319) in JMA's Global 4D-Var data assimilation system. *CAS/JSC WGNE Res. Activ. Atmos. Oceanic Modell.*, **42**, 01.09–01.10.

Kain, J. S., 2004: The Kain-Fritsch Convective Parameterization: An Update. *J. Appl. Meteor.*, **43**, 170–181.

Kain, J. S. and J. M. Fritsch, 1990: A one-dimensional entraining/detraining plume model and its application in convective parameterization. *J. Atmos. Sci.*, **47**, 2784–2802.

Kato, T., 1998: Numerical simulation of the band-shaped torrential rain observed southern Kyushu, Japan on 1 August 1993. *J. Meteor. Soc. Japan*, **76**, 97–128.

Kawai, H., 2002: Forecast of sulfur dioxide flow from Miyake volcano with a high resolution regional transport

model. *CAS/JSC WGNE Res. Activ. Atmos. Oceanic Modell.*, **32**, 05.24–05.25.

Kawai, H. and T. Inoue, 2006: A Simple Parameterization Scheme for Subtropical Marine Stratocumulus. *SOLA*, **2**, 17–20.

Kershaw, R. and D. Gregory, 1997: Parameterization of momentum transport by convection. I: Theory and cloud modelling results. *Quart. J. Roy. Meteor. Soc.*, **123**, 1133–1151.

Kessler, E., 1969: *On the distribution and continuity of water substance in atmospheric circulation*. Meteorol. Monogr., American Meteorol. Soc., Boston, MA, 84pp.

Kitada, T., 1994: Modelling of transport, reaction and deposition of acid rain. *Kishou Kenkyu Note*, **182**, 95–117, (in Japanese).

Kitada, T., G. R. Carmichael, and L. K. Peters, 1986: Effects of dry deposition on the concentration-distributions of atmospheric pollutants within land- and sea-breeze circulations. *Atmos. Env.*, **20**, 1999–2010.

Kohno, N., D. Miura, and K. Yoshita, 2011: The development of JMA wave data assimilation system. *Proceedings of the 12th International Workshop on Wave Hindcasting and Forecasting and Coastal Hazards Symposium*, Kohala Coast, Hawaii, 30 October - 4 November 2011, H2, (`http://www.waveworkshop.org`).

Kohno, N., K. Murotani, H. Minematsu, and D. Miura, 2009: The improvement of JMA operational wave forecasting system. *Proceedings of the 11th International Workshop on Wave Hindcasting and Forecasting and Coastal Hazards Symposium*, Halifax, Canada, 18 - 23 October 2009, R3, (`http://www.waveworkshop.org`).

Koizumi, K., Y. Ishikawa, and T. Tsuyuki, 2005: Assimilation of precipitation data to the JMA mesoscale model with a four-dimensional variational method and its impact on precipitation forecasts. *SOLA*, **1**, 45–48.

Kondo, J., 1975: Air-sea bulk transfer coefficients in diabatic conditions. *Bound.-Layer Meteor.*, **9**, 91–112.

Konishi, T., 1995: An experimental storm surge prediction for the western part of the Inland Sea with application to Typhoon 9119. *Pap. Meteor. Geophys.*, **46**, 9–17.

Kudo, A, 2011: Development of JMA's new turbulence index. *15th Conference on Aviation, Range, and Aerospace Meteorology*, Amer. Met. Soc., Los Angeles, CA, 1 - 4 August 2011.

Kuragano, T. and M. Kamachi, 2000: Global statistical space-time scales of oceanic variability estimated from the TOPEX/POSEIDON altimeter data. *J. Geophys. Res.*, **105**, 955–974.

Kurihara, Y., T. Sakurai, and T. Kuragano, 2006: Global daily sea surface temperature analysis using data from satellite microwave radiometer, satellite infrared radiometer and *in-situ* observations. *Weather Bulletin, JMA*, **73**, s1–s18.

Lin, Y.-L., R. D. Farley, and H. D. Orville, 1983: Bulk Parameterization of the Snow Field in a Cloud Model. *J. Climate Appl. Meteor.*, **22**, 1065–1092.

Liu, D. C. and J. Nocedal, 1989: On the limited memory BFGS method for large scale optimization. *Math. Programming*, **45**, 503–528.

Lord, S. J. and A. Arakawa, 1980: Interaction of a cumulus cloud ensemble with the large-scale environment. Part II. *J. Atmos. Sci.*, **37**, 2677–2692.

Louis, J.-F., M. Tiedtke, and J.-F. Geleyn, 1982: A short history of the operational PBL-parameterization at ECMWF. *Workshop on Planetary Boundary Layer Parameterization*, Reading, United Kingdom, 25 - 27 November 1981, ECMWF, 59–79.

Lyard, F., F. Lefèvre, T. Letellier, and O. Francis, 2006: Modelling the global ocean tides: Modern insights from FES2004. *Ocean Dyn.*, **56**, 394–415.

Lynch, P., 1997: The Dolph-Chebyshev Window: A Simple Optimal Filter. *Mon. Wea. Rev.*, **125**, 655–660.

Machenhauer, B., 1977: On the dynamics of gravity oscillations in a shallow water model, with application to normal mode initialization. *Contrib. Atmos. Phys.*, **50**, 253–271.

Mahfouf, J.-F., 1999: Influence of physical process on the tangent-linear approximation. *Tellus*, **51A**, 147–166.

Makihara, Y., 2000: Algorithms for precipitation nowcasting focused on detailed analysis using radar and raingauge data. *Technical Reports of the Meteorological Research Institute*, **39**, 63–111.

Matsumoto, K., T. Takanezawa, and M. Ooe, 2000: Ocean Tide Models Developed by Assimilating TOPEX/POSEIDON Altimeter Data into Hydrodynamical Model: A Global Model and a Regional Model around Japan. *J. Oceanogr.*, **56**, 567–581.

McFarquhar, G. M., S. Iacobellis, and R. C. J. Somerville, 2003: SCM Simulations of Tropical Ice Clouds Using Observationally Based Parameterizations of Microphysics. *J. Climate*, **16**, 1643–1664.

Mellor, G. L. and L. Kantha, 1989: An ice-ocean coupled model. *J. Geophys. Res.*, **94**, 10 937–10 954.

Mellor, G. L. and T. Yamada, 1974: A hierarchy of turbulence closure models for planetary boundary layers. *J. Atmos. Sci.*, **31**, 1791–1806.

Mellor, G. L. and T. Yamada, 1982: Development of a turbulence closure model for geophysical fluid problems. *Rev. Geophys. Space Phys.*, **20**, 851–875.

Mitsuyasu, H. and T. Honda, 1982: Wind-induced growth of water waves. *J. Fluid Mech.*, **123**, 425–442.

Miyamoto, K., 2006: Introduction of the Reduced Gaussian Grid into the Operational Global NWP Model at JMA. *CAS/JSC WGNE Res. Activ. Atmos. Oceanic Modell.*, **36**, 06.09–06.10.

Moorthi, S. and M. J. Suarez, 1992: Relaxed Arakawa-Schubert: A parameterization of moist convection for general circulation models. *Mon. Wea. Rev.*, **120**, 978–1002.

Moriyasu, S. and M. Narita, 2011: Modification of the Kain-Fritsch convective parameterization scheme in the Meso Scale Model. *CAS/JSC WGNE Res. Activ. Atmos. Oceanic Modell.*, **41**, 04.05–04.06.

Munk, W. H. and D. E. Cartwright, 1966: Tidal Spectroscopy and Prediction. *Phil. Trans. Roy. Soc. A*, **259**, 533–581.

Munro, R., C. Köpken, G. Kelly, J.-N. Thépaut, and R. Saunders, 2004: Assimilation of METEOSAT radiance data within the 4D-Var system at ECMWF: Data quality monitoring, bias correction and single-cycle experiments. *Quart. J. Roy. Meteor. Soc.*, **130**, 2293–2313.

Murphy, A. H., 1973: A New Vector Partition of the Probability Score. *J. Appl. Meteor.*, **12**, 595–600.

Naito, I. and N. Kikuchi, 1992: Atmospheric contributions to non-seasonal variations in the length of day. *Geophys. Res. Lett.*, **19**, 1843–1846.

Nakagawa, M., 2009: Outline of the High Resolution Global Model at the Japan Meteorological Agency. *RSMC Tokyo-Typhoon Center Technical Review*, **11**, 1–13.

Nakamura, H., 1978: Dynamical effects of mountains on the general circulation of the atmosphere: I. Development of finite-difference schemes suitable for incorporating mountains. *J. Meteor. Soc. Japan*, **56**, 317–340.

Nakanishi, M., 2001: Improvement of the Mellor-Yamada turbulence closure model based on large-eddy simulation data. *Bound.-Layer Meteor.*, **99**, 349–378.

Nakanishi, M. and H. Niino, 2004: An improved Mellor-Yamada level-3 model with condensation physics: Its design and verification. *Bound.-Layer Meteor.*, **112**, 1–31.

Nakanishi, M. and H. Niino, 2006: An improved Mellor-Yamada level-3 model: Its numerical stability and application to a regional prediction of advection fog. *Bound.-Layer Meteor.*, **119**, 397–407.

Nakanishi, M. and H. Niino, 2009: Development of an Improved Turbulence Closure Model for the Atmospheric Boundary Layer. *J. Meteor. Soc. Japan*, **87**, 895–912.

Noh, Y. and H.-J. Kim, 1999: Simulations of temperature and turbulence structure of the oceanic boundary layer with the improved near-surface process. *J. Geophys. Res.*, **104**, 15 621–15 634.

Nomura, A., 1998: *Global sea ice concentration data set for use with the ECMWF re-analysis system*. No. 4 in ECMWF Re-Analysis Project Series, ECMWF.

Ohara, T., H. Akimoto, J. Kurokawa, N. Horii, K. Yamaji, X. Yan, and T. Hayasaka, 2007: An Asian emission inventory of anthropogenic emission sources for the period 1980-2020. *Atmos. Chem. Phys.*, **7**, 4419–4444.

Olivier, J. G. J., A. F. Bouwman, C. W. M. van der Maas, J. J. M. Berdowski, C. Veldt, J. P. J. Bloos, A. J. H. Visschedijk, P. Y. J. Zandveld, and J. L. Haverlag, 1996: *Description of EDGAR version 2.0: A set of global emission inventories of greenhouse gases and ozone-depleting substances for all anthropogenic and most natural sources on a per country basis and on a 1 x 1 degree grid*. RIVM Rep. 771060 002/TNO-MEP Rep. R96/119, PBL Netherlands Environmental Assessment Agency.

Onogi, K., 1998: A Data Quality Control Method Using Forecasted Horizontal Gradient and Tendency in a NWP System: Dynamic QC. *J. Meteor. Soc. Japan*, **76**, 497–516.

Onogi, K., J. Tsutsui, H. Koide, M. Sakamoto, S. Kobayashi, H. Hatsushika, T. Matsumoto, N. Yamazaki, H. Kamahori, K. Takahashi, S. Kadokura, K. Wada, K. Kato, R. Oyama, T. Ose, N. Mannoji, and R. Taira, 2007: The JRA-25 Reanalysis. *J. Meteor. Soc. Japan*, **85**, 369–432.

Ou, S. and K.-N. Liou, 1995: Ice microphysics and climatic temperature feedback. *Atmos. Res.*, **35**, 127–138.

Palmer, T. N., G. J. Schutts, and R. Swinbank, 1986: Alleviation of a systematic westerly bias in general circulation and numerical weather prediction models through an orographic gravity wave drag parameterization. *Quart. J. Roy. Meteor. Soc.*, **112**, 1001–1039.

Parrish, D. and J. C. Derber, 1992: The National Meteorological Center's spectral statistical-interpolation analysis system. *Mon. Wea. Rev.*, **120**, 1747–1763.

Persson, A. O., 1991: Kalman Filtering - A new approach to adaptive statistical interpretation of numerical meteorological forecasts. *WMO Technical Document*, **421**, XX27–XX32.

Plant, W. J., 1982: A relationship between wind stress and wave slope. *J. Geophys. Res.*, **87**, 1961–1967.

Purser, R. J., W. S. Wu, D. F. Parrish, and N. M. Roberts, 2003: Numerical aspects of the application of recursive filters to variational statistical analysis. Part I: Spatially homogeneous and isotropic Gaussian covariances. *Mon. Wea. Rev.*, **131**, 1524–1535.

Räisänen, P., 1998: Effective longwave cloud fraction and Maximum-Random overlap of clouds: A problem and a solution. *Mon. Wea. Rev.*, **126**, 3336–3340.

Randall, D. and D.-M. Pan, 1993: Implementation of the Arakawa-Schubert cumulus parameterization with a prognostic closure. *The representation of cumulus convection in numerical models, AMS Meteorological Monograph Series*, **46**, 137–144.

Ray, R. D, 1999: A Global Ocean Tide Model From TOPEX/POSEIDON Altimetry: GOT99.2. Technical Memorandum NASA/TM-1999-209478, Goddard Space Flight Center. 58pp.

Reed, M., 1989: The physical fates component of the natural resource damage assessment model system. *Oil and Chemical Pollution*, **5**, 99–123.

Reynolds, R. W., 1987: A real-time global sea surface temperature analysis. *J. Climate*, **1**, 75–86.

Reynolds, R. W. and T. M. Smith, 1994: Improved Global Sea Surface Temperature Analyses Using Optimum Interpolation. *J. Climate*, **7**, 929–948.

Robert, A. J., 1966: The integration of a low order spectral form of the primitive meteorological equations. *J. Meteor. Soc. Japan*, **44**, 237–245.

Rothman, L. S., A. Barbe, D. C. Benner, L. R. Brown, C. Camy-Peyret, M. R. Carleer, K. Chance, C. Clerbaux, V. Dana, V. M. Devi, A. Fayt, J.-M. Flaud, R. R. Gamache, A. Goldman, D. Jacquemart, K. W. Jucks, W. J. Lafferty, J.-Y. Mandin, S. T. Massie, V. Nemtchinov, D. A. Newnham, A. Perrin, C. P. Rinsland, J. Schroeder, K. M. Smith, M. A. H. Smith, K. Tang, R. A. Toth, J. Vander Auwera, P. Varanasi, and K. Yoshino, 2003: The HITRAN molecular spectroscopic database: edition of 2000 including updates through 2001. *J. Quant. Spectrosc. Radiat. Transfer*, **82**, 5–44.

Saito, K., 1997: Semi-implicit fully compressible version of the MRI mesoscale nonhydrostatic model - Forecast experiment of the 6 August 1993 Kagoshima torrential rain. *Geophys. Mag. Ser.*, **2**, 109–137.

Saito, K. and J. Ishida, 2005: Implementation of the targeted moisture diffusion to JMA-NHM. *CAS/JSC WGNE Res. Activ. Atmos. Oceanic Modell.*, **35**, 05.17–05.18.

Saito, K., J. Ishida, K. Aranami, T. Hara, T. Segawa, M. Narita, and Y. Honda, 2007: Nonhydrostatic Atmospheric Models and Operational Development at JMA. *J. Meteor. Soc. Japan*, **85B**, 271–304.

Saito, K., T. Fujita, Y. Yamada, J. Ishida, Y. Kumagai, K. Aranami, S. Ohmori, R. Nagasawa, S. Kumagai, C. Muroi, T. Kato, H. Eito, and Y. Yamazaki, 2006: The Operational JMA Nonhydrostatic Mesoscale Model. *Mon. Wea. Rev.*, **134**, 1266–1298.

Sato, N., P. J. Sellers, D. A. Randall, E. K. Schneider, J. Shukla, J. L. Kinter III, Y-T Hou, and E. Albertazzi, 1989a: Effects of implementing the simple biosphere model (SiB) in a general circulation model. *J. Atmos. Sci.*, **46**, 2757–2782.

Sato, N., P. J. Sellers, D. A. Randall, E. K. Schneider, J. Shukla, J. L. Kinter III, Y-T Hou, and E. Albertazzi, 1989b: Implementing the simple biosphere model (SiB) in a general circulation model: Methodologies and results. NASA contractor Rep. 185509, NASA. 76pp.

Saunders, R., J. Hocking, P. Rayer, M. Matricardi, A. Geer, N. Bormann, P. Brunel, F. Karbou, and F. Aires, 2012: RTTOV-10 science and validation report. Tech. rep., EUMETSAT, 31 pp. (`http://research.metoffice.gov.uk/research/interproj/nwpsaf/rtm/docs_rttov10/rttov10_svr_1.11.pdf`).

Sekiyama, T. T. and K. Shibata, 2005: Predictability of total ozone using a global three-dimensional chemical transport model coupled with MRI/JMA98 GCM. *Mon. Wea. Rev.*, **133**, 2262–2274.

Sellers, P. J., Y. Mintz, Y. C. Sud, and A. Dalcher, 1986: A simple biosphere model (SiB) for use within general circulation models. *J. Atmos. Sci.*, **43**, 505–531.

Semtner, A. J., 1976: A model for the thermodynamic growth of sea ice in numerical investigation of climate. *J. Phys. Oceanogr.*, **6**, 379–389.

Shibata, K., M. Deushi, T. T. Sekiyama, and H. Yoshimura, 2005: Development of an MRI Chemical Transport Model for the Study of Stratospheric Chemistry. *Pap. Meteor. Geophys.*, **55**, 75–119.

Shibata, K., H. Yoshimura, M. Ohizumi, M. Hosaka, and M. Sugi, 1999: A simulation of troposphere, stratosphere and mesosphere with an MRI/JMA98 GCM. *Pap. Meteor. Geophys.*, **50**, 15–53.

Simmons, A. J. and D. M. Burridge, 1981: An energy and angular-momentum conserving vertical finite-difference scheme and hybrid vertical coordinates. *Mon. Wea. Rev.*, **109**, 758–766.

Simonsen, C., 1991: Self adaptive model output statistics based on Kalman filtering. *WMO Technical Document*, **421**, XX33–XX37.

Skamarock, W. C. and J. B. Klemp, 1992: The stability of time-split numerical methods for the hydrostatic and the nonhydrostatic elastic equation. *Mon. Wea. Rev.*, **120**, 2109–2127.

Slingo, A., 1989: A GCM parameterization for the shortwave radiative properties of water clouds. *J. Atmos. Sci.*, **46**, 1419–1427.

Smagorinsky, J., 1963: General circulation experiments with the primitive equations I. The basic experiment. *Mon. Wea. Rev.*, **91**, 99–164.

Smith, R. N. B., 1990: A scheme for predicting layer clouds and their water content in a general circulation model. *Quart. J. Roy. Meteor. Soc.*, **116**, 435–460.

Smith, S. D. and E. G. Banke, 1975: Variation of the sea surface drag coefficient with wind speed. *Quart. J. Roy. Meteor. Soc.*, **101**, 665–673.

Sommeria, G. and J. W. Deardorff, 1977: Subgrid-scale condensation in models of nonprecipitating clouds. *J. Atmos. Sci.*, **34**, 344–355.

Sundqvist, H., 1978: A parameterization scheme for non-convective condensation including prediction of cloud water content. *Quart. J. Roy. Meteor. Soc.*, **104**, 677–690.

Sundqvist, H., E. Berge, and J. E. Kristjánsson, 1989: Condensation and cloud parameterization studies with a mesoscale numerical weather prediction model. *Mon. Wea. Rev.*, **117**, 1641–1657.

Takeuchi, Y. and T. Kurino, 1997: Document of algorithm to derive rain rate and precipitation with SSM/I and AMSR. *Algorithm description of PIs for SSM/I and ADEOS-II/AMSR, 2nd AMSR Workshop*, Tokyo, Japan, 61.1–61.9.

Tanaka, T. Y., K. Orito, T. T. Sekiyama, K. Shibata, M. Chiba, and H. Tanaka, 2003: MASINGAR, a global tropospheric aerosol chemical transport model coupled with MRI/JMA98 GCM: Model description. *Pap. Meteor. Geophys.*, **53**, 119–138.

Tanguay, M., E. Yakimiw, H. Ritchie, and A. Robert, 1992: Advantage of spatial averaging in semi-implicit semi-Lagrangian schemes. *Mon. Wea. Rev.*, **120**, 113–123.

The WAMDI Group, 1988: The WAM model—A third generation ocean wave prediction model. *J. Phys. Oceanogr.*, **18**, 1775–1810.

Tiedtke, M., 1993: Representation of Clouds in Large-Scale Models. *Mon. Wea. Rev.*, **121**, 3040–3061.

Toth, Z. and E. Kalnay, 1993: Ensemble Forecasting at NMC: The Generation of Perturbations. *Bull. Amer. Meteor. Soc.*, **74**, 2317–2330.

Toth, Z. and E. Kalnay, 1997: Ensemble Forecasting at NCEP and the Breeding Method. *Mon. Wea. Rev.*, **125**, 3297–3319.

Tsujino, H., T. Motoi, I. Ishikawa, M. Hirabara, H. Nakano, G. Yamanaka, T. Yasuda, and H. Ishizaki, 2010: Reference Manual for the Meteorological Research Institute Community Ocean Model (MRI.COM) Version 3. Technical Reports of the Meteorological Research Institute 59, Meteorological Research Institute of Japan Meteorological Agency, Ibaraki, Japan. 241pp. (`http://www.mri-jma.go.jp/Publish/Technical/DATA/VOL_59/59_en.html`).

Udin, I. and A. Ullerstig, 1976: A numerical model for forecasting the ice motion in the Bay and Sea of Bosnia. *SMHI MMK*, **6**, 1–40.

Ueno, K., 1998: An energy dissipation term in a numerical prediction wave model. *Sokkou-Jihou*, **65**, S181–

S187, (in Japanese).

Undén, P., L. Rontu, H. Järvinen, P. Lynch, J. Calvo, G. Cats, J. Cuxart, K. Eerola, C. Fortelius, J. A. Garcia-Moya, C. Jones, G. Lenderlink, A. McDonald, R. McGrath, B. Navascues, N. W. Nielsen, V. Ødegaard, E. Rodriguez, M. Rummukainen, R. Rõõm, K. Sattler, B. H. Sass, H. Savijärvi, B. W. Schreur, R. Sigg, H. The, and A. Tijm, 2002: *HIRLAM-5 Scientific Documentation*. HIRLAM-5 Project, Swedish Meteorological and Hydrological Institute, 144pp.

Usui, N., S. Ishizaki, Y. Fujii, H. Tsujino, T. Yasuda, and M. Kamachi, 2006: Meteorological Research Institute multivariate ocean variational estimation (MOVE) system: Some early results. *Adv. Space Res.*, **37**, 806–822.

Veersé, F., D. Auroux, and M. Fisher, 2000: Limited-memory BFGS diagonal preconditioners for a data assimilation problem in meteorology. *Optimization and Engineering*, **1**, 323–339.

Wilks, D. S., 2006: *Statistical Methods in the Atmospheric Sciences, Second Edition*, International Geophysics Series, Vol. 91. Academic Press, 648pp.

Willmott, C. J., C. M. Rowe, and Y. Mintz, 1985: Climatology of the terrestrial seasonal water cycle. *J. Climatology*, **5**, 589–606.

WMO, 1993: *Guide on the Global Data-processing System*. WMO-No.305, World Meteorological Organization.

WMO, 2010a: *Manual on the Global Data-processing and Forecasting System Volume I - Global Aspects, Updated in 2012*. World Meteorological Organization.

WMO, 2010b: Standardized Verification System (SVS) for Long-Range Forecasts (LRF), Attachment II-8. *Manual on the Global Data-processing and Forecasting System Volume I - Global Aspects, Updated in 2012*, World Meteorological Organization.

WMO, 2012: *Final Report of the Coordination Group on Forecast Verification (CG-FV)*. Commission for Basic Systems (CBS), WMO, Reading, UK, 15 - 17 May 2012.

Wurtele, M. G., R. D. Sharman, and T. L. Keller, 1987: Analysis and simulations of a troposphere-stratosphere gravity wave model. Part I. *J. Atmos. Sci.*, **44**, 3269–3281.

Wyser, K., 1998: The effective radius in ice clouds. *J. Climate*, **11**, 1793–1802.

Xie, S. C.. and M. H. Zhang, 2000: Impact of the convection triggering function on single-column model simulations. *J. Geophys. Res.*, **105**, 14 983–14 996.

Yamaguchi, M., R. Sakai, M. Kyoda, T. Komori, and T. Kadowaki, 2009: Typhoon Ensemble Prediction System Developed at the Japan Meteorological Agency. *Mon. Wea. Rev.*, **137**, 2592–2604.

Yanagino, K. and S. Takada, 1995: Quantitative Analysis and Application to Weather Prediction by Neural Networks. *Technical Report of IEICE*, **NC95-37**, 63–70, (in Japanese).

Yoshimura, H., 2002: Development of a Semi-Implicit Semi-Lagrangian Global Model using Double Fourier Series. *The 4th International Workshop on Next Generation Climate Models for Advanced High Performance Computing Facilities.*, NCAR, Boulder, Colorado, 12 - 14 March 2002.

Yoshimura, H. and T. Matsumura, 2003: A Semi-Lagrangian Scheme Conservative in the Vertical Direction. *CAS/JSC WGNE Res. Activ. Atmos. Oceanic Modell.*, **33**, 03.19–03.20.

Yoshimura, H. and T. Matsumura, 2004: Semi-Lagrangian Toitsu model. *Report of Numerical Prediction Division (Suuchiyohouka Houkoku Bessatsu Houkoku)*, **50**, 51–60, (in Japanese).

Zhong, W. and J. D. Haigh, 1995: Improved broadband emissivity parameterization for water vapor cooling rate calculations. *J. Atmos. Sci.*, **52**, 124–138.

List of Authors

TAKEUCHI, Yoshiaki	Director, Numerical Prediction Division	Preface
EITO, Hisaki	Numerical Prediction Division	Subsection 3.5.4
FUJIEDA, Tsuyoshi	Editor, Numerical Prediction Division	Subsection 3.2.13, Section 3.9, Appendix A
FUJITA, Tadashi	Numerical Prediction Division	Subsection 2.6.1, Subsection 2.6.3.2 Subsection 2.7.1, Subsection 2.7.3, Section 4.5
FURUKAWA, Takahiro	Numerical Prediction Division	Subsection 3.2.9
HAMADA, Keiji	Office of Marine Prediction	Section 5.6
HARA, Tabito	Numerical Prediction Division	Subsection 3.5.1, Subsection 3.5.2, Subsection 3.5.6 Subsection 3.5.7, Subsection 3.5.10, Section 3.6
HASEGAWA, Hiroshi	Office of Marine Prediction	Section 5.5, Subsection 5.5.1, Subsection 5.5.2
HAYASHI, Yosuke	Numerical Prediction Division	Subsection 3.2.2, Subsection 3.2.10
HAYASHI, Yuuta	Numerical Prediction Division	Subsection 2.6.2
HAYASHIBARA, Hironori	Office of Marine Prediction	Subsection 5.5.3
HIRAI, Masayuki	Climate Prediction Division	Subsection 4.8.2
ISHII, Kensuke	Numerical Prediction Division	Subsection 2.6.3.1
ISHIKAWA, Ichiro	Climate Prediction Division	Section 5.1, Subsection 5.2.2, Section 5.3
ISHIZAKI, Shiro	Office of Marine Prediction	Section 5.2, Subsection 5.2.1
KADOWAKI, Takashi	Numerical Prediction Division	Section 2.5
KANEHAMA, Takafumi	Numerical Prediction Division	Subsection 3.2.8
KANESHIRO, Kaoru	Forecast Division	Subsection 4.8.1
KAWANO, Kouhei	Numerical Prediction Division	Subsection 3.5.3
KINAMI, Teppei	Numerical Prediction Division	Section 4.9
KINOSHITA, Nobumiki	Numerical Prediction Division	Subsection 2.7.2
KOHNO, Nadao	Office of Marine Prediction	Section 5.4, Section 5.7
KUMAGAI, Saori	Forecast Division	Section 4.4
KUSABIRAKI, Hiroshi	Numerical Prediction Division	Subsection 3.5.8, Subsection 3.5.9
KYOUDA, Masayuki	Numerical Prediction Division	Section 3.3
MATSUBAYASHI, Kengo	Numerical Prediction Division	Subsection 3.5.11
MATSUSHITA, Yasuhiro	Numerical Prediction Division	Section 4.1, Section 4.6, Section 4.7
MORIYASU, Satoshi	Numerical Prediction Division	Subsection 3.5.5
MUROI, Chiashi	Editor, Numerical Prediction Division	Section 2.1, Section 3.1
NAKAGAWA, Masayuki	Numerical Prediction Division	Subsection 3.2.1, Subsection 3.2.4, Subsection 3.2.5
NARITA, Masami	Numerical Prediction Division	Chapter 1
OCHI, Kenta	Numerical Prediction Division	Subsection 3.5.11
ONO, Kousuke	Numerical Prediction Division	Subsection 2.6.3.3
ONOGI, Kazutoshi	Climate Prediction Division	Section 2.10
SAKAMOTO, Masami	Numerical Prediction Division	Section 3.7
SATO, Yoshiaki	Numerical Prediction Division	Section 2.2, Section 2.3, Section 2.4, Subsection 2.5.7 Subsection 2.6.4, Subsection 2.7.4, Section 2.9
SEKIGUCHI, Ryohei	Numerical Prediction Division	Subsection 3.2.3
TADA, Hideo	Forecast Division	Subsection 4.6.4
TAKAYA, Yuhei	Climate Prediction Division	Section 3.4
TOKUHIRO, Takayuki	Climate Prediction Division	Section 3.3
TOYODA, Eizi	Numerical Prediction Division	Section 4.2, Section 4.3
YAMADA, Kazutaka	Atmospheric Environment Division	Section 3.8
YAMAGUCHI, Haruki	Numerical Prediction Division	Section 3.3
YONEHARA, Hitoshi	Numerical Prediction Division	Section 2.8, Subsection 3.2.11, Subsection 3.2.12 Subsection 3.2.6, Subsection 3.2.7
YOSHITA, Kumi	Office of Marine Prediction	Section 5.4

Outline of the Operational Numerical Weather Prediction at the Japan Meteorological Agency

—— Appendix to WMO Technical Progress Report on the Global Data-processing and Forecasting System (GDPFS) and Numerical Weather Prediction (NWP) Research ——

19 March 2013
Japan Meteorological Agency
1-3-4 Otemachi, Chiyoda-ku, Tokyo 100-8122, Japan